MAX-PLANCK-INSTITUT FÜR RADIOASTRONOMIE BONN

A LAsMA SURVEY OF THE MILKY WAY

Effects of Feedback on Molecular Clouds

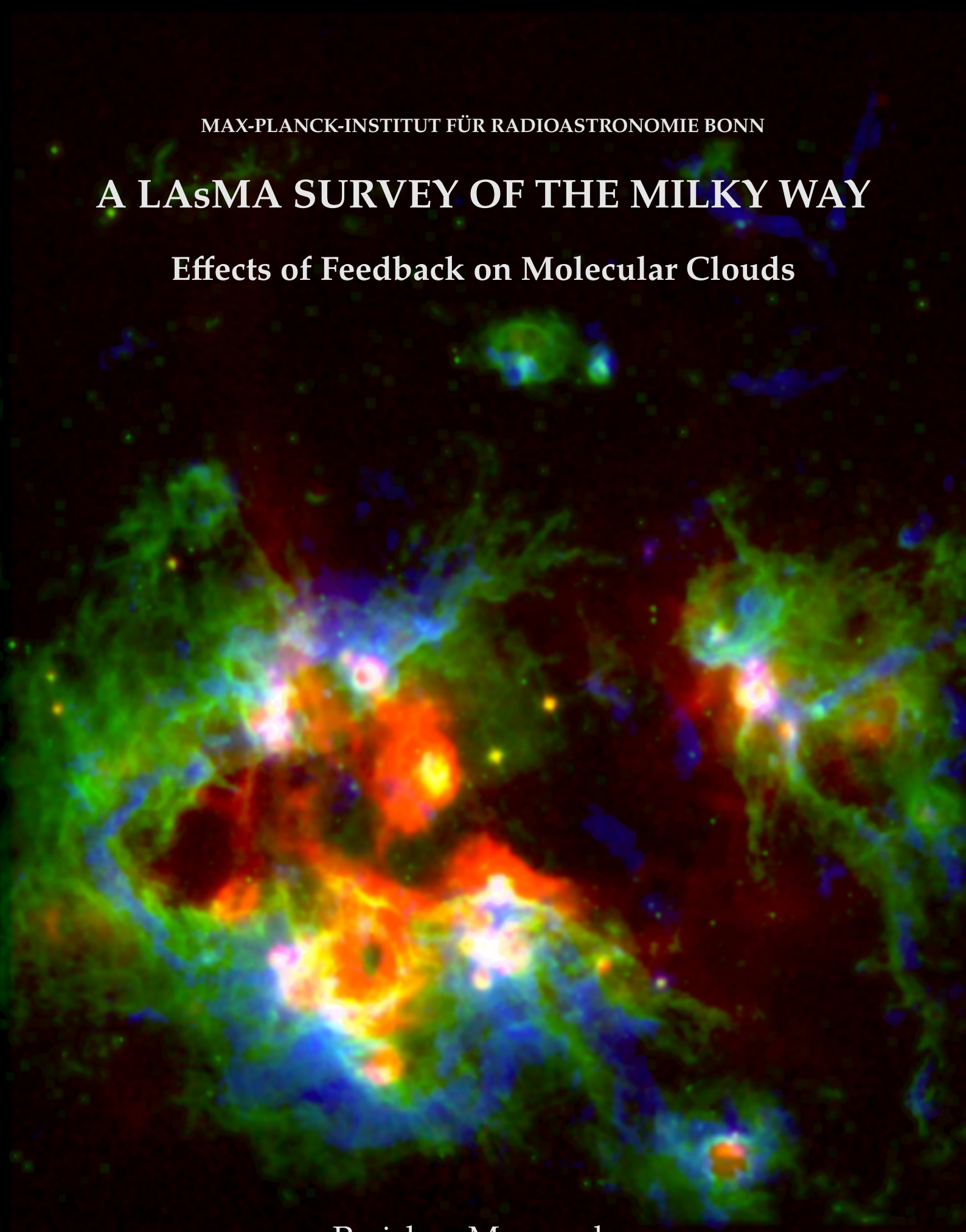

Parichay Mazumdar

2022

MAX–PLANCK–INSTITUT FÜR RADIOASTRONOMIE
BONN

A LAsMA Survey of the Milky Way
Effects of Feedback on Molecular Clouds

Dissertation

zur

Erlangung des Doktorgrades (*Dr. rer. nat.*)

der

Mathematisch–Naturwissenschaftlichen Fakultät

der

Rheinischen Friedrich–Wilhelms–Universität Bonn

vorgelegt von
Parichay Mazumdar
aus
Bargarh, Indien

Bonn 2022

Angefertigt mit Genehmigung der Mathematisch-Naturwissenschaftlichen Fakultät
der Rheinischen Friedrich–Wilhelms–Universität Bonn

1. Gutachter / *1st Reviewer*: Prof. Dr. Karl M. Menten
2. Gutachter / *2nd Reviewer*: Prof. Dr. Pavel Kroupa

Tag der Promotion / *Conferral Date*: 29.08.2022
Erscheinungsjahr / *Year of Publication*: 2022

RHEINISCHE FRIEDRICH–WILHELMS–UNIVERSITÄT BONN

Abstract

by Parichay Mazumdar

for the degree of

Doctor rerum naturalium

The advent of radio and (sub)millimeter astronomy has opened the world of molecular clouds (MCs) to astronomers' wonder. At the turn of the 21st century, MC surveys have helped us better understand them. How MCs form, their morphology, physical conditions, and many other aspects are active research areas. This dissertation takes another step toward understanding MCs by conducting the first large-scale high-resolution survey of giant molecular clouds (GMCs) in the Milky Way (LAsMAGal), covering ^{12}CO and ^{13}CO (3−2) lines simultaneously.

Part I and II provide an overview of the background knowledge related to molecular clouds and the star-formation theory and introduce the new 7-pixel receiver (LAsMA) used for the survey. The commissioning tests done on the instruments are also presented in part II.

In Part III, we examine if LAsMAGal is feasible and test observing strategies. The test observations showed 4 fold improvement in noise levels compared to the SEDIGISM ^{13}CO (2–1) survey (the most relevant survey towards the planned region for LAsMAGal).

Part IV presents LAsMAGal data towards the G305 star-forming GMC used to study feedback effects from the central cluster of OB stars. The distribution of CO excitation was compared to that of 8 μm emission imaged with Spitzer (dominated by UV-excited emission from polycyclic aromatic hydrocarbons). A ^{13}CO J = 3-2/2-1 excitation map was obtained by combining LAsMAGal and SEDIGISM data. Line profiles along radially outward directions showed a factor of $\sim$ 2–3 increase in gas excitation temperature as well as ^{13}CO J = 3-2/2-1 ratio at the GMC edge facing the center of the complex. Excitation temperature, J = 3-2/2-1 ratio and column density showed a positive correlation with 8 μm flux. Centroid velocities and stacked line profiles were examined to investigate the feedback effect on gas dynamics. The velocity probability distribution function displayed exponential wings, indicating turbulence driven by strong stellar winds. Stacked spectra in regions with stronger feedback had higher skewness than regions with weaker feedback. Therefore, feedback from the stellar cluster in G305 shows demonstrable effects on the gas excitation and dynamics of the GMC.

The next chapter investigates the effects of feedback on star formation in G305. First, the region is decomposed into clumps using dendrogram analysis. Their surface mass densities (Σ) positively correlated with incident 8 μm flux. Clumps were categorized into "mostly inside" (>67%), "partly inside" (10%>; <67%), and "outside" (<10%) subsamples

based on their overlap with an 8 μm flux mask. The 3 subsamples had a statistically significant difference in Σ. The “mostly inside" subsample also showed the highest level of fragmentation proving G305 clumps are triggered. Then, G305 clumps were compared with the Galactic average taken from a distance-limited sample of ATLASGAL 870 μm dust continuum and CHIMPS ^{13}CO (3–2) clumps. The G305 clump population was statistically different from the average Galactic population, ruling out redistribution due to feedback. Finally, the cumulative distribution functions (CDFs) of the clump masses and L/M ratios in G305 were compared to values of the Galactic sample. The CDFs were flatter in G305, indicating that clumps are heavier and more efficient at forming stars in G305, driving triggered star formation in this GMC.

The final part of the thesis updates the current status of LAsMAGal. The reduction pipeline is also presented, followed by the maps of the regions observed so far. Finally, a summary of the work is given in the final chapter.

To the phone call that made me turn left.

Calvin: *If people sat outside and looked at the stars each night, I'll bet they'd live a lot differently.*

Hobbes: *How so?*

Calvin: *Well, when you look into infinity, you realize that there are more important things than what people do all day.*

– Bill Watterson, Calvin and Hobbes

Acknowledgements

My journey of doing a Ph.D. at the MPIfR began much before the actual starting date. During my bachelor's studies, I did my first ever summer project at the National Center for Radio Astrophysics in Pune, India, during the summer of 2013. Working with Prof. Nissim Kanekar, I fell in love with radioastronomy. And for that, I would always be indebted to you, Nissim. You have been an absolute inspiration and role model for me. Thank you for engendering my love for research.

After my bachelor studies, I decided to move to Bonn to pursue a Master's degree in Physics at the Bonn-Cologne Graduate School (BCGS). It was the first time I had stepped foot outside my own country. It was a big culture shock. But, thanks to other students who were on a similar journey as I, the adjustment felt a little easier. Leo, Frankie, Bea, Urmi, Chuck, Smaran, Aditya, and last but in no way the least, Julia, thanks for making the transition to a whole new country a little easier. Julia, you left too soon, but I will always keep you close to my heart!

The work I did during my Ph.D. would not have been possible without the help of a lot of people from the MPIfR. First of all, I would like to thank Karl and Friedrich for being very supportive supervisors and believing in me and my work. Thank you for giving me the freedom to do independent research and, at the same time, treating me as a fellow researcher. I feel fortunate to have you guide me through my Ph.D. I could not have asked for better role models. Dario and James, thank you so much for teaching me the art of research and writing academic papers. Arnaud, thanks for teaching me how to operate APEX while keeping meticulous notes. A special thanks to all the APEX staff for making the observing trips extremely fun.

Working at the institute would not have been as fun if not for the supportive friends and colleagues I was blessed with. Hans, Nina, Dat, Rohit, Laure, and Vaselina, thank you for your friendship and support during all these years. MPIfR would not have been the same without you guys. Dat, thanks for being an awesome office mate! Rohit, thanks for being the best roommate I could have hoped for.

I would also like to express my heartfelt gratitude to all the non-scientific staff at MPIfR for taking care of all the organizational stuff. Without you all, we would all fall apart! Eva and Le, special thanks to you for organizing all the trips, contracts, and other paperwork with the utmost compassion and care. You made me feel welcome at the institute.

Then there is life outside of the world of physics. I am very blessed to have so many people who have enriched my life during these past years. Rahul, thanks for being the best neighbor and friend I could have asked for. I loved our late-night rants and discussions and your raging at FIFA. You have grown tremendously over these years, and I am proud of you! Charlie, thanks for being a tremendous friend over the last seven years and introducing me to the world of the Erasmus Student Network, where I made some of the wildest memories during my stay in Germany. Also, thanks for making the bouldering sessions fun (well, at least for others!) with your twister board.

Daphne, Ivan, Dome, and Seba, I will cherish all the times spent together. You made my life a whole lot easier during a difficult phase. Thanks for spending hours at ULB and taking me dancing to Carpe. Look at us all now, all grown up. Paloma and Vanessa, thank you for your constant support and Mensa lunches and hangouts and simply being there for me. Paula, Elisa, Nicole, and Till, thank you for the weekly board game nights. Cheers to the trip to Till's uncle's mansion. Our Spain trip is long overdue. Irene, Sonia, and Merlin, thanks for traveling from Cologne all the time just to hang out. You guys made a lot of my weekends fun. Imke, Bregje, Ruben, Niels, and Sebastian, thank you for escaping to the magical world of D&D with me. You guys are the best group of friends I did not foresee making pre-lockdown. I will always cherish Thorik, Harax, Pepin, and Goli. Do not forget, never pet an owlbear or lick gelatinous stuff.

Renate and Michael, thank you for providing me with a beautiful home here in Bonn. Johanna, Marcus, and Bettina, thanks for being the best neighbors ever. I will always cherish our hangouts together.

Ms. Erken, thank you for helping me navigate a difficult time in my life and become a better version of myself. The things I have learned from you will always be with me for the rest of my life.

Estera, thank you for being the best of the best of friends during the past few years. I cherish your enthusiasm and positivity. I hope you always stay the same (of course not, the sky is the limit for you, dear friend!). You are a bright ray of sunshine. I hope we never drift apart.

André and Nelly, I would like to thank you for providing me with a family away from my family. You have made me feel like I have a second home here in Europe. And also, thanks for the pancake restaurant vouchers. Nelly, I hope to learn sewing one day so that I don't bring my jumpers to get them fixed anymore.

Maa and Baba, you have always been an inspiration and motivation. I would not be the person I am today if not for all the values you have instilled in me throughout my life. I love you!

Imke, I wanted to save the best for the last. We both know life went through ups and downs over the past five years. The biggest reason why I am here today with a Ph.D. thesis in my hands is that you believed in me even when I did not. But at the same time, you did not hesitate to show some tough love if I was slacking. I have to fill up a book if I earnestly had to thank you for all you have done for me. And since I can't do that here, I would say just this; I am glad I took a chance and caught that train to Linz am Rhein. You make me wanna be better every day. Love you loads, you purple unicorn (sparkles, sparkles).

Contents

List of Figures

List of Tables

List of publications

Related to this thesis

1. High resolution LAsMA ^{12}CO and ^{13}CO observation of the G305 giant molecular cloud complex. I. Feedback on the molecular gas.
Mazumdar, P.; Wyrowski, F.; Colombo, D.; Urquhart, J. S.; Thompson, M. A.; Menten, K. M.; A&A 650, A164 (2021), DOI: 10.1051/0004-6361/202040205 [arxiv:2105.11703].

2. High resolution LAsMA ^{12}CO and ^{13}CO observation of the G305 giant molecular cloud complex. II. Effect of feedback on clump properties.
Mazumdar, P.; Wyrowski, F.; Urquhart, J. S.; Colombo, D.; Menten, K. M.; Neupane, S.; Thompson, M. A., A&A 656, A101 (2021), DOI: 10.1051/0004-6361/202142036 [arXiv:2109.09615].

Other co-authored publications

1. The SEDIGISM survey: Molecular cloud morphology. II. Integrated source properties.
Neralwar, K. R., Colombo, D., ..., **Mazumdar, P.**, ... et al., A&A, accepted., in print (2022), eprint arXiv:2205.02253

2. The SEDIGISM survey: Molecular cloud morphology. I. Classification and star formation.
Neralwar, K. R., Colombo, D., ..., **Mazumdar, P.**, ... et al., A&A, accepted., in print (2022), eprint arXiv:2203.02504

3. The SEDIGISM survey: a search for molecular outflows.
Yang, A. Y., Urquhart, J. S., ..., **Mazumdar, P.**, ... et al., A&A, 658, A160 (2022)

4. OGHReS: Large-scale filaments in the outer Galaxy.
Colombo, D., König, C., ..., **Mazumdar, P.**, ... et al., A&A, 655, L2 (2021)

5. The SEDIGISM survey: molecular clouds in the inner Galaxy.
Duarte-Cabral, A., Colombo, D., ..., **Mazumdar, P.**, ... et al., MNRAS, 500, 3027 (2021)

6. The SEDIGISM survey: First Data Release and overview of the Galactic structure.
Schuller, F., Urquhart, J. S., ..., **Mazumdar, P.**, ... et al., MNRAS, 500, 3064 (2021)

7. Terahertz Water Masers. II. Further SOFIA/GREAT Detections Toward Circumstellar Outflows, and a Multitransition Analysis.
Neufeld, D. A., Menten, K. M., ..., **Mazumdar, P.**, ... et al., ApJ, 907, 42 (2021)

8. A Giant Water Maser Flare in the Galactic Source IRAS 18316-0602.
Vol'vach, L. N., Vol'vach, A. E., ..., **Mazumdar, P.**, Schuller, F., Astronomy Reports, 63, 49 (2019)

Nomenclature

Frequently used symbols

A_{ij}	Einstein's A coefficient
α_{2000}	Right ascension
c	Speed of light
δ_{2000}	Declination
E	Energy
η_{mb}	Main beam efficiency
f	Filling factor
g	Statistical weight (g factor)
G	Gravitational constant
h	Planck's constant
J	Orbital angular momentum
k_B	Boltzmann's constant
λ	Wavelength
L	Luminosity
μ	Reduced mass
M	Mass
ν	Frequency
n	Numerical density
N	Column density
r, d	Distance
σ	RMS noise (or surface accuracy, or collisional cross section)
τ	Optical depth
t	Time
T	Temperature
α_{vir}	Virial parameter
θ	Beam size
v	Velocity

Numerical constants

arcminute (1′)	$= 60'' = \frac{1}{60}{}^\circ = \frac{1}{10800}$ rad
π	$= 3.14156$

Physical constants

Speed of light	$c = 299\,792\,458\,\mathrm{m\,s^{-1}} \approx 173\,\mathrm{AU\,day^{-1}}$
Gravitational constant	$G = 6.67430(15) \times 10^{-11}\,\mathrm{m^3\,kg^{-1}\,s^{-2}} = 4.30091(25) \times 10^{-3}\,\mathrm{pc\,M_\odot^{-1}\,km^2\,s^{-2}}$
Planck's constant	$h = 6.62607015 \times 10^{-34}\,\mathrm{J}$
Boltzmann's constant	$k_\mathrm{B} = 1.380649 \times 10^{-23}\,\mathrm{J\,K^{-1}}$
Electronvolt (1 eV)	$= 1.602176634 \times 10^{-19}\,\mathrm{J}$

Astronomical constants

Astronomical unit (1 AU)	$= 1.495978707 \times 10^{11}\,\mathrm{m}$
Parcec (1 pc)	$= 3.0857 \times 10^{16}\,\mathrm{m} \approx 2.1 \times 10^5\,\mathrm{AU}$
Solar mass ($1\,\mathrm{M_\odot}$)	$= 1.98847 \times 10^{30}\,\mathrm{kg}$
Solar luminosity ($1\,\mathrm{L_\odot}$)	$= 3.828 \times 10^{26}\,\mathrm{W}$

Part I

Background & Introduction

Chapter 1

Introduction

1.1 Between the stars: The interstellar medium

One of the outstanding discoveries of the past century in astronomy is that the space between stars is not entirely empty. Instead, our Galaxy contains huge quantities of material between them. Astronomers refer to this medium as the interstellar medium (or ISM). Everything constituting the ISM is referred to as interstellar matter.

The ISM consists mostly of gas ($\sim$ 99% by mass) made up of atoms and molecules. Most of this gas phase consists of atomic hydrogen followed by helium. Other heavier elements (e.g., C, N, O, Mg, Na, S, Si, etc.) and molecules made up of these elements (e.g., H_2, CO, H_2O, CH_3OH, SO, and many more) constitute the rest (Herbst 1995). The remainder of the interstellar matter ($\sim$ 1%) is in the form of solid particles made up of a large number of atoms and molecules called interstellar dust/grains. Dust grains typically consist of a silicate or graphite core surrounded by a mantle of ice most likely made up of water, methane, ammonia, carbon monoxide, and carbon dioxide (van Dishoeck 2014).

The ISM is still mostly empty. If all the interstellar gas in our Galaxy were to be spread out evenly in its volume, there would be roughly one atom in a cubic centimeter (dust is distributed even more sparsely). But as the interstellar matter is heterogeneously distributed, in some interstellar clouds the density can go up by more than a thousand times the average. Nevertheless, this is still extremely empty. For comparison, the air we are breathing in at the moment has a density of a whopping 10^{19} atoms in the same volume! But even though the density is very low, these clouds occupy enormous volumes resulting in them having considerable mass. It is estimated that about 10% of the baryonic mass of the Milky Way resides in the ISM in the form of gas and dust (the rest 90% of the mass is contained in the stars). This means the total mass of the ISM is about $10^{10}\,M_\odot$ (10 billion times the mass of the sun), plenty to create many more stars and planets in the future.

1.2 Phases of the ISM

Depending on where it is located and the conditions surrounding it, interstellar gas can be extremely cold (a few degrees above absolute zero) or extremely hot (more than a million degrees). Its composition can be ionic, atomic, or molecular and it can have a wide range of densities. Based on these factors, the ISM has different phases (Field et al. 1969; McKee & Ostriker 1977). Molecular clouds constitute one of these phases. In addition, matter in the ISM does not perennially stay in a single phase, but instead, cycles through all of

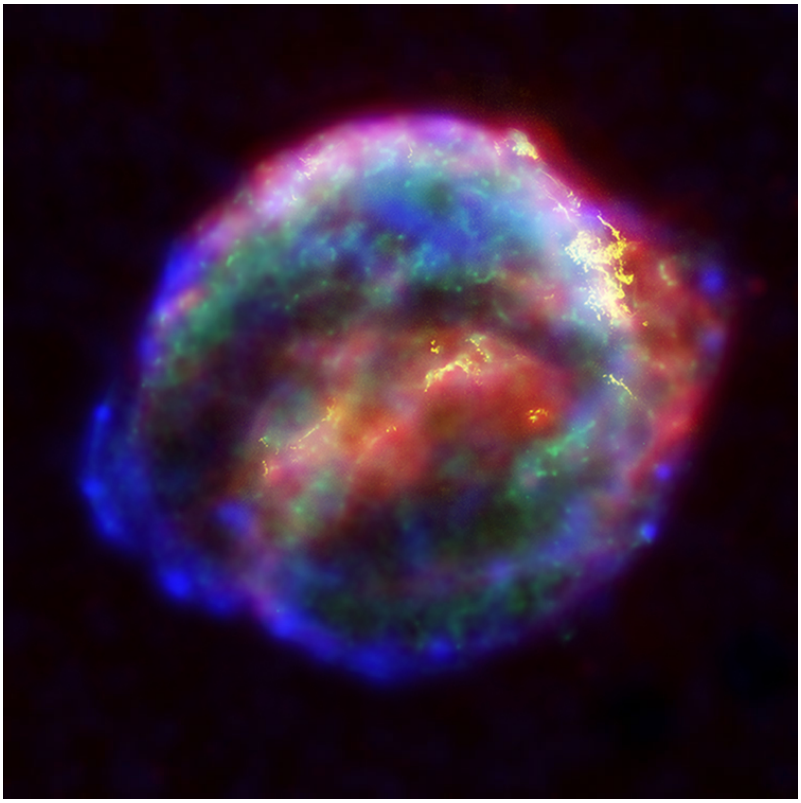

Figure 1.1: X-ray, Optical & Infrared Composite of Kepler's Supernova Remnant by NASA/ESA/JHU/R.Sankrit & W.Blair. Color Code: Blue (X-ray (4-6 keV), Chandra X-ray Observatory): primarily coming from the region directly behind the shock front. Green (X-ray (0.3-1.4 keV), Chandra X-ray Observatory): traces lower-energy X-rays marking the location of the hot remains of the exploded star. Yellow (Optical, Hubble Space Telescope): reveals gas heated to extremely high temperatures by the supernova shock wave slamming into the densest regions of surrounding gas. Red (Infrared, Spitzer space telescope): shows microscopic dust particles swept up and heated by the supernova shock wave.

them. In this section, we will briefly look at these phases (beginning from the hottest to the coldest phase) (see Wolfire et al. 2003, and references therein) followed by an overview of the life-cycle of the interstellar gas.

Hot ionized medium (HIM)

Before the advent of space-based telescopes that could observe the sky in the ultraviolet (UV) and X-ray regimes, astronomers believed that most of the ISM was filled with hydrogen at temperatures no warmer than those found in HII regions (which we will discuss soon in this section). But space-based telescopes observing in the UV regime detected absorption lines originating from oxygen atoms that had lost 5 electrons (astronomers use the Roman numeral I after an atomic symbol to represent emission from a neutral atom. Higher numerals are used to denote successively higher ionization. Hence, an

oxygen atom ionized five times is denoted as O VI). Later on, observations using X-ray telescopes showed that our Galaxy has many X-ray emitting bubbles of gas (see Fig. 1.1 Jenkins 1978; Rogerson et al. 1973). In order to remove 5 electrons from an oxygen atom and to emit X-rays, the gas had to be heated to at least a million degrees. Supernovae, which are extremely violent explosions marking the death of massive stars, have been shown to be a source of such high energy (Cox & Smith 1974; McKee & Ostriker 1977). Supernovae expel gas into their surrounding ISM up to speeds of about 30% the speed of light. Such high-velocity gas on encountering interstellar matter shocks and heats the gas to millions of degrees. Such a hot ionized medium (HIM) has extremely low densities of $< 0.003\,\mathrm{cm}^{-3}$ and occupies $\sim 30 - 70\%$ of the ISM volume (Ferrière 2001; Spitzer 1956).

Warm ionized medium (WIM)

This phase of the ISM consists of diffuse gas with temperatures ranging from 6000 to 12000 K and densities $\sim 0.1\mathrm{cm}^{-3}$. Its existence was first proposed by Hoyle & Ellis (1963). It covers about $20 - 50\%$ of the ISM volume (Ferrière 2001). It mostly consists of ionized hydrogen which has been ionized by the ultraviolet radiation coming from the Galaxy's ionization sources such as OB stars. Since the density of this medium is relatively low, UV radiation can easily penetrate through it and ionize the whole medium. Occasionally, an electron will be captured by a positively charged hydrogen nucleus and then it will cascade down to its ground state emitting photons. This process is called hydrogen recombination. About half the time, these cascades involve the transition of the electron from the $n = 3$ to 2 energy levels. This releases a photon of a characteristic red color corresponding to a wavelength of 6563Å, also known as the Hα line. The existence of diffuse Hα emission from the widespread WIM can be seen in the Wisconsin H-Alpha Mapper (WHAM) survey (Haffner et al. 2003) as a diffuse pervasive background of faint emission extending to 2 kpc above the galactic plane (see Fig. 1.2). About 90% of the H^+ (ionized hydrogen) in the galaxy resides in the WIM (Reynolds 1991).

HII regions

The remaining 10% of the galactic H^+ can be found in high density (10^2 to 10^4 ions cm^{-3}) bright regions surrounding hot stars. The stars heat their surrounding gas to 10000 K. They also emit a large amount of UV radiation that ionizes the hydrogen in their surroundings. Since the ionization of hydrogen atom creates simply a pair of proton and electron, the vicinity of a hot star consists of a hot ionized soup of gas. In this phase, the density is high enough such that an electron does not stay free for a long time. It soon gets captured by another free proton to form a neutral hydrogen atom which then absorbs the UV rays from the star again to start the whole ionization cycle. Because most of the gas is ionized in this state, astronomers call this an HII region (where the roman numeral again is used to denote the ionized state of hydrogen). As seen in the description of the WIM, ionized hydrogen has a typical red glow owing to the electrons cascading inside a hydrogen atom (see Fig. 1.3). Given the high density of HII regions, they are a much

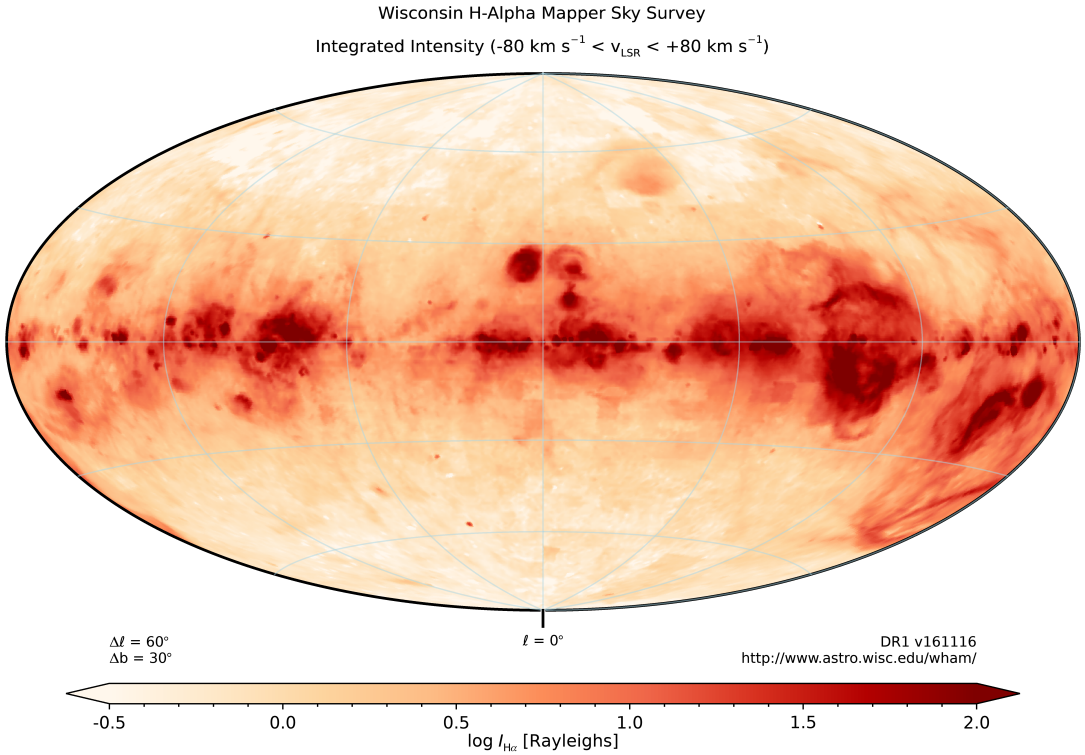

Figure 1.2: Wisconsin H-Alpha Mapper Sky Survey map of the Milky Way tracing the H-alpha emission.

Figure 1.3: The Orion Nebula. The red glow shows ionized hydrogen emission indicating the presence of hot young stars nearby that has ionized these clouds. The blue color is due to small dust particles scattering the light from these hot stars. Dust can also be seen silhouetted against the glowing gas. (credit: NASA, ESA, M. Robberto (Space Telescope Science Institute/ESA) and the Hubble Space Telescope Orion Treasury Project Team)

brighter foreground on the faint background WIM emission in the WHAM survey (see Fig. 1.2). HII regions occupy a tiny fraction (<1% by volume) of ISM (Ferrière 2001).

Warm neutral medium (WNM)

Away from the hot stars, the density of the photoionizing UV photons decreases allowing the recombined hydrogen atoms to stay in their neutral state. In this state the neutral atomic gas is still very hot ($\sim$ 8000K) but not very dense ($\sim$ 0.5cm^{-3}). This density is still higher than that of neutral gas in the HII regions; high enough for the gas to stay predominantly neutral but not high enough to prevent the distant UV rays from penetrating and heating them and in turn dictating their chemistry. These conditions are most prevalent at the boundaries of HII regions and molecular clouds (which we will discuss later in this section). This medium is commonly traced by HI 21cm emission. This emission originates from the hyperfine structure of hydrogen. The single electron in a hydrogen atom can have a spin state that is either parallel (at higher energy) or opposite (at lower energy) to that of the nuclear spin. When an electron changes its spin state from the former to the latter, the excess energy is emitted as a photon that has a wavelength of 21cm (in the radio frequency regime). The WNM occupies about 10 – 20% of the ISM volume (Wolfire et al. 2003, and references therein).

Cold Neutral Medium

This phase of the ISM mostly consists of atomic hydrogen gas in the form of sheets and filaments. The gas is very cold with temperatures ranging between 50 to 100K and much denser compared to its warm counterpart (50 atoms cm^{-3}). It covers only about 4% of the ISM volume but almost a third of its mass (Ferrière 2001). Detecting the CNM is difficult as atomic hydrogen at such low temperatures does not emit much radiation at any frequency. But if they are along the line of sight of a source of UV or visible light (like stars and quasars) they show absorption lines (Mebold et al. 1982).

Molecular Clouds

Molecular clouds are mostly made up of molecular hydrogen (H_2) but also consist of a plethora of other simple as well as complex molecules in small amounts. Although at first, it may appear surprising to detect molecules in the ISM which is filled with UV light from stars that is capable of breaking down the bonds in molecules dissociating them into constituent atoms, it is not that surprising if one remembers that the ISM also consists of dust. If dust aggregates in large amounts at a given place, it can block the UV rays allowing the molecules to survive. Such clouds appear dark in the optical and UV regime as the dust absorbs most of these radiations. In the absence of UV radiation, H_2 molecule (and many other molecules) can form inside these clouds, hence the name molecular clouds. In some cases, these clouds get extremely massive (about a million times the mass of the sun) when gravity accumulates enough interstellar gas. We call these, giant molecular clouds (GMCs). Most molecular clouds are gravitationally bound and have H_2 densities 100–$10^3 cm^{-3}$ (Ballesteros-Paredes et al. 2020). Due to such high densities, they consist of about 30% mass of the ISM despite occupying only a measly 0.05% of its volume (see Evans 1999, and references therein). Their high density also acts as an additional shield to the UV radiation which is usually the main source of heating in the ISM. Therefore, they tend to be extremely cold (T=10−20K). As we will see later, these molecular clouds are sites of star formation.

Historically, molecular clouds were hard to observe. In the visible and UV wavelength ranges, they could only be seen as dark clouds blocking the light coming from behind them. Although molecules such as CH and CN had been detected in the ISM based on their absorption lines in the visible spectra of the background stars, astronomers were oblivious to the existence of the richness of the molecular complexity of the ISM; at least until the technology had advanced enough for radio and infrared telescopes to come into existence. This is so because the vibrations and rotations of molecules usually leave a fingerprint in the radio and IR regimes of the electromagnetic spectrum. We will delve into the details of how these molecules emit later.

Even though H_2 is the most abundant molecule, it does not emit at the low temperatures existent in molecular clouds even in radio wavelengths. But, astronomers have detected other simple compounds in the ISM, e.g., water (H_2O), carbon monoxide (CO), ammonia (NH_3), etc. Of these, CO is the most abundant and tends to be present along with H_2. Aided by the fact that it emits strongly in the sub-millimeter regime even

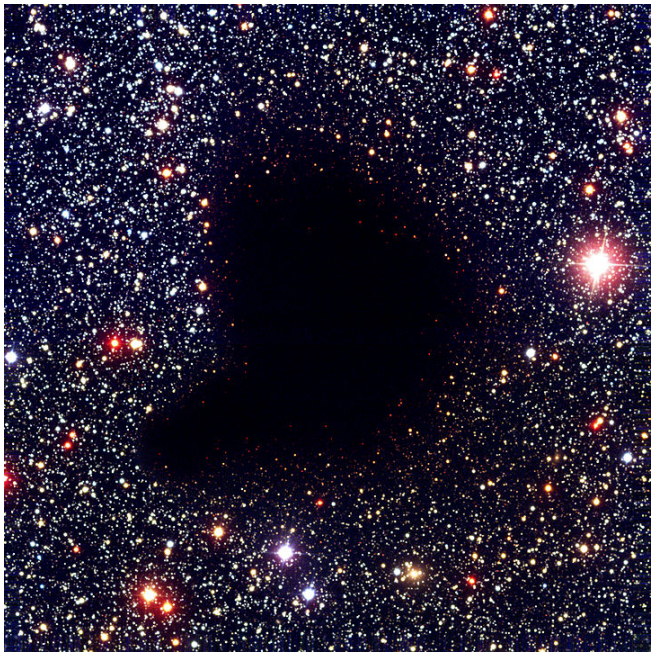

Figure 1.4: Color composite of visible and near-infrared images of Barnard 68, a dark cloud taken using the 8.2-m VLT ANTU telescope and the multi-mode FORS1 instrument. Dust in the cloud renders it completely opaque to the observed radiation coming from behind it. Source: ESO

at the extremely low temperatures existent in molecular clouds, it is primarily used by astronomers to study these clouds. However, recent developments suggest that not all molecular gas is traced by CO emission. A significant fraction of the total mass of the molecular clouds is believed to reside in clouds devoid of CO (Wolfire et al. 2010; Allen et al. 2015; Smith et al. 2014). These clouds are commonly referred to as CO dark clouds.

As alluded to earlier in this section, in addition to the simple molecules, complex molecules have also been detected in molecular clouds. These are mostly combinations of hydrogen, carbon, nitrogen, oxygen, and sulfur atoms. Some examples of complex molecules include formaldehyde (H_2CO), methanol (CH_3OH) and even benzene (C_6H_6).

A major part of this dissertation is focused on studying the properties of molecular clouds. We will discuss these structures in more detail in a later section.

Interstellar dust

As we have noticed in the previous section, even if dust only consists of 1% of the ISM mass, its influence on the latter is immense. Historically, large optical and near-IR telescopes frequently observed dark regions in the sky that were free of stars like the one shown in Fig. 1.4. American astronomer E.E. Bernard is credited for being the first to demonstrate that these were clouds of dark material that blocked the background starlight. This dark material is in fact made up of dense dust grains. Such dark regions are quite common in pictures of the Milky Way. The dark ridge along the Milky Way in the night sky that

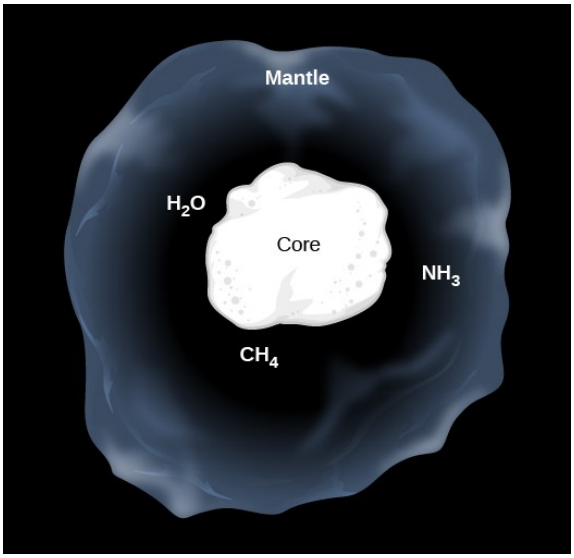

Figure 1.5: Model of an interstellar dust grain believed to consist of a solid core surrounded by a mantle of ice. Their typical sizes range between 10^{-8} and 10^{-7} m. This image has been taken from Fraknoi et al. (2016).

appears to split it into two is actually a collection of such dark obscuring clouds.

The most widely accepted model of interstellar dust pictures them as grains with rocky cores that are rich in carbon (like soot) or silicates (like sand). Their size distribution also spans a large range of values with most of the dust grains having a typical size of $\sim 0.1\,\mu$m. But these grains can get as large as a few μm to about a few cm in dense cores and circumstellar disks (Testi et al. 2014; van Dishoeck 2014; Oliveira et al. 2011; Draine 2003). Dust grains occurring in dark clouds are covered by icy mantles which are mostly made up of water (H_2O), methane (CH_4), and ammonia (NH_3) (see Fig. 1.5). These ice mantles, in turn, host many chemical reactions that produce complex organic molecules.

The dust grains are too cold to emit any visible light. But, they absorb visible and UV radiations very efficiently which heats them up. They then re-emit the absorbed energy in IR and microwave wavelengths. This emission is thermal in nature with the peak of the emission spectrum lying in the IR regime. Our atmosphere is not completely transparent to such wavelengths. So, space-based IR telescopes are best suited to observe these dust clouds (see Fig.1.6). Although warm dust is only observable in IR, cold dust does show thermal emission in the sub-millimeter regime and can be imaged from ground-based sub-millimeter telescopes (see Fig. 1.7). Dust clouds can also scatter the lights from nearby stars appearing as reflection nebula. Since absorption and scattering both result in the dimming of intercepted stellar radiation by dust clouds, this process is commonly referred to as stellar extinction.

Figure 1.6: Infrared image of the plane of the Milky Way. This Spitzer space telescope has been used to make this image of a part of the Milky Way spanning galactic longitudes of 335.2 to 343.5 degrees centered at a galactic latitude of 0 degrees with a width of 2 degrees. The dust grains emit at 3.6 microns (seen here in blue color), 8 microns (green), and 24 microns (red). The flat band of green seen here is mostly dust in the Milky Way's disk. In visible light, the same dust renders this area nearly featureless and dark. The red bubbles visible throughout indicate regions where the dust has been warmed up by young stars which then emits it at 24 microns. The densest regions of dust are so cold and opaque that they appear as dark clouds even at infrared wavelengths.

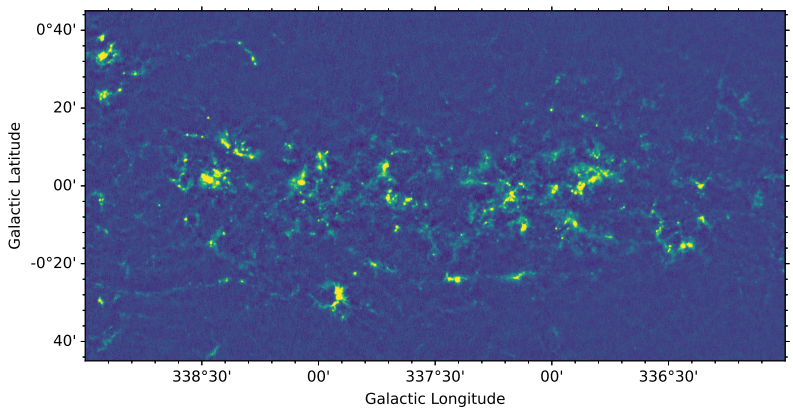

Figure 1.7: ATLASGAL cutout of the Milky Way. The APEX telescope was used for making this image at a wavelength of 870 μm . This emission traces the cold dust that emits thermally at sub-millimeter wavelengths.

Dust also causes interstellar radiation to redden. This is because the tiny dust particles are much more efficient at absorbing and scattering the incident green, blue and ultraviolet light thereby preventing it to reach observatories on Earth. But some of the orange and red wavelengths are more successful in traveling through the dust clouds evading scattering and/or absorption, consequently reaching us. Hence, the star being observed appears redder than it actually is. In certain cases, the extinction is extreme, and only IR radiation from the stars reaches us on Earth (see Fig. 1.8).

1.3 Life-cycle of the ISM

All the different phases of the ISM introduced in the previous section do not exist in isolation. The interstellar clouds are constantly changing (shifting, merging with each other, growing, or dispersing) forming a cycle in which matter moves from one phase to the other. This process is also closely related to the process of star-formation. Here, we paint a very simplistic picture in order to highlight the connection between various phases of the ISM.

The UV radiation emanating from the stars fills the ISM with highly ionizing radiation. When the density of gas in the ISM is high enough to shield itself from the UV radiation, atomic hydrogen can form resulting in cold HI clouds into which only far-ultraviolet (FUV) radiation can penetrate. As these clouds gather more matter increasing their density and further shielding their insides from ionizing radiation, hydrogen molecules start to form resulting in molecular clouds. Inside these clouds, perturbations in densities result in regions with higher density gathering more and more mass and eventually fusing their Hydrogen forming stars. These stars then emit ionizing radiation resulting in the formation of HII regions and warm ionized regions inside the molecular clouds. Surrounding these is exposed gas which is dense enough to resist ionization but still heated to high temperatures resulting in the warm neutral medium. The stars also

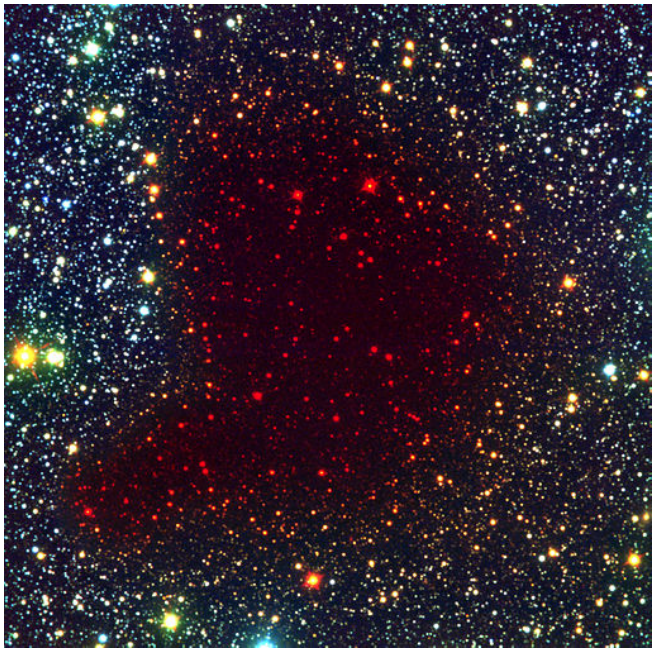

Figure 1.8: Same as Fig.1.4 except that the red color in this image is a false-color of the infrared emission at 2.2 microns. The background stars are only visible at these wavelengths because of the extinction of the visible light due to the foreground dust. Source: ESO

produce heavier elements inside them along with dust particles in their envelopes at the end of their life which they then disperse into their surrounding molecular clouds enriching the ISM. During the early phases of their life cycle, the stars in the molecular clouds disrupt the latter dispersing the constituents of the parent clouds. This process happens simultaneously while new stars are still being formed inside the molecular cloud. The stars massive enough to explode as supernovae have very short life spans and explode in the vicinity of their parent molecular clouds completely unbinding them. Intense energy from these sources completely ionizes the gas around them resulting in the hot ionized medium. The process of the interaction of the stars with their surrounding molecular cloud is referred to as feedback (which we will discuss in more detail in Sec. 1.5).

Figure 1.9 presents a sketch of the life-cycle of interstellar matter. In this dissertation, we will focus on detecting molecular clouds and how star formation and evolution impact their properties. The next two sections will therefore focus on the process of star formation and its impact on molecular clouds. Following this, we will explain the mechanisms by which molecular clouds emit radiation.

1.4 Star Formation

The details of the star formation process depend on the mass of the stars and their environment. Before providing a brief overview of star formation it is important to define

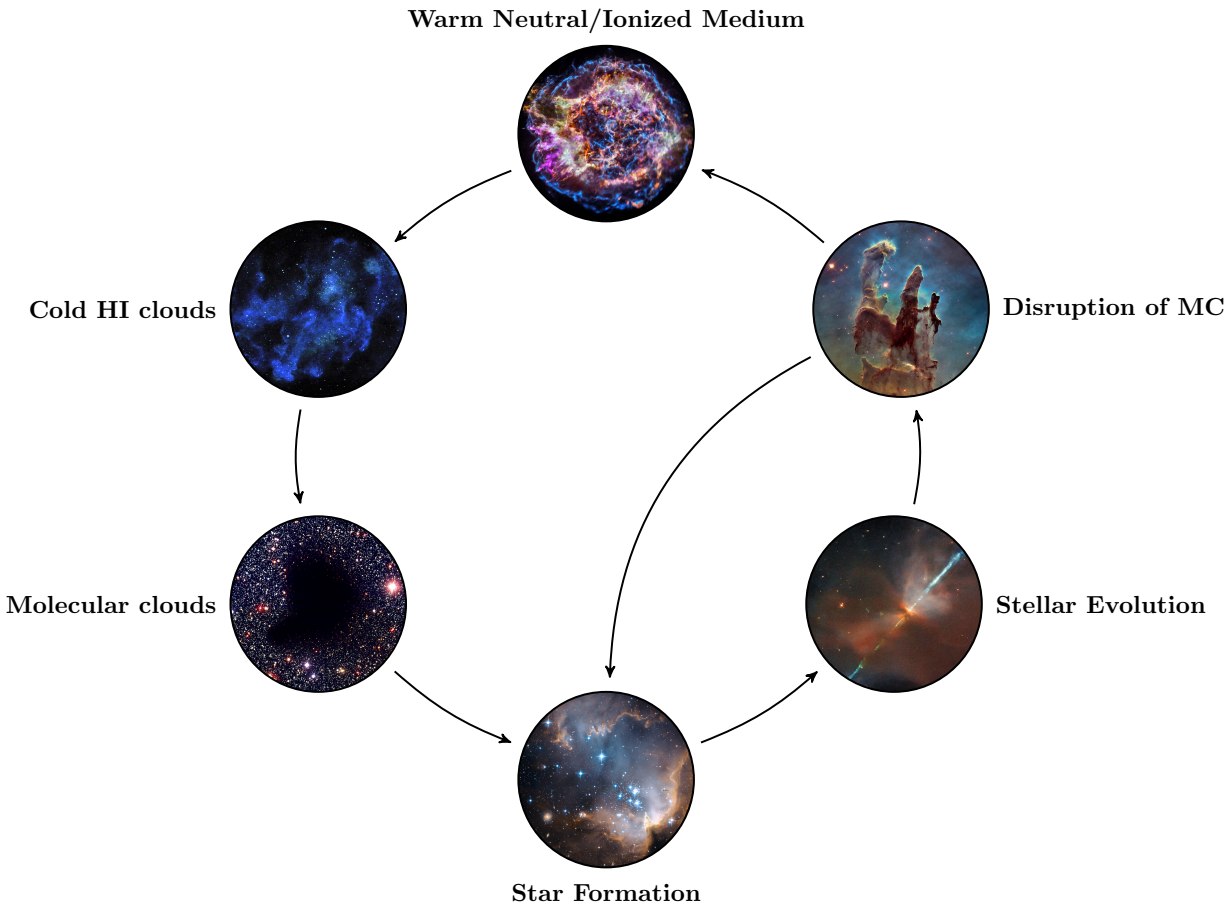

Figure 1.9: A simplified sketch of the life-cycle of interstellar matter.

a star. A well-accepted definition of a star is a gravitationally bound body of luminous gas that is massive enough to ignite the fusion of hydrogen into helium in its core by its own gravitational force.

1.4.1 High-mass vs. low-mass stars

Astronomers and astrophysicists generally classify stars as low-, and high-mass stars depending on their masses. The important distinction between high- and low-mass stars is their luminosity. The luminosity of a star, and consequently the amount of radiation emitted by it, is very strongly dependent on its mass approximately given by (Harwit 1988)

$$M_* = L_*^{3.5}. \tag{1.1}$$

Increasing luminosity also means higher surface temperature for stars, which in turn means higher energy photons being emitted given that stars are effectively black body radiators. This means that there exists a certain mass limit above which the energy of photons emitted by a star is high enough to ionize the neutral hydrogen in its vicinity ($h\nu > 13.6\,\mathrm{eV}$ or $\lambda \leq 912\,\text{Å}$). This translates roughly to a stellar mass of $7\,\mathrm{M}_\odot$. Stars more massive than this can ionize their surroundings creating an *HII region* (see Sec. 1.2). This difference in their ability to ionize their surroundings is used to differentiate between the stars as low- [0.1–7 $\mathrm{M}_\odot$] and high-mass [$> 7\,\mathrm{M}_\odot$] stars with the latter having effective temperatures high enough to create HII regions. High-mass stars are known to be as massive as $100\,\mathrm{M}_\odot$(e.g., see Wu et al. 2016). Depending on their spectral type and luminosity stars are classified into 7 spectral types, namely O, B, A, F, G, K, and M. O and B stars (referred to together as OB stars) are the most luminous, massive, and hottest of all stars (Habets & Heintze 1981). They are also the rarest type (Ledrew 2001). All high-mass stars are OB stars. The surface temperature and masses of the stars decrease from O to M with M being the least massive but the most commonly occurring stellar type (Russell 1914; Habets & Heintze 1981; Ledrew 2001).

1.4.2 Sites of star formation: Molecular clouds

Stars form inside molecular clouds where molecular hydrogen is effectively shielded from ionizing radiation. Elmegreen (1985, 1993) showed that in order to provide sufficient shielding a minimum column density of $20\,\mathrm{M}_\odot\,\mathrm{pc}^{-2}$ is needed. Molecular clouds typically have much higher column densities of about $100\,\mathrm{M}_\odot\,\mathrm{pc}^{-2}$. They are generally surrounded by a less dense layer of atomic gas that aids the dust particles in shielding the cloud from ionizing UV radiation. In our Galaxy, molecular clouds can be observed almost everywhere (e.g. spiral arms, galactic center, interarm regions, and high galactic latitudes). But the distribution of their mass is not uniform throughout our Galaxy. Figure 1.10 shows the total mass of clouds in galactocentric rings of width 0.5 kpc (top) as well as the median surface mass density of molecular clouds (bottom) as a function of galactocentric radius (Miville-Deschênes et al. 2017). Moving radially outwards from the center of the galaxy, the mass distribution first peaks in the Central Molecular Zone (CMZ), located

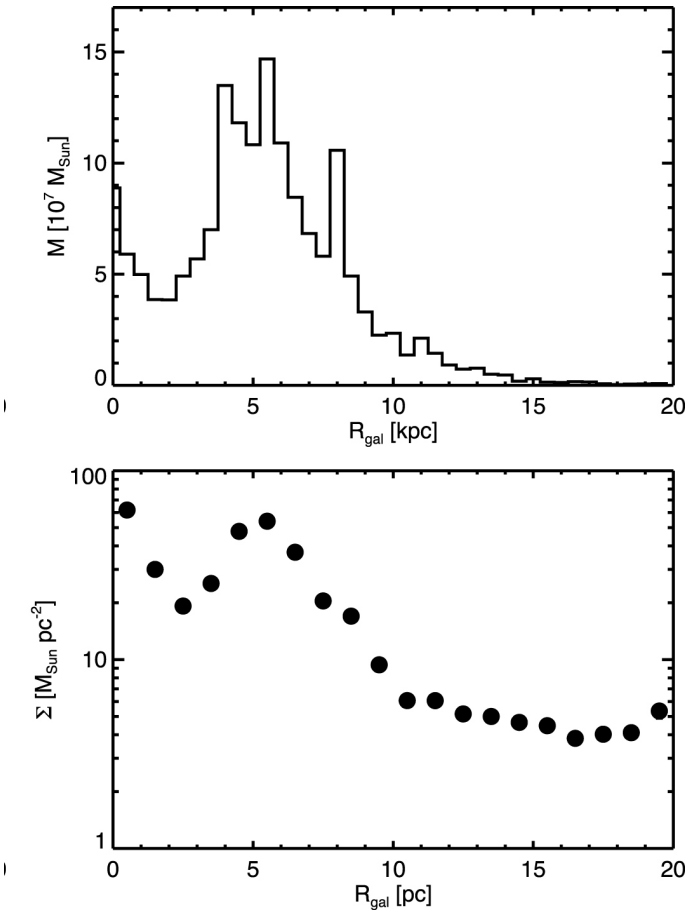

Figure 1.10: Top: Total mass of clouds in galactocentric rings of width 0.5 kpc as a function of galactocentric radius (R_{gal}). Bottom: Median cloud mass surface density of the molecular clouds in the Milky Way as a function of R_{gal}. This figure has been taken from Fig. 9 of Miville-Deschênes et al. (2017).

in the central few hundred parsecs around the Galactic center (Ballesteros-Paredes et al. 2020; Molinari et al. 2011, and references therein). This region also contains the most massive clouds as can be seen from their median mass surface density. Cloud masses as well as their average distribution then decrease between 0.5 and 3 kpc, before increasing again in the Molecular Ring (4–8 kpc). The mass distribution peaks here. Past the Molecular Ring, the gas mass distribution and cloud mass surface density fall off. Molecular clouds are still detectable towards the outer galaxy. Molecular clouds are usually categorized as isolated and giant molecular clouds.

Isolated Molecular Clouds (IMC)

IMCs are small, round, dense, optically dark nebulae that were first studied in the 1940s by Bok & Reilly (1947). These nebulae are now known as *Bok globules* (following Bart's suggestion to name these globules). Their size ranges from 0.1-1.0 pc with masses ranging between 1-100 $M_\odot$. They have an average mass of about 11 $M_\odot$and a radius of around 0.35 pc (Clemens et al. 1991). These are believed to host the formation of single or small groups of low mass stars (0.1-2 $M_\odot$). Because of their isolation, Bok globules are ideal candidates to study spontaneous star formation processes that are not influenced by any

external environmental effects.

Giant Molecular Clouds (GMC)

GMCs are massive molecular clouds with masses up to $10^6\,M_\odot$ and sizes ranging from several parsecs to several tens of parsecs. Their mean particle density ranges between $\sim 1-3\times10^2\,cm^{-3}$ and have a narrow range of kinetic temperature $\sim 10-20\,K$ (Pratap et al. 1997; Heyer & Dame 2015). The distribution of gas inside a GMC is not uniform. GMCs show a hierarchical structure (Blitz & Williams 1999; Rosolowsky & Leroy 2006; Pokhrel et al. 2018) consisting of many smaller ($1-5\,pc$) regions of higher density ($10^2-10^3\,cm^{-3}$) and masses between $10^2-10^4\,M_\odot$ called *clumps* (Tsuboi & Miyazaki 2012; Rigby et al. 2019). These clumps in turn contain regions of even higher density called *cores*. The densities and sizes of these cores range between $10^4-10^6\,cm^{-3}$ and $0.03-0.1\,pc$ respectively (André et al. 2010). Embedded inside the densest and largest of cores (spanning sizes $0.5-1\,pc$ and H_2 densities $10^4-10^6\,cm^{-3}$) in GMCs are stellar clusters. These embedded clusters form stars spanning a large range of stellar masses and are believed to account for a large fraction of all star formation occurring locally (Lada & Lada 2003).

1.4.2.1 Support mechanisms within molecular clouds

Molecular clouds are believed to have an average lifespan in the range $10-30\,Myr$ (Blitz & Shu 1980; Chevance et al. 2020). However, under the influence of gravity alone, molecular clouds will collapse within the global free-fall times given by

$$t_{ff} = \sqrt{\frac{3\pi}{32G\rho}} \sim 1\times10^6\,yr, \tag{1.2}$$

which is shorter by a factor of 30. Additionally, an unhindered collapse would mean that molecular clouds would form stars very efficiently and quickly resulting in a Galactic star formation rate of $\sim 250\,M_\odot yr^{-1}$ (McKee & Holliman 1999). But observations indicate a Galactic star-formation rate of $\sim 3\,M_\odot yr^{-1}$ (McKee & Williams 1997) which means molecular clouds are way less efficient at forming stars (only a few percent of their mass being used up to create stars) and most of their mass is eventually dispersed.

For such low star formation rates to be possible molecular clouds need a mechanism to counteract gravity on a cloud scale but at the same time allow for gravity to form stars on a local scale. Some mechanisms that have been suggested as being capable of this are thermal pressure, magnetic fields, and turbulence. Thermal pressure arises from the kinetic energy of the gas, meaning the higher the temperature, the higher the pressure. But molecular clouds have a typical kinetic temperature of $\sim 10-20\,K$ which is insufficient to support the cloud against gravity. Magnetic field lines can be effective in supporting the molecular clouds against gravitational collapse. They can only do so in a direction perpendicular to the direction of magnetic field lines in the cloud. Ions spiral along the field lines hindering the motion of neutral particles perpendicular to the field lines, thereby slowing down the collapse of the molecular cloud considerably. Finally,

turbulence causes the broad velocity components observed in molecular lines spectra which can not be explained by thermal pressure alone. This broadening represents the internal velocities of molecular clouds which appear to be supersonic up to ten times the speed of sound in the medium ($\sim 200\,\mathrm{m\,s^{-1}}$). Turbulence is present at all scales, however, what causes turbulence is still unclear. The mechanisms driving turbulence may be scale-dependent: at $\sim 100\,\mathrm{pc}$ turbulence might be driven by expanding HII regions and supernovae, whereas at $0.1 - 10.0\,\mathrm{pc}$ stellar winds and outflows have been suggested (Vázquez-Semadeni et al. 2000).

1.4.3 From clouds to clumps to cores

Inhomogeneity of the density inside molecular clouds results in some regions having a stronger gravitational field. This pulls in more gas and dust creating clumps inside the cloud which have a higher mass. This in turn causes the gravitational field to grow stronger and pull in more mass towards the clump. This results in a runaway collapse forming a single low-mass star. But, clumps are observed to survive for much longer and gather much more mass ($10 - 1000\,\mathrm{M_\odot}$). We have already discussed some mechanisms that can support the molecular clouds against gravitational collapse and these possibly also support the clump until a certain point where a critical mass has been reached and the collapse can begin.

Jeans mass, M_J, and Jeans length, R_J, are defined as the critical mass and radius above and below which a spherical clump in thermal balance becomes gravitationally unstable and collapses in free fall. These are defined as:

$$M_J \equiv \left(\frac{5k_BT}{G\mu m_H}\right)^{3/2}\left(\frac{3}{4\pi\rho_0}\right)^{1/2} \tag{1.3}$$

$$R_J \equiv \left(\frac{15k_BT}{4\pi G\mu m_H\rho_0}\right)^{1/2} \tag{1.4}$$

where ρ_0 is the mean density of the gas, G is the gravitational constant, μ is the mean molecular weight, m_H is the atomic mass of hydrogen, and k_B is the Boltzmann's constant. In a typical cold neutral medium with temperature $\sim 50\,\mathrm{K}$ and $\rho \approx 10\,\mathrm{cm^{-3}}$ and $\mu \approx 1$, the corresponding Jeans mass is $M_J \approx 3600\,\mathrm{M_\odot}$. However, the actual masses in the CNM are way below this value, and hence, they are not likely to collapse and fragment. For the typical conditions existent in molecular clouds however (i.e. $T = 10\,\mathrm{K}$, $\rho \approx 10^3\,\mathrm{cm^{-3}}$ and $\mu \approx 2$), the Jeans mass is only $M_J \approx 10\,\mathrm{M_\odot}$, making fragmentation into clumps highly likely.

Under free-fall, the collapse remains isothermal so long as the clump is optically thin, allowing the released gravitational potential energy to be radiated away (Larson 1969). High densities resulting from the collapse can couple the gas to the dust, radiating the energy more efficiently, allowing the clump to maintain a constant temperature of about 10 K over a wide range of densities.

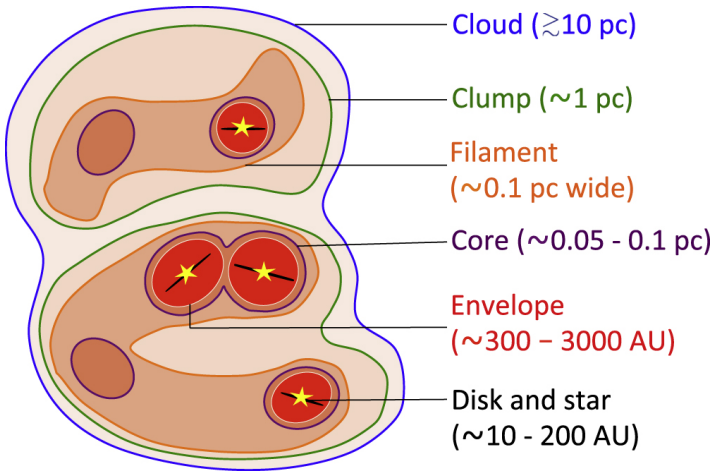

Figure 1.11: Cartoon describing hierarchical fragmentation inside a molecular cloud. This has been taken from Fig. 1 of Pokhrel et al. (2018).

As the clump collapses, its density increases many-fold while the temperature stays constant. This implies that the Jeans mass decreases inside the collapsing clump. Any local density inhomogeneity inside this collapsing clump that now satisfies the new Jeans criteria itself starts collapsing locally. This fragments the clump further into multiple smaller molecular cores.

But does the collapse of a cloud and therefore its fragmentation stop at any point? So far, we have operated under the assumption that the collapse is isothermal. Although true during the initial stages of a collapse during which the clump can cool efficiently, this assumption breaks down as a cloud collapses to a high enough density to make its core optically thick. At this point, the collapse changes into an adiabatic process (Masunaga & Inutsuka 1999). Consequently, the increasing gravitational potential energy is trapped inside the core increasing its temperature which in turn increases the Jeans mass.

Finally, the fragmented cores that are more massive than the critical mass will continue to collapse eventually forming a star. Figure 1.11 shows a cartoon representation of the hierarchical fragmentation inside molecular clouds.

1.4.4 From cores to stars: low-mass star formation

The adiabatic collapse of a core as mentioned above increases the temperature and pressure which opposes the gravitational pull exerted by the condensed mass at the center of the core. This slows down and eventually halts the collapse of material near the core's center when hydrostatic equilibrium is reached. The collapse also causes the core to rotate in order to preserve angular momentum, resulting in a rotating spherical core surrounded by a slower rotating extended envelope of gas and dust. This central core is referred to as a *pre protostellar core*.

At this point, the core's luminosity is provided by the loss of kinetic energy resulting

from the material free falling towards the hydrostatic core. The temperature slowly increases as the material keeps falling on the core's surface. At about 2000 K the molecular hydrogen inside the core starts to dissociate into atomic hydrogen (Larson 1969). Being an endothermic reaction this causes the temperature of the core to drop disrupting the delicately balanced hydrostatic equilibrium and therefore triggering a second collapse of the core (Larson 1969; Masunaga & Inutsuka 2000). The size of the core reduces to a fraction of its size before the equilibrium is reestablished. At this stage, the central core is called a *protostar*.

The protostar still has a fraction of the final star's mass. Most of the mass is still in the envelope surrounding it. Further collapse of the core coupled with conservation of angular momentum results in a much faster rotation of the core and the envelope. Consequently, the latter forms an accretion disk around the protostar. The protostar continues to accrete mass onto its surface whose angular momentum is released via bipolar outflows (i.e., the protostar ejects materials along its polar axis). At this stage it is observationally characterized by strong, centrally peaked submillimeter (sub-mm) emission with an extended envelope. Lada (1987) and Andre et al. (1993) first proposed the classification of the protostar into various classes based on the spectral index of their emission in the infrared and sub-mm regimes. This stage of the protostar with peaked sub-mm emission is classified as Class 0.

After a large fraction of the star's mass has been accreted onto the protostars, the accretion disk begins to be internally heated radiating at infrared wavelengths (Class I). After about a few hundred thousand years ($\sim 0.4-0.5$ Myr) of accretion, the central core's temperature reaches about 10^6 K, and deuterium burning begins inside the protostar. The pressure generated from the deuterium burning slows down the collapse. Material keeps accreting slowly to the surface of the protostar. The majority of the accretion process is complete and most of the envelope is dispersed by the bipolar outflows. The protostar now becomes visible and is referred to as a *T-Tauri* or pre-main sequence star (Class II and III). The rest of the circumstellar material is slowly dispersed by the radiation pressure and stellar winds. The pre-main-sequence star finally becomes a full-fledged star and spends the rest of its life illuminating the sky. Figure 1.12 summarizes the different stages of low mass star formation.

1.4.5 Embedded stellar clusters and initial mass function

Stars do not usually form in isolation. Instead, they are found in clusters, forming together, deep inside GMCs. They contain stars spanning a wide range of stellar masses. Observations of these embedded clusters shed light on how stars form and evolve. Being deeply embedded inside dense gas and dust, these were extremely hard to detect with optical telescopes. But the development of IR astronomy and arrays have drastically changed the situation (see Figure 1 of Lada & Lada 2003). Surveys as well as case studies of embedded clusters have shown that the majority of stars observed locally, form inside these clusters (Lada et al. 1991; Hodapp 1994; Carpenter 2000; Lada & Lada 2003). Although most stars form in clusters, only a few very massive ones survive long

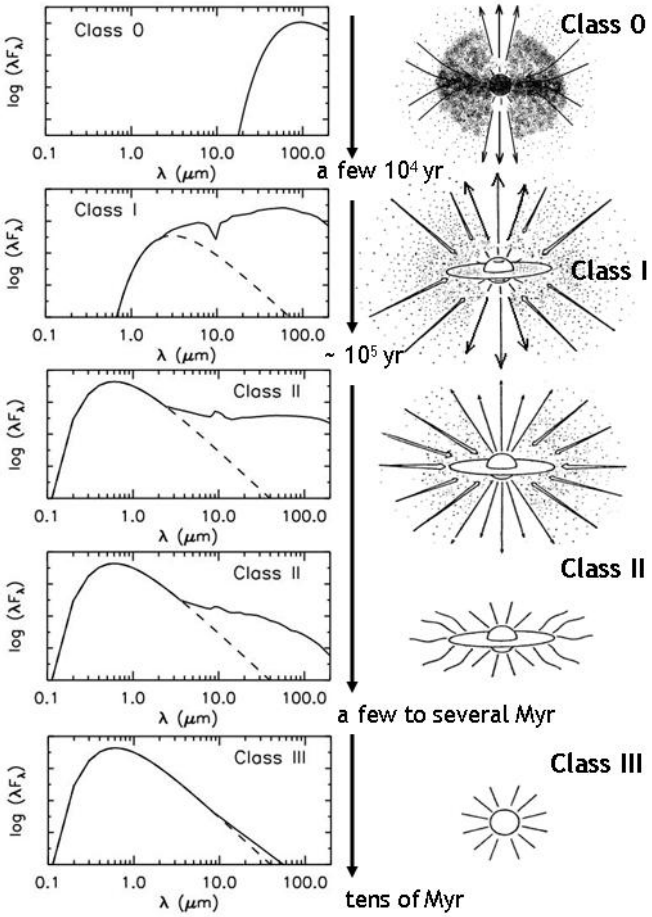

Figure 1.12: Illustration of evolutionary stages during the formation of low mass stars. These stages have been based on Lada (1987) and Andre et al. (1993). Source: http://www.elisefurlan.com/Research.html

enough to emerge from their parent molecular clouds to be observable as open clusters. Internal forces between the stars of a cluster, Galactic tidal forces, and forces from passing molecular clouds disperse most of the other massive clusters before maturity. Lada & Lada (2003) found that less than 10% of clusters survive longer than 10 Myr (the typical lifetime of a GMC is 10-30 Myr).

Once formed, the evolution of a star is completely determined by its mass. So, the evolution of any system made up of stars, such as galaxies and clusters, can also be described by the initial distribution of their stellar masses at birth. This distribution is referred to as the initial mass function (IMF). The theory of stellar evolution cannot predict the form of IMF. Therefore, this quantity has to be derived from observations. Significant contributions towards predicting the IMF through observations have been made by Salpeter (1955), Scalo (1986), Kroupa (2001), and Chabrier (2003).

1.4.6 Star formation in embedded clusters

How stars form inside massive dense embedded clusters is not very well understood. It likely involves the core dissipating turbulence, followed by its fragmentation; the fragments then become gravitationally unstable, eventually forming protostellar cores. These cores then accrete matter from their infalling envelopes as well as from the general potential well they are embedded in (see Clarke et al. 2000; Elmegreen et al. 2000, for a detailed review). The protostellar cores which result in the formation of isolated low-mass stars have sizes much larger than the separation between stars in an embedded cluster. So, the protostellar cores forming in clusters must have smaller radii than their isolated counterparts. This implies that clusters have to show a high degree of fragmentation to form stars. This can occur by progressively cooling a collapsing massive core which continually reduces its Jean's mass (Myers 1998). Colliding flows in a turbulent decay process can shock each other, leading to density enhancements which can also cause fragmentation. If these enhancements are massive enough, they can separate from their turbulent velocity field and become gravitationally bound (Klessen & Burkert 2000, 2001).

The gravitationally unstable cores then begin to accrete matter from their surroundings, gaining mass through infall. Since there are a lot of cores moving around inside the cluster, they compete with each other to capture the residual gas outside their protostellar potential well (Bonnell et al. 2001a). This starts a process of competitive accretion. Clusters with higher protostellar mass and those closer to the center of the cluster experience higher accretion rates, leading to a mass spectrum of the protostars similar to the stellar IMF (Bonnell et al. 2001b; Klessen 2001). But this process of general accretion can not account for very massive stars with masses larger than 10 $M_\odot$ as radiation pressure from such a star would be large enough to reverse infall and stop it from growing. However, cores in the deeper parts of the cluster can collide and coalesce creating very massive stars (Bonnell et al. 1998; Vázquez-Semadeni et al. 2017).

Another theory that attempts to explain high mass star formation is the turbulent core accretion model (McKee & Tan 2002). In this model, a single dense core collapses to form a young stellar object (protostar). But the thermal support is not enough to prevent the early

fragmentation of dense cores. To circumvent this, it is predicted that turbulence and/or magnetic fields support high mass starless cores to form a single high mass star (or a small number of them). In this model, the cores are assumed to be close to virial equilibrium where the kinetic energy of the turbulent core (not the thermal pressure) balances out the gravitational energy. But even in this case, the radiation pressure generated from such a massive star can halt the collapse. Hence, non-spherical accretion is needed to overcome this problem.

Once formed, stars will immediately start to disrupt their surroundings. High mass stars are particularly destructive. Not only can they destroy the cluster forming the stars, but can also disperse the entire GMC (Whitworth 1979). Outflows from a population of low-mass stars can also disrupt a molecular cloud core in a short amount of time (Matzner & McKee 2000). We will have a detailed look at how embedded OB stars impact their parent structures in Sec. 1.5. How efficiently a clump converts its gas into stars while being depleted of fuel by the embedded stars is given by the star-forming efficiency of the cloud (SFE),

$$SFE = \frac{M_{stars}}{(M_{gas} + M_{stars})}. \tag{1.5}$$

Observed values of SFE range from 10-30% (Lada & Lada 2003) for embedded clusters. However, for entire GMCs the SFEs are significantly lower (1-5% Duerr et al. 1982). Less evolved clusters have lower SFEs while those about to emerge from their parent molecular cores have a typical SFE of 30%. This suggests that the SFE of a cluster evolves with time and reaches about 30% by the time the cluster emerges from its cores.

1.4.7 Observing high-mass star formation

As alluded to in the previous section, the fact that most star-forming regions are deeply embedded inside a dense envelope of material makes direct observations of the processes related to their formation extremely difficult. Therefore, astronomers rely on observing the effect these processes have on their surroundings to study embedded star formation, especially high-mass star formation. Major indicators of ongoing high-mass star formation are ultra-compact HII (UC HII) regions, infrared emission, masers, and hot cores. However, recent advancements in technology with interferometers like ALMA and NOEMA have made it possible to probe into cores and resolve them even at larger distances (e.g. Sect. 2.2.3 in Rosen et al. 2020, and references therein).

UC HII regions

The ionizing FUV radiation from young high-mass stars deeply embedded inside dense molecular clouds can photoionize the gas surrounding them. This results in a very compact HII region with a typical diameter of ≤ 0.1 pc and electron densities $\geq 10^4$ cm^{-3} referred to as ultra-compact (UC) HII regions (Wood & Churchwell 1989). Beyond this small compact zone, the high-density dust enshrouding this region absorbs all the stellar radiation causing it to heat up. The dust then re-emits the energy in FIR wavelengths with

a peak at ~ 100 μm. The UC HII regions are, therefore, one of the most luminous sources in the Galaxy at 100 μm. Additionally, when the ions in the UC HII region recombine to form Hydrogen, they emit photons at radio and sub-mm wavelengths (commonly referred to as radio recombination lines or RRLs) making them appear as bright compact continuum sources in cm continuum surveys (Brunthaler et al. 2021; Hoare et al. 2012).

Masers

Maser emission requires population inversion which means that higher energy levels are relatively more populated than the lower energy levels. This is usually achieved, in molecules with complex level diagrams, by collisions inside an extremely dense environment or by an extremely high density of photons that can maintain this inversion of population. Newly formed high-mass stars or embedded protostars are believed to provide this necessary photon flux and/or densities needed to maintain population inversion. Multiple molecular surveys have found H_2O, OH and CH_3OH (especially class II methanol masers) masers to be ubiquitous towards high-mass star-forming regions (Comoretto et al. 1990; Menten 1991; Kurtz et al. 2000; Pestalozzi et al. 2005). Being confined to a very small and extremely dense region with particle densities between $10^6 - 10^9$ cm^{-3} (Kylafis & Norman 1991; Gray et al. 1991; Sobolev et al. 1997; Cragg et al. 2001, 2002), masers are very useful in probing the kinematic and physical properties of high-mass star-forming regions. In addition to high mass star-forming regions, certain other environments can also create population inversion in some masing molecules, e.g., OH 1720 MHz maser is known to be associated with supernova remnants (Frail et al. 1996).

Hot Cores

Hot cores have a diameter ≤ 0.1 pc, particle densities $\geq 10^7$ cm^{-3}, and temperatures higher than 100 K (Kurtz et al. 2000). They are also defined by their high abundance of complex organic molecules evaporating from grain mantles at such high temperatures (Millar 1997; van Dishoeck & van der Tak 2000). Kurtz et al. (2000) proposed that these cores are the earliest evolutionary stage of high-mass star formation preceding UC HII regions. They are heated internally by a massive protostar. Large bipolar outflows, as well as masers, have been detected towards many hot cores which usually indicate early stages of infall and outflow (Burton et al. 2002; Beuther 2007; Cyganowski et al. 2010; Beltrán et al. 2011).

1.5 Feedback and triggered star formation

From the moment they start to form, up until they die as violent supernovae, OB stars deposit a lot of their energy and momentum into their surroundings. This manifests in multiple forms such as protostellar outflows, radiation pressure, stellar winds, photoionization, and eventually supernovae, all of which will be briefly explained in this section. Krumholz et al. (2014) provides an extensive review of different feedback mechanisms from stars and stellar clusters.

1.5.1 Feedback mechanisms

Protostellar outflows

As already mentioned, protostellar outflows are an integral part of star formation. They help conserve angular momentum while matter is channeled towards the protostar's surface via accretion disks. Outflows play a vital role in setting the mass budget of a star by expelling large amounts of gas away from the newly formed star. By ejecting both energy and momentum into the surroundings of the star, outflows modify the environment around stars (Shu et al. 1999); especially when a large number of them are formed close to each other in space and time, e.g. a clump forming a cluster of stars. In this case, the combined momenta from the outflows can either completely unbind the clumps (if injected simultaneously) or maintain the star formation in the clump by supporting it against collapse past a single free-fall time (Li & Nakamura 2006; Matzner 2007). In a recent statistical study of outflows towards massive protoclusters associated with UC HII regions, Baug et al. (2021) showed that the observed outflows, while not being able to generate the observed turbulence in these sources, can sustain it by injecting energy at the same rate as it is being dissipated away.

Radiation pressure

This form of feedback is important in a cluster containing massive stars. The radiation coming from stars can inject both energy and momentum into their surrounding. If a cluster has a mass less than $\sim 10^4\,M_\odot$ (Cerviño & Luridiana 2004), then the radiation pressure is not significant enough in comparison to the outflows. However, if a star has a mass over $20\,M_\odot$(Krumholz et al. 2009) or a cluster of stars is more massive than $10^{3.5}\,M_\odot$(Cerviño & Luridiana 2004; Krumholz et al. 2014), the radiation pressure becomes significantly strong.

Stellar winds

Strong stellar winds are produced by stars with a surface temperature greater than $\sim 2.5\times 10^4$ K (Vink et al. 2000). Such high temperature corresponds to stars with a mass of $40\,M_\odot$. The momentum carried by stellar winds is slightly less than that of the stellar radiation field (Kudritzki et al. 1999). Therefore as a momentum-injecting form of feedback, stellar winds can only provide mild enhancements to the radiation pressure at best.

Photoionization

High-mass stars are hot enough to emit ionizing photons. They can ionize the gas around them, creating a bubble-like structure known as HII regions. These HII regions have very high temperatures ($\approx 10^4$ K) and pressure, which causes them to expand. This expanding bubble of hot gas interacts with the cold molecular gas of the natal molecular cloud and can deposit large amounts of energy and momentum on the latter. There are three major questions currently under active research. The first is whether the expanding HII region

can drive turbulence at the scale of GMCs. Mellema et al. (2006) and Walch et al. (2012) showed via simulations of expanding HII regions that ionization can deposit substantial kinetic energy into the GMC, but few authors have addressed this issue in great detail. The second and third areas of research focus on the ability of the HII regions to trigger star formation or completely halt star formation at low efficiencies by disrupting the protoclusters. We will briefly discuss the ability of HII regions in triggering star formation in Section 1.5.2.

Supernovae

The final and most violent form of feedback comes from the death of a massive star. Each supernova is an extremely violent explosion and yields $\sim 10^{51}$ erg of energy (Dubner & Giacani 2015). A supernova can occur only as early as ≈ 4 Myr after the onset of the first star in an OB cluster (Matzner 2002). But most protoclusters convert most of their mass into stars in the absence of feedback on a much shorter time scale. Therefore, supernovae do not play a dominant role in cluster formation unless the clusters have a mass higher than $\sim 10^6\,M_\odot$ (Krumholz & Matzner 2009; Fall et al. 2010). On the contrary, at the scale of GMCs and galaxies, which have lifetimes significantly larger than a massive star, feedback from supernovae plays a crucial role in driving their evolution (Krumholz et al. 2014; Gatto et al. 2017).

1.5.2 Triggered star formation

The sources of feedback studied so far are examples of so-called negative feedback, which means that they either disrupt or halt star formation. However, feedback can also be positive, as in promoting or accelerating the formation of stars. This positive form of feedback is usually called *triggered* or induced star formation. Triggering can mean an increase in star formation rate, star formation efficiency, or simply the total number of stars formed. Although very easy to define, it is challenging to distinguish between different kinds of triggering from observations. Therefore, the mechanisms by which feedback can trigger star formation have been an area of active research. Two of the most prominent mechanisms are called the collect and collapse (C&C) model (Elmegreen & Lada 1977) and the radiation driven implosion (RDI) model (Bertoldi 1989).

In the C&C model, which was first suggested by Elmegreen & Lada (1977), an expanding shell of warm ionized gas from an HII region accumulates a region of cold, dense gas at the edge of the shell. When enough mass is accumulated over a long time, the overdensities inside this shell can fragment and start forming clusters of stars. This process of triggering is relatively slow. Simulations of regions where star formation has been triggered by ionization pressure (e.g., Dale et al. 2005; Gritschneder et al. 2009) usually run for too short a time (< 1 Myr) for detecting the effects of the C&C model. Instead, their star formation is triggered by the RDI model, which causes forced compression of already existing clumps. In this mechanism, as the highly pressurized ionization front from the star reaches the cold molecular gas, it drives a shock wave into the cloud. As a

consequence, many previously stable clumps get destabilized by the additional pressure and can hence collapse and form stars. Bertoldi (1989) and Bertoldi & McKee (1990) used RDI models to show that shocks induced by photoionization can lead to the formation of dense clumps inside molecular clouds, which can then collapse to form a new generation of stars. Thompson et al. (2012) studied YSOs towards mid-infrared bubbles, which are regions being swept up by stellar feedback, and found a significant overdensity of observed YSOs towards them, suggesting that these were triggered by the expansion of the bubbles.

1.6 Observing molecular clouds

So far, we have been looking into the different phases in which the ISM can exist and how stars form in molecular clouds. In this section, we will try to understand how molecular clouds emit radiation.

1.6.1 Emission mechanisms

If the radiation is emitted at a specific frequency, we call it *spectral line emission*. Here we discuss spectral line emissions from atoms and molecules. Quantum mechanics tells us that the electrons in atoms can only exist in quantized energy states around their nucleus, meaning that if an electron transitions from a higher energy state to a lower one, the excess energy is released by the atom in the form of a photon. Furthermore, this photon can only have discrete energy values depending on the energy difference between the atom's quantum states and selection rules defined by the laws of quantum mechanics. Such a transition is called an electronic transition, as it involves an electron jumping between distinct energy levels. The spectral lines from the hydrogen atom are an elementary example with well-known electronic transitions between its atomic levels (see Fig. 1.13).

Molecules, on the other hand, also have additional mechanisms for spectral line emission. When a nucleus of a molecule is displaced from its equilibrium position, it starts to vibrate. The vibrations have discrete energy states, which give rise to vibrational transitions. These correspond to energies of about $\sim 0.1\,\mathrm{eV}$ or $10^3\,\mathrm{K}$ and usually lie in the infrared part of the electromagnetic spectrum. For a simple diatomic molecule, the vibrations can only happen in one direction. However, molecules involving more than two atoms have complex vibrational states such as bending and torsional vibrations. In a cold molecular cloud with a temperature of about 10 K vibrational modes are not excited and hence not observed.

Another way in which molecules emit is through rotational transitions. They occur when the angular momentum of molecules changes, causing a change in their electric fields. Excitation of rotational states of molecules requires typical energies of $\sim 10-100\,\mathrm{K}$, which are easily attainable in a molecular cloud. An additional constraint for a molecule to emit this kind of radiation is to have a permanent dipole moment. A monoatomic molecule like H_2 is symmetric about its center of mass and hence, does not possess any permanent dipole moment. Therefore, any rotation of this molecule would not create any

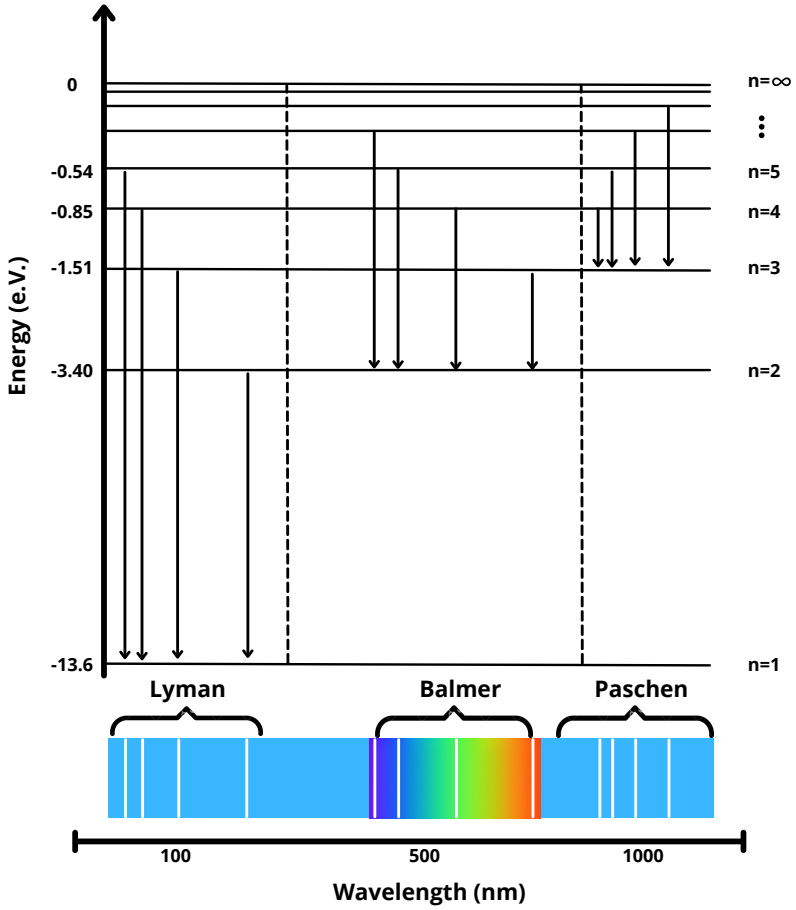

Figure 1.13: Sketch of orbital transitions in a Hydrogen atom. Each line represents an electron jumping from a higher to a lower energy state. The axes are not to scale.

changes in its electric field, rendering it unable to emit dipole radiation via rotation under conditions existent in molecular clouds. But, molecular clouds are rich in other simple non-symmetric molecules, the most abundant of them being CO. This molecule has a charge asymmetry about its axis and thus possesses a permanent dipole moment. Since, in this dissertation, line emission from CO rotational transitions in molecular clouds is observed and analyzed, we will have a detailed look at this emission mechanism in the next section.

Contrary to spectral line radiation, certain mechanisms emit radiation that covers a broad range of frequencies. These emission mechanisms are referred to as *continuum emissions*. Two of the most important mechanisms in the interstellar medium that give rise to this kind of emission are thermal dust and bremsstrahlung radiation. The thermal radiation from dust follows a modified blackbody spectrum. Bremsstrahlung radiation, on the other hand, arises when charged particles in space decelerate on passing through the electric fields of nuclei in their vicinity.

1.7 Emission and transmission of radiation

As the sources being studied here are at vast distances, the only tool available to probe molecular clouds is the radiation these regions either emit, absorb, or scatter. As previously mentioned, the most valuable wavelengths to probe molecular clouds are infrared, (sub)millimeter, and radio. This thesis deals with observations made at submillimeter wavelengths, which cover rotational transitions of many molecules. In this section, we will discuss how molecular clouds emit radiation and how this radiation travels through the ISM to be detected by radio telescopes on Earth.

First, we present some basic definitions that will aid in the following explanations. Imagine a surface of area $d\sigma$ intercepting power dP at an angle θ from a source of angular size $d\Omega$ (see figure 1.14).

dP is then given by

$$dP = I_\nu \cos\theta \, d\Omega \, d\sigma \, d\nu \tag{1.6}$$

where $d\nu$ is the bandwidth, in Hz, and I_ν is the *specific intensity* in units of $\mathrm{W\,m^{-2}\,Hz^{-1}\,sr^{-1}}$.

On integrating Eq. 1.6 over the whole solid angle of the source we obtain the *total flux density* of the source in units of $\mathrm{W\,m^{-2}\,Hz^{-1}}$,

$$S_\nu = \int_{\Omega_s} I_\nu(\theta, \phi) \cos\theta \, d\Omega \tag{1.7}$$

Specific energy density, $(u_\nu(\Omega))$ is another useful quantity related to the specific intensity. It is defined as the energy per unit volume per solid angle per unit frequency. It is related to the specific intensity

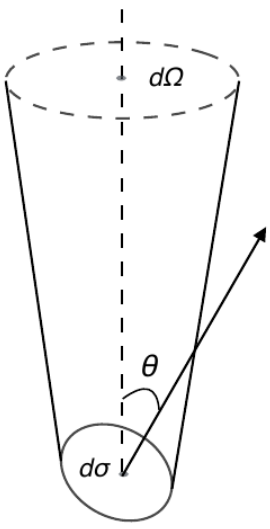

Figure 1.14: A sketch to illustrate the definition of brightness

by the relation $u_\nu(\Omega) = I_\nu/c$, where c is the speed of light. The *total spectral energy density* can be obtained by integrating over the whole sphere, 4π steradian,

$$u_\nu = \int_{4\pi} u_\nu(\Omega)\, d\Omega = \frac{1}{c} \int_{4\pi} I_\nu\, d\Omega \tag{1.8}$$

Black body radiation & Rayleigh-Jeans approximation

A black body is an idealized physical body that absorbs all incident electromagnetic radiation, regardless of frequency or angle of incidence. Black body radiation is the thermal electromagnetic radiation emitted by a black body in thermodynamic equilibrium with its environment. Its specific intensity depends only on the body's temperature. Planck showed that the specific intensity of a black body at a frequency ν in thermal equilibrium at absolute temperature T is given by

$$B_\nu(\nu, T) = \frac{2h\nu^3}{c^2} \frac{1}{e^{\frac{h\nu}{k_B T}} - 1} \tag{1.9}$$

where, h is the Planck's constant and k_B is the Boltmann's constant. For a gas cloud, the observed specific intensity can be related to an equivalent blackbody temperature according to the above equation. We call this the brightness temperature, T_B (i.e., $I_\nu \equiv B_\nu(\nu, T_B)$). In the limit of low frequencies ($k_B T \gg h\nu$), Planck's law tends to the Rayleigh-Jeans law in which the intensity becomes a simple linear function of temperature:

$$B_{\nu,\mathrm{RJ}}(\nu, T) = \frac{2\nu^2 k_B T}{c^2} \tag{1.10}$$

For observations of the cold ISM, radio astronomers work in the Rayleigh-Jeans limit. They have defined another unit of temperature called *antenna temperature*, T_A, which relates the observed specific intensity to a corresponding temperature according to the equation 1.10 (i.e., $I_\nu \equiv B_{\nu,\mathrm{RJ}}(T_A)$). T_A, used as a definition, is also valid for shorter wavelengths. However, it is only equal to the brightness temperature in the long-wavelength ($k_B T \gg h\nu$) limit.

1.7.1 Rotational line fundamentals

This section will describe the dominant mechanism by which molecules in a cloud emit radiation, namely rotational transitions. We will focus on low-lying rotational transitions of CO as this forms the basis of our thesis.

1.7.1.1 Energy levels of diatomic molecules

Diatomic molecules such as CO can be approximated as a rigid diatomic molecule that contains a carbon and an oxygen atom bound by a strong bond. In this model, we can ignore the vibration of the atoms about the central axis and simplify the calculations of the

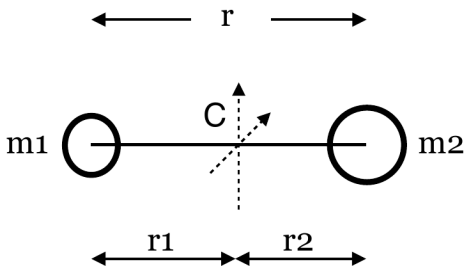

Figure 1.15: A rigid diatomic molecule with masses m_1 and m_2 joined by a thin rod of length $r = r_1 + r_2$. The center of mass is at C. The dashed lines through C denote the orthogonal axes of rotation.

rotational energy states. Although in reality, molecules rotate and vibrate simultaneously. High-speed rotations affect vibrations and vice versa. But for low temperatures, this effect is negligible, and hence our approximation gives accurate results.

We consider a rigid diatomic molecule with masses m_1 and m_2 as shown in the Fig.1.15. There are two independent rotations of the molecule about the axes shown in the figure, which pass through C and are perpendicular to the bond length. A rotation with respect to the molecular axis does not correspond to any change in the molecule as the new configuration is indistinguishable from the old one. The moment of inertia of the molecule can be written as

$$I = \mu r^2, \mu = \frac{\mathrm{m_1 m_2}}{\mathrm{m_1 + m_2}}, \tag{1.11}$$

where μ is called the reduced mass. So, the rotation of a diatomic molecule is equivalent to a rotation of a single mass μ about the origin at a distance equal to the bond length of the molecule. The kinetic energy of this rotational motion is $E_{kin} = L^2/2I$, where L is the angular momentum. The quantized rotational energy levels are,

$$E_J = \frac{h^2}{8\pi^2 I} J(J+1) = BJ(J+1), \tag{1.12}$$

where, $B = h^2/8\pi^2 I$ is defined as the rotational constant and J denotes the angular momentum quantum number. J can only take integer values such as 1, 2, 3, etc. Only transitions that involve a change in J by 1 are allowed, i.e.

$$\Delta J = \pm 1. \tag{1.13}$$

In addition to this requirement, the molecule has to possess a dipole moment, as alluded to earlier. Considering the selection rule, we can easily see that the allowed spectral lines of rotational transitions will occur at multiples of the ground state frequencies.

Thus far, we have explained the theory behind the existence of energy levels in molecules. However, how molecules jump between various energy levels remains to be seen. In the next section, we will look at the processes that cause molecules to jump between different energy levels, thereby emitting or absorbing radiation.

1.7.1.2 Transitions between energy levels: Emission and absorption

Radiation and collisions are two major processes that excite and de-excite atoms and molecules between various levels. In this section, we will have a brief look at both processes.

Radiative processes: Absorbing a photon with the right energy can excite an atom or molecule to a higher energy level. It can then de-excite to a lower level by emitting a photon with a frequency corresponding to the energy difference between these levels. Here we will look at emission and absorption caused by atoms, molecules, ions, or anything with quantized energy levels. We will denote the absorber by X. u and l denote upper and lower energy levels, respectively. During absorption, the absorber absorbs radiation and undergoes upward transition.

$$\textbf{absorption :} \qquad X_l + h\nu \rightarrow X_u\,, \qquad h\nu = E_u - E_l \tag{1.14}$$

If n_l is the number density of X in level l, then the rate of change of n_l due to absorption is given by

$$\left(\frac{dn_u}{dt}\right)_{l\rightarrow u} = -\left(\frac{dn_l}{dt}\right)_{l\rightarrow u} = n_l B_{lu} u_\nu \tag{1.15}$$

The rate of change of n_l depends on n_l itself and also on the number density of photons of the right frequency, which, here, is represented by the radiation energy density per unit frequency u_ν. Then B_{lu} is just a proportionality constant which is called *Einstein's B coefficient* for transition $l \rightarrow u$.

For X existing in an excited state u, there are two ways to emit a photon and decay to a lower energy state l,

$$\textbf{spontaneous emission :} \qquad X_u \rightarrow X_l + h\nu\,, \qquad h\nu = E_u - E_l \tag{1.16}$$

$$\textbf{stimulated emission :} \qquad X_u + h\nu \rightarrow X_l + 2h\nu\,, \qquad h\nu = E_u - E_l \tag{1.17}$$

Spontaneous radiation does not need a radiation field. It can be characterized by a probability per unit time A_{ul} : *Einstein's A coefficient*. But stimulated emission requires photons of exact frequency, polarization, and direction of propagation to take place and hence is similar to the mechanism of absorption with its proportionality constant B_{ul} : *Einstein's B coefficient* for transition $u \rightarrow l$. So, the total rate of depopulation of u due to emission can be given as:

$$\left(\frac{dn_l}{dt}\right)_{u\rightarrow l} = -\left(\frac{dn_u}{dt}\right)_{u\rightarrow l} = n_u(A_{ul} + B_{ul} u_\nu) \tag{1.18}$$

In a steady state when the level population is unchanged we can write

$$\frac{dn_u}{dt} = \left(\frac{dn_u}{dt}\right)_{l\rightarrow u} + \left(\frac{dn_u}{dt}\right)_{u\rightarrow l} = 0 \tag{1.19}$$

$$\implies n_l B_{lu} u_\nu - n_u(A_{ul} + B_{ul} u_\nu) = 0 \tag{1.20}$$

If we now place the absorbers X in a black body radiation field and allow them to come to thermal equilibrium with the field, then according to Boltzmann's law, their level populations must be populated as

$$\frac{n_u}{n_l} = \frac{g_u}{g_l} e^{-E_{ul}/k_B T} \tag{1.21}$$

where g_u and g_l are constants known as Landé's g-factors for the levels u and l and are quantum mechanical in origin. Additionally, the radiation field in thermal equilibrium will be the same as the black body radiation field at temperature T with a specific energy density given by

$$(u_\nu)_{\mathrm{LTE}} = \frac{8\pi h\nu^3}{c^3} \frac{1}{e^{(h\nu/k_B T)-1}} \tag{1.22}$$

Using Eq. 1.20, 1.21, and 1.22 one can show that all the Einstein's coefficients are related as follows:

$$B_{ul} = \frac{c^3}{8\pi h\nu^3} A_{ul} \tag{1.23}$$

$$B_{lu} = \frac{g_u}{g_l} B_{ul} \tag{1.24}$$

Collisional processes: Collisions excite atoms and molecules into higher energy levels which can then decay back into ground states, releasing radiation. These radiative losses result in the cooling of the gas. Estimating the level population from observations of either absorption or emission lines can help us probe the gas's temperature, density, or radiation field. Therefore, studying the collisional excitation is an essential tool in astronomy since it serves as a diagnostics of the physical conditions in the ISM.

Consider a two-level system without any background radiation. So, only collisional processes and radiative decay are relevant. Let n_c be the density of the colliding species. The population of an excited state can then be written as

$$\frac{dn_u}{dt} = n_c n_l k_{lu} - n_c n_u k_{ul} - n_u A_{ul} \tag{1.25}$$

where $k_{ul} \equiv \langle \sigma v \rangle_{u \to l}$ is the collisional rate coefficient, i.e. the average of the collisional cross section over a certain velocity distribution, and $A_{ul} \equiv A_{u \to l}$ denotes the radiative transition probabilities. In a steady state where the population of the levels stays constant over time, (i.e.$dn_u/dt = 0$) we get

$$\frac{n_u}{n_l} = \frac{n_c k_{lu}}{n_c k_{ul} + A_{ul}}. \tag{1.26}$$

The two collisional rate coefficients are also related as follows:

$$k_{lu} = \frac{g_u}{g_l} k_{ul} e^{-E_{ul}/k_B T_{kin}} \tag{1.27}$$

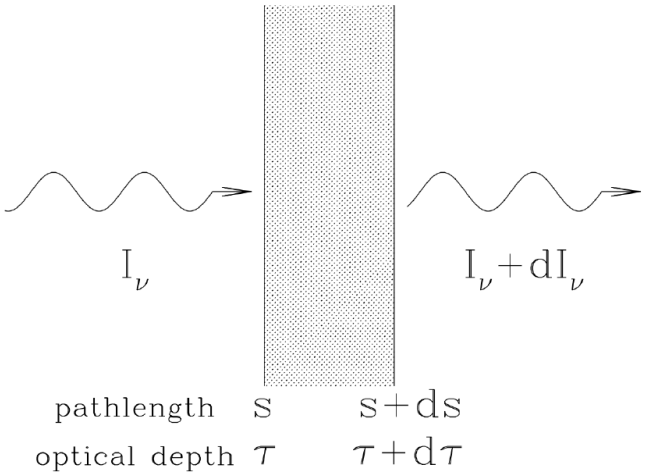

Figure 1.16: Radiative transfer illustration. This figure has been taken from Draine (2011).

where T_{kin} is the kinetic energy. One can see from this equation that as kinetic energy in the medium increases, the probability of collisions populating the upper energy level also goes up, which is intuitively true.

In the limiting case of $n_c \rightarrow \infty$ Eq. 1.26 becomes the same as Eq. 1.21.

If we want a general case where both radiation and collisions excite and de-excite the population levels, then we would need to add a rate of absorption $\bar{n}_\gamma(g_u/g_l)A_{ul}n_l$, and a rate of stimulated emission, $\bar{n}_\gamma A_{ul}n_u$ to Eq. 1.25, where $\bar{n}_\gamma$ is the averaged number of photons, more generally known as the photon occupation number. Then the steady-state equation for the most general case of a two-state system becomes

$$\frac{n_u}{n_l} = \frac{n_c k_{lu} + \bar{n}_\gamma(g_u/g_l)A_{ul}}{n_c k_{ul} + (1+\bar{n}_\gamma)k_{ul}} \tag{1.28}$$

1.7.2 Radiative transfer

So far, we have seen how a molecular cloud can emit radiation. After being emitted, the radiation propagates from the clouds to a radio telescope on Earth to be detected. But the journey in between is not always straightforward. The ISM in between can interact with this radiation by absorbing some of it and/or adding its own radiation to it. We will briefly discuss what happens when radiation travels through an interacting medium. The equation explaining the result of this interaction is commonly referred to as the radiative transfer equation.

Consider radiation of intensity I_ν passing through and interacting with a medium shaped like a slab (see Fig. 1.16). The path length in the direction of propagation is measured by the quantity s. Let us assume that on traveling through the medium, the intensity can be suppressed due to absorption or enhanced by emission (neglecting

scattering) from the slab. To quantify these, we define two quantities. The first is called the *attenuation coefficient* (κ_ν). It has a dimension of $1/l$. It quantifies the fraction by which intensity gets absorbed on traveling a distance ds in a medium at a given frequency ν. The second quantity is a characteristic of the medium called its *emissivity* (j_ν). It has a dimension of power per unit volume per unit frequency per unit solid angle. On multiplying it by the distance ds, we obtain the amount of intensity the slab adds to the incident radiation at any given frequency ν. Using these two quantities, it is then straightforward to see that the evolution of intensity follows the following equation of radiative transfer as it travels through the medium:

$$dI_\nu = -I_\nu \kappa_\nu ds + j_\nu ds. \tag{1.29}$$

To cast the Eq. 1.29 into a convenient form, astronomers replace the independent variable s with a new quantity, *optical depth* (τ_ν), defined as

$$\tau_\nu \equiv \kappa_\nu ds. \tag{1.30}$$

Equation 1.29 then becomes

$$dI_\nu = -I_\nu d\tau + S_\nu d\tau \tag{1.31}$$

where S_ν is called the *source function* defined as $S_\nu \equiv j_\nu/\kappa_\nu$. This equation is called the *equation of (radiative) transfer*. The difficulty in solving the equation of transfer is that the source function is often a function of intensity, making the equation of transfer nonlinear. Nevertheless, one can obtain a formal solution to the Eq. 1.31 if we integrate it by taking the $I_\nu d\nu$ to the left hand side and multiplying by an integrating factor e^{τ_ν}. Setting the limits of integration from an arbitrarily initial point defined as $\tau_\nu = 0$ with intensity $I_\nu(0)$ we obtain the integral form of the equation of radiative transfer (we have multiplied a factor $e^{-\tau_\nu}$ at the end):

$$I_\nu(\tau_\nu) = I_\nu(0)\, e^{-\tau_\nu} + \int_0^{\tau_\nu} e^{-(\tau_\nu - \tau')} S_\nu d\tau' \tag{1.32}$$

This is a general solution to the Eq. 1.31 as long as we neglect scattering. This equation can be interpreted very easily as follows:

The initial intensity, $I_\nu(0)$, gets attenuated by a factor $e^{-\tau_\nu}$ but also gets enhanced due to the emission by the medium itself. This enhancement is equal to $S_\nu d\tau'$ times an attenuation factor ($e^{-(\tau_\nu - \tau')}$). This attenuation is due to self-absorption by the medium and begins at the point of emission.

In the simple case of a homogeneous material that only absorbs, only the first term of Eq. 1.32 remains. Thus, over a few optical depths, the intensity goes down exponentially. From the definition of optical depth, radiation traveling in a weakly absorbing cloud $\kappa_\nu \ll 1$ would need to travel a large distance ds before the intensity drops substantially. So, a small cloud with a small κ_ν satisfies the condition $\tau_\nu \ll 1$ and hence is transparent to the incident radiation. Such clouds are referred to as *optically thin*. On the other hand,

a cloud with $\tau_\nu \gg 1$ would absorb most of the incident radiation and hence appear to be opaque. These clouds are referred to as *optically thick*.

A common simplification is to assume an emitting cloud without background radiation to have a uniform emissivity, i.e. $S_\nu = \text{const.}$. Then Eq. 1.32 simplifies to

$$I_\nu(\tau_\nu) = I_\nu(0)\, e^{-\tau_\nu} + S_\nu(1 - e^{-\tau_\nu}) \tag{1.33}$$

Observers are usually interested in the emitting cloud. However, the observed intensity is usually the sum of the source and background intensity. Hence, they need to subtract the background intensity to retrieve the emitting source intensity. We can write this as

$$I_\nu(\tau_\nu)^{\text{source}} = I_\nu - I_\nu(0) = [S_\nu - I_\nu(0)](1 - e^{-\tau_\nu}) \tag{1.34}$$

Now, if the emitting cloud is approximated to be a blackbody at temperature T, its intensity can be written as

$$I_\nu = B_\nu(T) = \frac{2h\nu^3}{c^2}\left(\frac{1}{e^{\frac{h\nu}{k_B T}} - 1}\right). \tag{1.35}$$

Finally, at radio and sub-millimeter wavelength the Rayleigh-Jeans approximation ($k_B T \gg h\nu$) can be applied giving us the classical approximation of the Planck's law

$$B_\nu = \frac{2\nu^2}{c^2} k_B T_B \tag{1.36}$$

where, T_B is usually defined by radio astronomers as the Rayleigh-Jeans brightness temperature of the source. Rearranging, this equation gives us

$$T_B = \frac{c^2}{2k_B\nu^2} I_\nu \tag{1.37}$$

The Eq. 1.37 can be considered an independent definition in itself regardless of the classical Rayleigh-Jeans approximation. In that case, it is commonly referred to as *radiation temperature*:

$$J_\nu(T) = \frac{c^2}{2k_B\nu^2} I_\nu = \frac{h\nu}{k_B}\left(\frac{1}{e^{\frac{h\nu}{k_B T}} - 1}\right) \tag{1.38}$$

As we can see, by construction $J_\nu(T)$ and T_B are equal.

$J_\nu(T)$ is also proportional to the intensity observed above the background as can be seen from Eq.1.35. We can then use Eq.1.34 along with Eq. 1.37 to get

$$T_B = J_\nu(T) = [J_\nu(T_{ex}) - J_\nu(T_{bg})](1 - e^{-\tau_\nu}) \tag{1.39}$$

This form of the radiative transfer equation will be used in later chapters to infer the temperature, optical depths, and densities of observed molecular clouds.

1.8 Motivation for the thesis

So far, we have provided an overview of the background knowledge essential for the rest of this thesis. In this section, we summarize some questions that motivated this dissertation.

As mentioned in section 1.4, molecular clouds (MCs) are the primary reservoirs of cold star-forming gas in the Milky Way and other galaxies. Therefore, any attempt to understand the theory of star-formation must address the theory of MCs' formation, evolution, and dissipation. Their nature, lifetimes, and whether they are virialized structures are all areas of active research. The physics of these regions is very complex and requires extensive exploration to understand their structure and evolution (Dobbs et al. 2014; Ballesteros-Paredes et al. 2020, and references therein for an extensive discussion of molecular clouds).

Many mechanisms are believed to contribute towards the formation of MCs. First, thermal instabilities (Field 1965) are believed to enable gas to efficiently transition from a diffuse, warm phase to dense, cold clouds. After this, multiple mechanisms have been proposed that may work together to enable clouds to gather mass. Some prominent mechanisms are agglomeration, converging flows, spiral arm passages, cloud-cloud collisions, shock-waves, and large-scale instabilities (see Section 2 in Ballesteros-Paredes et al. 2020, for a detailed discussion of each of these mechanisms).

The characterization of the lifecycle of MCs is also pertinent in understanding the theory of star formation. However, measuring the lifetimes of MCs has been notoriously hard, both theoretically and observationally. The lack of MC associations with stars with ages $\sim$ 10 Myr or more in the Milky Way (e.g., see Hartmann et al. 2001), combined with the fact that in the Solar Neighborhood, most MCs are associated with only stars younger than $\sim$ 3 Myr (Ballesteros-Paredes et al. 1999), has led many to suggest that molecular clouds are transient structures that disperse after star formation. But another view considers GMCs to be long-lived objects with lifetimes up to about 100 Myr (McKee & Ostriker 2007, and references therein).

Another area of active research that has been made possible by the advent of multiple large-scale surveys of the molecular clouds in the Milky Way is the statistical studies of their properties such as densities, velocity dispersions, masses, star-formation rates, etc. (e.g. Duarte-Cabral et al. 2021; Rigby et al. 2019). Large statistical samples can help us study the distribution of relevant properties of clouds. Some studies have also investigated the dependence of MC properties on their galactic environments (e.g., Colombo et al. 2021). These studies also enable us to test and refine our understanding of Galactic structure (Duarte-Cabral et al. 2015; Ragan et al. 2014). Unfortunately, early surveys of MCs usually had a poor angular resolution which could not resolve molecular clouds. Since star formation happens inside clumps, resolving MCs into clumps in a large-scale survey can help us unravel the following stages of star formation. This issue of poor angular resolution has been partially remedied by higher resolution surveys such as the CHIMPS (Rigby et al. 2016) survey towards the northern sky. However, the coverage of the Milky Way remains incomplete at this resolution towards the south: SEDIGISM (Schuller et al.

2021) has a resolution of ∼ 30″ which is not enough to resolve clumps.

Since GMCs form massive stars, which can then influence their parent cloud evolution via multiple feedback processes, understanding the exact feedback mechanisms and their relative importance is vital in understanding the theory of star-formation as well as GMC-formation and evolution. Feedback is believed to be an important factor along with magnetic fields in explaining the discrepancy between observed molecular depletion and free-fall times (depletion times being about 1-3 orders of magnitude longer than free-fall times) (Krumholz et al. 2012; Federrath & Klessen 2013). It is also essential in the dispersion of stellar clusters and producing the observed IMF (Krumholz et al. 2014). Although many numerical simulations look at the destructive aspects of stellar feedback (see Krumholz et al. 2014, and references therein), there are only a few observational studies on the effects of feedback on the molecular gas. Additionally, feedback may also trigger the formation of stars inside GMCs, but observational evidence is scarce (Thompson et al. 2012; Hindson et al. 2010).

The understanding of molecular clouds and various processes related to star formation inside them can be studied by studying the cold molecular gas itself. This thesis was motivated by the need to understand the physical properties of molecular clouds, which is essential to understanding the theory of their formation and evolution. Therefore, the thesis presents the planning and observation of a new, sensitive, high-resolution survey of GMCs.

1.9 Structure of the thesis

The thesis has been divided into six chapters, including this introduction. We present the structure of the thesis below:

- In Chapter 2 we will present the details about the telescope and the new instrument used in carrying out the observations for this thesis. In addition, the results of characterization and commissioning work done on the instrument will also be presented here.
- Chapter 3 will present the results of a pathfinder study done to kick start a survey of GMCs in the Milky Way in ^{12}CO (3−2) and ^{13}CO (3−2) rotational transitions.
- The following two chapters (Ch. 4 and 5) will focus on the giant molecular cloud G305 as a part of a science demonstration case for the galactic survey. Both these chapters will focus on investigating the effects of feedback from OB stars on the parent cloud complex.
    - In Chapter 4 we present the results of the feedback on the excitation and dynamics of the gas in the molecular cloud.
    - Chapter 5 explores the impact the feedback has on the ongoing star formation in the GMC by studying the hierarchical structure of the molecular cloud and comparing it with the average galactic properties of molecular clouds.

- Chapter 6 will outline the current status of the survey and future prospects.
- Finally, Chapter 7 will provide a summary of the thesis and its findings.

Part II

Commissioning the Instrument

Chapter 2

The Large APEX sub-Millimeter Array (LAsMA) and its commissioning

2.1 APEX and LAsMA

All observations for this thesis have been done using the newly installed LAsMA receiver on the APEX telescope. Below we provide a summary of the telescope and the receiver.

2.1.1 APEX

The Atacama Pathfinder EXperiment (APEX) telescope (Güsten et al. 2006) is a 12-metre diameter telescope, operating at millimeter and sub-millimeter (sub-mm) wavelengths - between infrared light and radio waves (Fig. 2.1). It is a collaboration between the Max Planck Institute for Radio Astronomy (MPIfR), the Onsala Space Observatory (OSO), and European Southern Observatory (ESO). It is located at an altitude of 5100 m at Llano de Chajnantor, in the Chilean Andes. Being one of the driest places on the planet, this is known to be one of the best locations in the world for sub-mm astronomy. Observations at sub-mm wavelengths need arid atmospheric conditions because of the absorption by the water present in the atmosphere. The precipitable water vapor (PWV) determines the atmospheric transparency for sub-mm observations. Typical PWV values at the telescope site are around 1.0 mm and fall below 0.5 mm about a quarter of the time. The median PWV drops by a factor of 2-3 during winter when compared to the rest of the year (Güsten et al. 2006). As seen from Fig. 2.2, these conditions are ideal for observing sources at sub-mm wavelengths.

It is also the largest sub-millimeter single-dish telescope currently operating in the southern hemisphere. The dish is a modified prototype of one of the Atacama Large Millimeter Array (ALMA) interferometer antennas. ALMA is an array of 64 antennas of 12 m diameter each, also situated in the same location in the neighborhood of APEX. APEX provides a quick turnaround for pathfinder studies that can be followed up with ALMA for more detailed observations. Being a single-dish also makes it very suitable for large-scale science surveys (Schuller et al. 2009, 2017). Furthermore, operating at sub-millimeter wavelengths means APEX complements other telescopes such as the former Herschel Space Observatory and the Stratospheric Observatory for Infrared Astronomy (SOFIA) that reach higher frequencies well above 1 THz; a regime not accessible from the

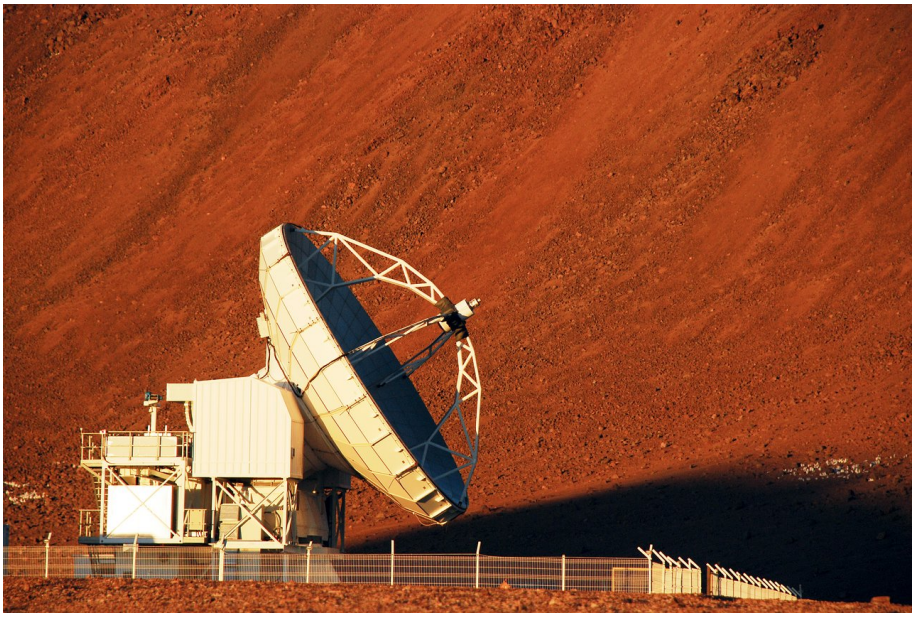

Figure 2.1: APEX Telescope at Llano de Chajnantor, Chile. The cabin behind the main dish, called the Nasmyth-B cabin, houses the new LAsMA receiver. This image has been taken from http://www.apex-telescope.org/ns/the-telescope/.

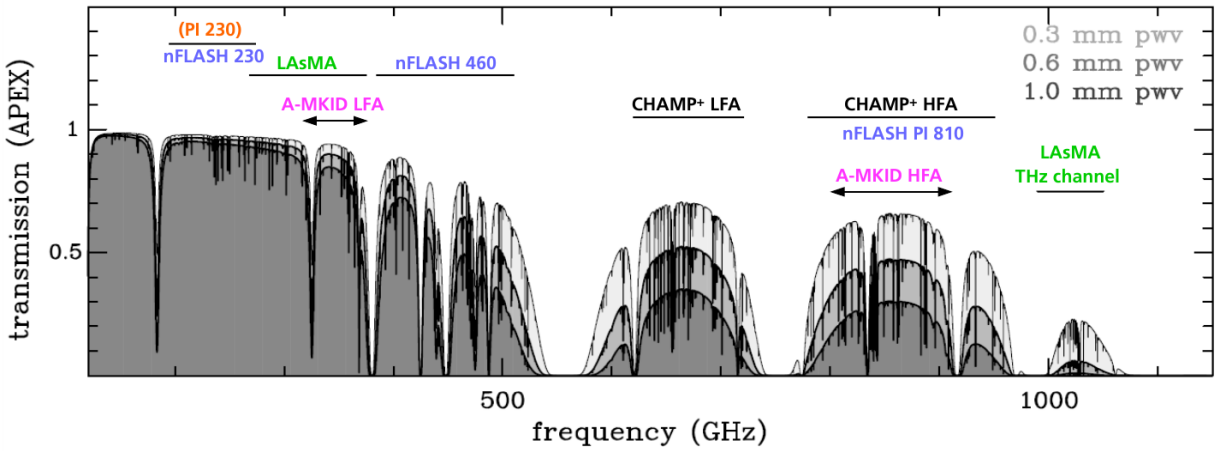

Figure 2.2: Zenith transmission of the atmosphere above Llano de Chajnantor at submillimeter wavelengths. Different receivers covering different frequency ranges are marked on top. (Image Credit: B. Klein)

Figure 2.3: LAsMA in APEX's B-cabin. Image taken from LAsMA page at MPIfR website.

ground. Equipped with a plethora of receivers[1], e.g. nFLASH, SEPIA, LASMA, CHAMP etc., APEX covers a broad range of frequencies starting from ~ 160 GHz up to ~ 850 GHz, serving a broad range of scientific needs.

2.1.2 LAsMA

The Large APEX sub-Millimeter Array (LAsMA) is a receiver installed in 2017 inside the Nasmyth-B cabin on the APEX telescope (Güsten et al. 2008, Fig. 2.3). It is a single polarization heterodyne receiver with 7 pixels that operates in the 870 μm atmospheric window. It covers a radio frequency (RF) range of 268 to 375 GHz. The 7 pixels are arranged in a hexagonal pattern on-sky with one central pixel surrounded by the six other pixels, one at each vertex of the hexagon (Fig. 2.4). The pixels have a fixed spacing between each other equal to about 40″ and a full-width-half-power beam size ranging from 17″ to 23″ depending on the frequency of operation.

Figure 2.5 shows a cross-section view of the receiver architecture. LAsMA uses seven state-of-the-art 345 GHz dual-sideband (2SB) Superconductor-Insulator-Superconductor (SIS) mixers developed at the Institut de Radioastronomie Millimétrique (IRAM). These are similar to the ALMA band 7 mixers and provide an intermediate frequency (IF) bandwidth of 4–8 GHz for each sideband. The Virginia Diodes, Inc.(VDI) manufactured local oscillator (LO) is based on an amplifier-multiplier chain (AMC). The final stage of this multiplier chain is situated inside a cryostat in order to increase the output power

[1]for more information, see https://www.apex-telescope.org/ns/instruments/

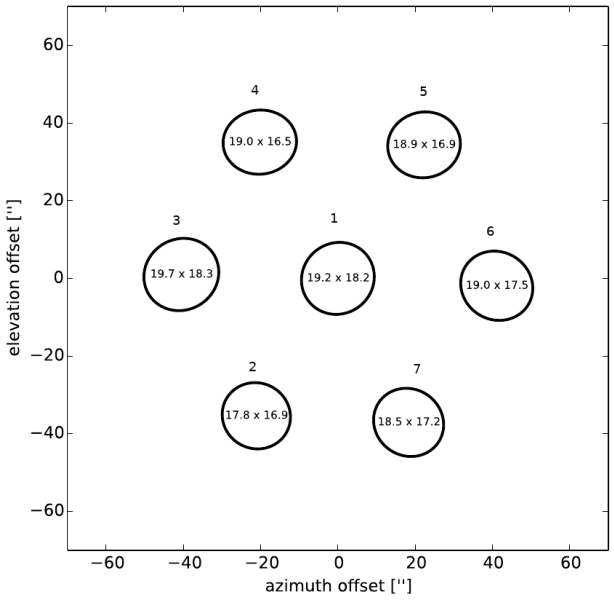

Figure 2.4: LAsMA beam shapes derived from deconvolved beam maps from multiple observations of Mars performed during the commissioning phase. The numbers above the pixels are the nomenclature used to refer to the pixel number in an unrotated beammap (derotation angle=0). (Credit : Dr. A. Weiss)

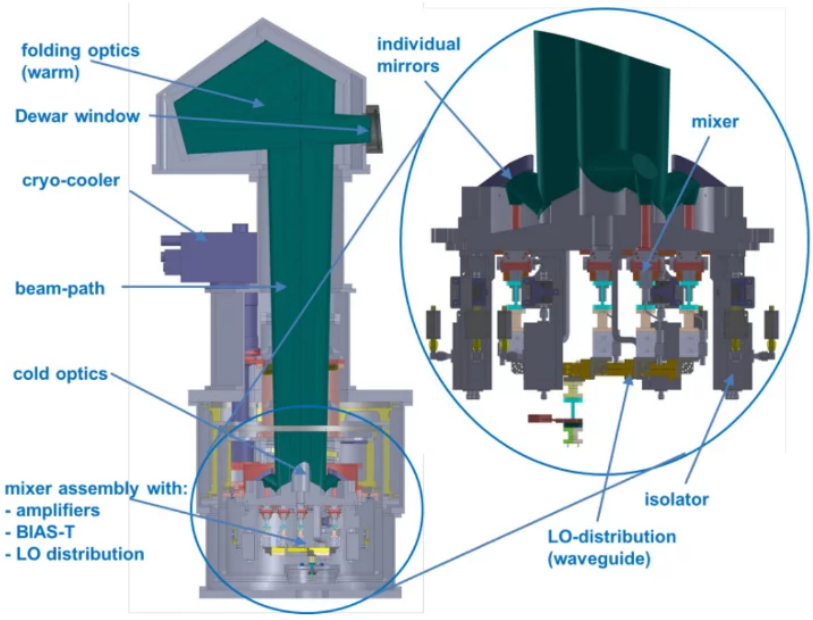

Figure 2.5: A longitudinal cross section view of the LAsMA calibration unit. Image taken from https://www.mpifr-bonn.mpg.de/5278286/lasma.

by cooling it to about 100 K. A K-mirror type image derotator is installed as a part of the warm optics to compensate for image rotation on-sky.

The backend consists of Fast Fourier Transform Spectrometers (FFTS4G; Klein et al. 2012) that cover the IF bandwidth of 4–8 GHz instantaneously with 65536 spectral channels with a width of 61.03 kHz. The sideband suppression is > 15 dB.

2.2 LAsMA commissioning

2.2.1 Pixel positioning

Before observations, the positions of the pixels were measured. Usually, the pointing model at APEX applies the pointing corrections to the central pixel. Then, the correction to the rest of the pixels is applied assuming a fixed separation between them with respect to the central pixel. Therefore, it is essential to know the relative offsets of the outer pixels with respect to the central pixel for imaging. This pixel positioning was measured with beam maps on planets. These were done on Mars, Jupiter, and Saturn. Multiple beam maps were observed on each planet with the pixel array rotated in multiples of 60° in the horizontal (HO) coordinate system (referred to from now on as derotation angle; see Section 2.2.2 for the relevance of observing at different derotation angles). The rotation of pixels here was performed as a consistency check to ensure rotation in multiples of 60° preserves the relative positioning amongst the pixels. Figure 2.4 shows the deconvolved beam sizes for all the pixels.

When APEX is pointed towards a source, a pointing model is used to position the receiver exactly on the source. However, the model is not exact; its accuracy can vary with the position on sky and time of the observations and usually deteriorates over time, therefore needing regular calibration. This calibration is done by conducting a cross scan on the source (referred to as pointing observations here onward). The telescope observes the source over a range of offsets in azimuth and elevation during a pointing observation, either continuously for continuum sources (e.g., planets) or in discrete steps for line pointing sources. A Gaussian function is then fitted to the intensity of the source as a function of offset (a built-in function called `redpoint` performs this fitting at APEX), and the corrections are then applied to the pointing model. A deviation of less than 20% of the beam size is considered acceptable in pointing. Otherwise, the pointing corrections are refined with another pointing.

For LASMA, this pointing correction is done only with the central pixel during regular observations. If the relative offsets for the outer pixels are exact, the correction applied to the central pixel should be the same needed for the outer ones. To verify this, we tested the accuracy of the relative offsets for the outer pixels obtained from previous beam map observations on planets by doing CO (3–2) line pointing observations on IRC+10216. The spectral line set-up was chosen to be the same as that used in the survey ($\nu_{\rm LO}$ = 338.190 GHz). During this test, the central pixel was first pointed towards IRC+10216, and the corrections were applied to the receiver array. One of the outer pixels was then pointed at the source using their relative offsets. A pointing was performed

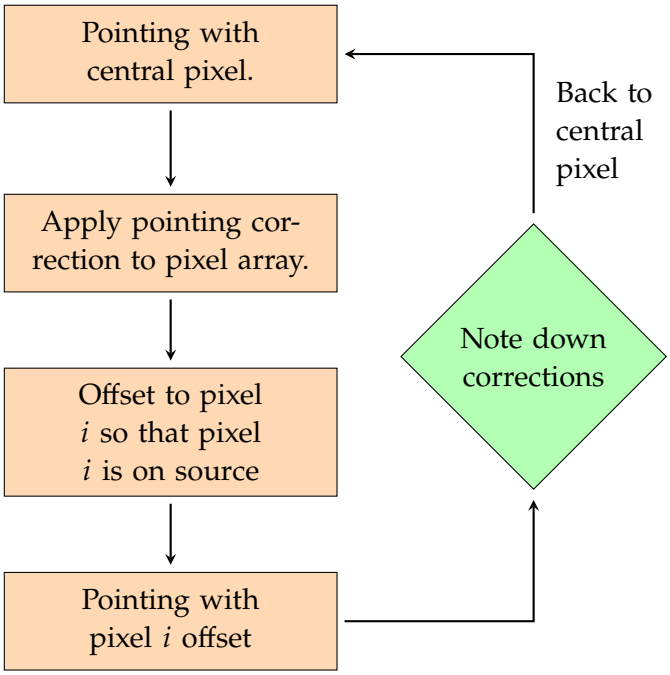

Figure 2.6: Flowchart showing the process of testing the pointing accuracy of outer pixels.

again, with the source now centered on the outer pixel. In the ideal case where the relative offset is exact, this should result in a pointing correction of $(x, y) = (0, 0)$. Figure 2.6 shows the algorithm used to test the pointing accuracy of the outer pixels.

Table 2.1 lists the corrections for the outer pixels. The final column lists the maximum measured peak antenna temperature for the source on each pixel (given by the peak of the Gaussian fit to the cross scans). The maximum correction calculated for the outer pixels is only $\approx 6\%$ of the beam size (measured on pixel 2), which is within the accuracy of the measurement, thereby confirming the offsets measured from the beam maps. Hence, we can safely assume that the pointing corrections applied to the central pixel work for all outer ones as well. Despite this, we note that the peak source temperature measured on the source for each pixel varies significantly. Therefore, the beam efficiency, which is measured only for the central beam in LASMA, is not always applicable to outer pixels. However, for our mapping observations, each pixel observes all the positions. Hence, we are instead interested in the average efficiency of all receiver elements in order to calibrate the observed flux.

2.2.2 Derotation dependent gains: Calculating main-beam efficiency

In the course of an observation, the telescope tracks a source on the sky. During this process, the orientation of the source changes with respect to the receivers in the Nasmyth cabin (partly due to the change of elevation owing to the fact that the receiver is static inside the Nasmyth cabin and partly due to the rotation of the sky). Therefore, in order to preserve the source's orientation with respect to the receiver, a K-mirror derotates the

Table 2.1: Correction to the relative offset of LAsMA outer pixels with respect to the central pixel. Δ Alt and Δ Az stand for the corrections in altitude and azimuth coordinates respectively.

Pixel	Δ Alt (″)	Δ Az (″)	T_{peak} (K)
1	–	–	28.6±0.2
2	1.25	-0.04	26.7±0.2
3	0.45	0.27	23.6±0.2
4	0.57	-0.38	24.7±0.2
5	-0.28	-0.34	25.7±0.2
6	0.10	-0.26	25.4±0.2
7	1.05	-0.38	25.3±0.2

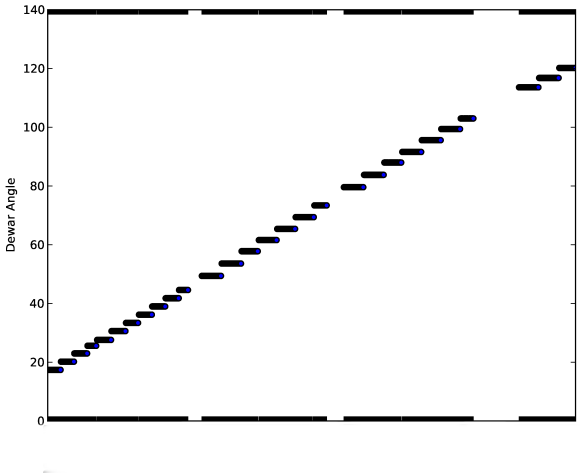

Figure 2.7: Progression of derotation angle of LAsMA pixels with time during a single on-the-fly (OTF) scan. The x-axis represents the progression of time.

signal before it reaches the latter. This angle of rotation of the mirror is saved in the data by the "derotation angle" variable (see Fig. 2.7).

During the commissioning phase, beam maps on Mars were created for a range of derotation angles equal to multiples of 60° in horizontal mode.[2] Table 2.2 lists the derotation angles of different beam maps observed. At this point, it is prudent to distinguish two very similar-sounding terms: *pixel numbers* (or simply pixels) and *pixel positions*. Pixel position is used to refer to the position of pixels numbered 1 to 7 on the sky at a 0° derotation (also referred to as an unrotated beam map). On derotating at multiples of 60°, the pixels will swap positions with each other. In this case, although the configuration appears to be the same, the pixel numbers will be different from their corresponding sky

[2]The data for these observations can be found under the project account t-0105.f-9991a-2020 at APEX, and the functions used to create the beam maps were written by J. P. Pérez-Beaupuits and can be found in /homes/t-0105.f-9991a-2020/Reduction/beammaps/multiPixel.

Table 2.2: Nominal derotation angle in horizontal mode and their corresponding derotation angle derived from the fits header along with the source elevation for different observations of Mars done during commissioning. The three quantities are related by the equation $\Theta_{cab} = \Theta_{HO} + 21.7 + El$, where 21.7 is an arbitrary encoder offset.

Scan Number	Derot Nominal $\Theta_{HO}(^o)$	Derot Header $\Theta_{cab}(^o)$	Elevation $El\ (^o)$
30995	0	78.4	56.7
30997	60	136.2	54.4
30999	120	193.6	51.9
31006	180	249.2	47.5
31008	240	306.0	44.2
31010	300	2.4	40.7

positions. This is illustrated in Figure 2.8.

Having distinguished between pixel numbers and positions, we return to the beam maps done on Mars at different derotation angles. Figure 2.9 shows the relative intensity for each pixel with respect to the mean intensity for all pixels for a given scan. The beam positions and shapes are derived from the Gaussian fits as a function of the sky position. In this presentation of the result, each outer position shows the parameters for pixels numbered 2 to 7. This is so because by rotating the dewar in steps of 60°, the pixels will exchange their positions on the sky (as alluded to in the previous paragraph). Here also, one can see that pixel positions 3 and 4 have a lower efficiency. They appear to be most likely affected by shadowing or have a systematically lower coupling to the telescope. This effect is independent of the pixel number and only depends on the sky position. Furthermore, the beam shape and position are independent of the derotation angle for positions 1, 5, 6, and 7. In contrast, positions 2, 3, and 4 show a larger scatter in the beam ellipticity and relative position. The averaged and deconvolved response of the array as shown in Fig. 2.10 also demonstrates the lower efficiency of positions 3 and 4.

During mapping observations, for which all pixels fully sample the region (except for the map edges), the flux calibration needs the average efficiency of all pixels instead of just the central one. The calibrator labels the pixels as 1-7 for the lower sideband (LSB) and 8-14 for the upper sideband (USB). Thus, all efficiency measurements usually done on LAsMA are only for Pix 1 and 8 for LSB and USB, respectively. Figure 2.11 shows the calibrated Mars brightness temperature (T_A^*) as a function of the derotation angle for the central pixels (1 and 8) and the mean of all pixels in the LSB (1-7) and the USB (8-14). The central beams display a stronger dependence (factor of ~ 2 greater) on the derotation angle compared to the average of all pixels. The standard LAsMA efficiency measurements are done using the `derotmode='ho'` and `derotangle=0`. This roughly translates to a range of 50° to 100° for the derotation angle within the observable elevation range of 30° to 80°. According to Fig. 2.11, this means that efficiencies are measured at the maximum response range of the central pixel. We calculate the ratio between the response for the efficiency measurement compared to the mean of all LSB/USB receivers over all angles

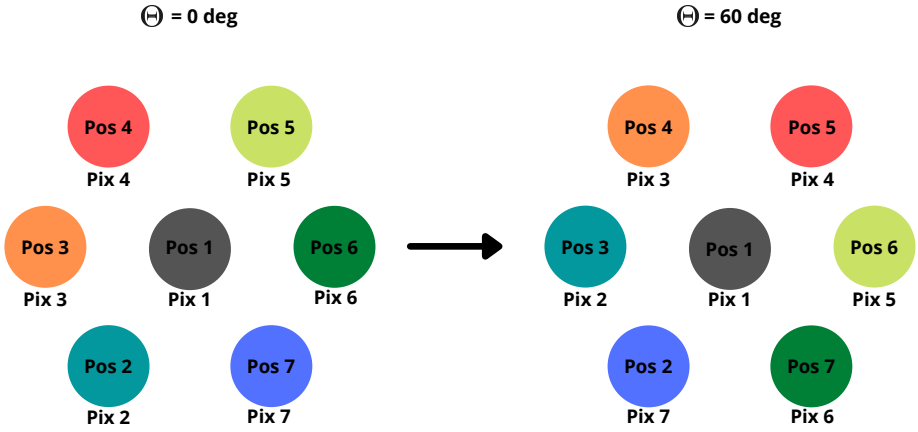

Figure 2.8: Labeling of pixel numbers and pixel positions at derotation angles of 0° and 60°. This is intended to clarify the distinction between the two terminologies.

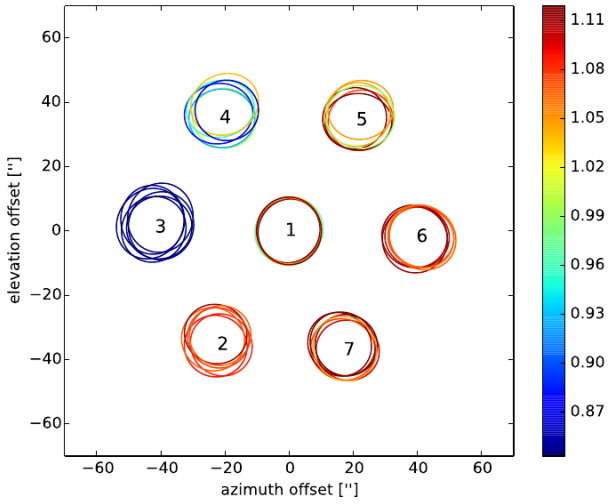

Figure 2.9: Results of the 2D Gaussian fits for each pixel and each beam map for different derotation angles. Positions of the central beam are not shifted to the origin. The relative response is shown in color coding. Labels for a given position correspond to the pixel position for an unrotated beam map.

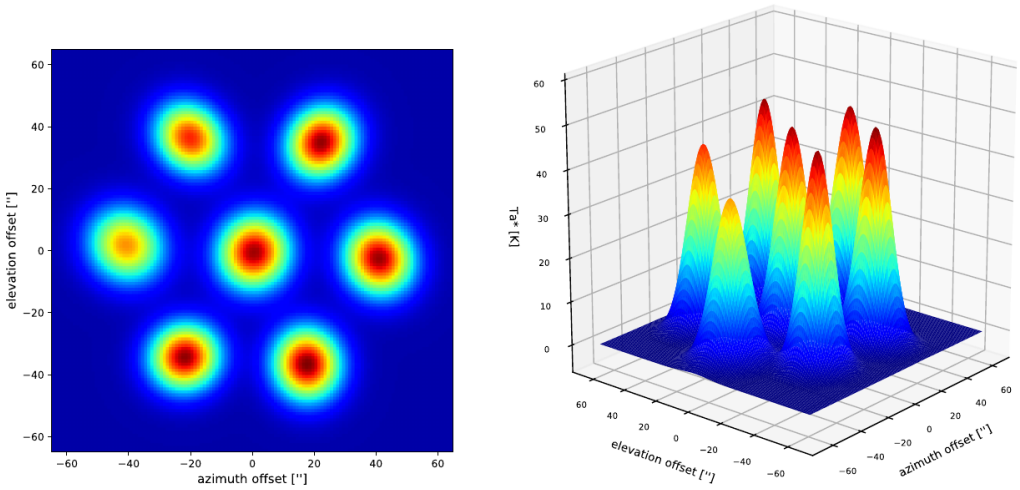

Figure 2.10: Averaged and deconvolved array response derived from Gaussian fits shown in 2 and 3D representations.

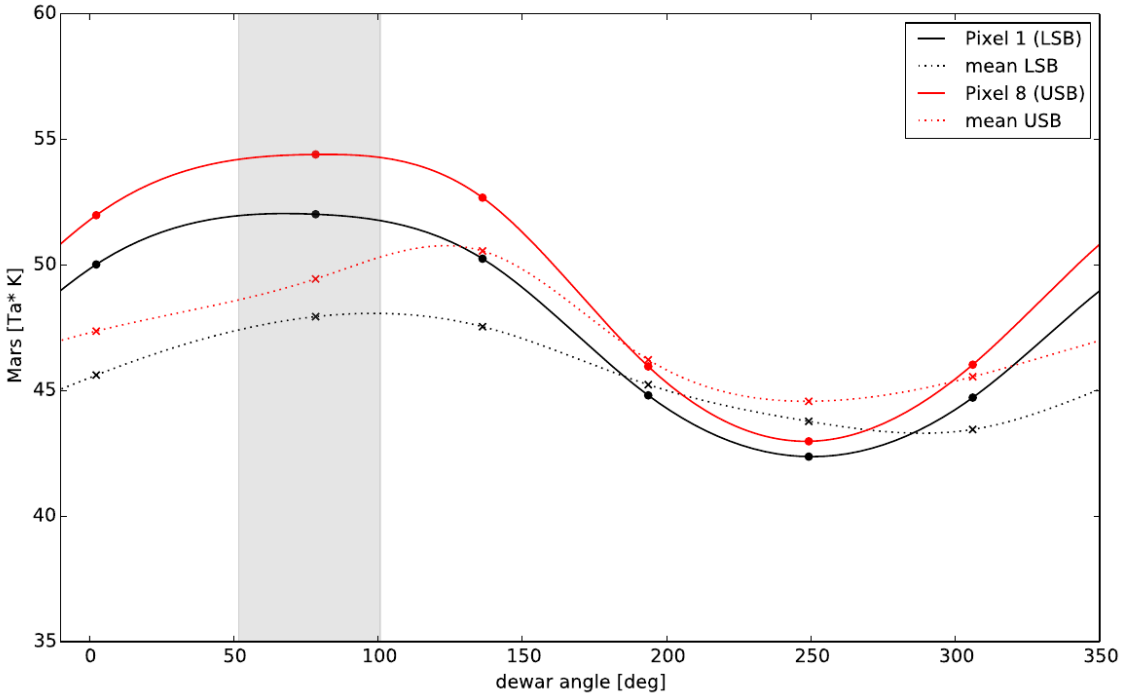

Figure 2.11: Mars brightness temperature as a function of the derotation angle. The grey shaded area shows the derotation angle range used for the measurements of the beam efficiencies.

to derive the main beam efficiency of a calibrated standard map as

$$\eta_{mb,array} = 0.87\,\eta_{mb} \tag{2.1}$$

where η_{mb} is the main beam efficiency of the central pixel.

This was followed up with observations of Jupiter with all pixels. Instead of pointing on each pixel individually, we performed on-the-fly (OTF) scans of Jupiter at angles of 0, +60, and -60 degrees (in the horizontal coordinate system) so that all 7 pixels are covered (3 per angle). This was done in different derotation angles increasing by multiples of 30° and the OTF scans being repeated each time in the rotated frame. A calibration was always performed before each set of 3 OTFs per angle.

Following this, a peak intensity and receiver temperature (T_{rec}) vs. nominal derotation angle plot was made for each pixel in both sidebands. Figure 2.12 shows the results. Inspecting the nature of the variations of peak intensities indicates a sinusoidal nature for the derotation-dependent gain for all pixels. Additionally, all the angles of minima for the outer pixels are shifted by multiples of 60 degrees. Similar to the beam map analysis of Mars, this hints at the possibility that the angle-dependent response of the outer pixels could be explained by a difference in the optical path traveled by the signal to reach these pixels depending on their location in the array. To confirm this, we shifted the associated derotation angle corresponding to the individual angle of the given pixel (i.e. $\theta \rightarrow \theta + i(\pi/3)$). As can be seen from Fig. 2.12, the pixels have similar losses for the same optical paths. Since the peak losses for the outer pixels are situated at multiples of 60 degrees, the average loss for any given derotation angle should remain independent of the derotation angle. This can be seen from Eq. 2.2.

$$\begin{aligned}\sum_{i=1}^{6} \sin\left(\theta + i\cdot\frac{\pi}{3}\right) &= \sum_{i=1}^{6}\left(\sin\theta\,\cos\frac{i\pi}{3} + \cos\theta\,\sin\frac{i\pi}{3}\right)\\ &= \sin\theta\sum_{i=1}^{6}\left(\cos\frac{i\pi}{3}\right) + \cos\theta\sum_{i=1}^{6}\left(\sin\frac{i\pi}{3}\right)\\ &= 0\end{aligned} \tag{2.2}$$

The lower panel of Fig. 2.12 also confirms this. To ensure this result was reproducible, the Jupiter OTF scans were repeated on different observing runs spanning the duration of the observations. The results obtained did not vary significantly.

To calculate the beam efficiency differences, we compared the peak intensities for the central pixels versus the mean of all pixels. Figure 2.13 shows the same plot as Fig. 2.11 but for the Jupiter measurements. Intensities as a function of derotation angle are comparable to the Mars measurements. The dependence of the mean intensities of all pixels on the derotation angle is smaller than the variations seen for the central pixel (±2% compared to ±6%). Additionally, the intensity of the central beam for the derotation angles expected for the beam efficiencies measurements (50–100°) is roughly located in the maximum response range of the central pixel. Averaging over both sidebands, the

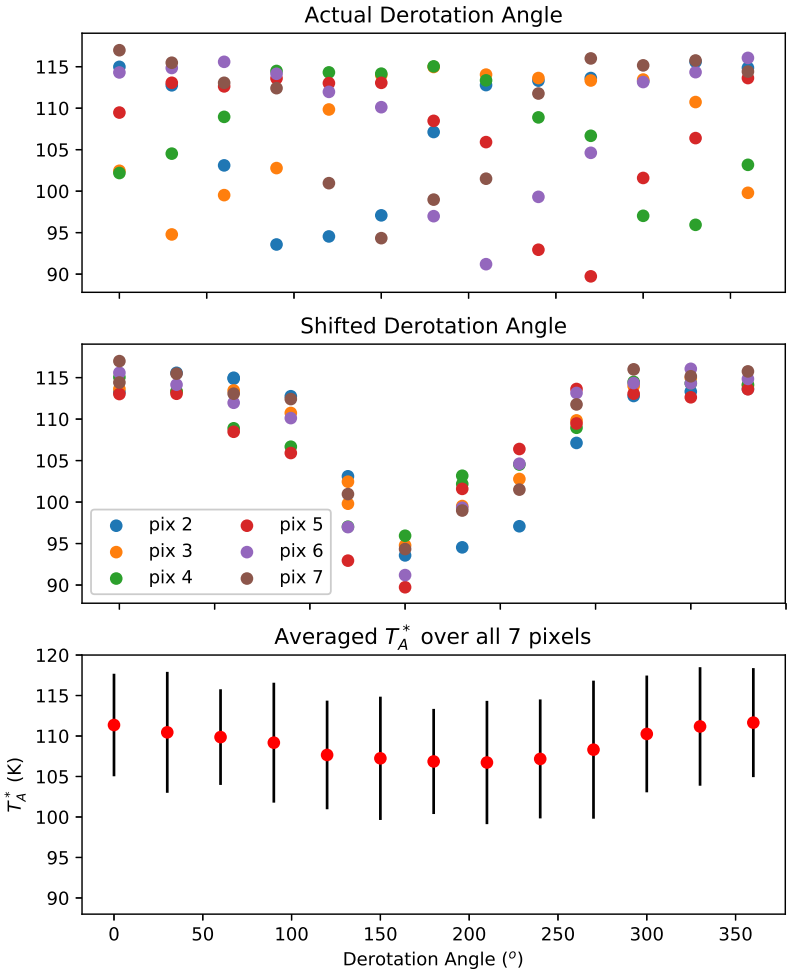

Figure 2.12: T_A^* vs derotation angle plots for observations of Jupiter. Upper panel: Plot of outer pixels of LAsMA vs. their nominal derotation angle. Middle panel: Each pixel has been shifted by a multiple of 60 degrees to align their optical paths to each other. Lower panel: T_A^* averaged over all 7 pixels for each derotation angle.

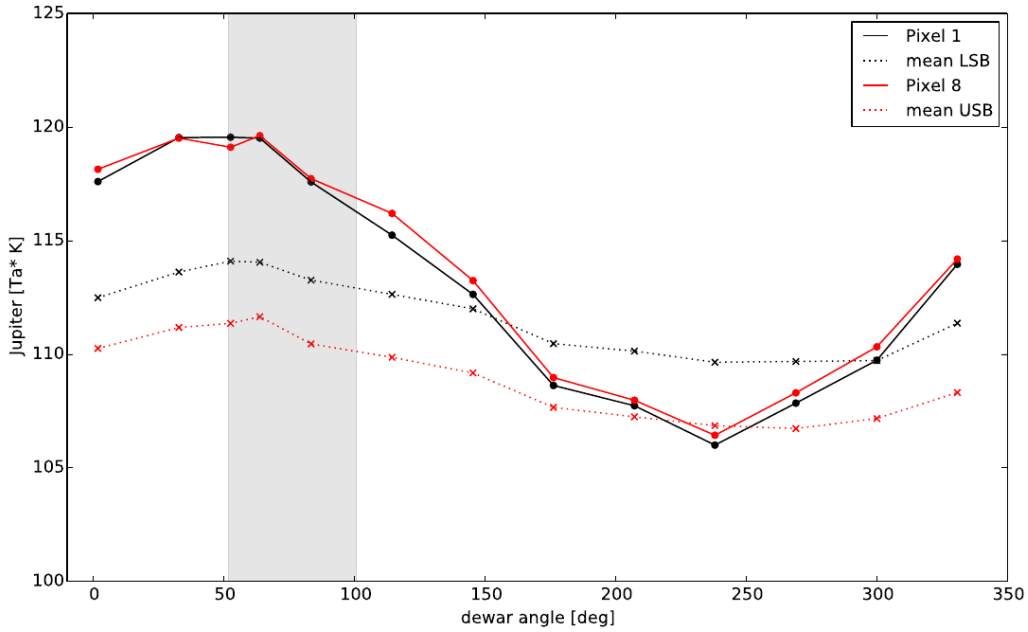

Figure 2.13: Jupiter brightness temperature measured as a function of the derotation angle. The grey shaded area shows the derotation angle range used for the measurements of the beam efficiencies.

intensity for the central beam within this angle range is 8% higher than the mean of the all LSB/USB receivers over all angles, which reduces the main beam efficiency to calibrate a standard map to:

$$\eta_{mb,array} = 0.93\,\eta_{mb} \tag{2.3}$$

Combining, Eq. 2.1 and 2.3 we derive the final estimate of the array efficiency as:

$$\eta_{mb,array} = 0.9\,\eta_{mb} \tag{2.4}$$

2.2.3 Sideband rejection

With finite sideband rejection, very strong signals in the image band may leak into the signal band leading to potential blending with lines in the signal band. The atmospheric calibration also depends on the sideband rejection. To test the sideband rejection with different local oscillator (LO) setups (commonly referred to as line setups), we calculated them with the receiver at different LO frequencies. The observations were done on IRC+10216. Sideband rejection is also dependent on the intermediate frequency (IF) at which the signal is observed. Since the spectrometers operate over the IF range ($4 < |\nu_{\rm IF}| < 8$), the LO setups were also chosen such that the signal is observed at the left, center and right ends of the IF range.

Figure 2.14 shows the observed intensities in signal and image band for different LO and IF setups in all pixels. Table 2.3 shows a summary of the calculated sideband rejections

for all these setups. We notice that, especially for lines in the center of the IF range, the sideband rejection is excellent (< −16 dB). Towards the edge of the LSB, pixels 4 and 6 demonstrate slightly weaker dampening of the signals from the image band (> −15 dB, which is the image band gain used in calibration). This means that if two signals of interest are at the same intermediate frequency, then bright lines from one sideband can blend with the emission of the other. This has to be kept in mind while choosing the LO frequency. The observations done in this thesis involve observing the ^{12}CO (3−2) and ^{13}CO (3−2) lines simultaneously. The only way to achieve this is to have an LO frequency such that the two lines are situated roughly towards the edge of the IF band. Therefore, we carefully chose the LO frequency to be 338.090 GHz so that there is a 200 MHz distance between the signal and interfering image frequency from the other band (see Fig. 3.2 in Chapter 3). This translates to a velocity separation of $\sim 170\,\mathrm{km\,s^{-1}}$ between the two lines, which is enough to avoid overlap from all of the galactic emission except the nuclear disk, where the velocity of the emitting gas can go as high as $\sim 250\,\mathrm{km\,s^{-1}}$ (Dame et al. 2001).

Table 2.3: Sideband rejection calculated for all LAsMA pixels for different LO frequencies and at various IF values.

Line	IF (GHz)	Pixel	Sideband Rejection (dB)
CS (6–5)	-6	1	<-17.8
		2	<-18.3
		3	<-17.8
		4	<-19.5
		5	<-18.8
		6	<-17.4
		7	<-19.0
CS (6–5)	6	1	-19.2
		2	-16.2
		3	-16.7
		4	-17.1
		5	-15.8
		6	-18.7
		7	-18.2
HCN (4–3)	4.2	1	-14.8
		2	-11.7
		3	-13.4
		4	-14.7
		5	-14.0
		6	-12.7
		7	-15.3
CO (3–2)	-4.5	1	-12.2
		2	-11.2

Line	IF (GHz)	Pixel	Sideband Rejection (dB)
		3	-13.6
		4	-14.7
		5	-12.1
		6	-13.4
		7	-13.5
CO (3–2)	7.7	1	-18.4 (-16.6)[a]
		2	-14.5 (-14.2)[a]
		3	-16.4 (-18.1)[a]
		4	-19.8 (-21.0)[a]
		5	-14.6 (-15.8)[a]
		6	-13.9 (-14.8)[a]
		7	-17.2 (-17.5)[a]
^{13}CO (3–2)	-7.5	1	-14.1 (-14.9)[a]
		2	-10.3 (-10.7)[a]
		3	-12.7 (-13.3)[a]
		4	-9.7 (-9.9)[a]
		5	-13.8 (-15.6)[a]
		6	-9.9 (-12.3)[a]
		7	-13.6 (-18.6)[a]

[a] For the ^{12}CO (3–2) (at 7.7GHz IF) and ^{13}CO (3–2) lines, SB rejection was calculated with both peak temperatures and integrated intensities (in parenthesis). Other calculations are only for peak intensity. But one can check the sideband rejection for integrated intensities with the macro: sideband_rejection.class by commenting out relevant lines (line 131 and 132) inside project t-0101.f-9992a-2018.

2.3 Summary

In this chapter, the Atacama Pathfinder EXperiment (APEX) telescope was introduced as the telescope to be used for the observations done for the duration of this dissertation research. The newly installed 7-pixel receiver called the Large APEX sub-Millimeter Array (LAsMA) was presented as the instrument to be employed for the observations mentioned above. The commissioning tests and characterizations done for the new receiver were then discussed. A summary of these tests and their respective findings has been provided below.

- Beam maps on planets were carried out to determine the offsets of the outer LAsMA pixels, which were then followed up by pointing test observations on IRC+10216 in order to confirm the findings of the beam maps.

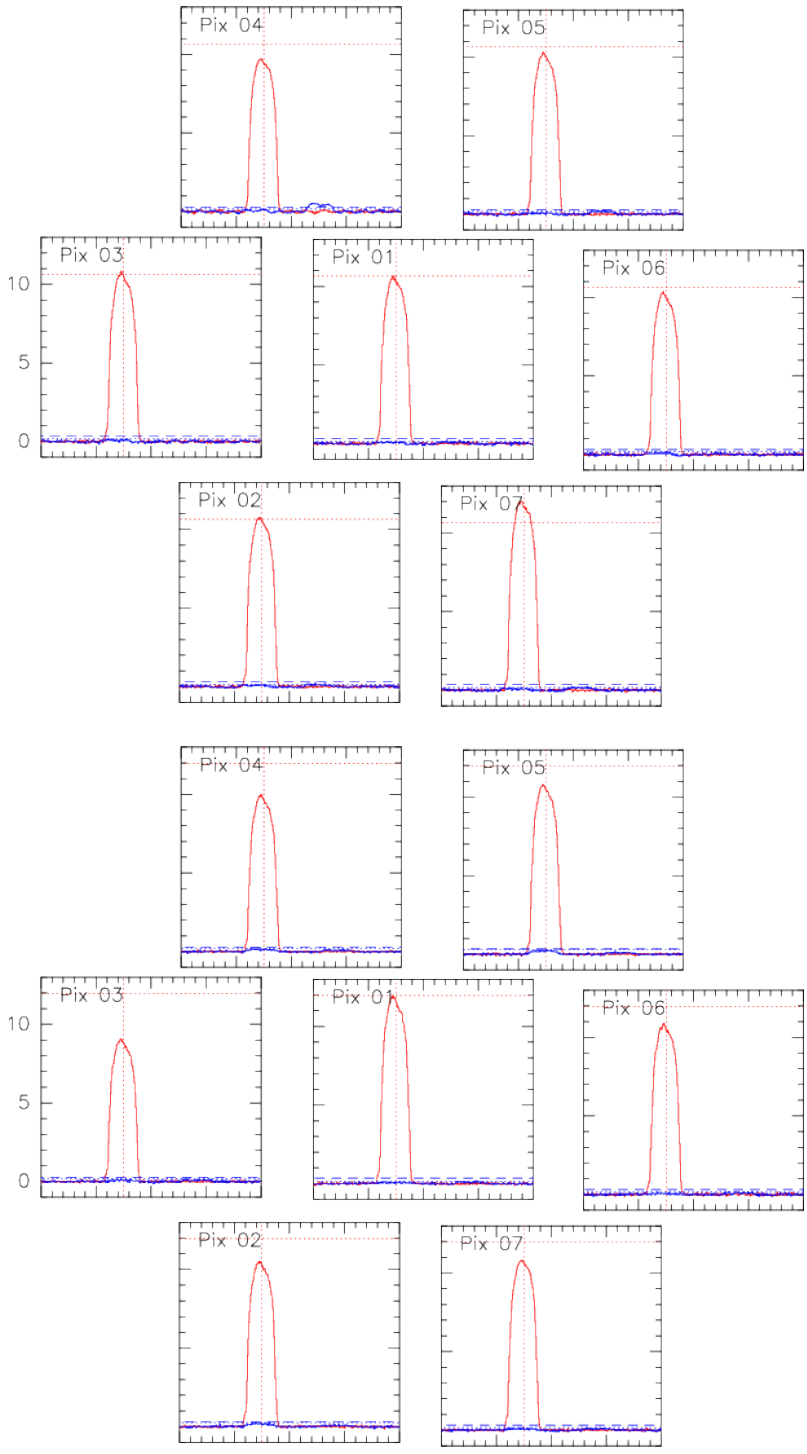

Figure 2.14: LAsMA Sideband Rejection measured on IRC+10216 on all pixels for CS (6–5) line in LSB (top) and USB(bottom). Dotted horizontal red line marks the peak intensity of central pixel. Dotted blue line shows peak intensity of the image band. Dashed blue line marks the -15dB level for image band which is used for calibrating the image band.

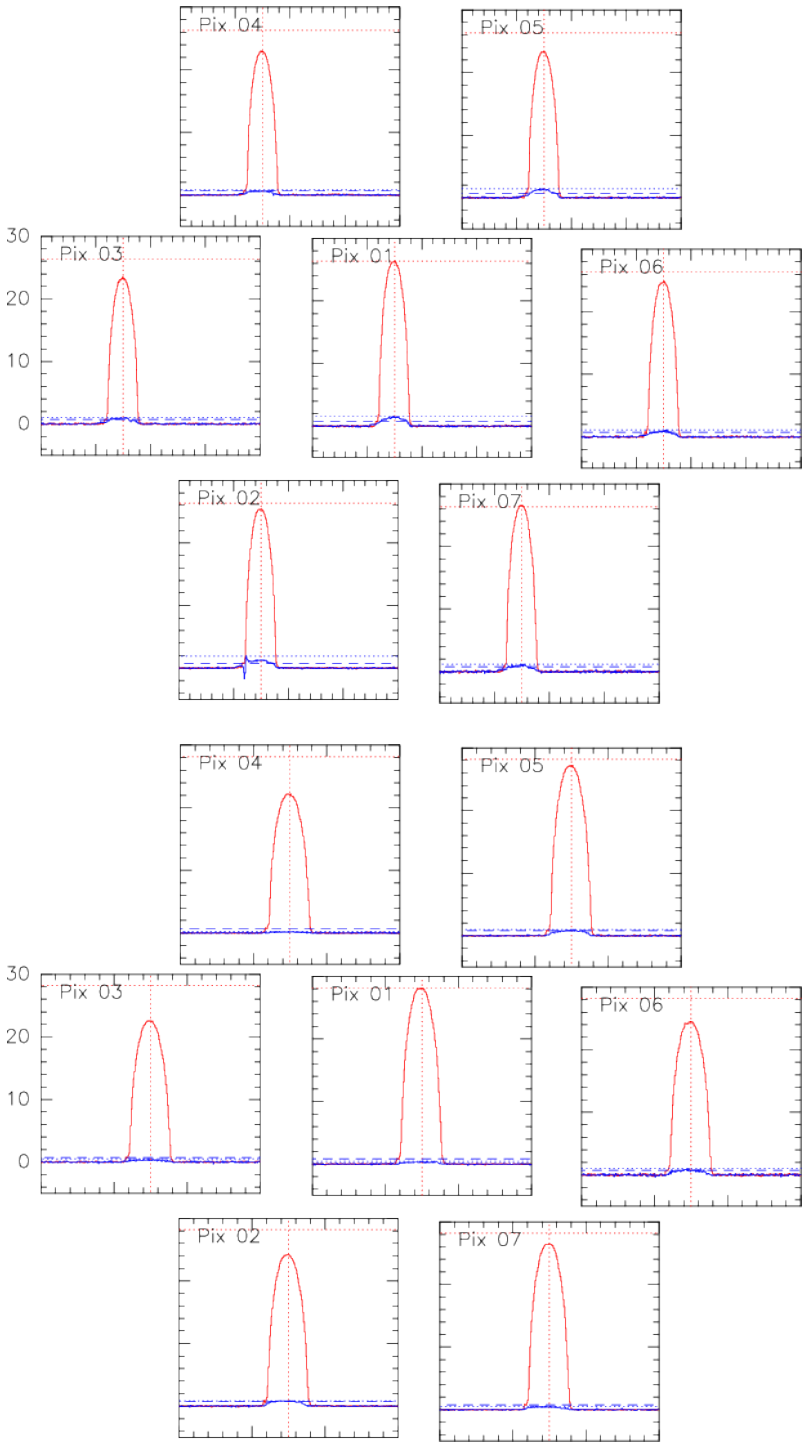

Figure 2.14: contd.: LASMA Sideband Rejection measured on IRC+10216 on all pixels for CO (3–2) line in LSB (top) and USB(bottom).

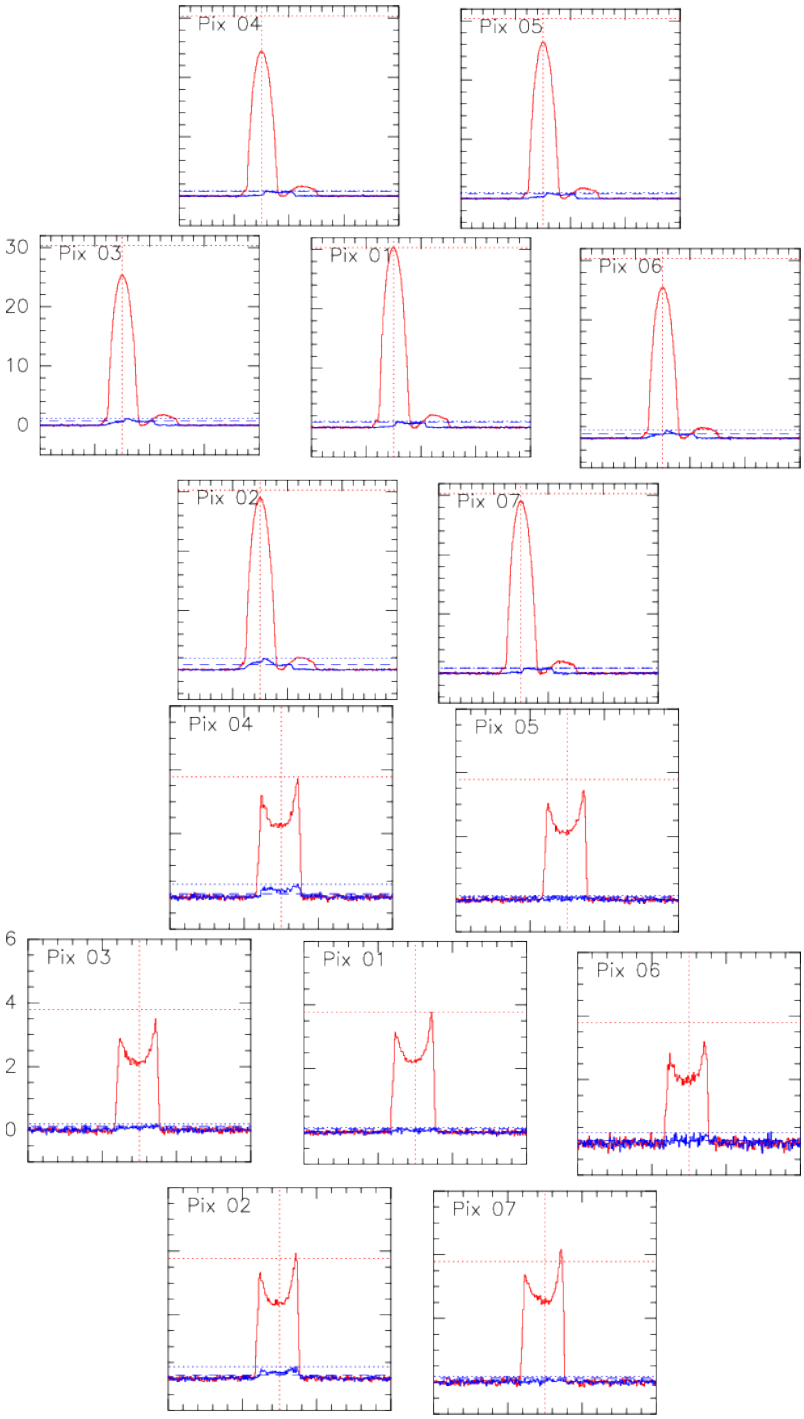

Figure 2.14: contd.: LASMA Sideband Rejection measured on IRC+10216 on all pixels for HCN (4–3) line in USB (top) and ^{13}CO (3–2) line in LSB (bottom).

- The behavior of different pixels as a function of derotation angle was analyzed using beam maps of Mars and OTF tests on Jupiter. It was found that for mapping purposes, the averaged response of the 7-pixel array could be given by the equation

$$\eta_{mb,array} = 0.9\,\eta_{mb} \tag{2.5}$$

  where η_{mb} is the main beam efficiency of the central pixel (usually measured during calibrations done before observing with the instrument).

- Finally, the sideband rejection of the receiver was tested for all pixels at different LO frequencies as well as IF values. This was then used to determine the LO frequency most suitable for conducting a survey of the inner galaxy in ^{12}CO (3−2) and ^{13}CO (3−2) lines using the LAsMA receiver. This was found to be $\nu_{\rm LO}$ = 338.090 GHz.

Part III

Survey Feasibility

Chapter 3

Pathfinder study for a large scale survey of the inner Galaxy using LAsMA (LAsMAGal)

3.1 Introduction

The coldest and densest regions of the interstellar medium (ISM) exist as molecular clouds (MCs). These clouds are the birthplace of stars. They have a hierarchical composition (Rosolowsky et al. 2008) with dense substructures (clumps and cores) nesting inside larger, less dense clouds. Their structure may also be fractal or multifractal (Stutzki et al. 1998). The densities of these structures range from a few hundred cm^{-3} in molecular clouds up to $\sim 10^6 cm^{-3}$ in the dense cores, which is where stars are born. In order to scrutinize the star formation process, it is essential to study these dense sub-structures and their properties in detail.

The molecular component of the Galaxy can be traced by the rotational transitions of carbon monoxide (CO). CO is ubiquitous throughout the Galactic plane and is used to trace molecular hydrogen. Many large-scale CO surveys already exist today, which complement each other very well (see Fig. 3.1). Some notable examples include the CO Survey of the Galaxy by Dame et al. (2001); the Boston University-Five College Radio Astronomy Observatory Galactic Ring Survey (GRS: Jackson et al. 2004); the Three-mm Ultimate Mopra Milky Way Survey (ThrUMMS: Barnes et al. 2015); Structure, excitation, and dynamics of the inner Galactic interstellar medium (SEDIGISM: Schuller et al. 2017); $^{13}CO/C^{18}O$ ($J = 3 \rightarrow 2$) Heterodyne Inner Milky Way Plane Survey (CHIMPS: Rigby et al. 2016); and the CO High-Resolution Survey (COHRS: Dempsey et al. 2013). These provide first-hand information on the molecular gas distribution in the Galactic plane. This information can be used to test various existing Galactic models.

In the fourth quadrant, the most relevant survey is the SEDIGISM survey (see Fig. 3.1) which uses the $J = 2 \rightarrow 1$ transition of the $^{13/18}CO$ isotopologues which improves angular resolution considerably compared to Dame et al. (2001). Most of the other surveys in this part of the Galactic plane have a poor angular resolution, making it difficult to study clump scales and, hence, the process of star formation. Additionally, for studies of the sub-parsec (sub-pc) clump scales, compared to SEDIGSM, even higher resolution and access to higher densities are required. Therefore, we decided to explore the possibility of a high-resolution Galactic plane survey of the inner Galaxy in the fourth quadrant using $J = 3 \rightarrow 2$ transition of $^{12/13}CO$ isotopologues (hereafter referred to as LAsMAGal).

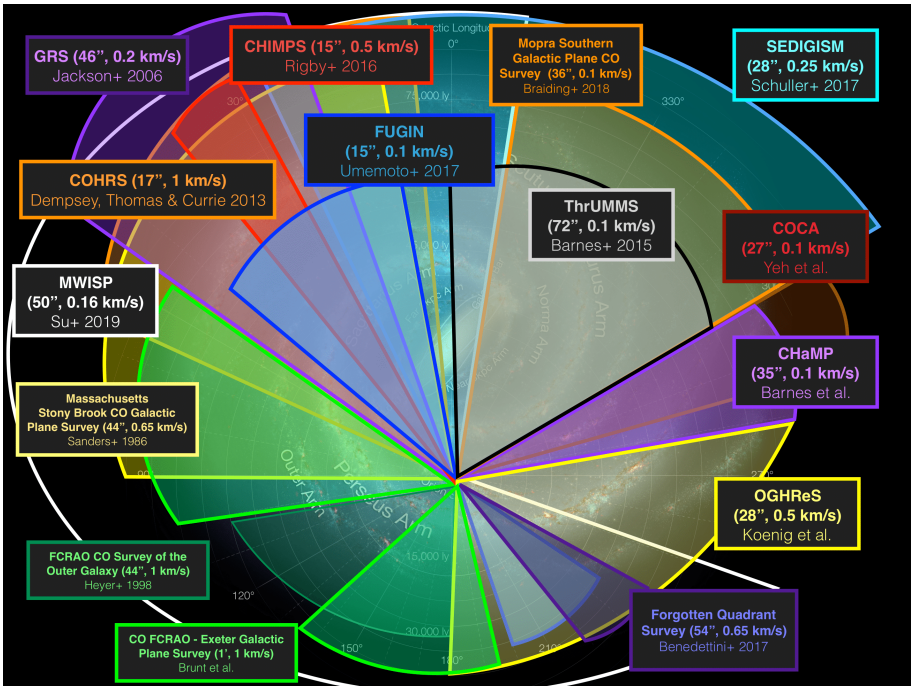

Figure 3.1: A pictorial representation summarizing the major Galactic CO surveys to date. Credits: D. Colombo

For this, we decided to use the LAsMA 7-pixel receiver on the APEX telescope. In the 345 GHz atmospheric window, the receiver has a spatial resolution of 19″.

3.2 Motivation

The $J = 3 \rightarrow 2$ transition has a critical density of 1.6×10^4 cm^{-3} at 10 K and therefore traces moderately dense gas. The usefulness of the $J = 3 \rightarrow 2$ has been very well demonstrated by the success of the CHIMPS survey in the northern hemisphere. The ^{13}CO isotopologue being about 50-100 times less abundant, traces substructures of the molecular clouds with low or moderate optical depths allowing us to probe inside the clumps.

LAsMAGal will also compliment SEDIGISM data that already exists towards the fourth quadrant. Observations of different isotopologues of CO in different J transitions will allow us to determine physical conditions such as optical depth, excitation temperature, and column density of the molecular clouds (Rigby et al. 2019). With the spectroscopic velocity measurements combined with a galactic rotation model, we can estimate the distances of the clouds and, consequently, their masses. Observation of dense clumps with optically thin emission lines in high resolution will also enable us to assign kinematic velocities to star-forming clumps observed in continuum surveys such as ATLASGAL (Schuller et al. 2009) with less ambiguity than other tracers. Our survey and ATLASGAL have the same spatial resolution, making it straightforward to assign velocities to the clumps identified in the latter. ^{12}CO often shows multiple complex emis-

sion features along the line of sight inside the Galactic plane, corresponding to structures at different distances along the line of sight. Eden et al. (2012) also demonstrate that the same issue exists with ^{13}CO $J = 1 \rightarrow 0$ spectra. The ^{13}CO $J = 3 \rightarrow 2$ transition is more likely to show only one narrow emission feature, making it easier to identify which emission feature corresponds to the dense star-forming region.

In addition to complementing existing surveys towards the southern Galaxy, LAsMA-Gal also adds new science capabilities. LAsMA now allows us to observe both ^{12}CO (3−2) and ^{13}CO (3−2) simultaneously. With the former, we can trace the more extended and diffuse cloud structures. This will help us test and refine the structure of the Milky Way. The present accepted model of the Galaxy contains four main spiral arms (e.g. Reid et al. 2019; Hou & Han 2014; Urquhart et al. 2014a). However, their exact locations are still lacking precision. Additionally, there are many other features, such as spurs, that need to be explained and incorporated into the model. In contrast, the positions and velocities of older stars like K and M giants are better explained by a two-arm model instead of four (Steiman-Cameron et al. 2010, and references therein). Ragan et al. (2014) used position-velocity analysis to postulate that giant molecular filaments in the Galactic plane are largely inter-arm in nature which may be analogous to spurs seen in nearby spiral galaxies (e.g. Elmegreen 1980). A large-scale and sensitive Galactic survey like LAsMA-Gal, which covers a range of density regimes with ^{12}CO and ^{13}CO observations, can help constrain models of our Galaxy, specifically those with synthetic position-velocity observations (e.g. Duarte-Cabral et al. 2015; Pettitt et al. 2015). The ability to simultaneously trace diffuse gas along with the denser sub-structures inside them will allow us to study large-scale filaments and the velocity structure along them, discern the sub-structures inside molecular clouds in more detail, and search for outflows. These can then be used to investigate the effects of feedback from massive stars on their surroundings and further our understanding of high mass star formation.

3.3 Test region: Far edge of the Galactic bar

Our initial aim was to cover the same region as SEDIGISM ($-60° < l < 18°$ and abs $b < 0.5°$) which adds up to a total of 78 square degree. This meant that the survey would be very time-consuming and needed to be carried out as efficiently as possible. Therefore, we first needed to observe a sample region to test the quality of data and determine the most efficient way to carry out observations. The far edge of the Galactic bar was chosen for this purpose. The near edge of the Galactic bar consists of the famous W43 region, which is a giant molecular cloud complex consisting of more than 20 molecular clouds (Rathborne et al. 2009). It is the location where the Galactic bar meets the Scutum-Centaurus arm (Carlhoff et al. 2013; Nguyen Luong et al. 2011) and is undergoing a remarkably efficient episode of high-mass star-formation (Motte et al. 2003). This near end of the Galactic bar is a highly studied region (Carlhoff et al. 2013; Nguyen Luong et al. 2011, and references therein). Additionally, Beuther et al. (2017) observed the galactic bar-arm interaction of the nearby galaxy NGC 3627 and compared it to the observations of W43 to find that both

these regions were very similar in terms of their spectral signatures. They also argued that the high rate of star formation at the intersection of the bar and the arm might be caused by these crossing gas orbits and interacting or colliding gas clouds. However, the far edge of the bar is not very extensively studied. Mercer 81 (Davies et al. 2012b) and VVV CL086 (Ramírez Alegría et al. 2014) are the only two reported young massive clusters at this end of the Galactic bar. Davies et al. (2012b) argues that, like the near end, this region may also be as actively star-forming. Based on these evidences, we expect active star-formation to be going on at the far edge of the Galactic bar. Given its distance of 11 kpc, the higher angular resolution of LAsMA CO(3 − 2) observations compared to SEDIGISM will allow us to resolve individual clumps, making it an excellent candidate for the test region.

3.4 Observing strategies

In order to carry out a very time-consuming survey of the Galaxy, optimization is of utmost importance. Hence, it is important to test observing strategies to come up with one that is the most time-efficient. The test region was observed both in ^{13}CO ($\nu_{\rm rest}$ ~ 330.588 GHz) and ^{12}CO (3-2) ($\nu_{\rm rest}$ ~ 345.796 GHz) simultaneously. For this, the local oscillator frequency was set at 338.090 GHz.

This frequency was chosen in order to avoid contamination of the ^{13}CO (3-2) lines due to bright ^{12}CO (3-2) emission from the image band (see Fig.3.2). For this setup, the FWHM is ~ 19 ″, and the velocity resolution is 0.053 km s^{-1}.

Additionally, as can be seen from Fig. 3.2, the ^{13}CO (3−2) line's atmospheric transmission is affected by a strong telluric water line at 325 GHz. For a typical elevation of 45° during observations, it already reaches ~ 0.65 for a precipitable water vapor (pwv) level of only 1.5 mm. Therefore, in order to recover most of the signal, we restricted our observations to pwv levels below 1.5 mm. Figure 3.3 shows the weather conditions at Chajnantor (site of APEX telescope) over the years 2016 and 2017. We have desirable weather conditions about 60% of the time.

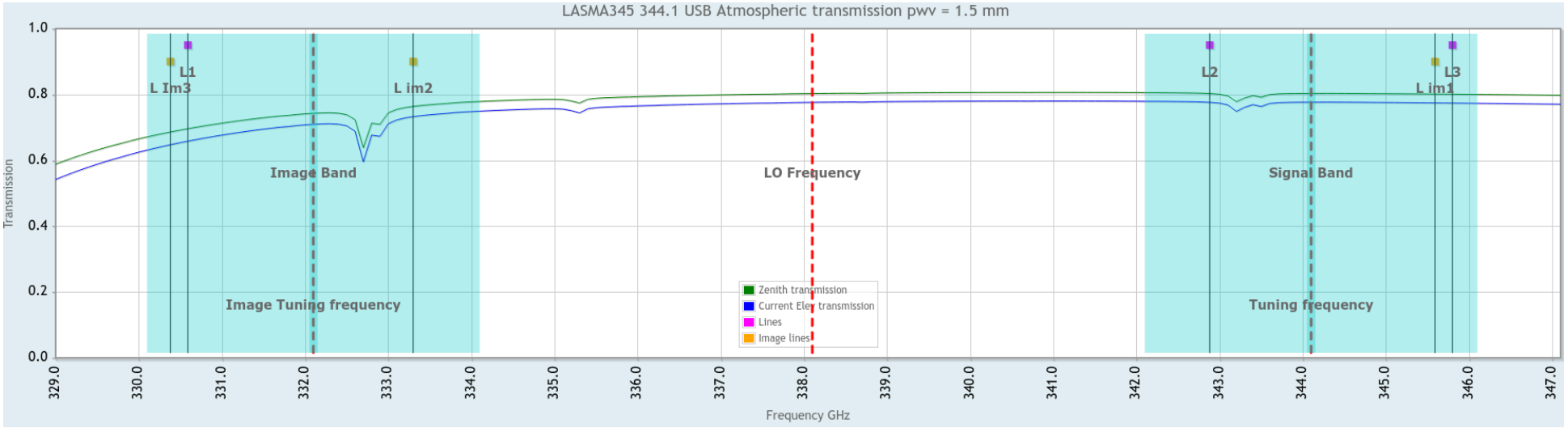

Figure 3.2: Frequency set up used for the survey. L1 shows the ^{13}CO (3–2) line at 330.59 GHz, L2 is the CS(7-6) line at 342.88 GHz, whereas L3 denotes ^{12}CO (3–2) at 345.8 GHz. The transmission values are shown for an elevation of 45°. This figure has been created using the Instrument Setup Tool provided by the APEX webpage at https://www.apex-telescope.org/sites/chajnantor/atmosphere/transpwv/atmosphericSelector.php.

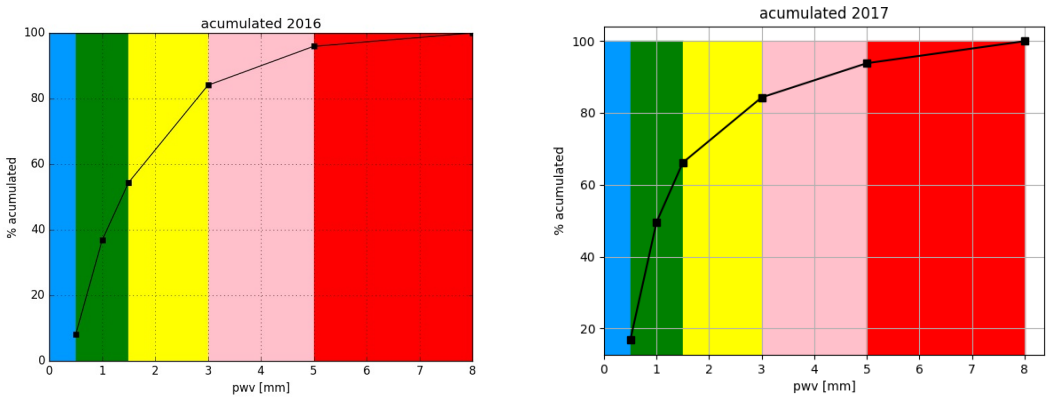

Figure 3.3: Historical pwv conditions at Chajnantor over the years 2016 and 2017. The y-axis shows the cumulative percentage of time with pwv levels lower than the corresponding x-value of pwv. The figure has been collected from the APEX website : https://www.apex-telescope.org/weather/.

A one-degree by one-degree region was divided into four quadrants, each with its own source name. For instance, a one-degree squared region (345.5°<l<346.5°; −0.5°<b<0.5°) would be divided into four regions named G345.75+0.25, G345.75-0.25, G346.25+0.25, and G346.5-0.25. Each of these sources was observed in a position switching on-the-fly (OTF) mode. The reference-positions were carefully chosen and tested to ensure no strong emission line (>200 mK) was present in the velocity range of −150 to 50 km s^{-1}. Each of these four regions was further divided into nine sub-maps of size 10 by 10′. Before scanning each sub-map, the pixel array was rotated by 19.1 degrees in galactic coordinates in order to minimize overlap between pixels along the direction of scanning and ensure maximal coverage (see Fig.3.4).

The step size in the direction of scanning was chosen to be 7″ (about one-third of the beam size to ensure Nyquist sampling). The data was recorded at the fastest possible rate available equal to 0.1s per dump. In the beginning of the test observations the online calibrator could not yet keep up with the high data rates of ∼ 10^7 floating data points per second (= 65536(channels) × 10(dumps) × 7(pixels) × 2(sidebands)). Therefore data was calibrated offline in the beginning. The online calibrator was subsequently optimized and can now process these data rates. On reaching the edge of every mapped

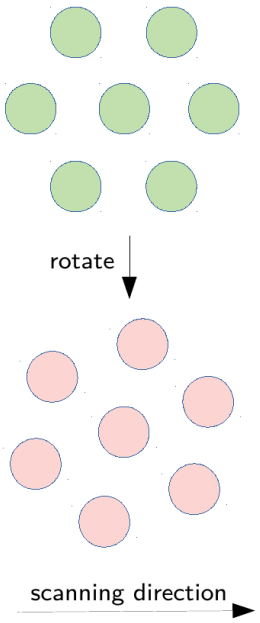

Figure 3.4: An illustration of LAsMA pixels rotated by 19 degrees to optimize overlap along scanning direction and ensure maximal coverage.

area, the array was shifted perpendicular to the scan direction by half the beam-width (9″), and the scan was then carried out in the reverse direction. This process was repeated until the whole submap was observed. The same submap was then observed in a 90° rotated frame to ensure Nyquist sampling was achieved along both directions and also to reduce systematic scanning effects. A calibration measurement was made every 10-15 minutes during each scan. This setup of a sample spacing of $\sim 7''$ along with a sampling time of 0.1 sec resulted in datacubes of size $10' \times 10'$ in approximately 1 hour. This implied a region of one-degree square needed about 36 hours of observing time and would create 161336 spectra. Covering the whole region of the SEDIGISM survey with this setting would require >2000 hours of observations.

3.5 Data reduction

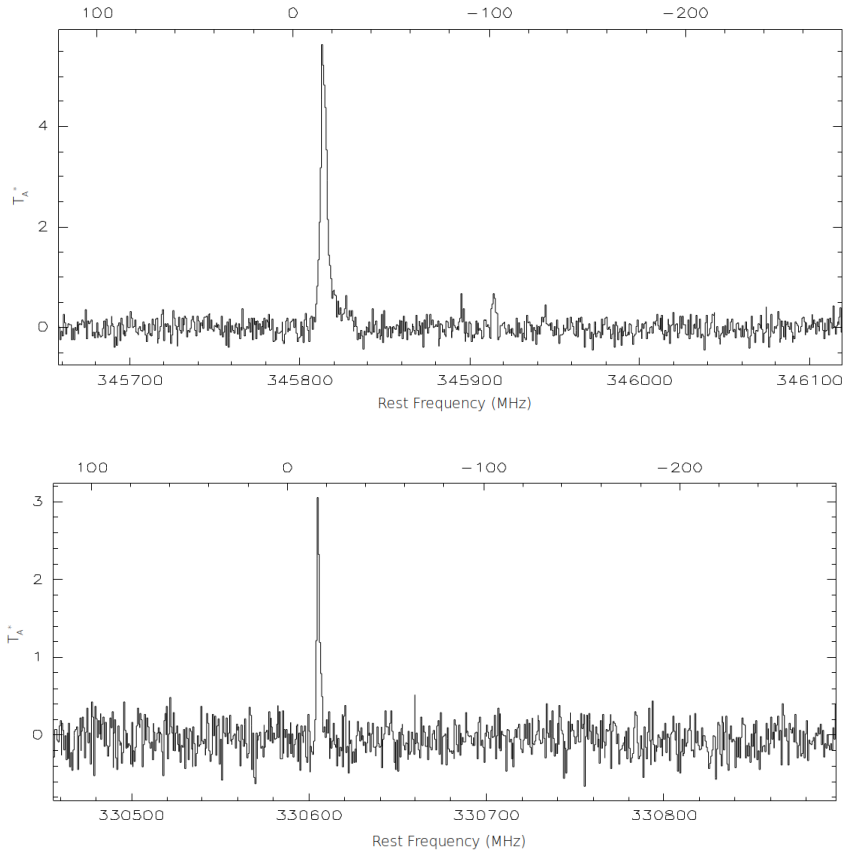

Figure 3.5: Example spectra extracted from the two sidebands from the test region (Galactic bar). The top panel corresponds to a subsection of the upper sideband centered on the ^{12}CO rest frequency and the lower one corresponds to a subsection from the lower sideband centered on the ^{13}CO rest frequency. The corresponding velocity ranges are given at the top of the figures in km/s.

The calibrated data[1] were reduced using the GILDAS package[2]. A velocity range of $-200\,\mathrm{km\,s^{-1}}$ to $200\,\mathrm{km\,s^{-1}}$ was extracted from every spectrum and resampled to an adequate velocity resolution of $0.5\,\mathrm{km\,s^{-1}}$ to reduce the noise. The velocity range $-150\,\mathrm{km\,s^{-1}}$ to $50\,\mathrm{km\,s^{-1}}$ was masked before fitting a 3rd order baseline to each spectrum. The reduced, calibrated data obtained from the different scans were then combined and gridded using a 6″ cell size. The gridding process includes a convolution with a Gaussian kernel with an FWHM size of one-third of the telescope FWHM beam-width. The data cubes obtained have a final angular resolution of $\sim 20''$. Spectra from all the pixels were then averaged to find the portions of the spectra containing line emission, which were then masked. The process of baseline removal was again repeated for the spectra of each pixel to obtain a more stable baseline and a cleaner map (see Fig.3.5 for an example spectrum obtained after data reduction).

3.6 Results of test observations : Noise comparison

After the first test run, six submaps were observed in order to investigate the quality of the data. This covered a longitude range of 346 to 346.5 degrees and a latitude range of -10 to 10′. As a quality check, the noise in the data was compared to an existing survey, in this case, SEDIGISM being the most relevant survey in the fourth quadrant.

We first investigated the noise of the LAsMAGal data. For this, 50 spectral channels devoid of any emission were chosen for each of ^{12}CO and ^{13}CO datacube. The standard deviation of the emission over these channels was then calculated for each position on the map grid, referred to as pixel from now onward. This was then repeated for the same region extracted from the SEDIGISM survey data to compare the sensitivity of the two surveys. But, before making any meaningful comparisons between the two surveys, many factors have to be considered. Firstly, both the surveys have different beam sizes. SEDIGISM has a beam size of $\sim 30''$ (Schuller et al. 2017) which is larger than LAsMAGal's resolution. The LAsMAGal map was convolved with a Gaussian kernel to the same spatial resolution as SEDIGISM. In addition, the SEDIGISM map was also reprojected to the same grid as that of LAsMAGal. Secondly, the channel width of SEDIGISM is a factor of 4 lower than LAsMAGal. Therefore, SEDIGISM data was also smoothed to the same spectral resolution as LAsMAGal. Lastly, since the data from SEDIGISM is reported in main beam temperature (T_{MB}) scale adopting a main beam efficiency of 0.75, the LAsMAGal data was also converted to the T_{MB} scale using a main beam efficiency of $\eta_{\mathrm{MB}} = 0.73$ and a forward efficiency of $\eta_f = 0.95$. The result is shown in Fig. 3.6.

The LAsMA data appears to have much lower noise levels than SEDIGISM at a first glance. In order to quantify this, a histogram of the distribution of the noise values was then plotted for both surveys (see Fig. 3.7). The median noise in the ^{12}CO (3–2) spectral window is about 4 times lower than that of the ^{13}CO (2-1) transition from SEDIGISM.

It stands to be seen if this difference in the noise levels is to be expected. According to

[1] See Chapter. 2 for a detailed explanation of the data calibration process.
[2] http://www.iram.fr/IRAMFR/GILDAS

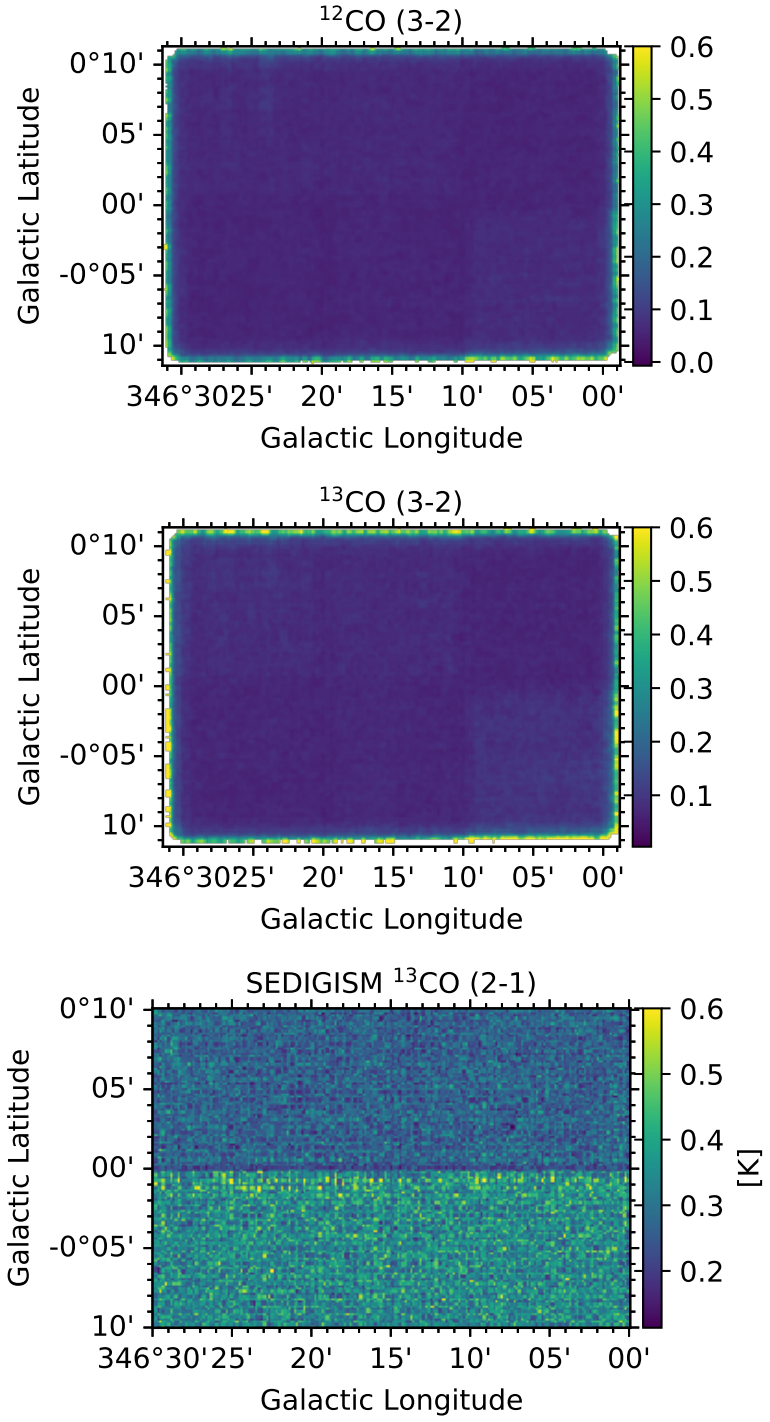

Figure 3.6: Pixel wise noise map of the test region for LAsMAGal and SEDIGISM.

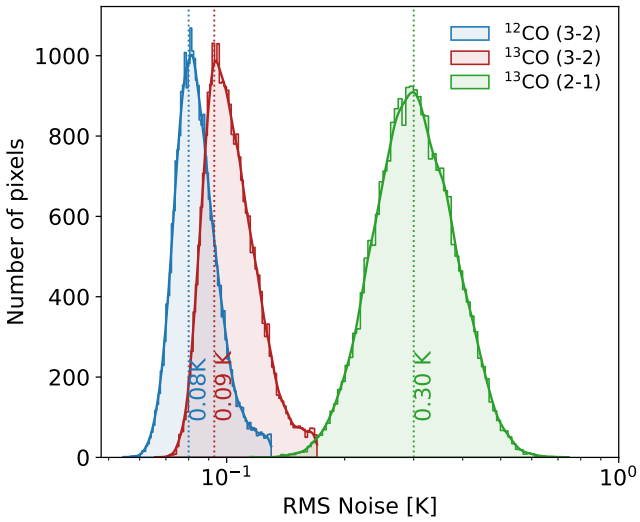

Figure 3.7: Histogram distribution of rms noise of pixels in the test region of LAsMAGal. The vertical dotted lines represent the mode of the distribution for the two sidebands.

the radiometer formula, the rms noise $\sigma_{\rm rms}$ can be calculated using

$$\sigma_{\rm rms} = \frac{T_{\rm sys}}{\sqrt{\Delta\nu\,\tau}}, \tag{3.1}$$

where $T_{\rm sys}$ is the system temperature, $\Delta\nu$ is the bandwidth of an individual backend channel and τ is the integration time. Using this we can calculate the theoretical noise ratio as

$$\frac{\sigma_{\rm s}}{\sigma_{\rm l}} = \left(\frac{T_{{\rm sys},s}}{T_{{\rm sys,l}}}\right)\sqrt{\left(\frac{\Delta\nu_l}{\Delta\nu_s}\right)\left(\frac{\tau_l}{\tau_s}\right)} \tag{3.2}$$

where the suffix s is used to denote SEDIGISM and l is used to denote the ^{12}CO (3–2) data of LAsMAGal.

In order to calculate the system temperatures, we used the time estimator tool[3] provided on the APEX webpage. The average pwv values for SEDIGISM were obtained from the SEDIGISM archives to be ~ 2 mm. At an average elevation of 60° this translates to a system temperature of $T_{\rm sys} \sim 150$ K for SEDIGISM and ~ 230 K for LAsMAGal. The reason for the higher system temperature in LAsMAGal was the very high system temperature of pixel 6 of LAsMA (about 300 K). Next, we calculated the ratio of the channel width. Given a fixed velocity resolution, the channel width ratio is directly proportional to the ratio of the rest frequency of the line being probed. Finally, in order to calculate the ratio of integration time, we need to take two factors into consideration. Firstly, LAsMA has 7 pixels. So the integration time would be seven times the integration time of a single pixel. Secondly, the integration time is inversely proportional to the scanning speed of the OTF

[3] https://www.apex-telescope.org/heterodyne/calculator/ns/otf/index.php

mapping. Given that both surveys have identical dump times (0.1s), the scanning speed is in turn directly proportional to the step size. In simple terms, if a survey has a larger step size, it will scan an area faster, and hence integration time for a constant area would be smaller. The x- and y-step size for SEDIGISM are 13 and 15″ respectively, while that for LAsMAGal are 7 and 9″. Taking these all into account Eq.3.2 becomes,

$$\frac{\sigma_s}{\sigma_l} = \frac{150}{230}\sqrt{\left(\frac{345.796}{220.399}\right)\left(\frac{13\times15\times7}{7\times9}\right)} \approx 4 \tag{3.3}$$

where 220.399 is the frequency of the ^{12}CO (2–1) line in GHz units and 347.796 is that for the ^{12}CO (3–2) line.

The observed factor of 4 improvement in noise implies that LAsMAGal will be able to detect much more diffuse gas compared to SEDIGISM. Using the RADEX code (van der Tak et al. 2007) we calculate the column density of gas traced by the survey to take into account excitation differences for the (2–1) and (3–2) lines. We assume a kinetic temperature of 20 K which is representative of the range of temperatures found in molecular clouds (Sect 5.1.2 of Heyer & Dame 2015), a density of 1×10^3 cm^{-3}, an abundance of [CO]/[H_2]=1×10^{-4}, and ^{12}CO/^{1}3CO=60. The abundance ratios have been adopted as identical to SEDIGISM survey (Schuller et al. 2017) to make a fair comparison of the sensitivity. At a resolution of 0.25 km s^{-1} (this resolution has been chosen to make a fair comparison with SEDIGISM sensitivity), our survey can make a 3σ detection of molecular clouds with H_2 column densities $\sim$ 1×10^{20} cm^{-3} using the ^{12}CO (3–2) line and $\sim$ 4×10^{21} cm^{-3} using the ^{13}CO (3–2) line. In comparison, the SEDIGISM survey can detect clouds with column densities greater than $\sim$ 3×10^{21} cm^{-3} using the ^{13}CO (2–1) line at the same velocity resolution (Schuller et al. 2017). Additionally, it should be taken into consideration that if the repairs of LAsMA pixel 6 reduce its receiver temperature in the future, the sensitivity of the survey can even improve further.

3.7 Survey strategy options

Although our survey has greater sensitivity than SEDIGISM, the actual time needed (including observational overheads) to cover one square degree is much larger for our survey when compared to SEDIGISM. As alluded to at the end of Sec. 3.4, an unbiased survey of the whole region covered by the SEDIGISM survey would require about 2000 hours of observations using LAsMA. The same region, excluding the CMZ and W43 extensions, took 753.1 hours for SEDIGISM. Given the significant competition from other high-priority projects at APEX at the time of the survey planning, a 2000-hour survey could not be implemented. For this reason, an alternative strategy was needed to carry out the survey. Hence, we weighted the different alternatives for the survey along with their pros and cons. These strategies are described here.

a) *Unbiased survey in a narrower b range*: As the name suggests, one alternative is to cover the whole range of galactic longitude as in SEDIGISM using the same observational setup as described in Sect. 3.4 but in a narrower range of latitude $|b| < 0.25°$.

Pros:

- Preserve high sensitivity to lower column density gas.
- Studying the diffuse structure of the molecular clouds such as their filamentary structures and outflows.

Cons:

- Cover less area of the galactic plane.
- Incomplete coverage of multiple clouds including famous complexes, e.g. W43.

b) *Fast mode***:** Another alternative is to cover the whole range of SEDIGISM but have a larger step size orthogonal to the scanning direction. This could be achieved by translating the pixel array along the orthogonal direction by almost three times the beam size (the size of the whole array). Nyquist sampling would still be ensured by sampling the same way as before in the direction of scanning. This way, we can cover the whole range of SEDIGISM in $\sim$ 1000 hours. This strategy was tested on a small sub-map, and the advantages and disadvantages are mentioned below.

Pros:

- Cover the whole range of (l, b) as SEDIGISM.
- Molecular clouds are more likely to be observed completely.
- Study the well known complexes using excitation studies.

Cons:

- Significant loss in sensitivity (by a factor of $\sim$ 2.5). Consequently, the ^{13}CO (3–2) line loses the ability to detect all molecular clouds down to the column density threshold of 5×10^{21} cm^{-2} needed for star formation (Lada et al. 2010). The ^{12}CO (3–2) line cannot detect very diffuse gas associated with molecular clouds, losing significant ability to study the filamentary nature of clouds and detect new outflows associated with star formation.
- Strip-like patterns in the map. These systematic effects are caused by variations of sensitivities and gains for different pixels. Compounding the problem is the fact that the derotator angle dependence of each pixel's gain is not averaged out in this method (see Chapter 2). Therefore, until the receiver is not optimized, this strategy will not work.

c) *Biased survey***:** The final alternative is to cover selected prominent regions based on SEDIGISM data without altering the observing strategy.

Pros:

- Preserve high sensitivity to lower column density gas.

- Study the well known complexes in great detail using excitation studies.

Cons:

- Cover less area of the Galactic plane.
- An unbiased study of the galaxy is not possible. Owing to the high sensitivity, we potentially lose the ability to study the filamentary nature of large-scale diffuse gas in the galaxy in detail.

3.8 Science demonstrations of a high sensitivity survey

To demonstrate the capabilities of a high sensitivity survey, we decided to observe one of the most prominent galactic molecular complexes with LAsMA. Two factors were taken into consideration in choosing such a region. Firstly, it should allow testing some of the prominent science goals of the survey, in particular the effects of feedback on molecular clouds. Furthermore, it had to be observed in a relatively short time frame. Two candidates were deemed to fit these criteria; the G305 giant molecular cloud (Fig. 3.8), and the NGC 6334 complex (popularly known as the Cat's Paw Nebula, Bear Claw Nebula, or Gum 64; see Fig. 3.9). NGC 6334 has been studied much more extensively (Sadaghiani et al. 2020; Russeil et al. 2012, and references therein) in comparison to G305 (Hindson et al. 2013; Borissova et al. 2019, and references therein). Also, it covers a larger area which would require longer observing time. Therefore, we chose to observe the G305 star-forming complex for the purposes of science case demonstrations.

3.9 Summary

We set out to test the possibility of carrying out a new survey of the inner Galaxy using the new LAsMA receiver installed on the APEX telescope (LAsMAGal). As a pathfinder, the far edge of the Galactic bar was chosen as a test region. Different observing strategies were tested, and the one picked for the survey included a step size of $7'' \times 9''$ in the $x - y$ direction and a dump time of 0.1s. This setup led to a factor of 4 reduction in noise compared to the SEDIGISM survey. This meant that LAsMAGal could detect much fainter gas that would be instrumental in studying the filamentary nature of the Galaxy and detecting star-forming regions by discovering outflows. Additionally, it could also help build a better model of the Galaxy by providing more information about the diffuse gas in the inter-arm regions. However, the large observational overheads meant that it was not feasible to observe the whole region covered by SEDIGISM with LAsMA as that would require about 2000 hours of observational time. Some alternative methods were explored, and their pros and cons have been provided in this chapter. Finally, for the prime purposes of this thesis, the G305 giant molecular cloud was chosen as the first target for a high sensitivity survey.

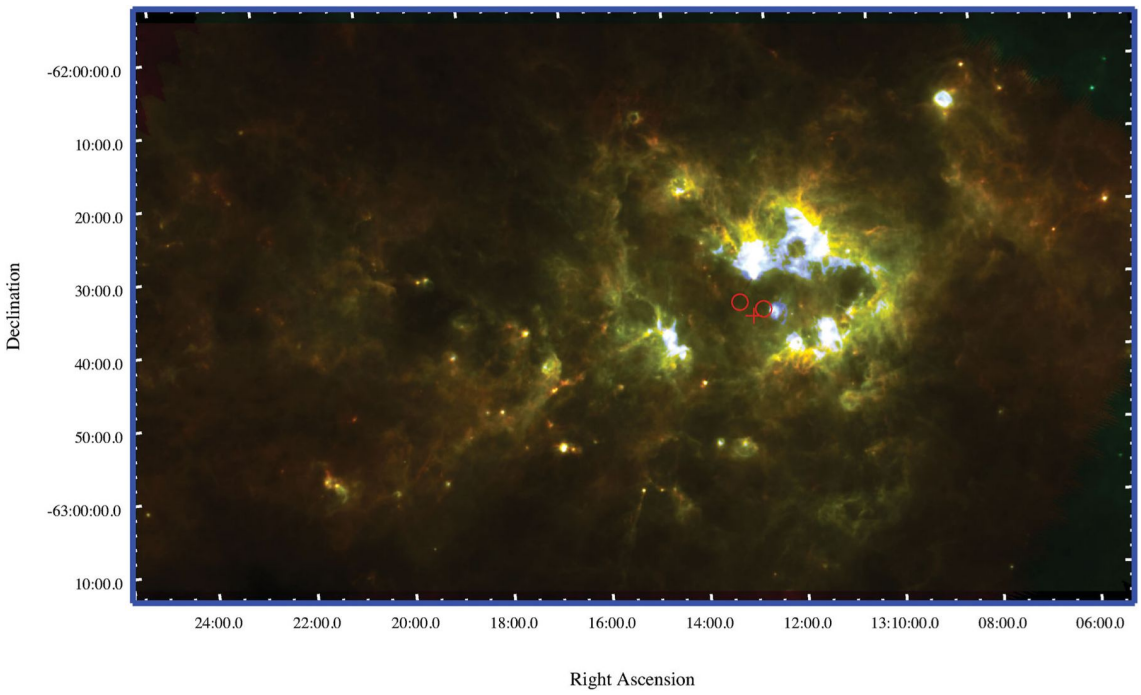

Figure 3.8: Herschel Hi-Gal image of G305 star forming complex. Blue = 70 μm, green = 160 μm and red = 350 μm. The red circles indicate the positions of the two OB stellar clusters Danks 1 and 2, and the red cross marks the Wolf-Rayet star WR 48a. This image has been taken from Fig. 1 of (Faimali et al. 2012).

Figure 3.9: Spitzer image of NGC 6334 star forming region. Blue = 3.6 μm, green = 5.8 μm, and red = 8.0 μm. [Source: Wikimedia Commons].

Part IV

Science Capabilities

Chapter 4

G305 giant molecular cloud : I. Feedback on molecular gas

This chapter was originally published as a paper titled "High resolution LAsMA ^{12}CO and ^{13}CO observation of the G305 giant molecular cloud complex : I. Feedback on the molecular gas" in *Astronomy & Astrophysics* (Mazumdar et al. 2021a) [1]. Layout changes were made to adapt to the different print formats. The following sections are copied from the accepted paper after language editing, as submitted to the publisher on 26 May, 2021.

4.1 Introduction

Massive stars ($M > 8M_{\odot}$) are rare and usually form inside giant molecular clouds (GMCs) as the dominant members of young stellar clusters (Motte et al. 2018). They are short-lived (≤ 30 Myr), but are known to inject large amounts of feedback into the interstellar medium in the form of stellar winds, ionizing radiation, and supernovae (Krumholz et al. 2014). These feedback mechanisms can in turn trigger or disrupt the formation of the next generation of stars when they interact with the natal molecular cloud. They can sweep up the surrounding gas and create parsec-scale cavities around them (Deharveng et al. 2010a), forming dense shells of gas as a result and thereby triggering star formation. Conversely, they can also completely disperse their surrounding molecular gas suppressing star formation (Krumholz et al. 2014, and references therein). The ability to both constructively and destructively affect the formation of subsequent generations of stars means that high mass stars play a significant role in driving the evolution of GMCs (Zinnecker & Yorke 2007a). Here, we study the feedback of massive stars in the G305 HII region and molecular cloud complex.

G305: A brief history

The GMC associated with G305 is one of the most massive and luminous clouds in the Milky Way (Fig. 4.1). It is located in the Galactic plane at $l \sim 305°$, $b \sim 0°$ and at a kinematic distance of 4 kpc (derived from a combination of radio and Hα observations by Clark & Porter (2004); Davies et al. (2012a) measured its spectrophotometric distance to be 3.8 ± 0.6 kpc and most recently Borissova et al. (2019) measured the *Gaia* DR2 average distance to be 3.7 ± 1.2 kpc); this places it in the Scutum-Crux spiral arm. Given this distance, the complex has a diameter of ~ 30 pc (Clark & Porter 2004) and a molecular mass

[1] P. Mazumdar et al. 2021, A&A, 650, A164, reproduced with permission from ©ESO

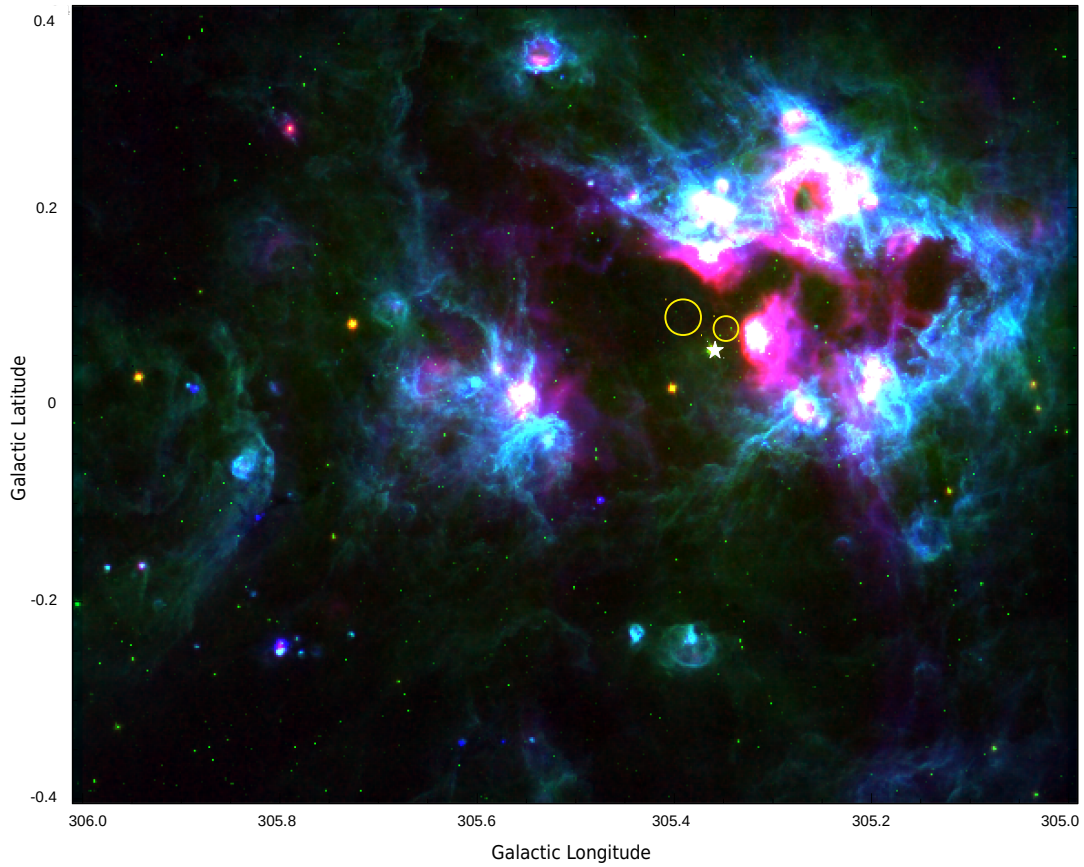

Figure 4.1: Three-color image (green = *Spitzer*-IRAC4 8 μm, red = Midcourse Space Experiment (MSX) 21.3 μm, blue = *Herschel*-PACS 70 μm) of the G305 star-forming complex. The 21.3 μm emission is dominated by hot dust in the HII region. The colder gas is traced by the 70 μm emission. The interface between the ionized and molecular gas appears as a blend of green (strong 8 μm emission from PAHs), blue (colder molecular gas) and occasionally red (interfaces very close to HII regions). The positions of Danks 1 and 2 clusters have been marked with the smaller and the larger yellow circles respectively and the wolf-rayet star WR48a has been marked as a filled white star.

of $\sim 6 \times 10^5$ $M_\odot$ (Hindson et al. 2010). The G305 complex consists of a large central cavity that has been cleared by the winds from massive stars belonging to two visible central clusters (Danks 1 and 2) and the Wolf-Rayet star (WR48a) (Clark & Porter 2004; Davies et al. 2012a). The cavity is surrounded by a thick layer of molecular gas (traced by CO and NH_3 emission; Hindson et al. 2010, 2013). Radio continuum observations by Hindson et al. (2012) have revealed that the cavity is filled with ionized gas and identified six ultra-compact HII (UC HII) regions and also one bright rimmed cloud (BRC) at the periphery of the cavity, indicating molecular gas irradiated by UV radiation (Sugitani & Ogura

1994; Thompson et al. 2004), which may cause implosion (Bertoldi 1989) or evaporation. A number of studies have reported star formation tracers (water and methanol masers, HII regions and massive young stellar objects, MYSOs) (Clark & Porter 2004; Lumsden et al. 2013; Urquhart et al. 2014a; Green et al. 2009, 2012). Furthermore, Hindson et al. (2010) found the concentration of star formation tracers to be enhanced inside a clump of NH_3 bearing molecular gas that faces the ionizing sources, which is consistent with the hypothesis that the star formation has been triggered. Analysis of the stellar clusters in the complex reveals them to have ages of 1.5 Myr for Danks 1 and 3 Myr for Danks 2, with the former possibly being triggered by the latter (Davies et al. 2012a). Additionally, a diffuse population of evolved massive stars was also found to exist within the confines of the G305 complex that had formed around the same time as the two clusters (Leistra et al. 2005; Shara et al. 2009; Mauerhan et al. 2011; Davies et al. 2012a; Faimali et al. 2012; Borissova et al. 2019).

How feedback from the massive stars affects molecular clouds is still poorly understood. However, the extensive amount of work done in identifying and characterizing the ongoing star formation taking place in this complex (UC HIIs, deeply embedded protostars and protoclusters) and mapping the distribution of molecular and ionized gas, makes G305 the ideal laboratory to study the role of feedback in affecting molecular cloud structures and creating future generation of stars. We have divided our work into two separate parts. In this paper, we want to further our understanding of how feedback from the central population of stars and the UC H II regions in G305 have affected the molecular gas. In the second paper of this series we will decompose the GMC into clumps and investigate whether any discernible differences exist in properties of clumps experiencing feedback compared to those further away from the feedback region.

So far, the evidence of feedback on the molecular gas in G305 has mostly been phenomenological and qualitative. In this paper, we study the excitation and kinematics of the gas in the complex since that is the most direct evidence of the feedback affecting the molecular cloud. Hindson et al. (2013) observed the J = 1-0 line of the CO main isotopologue to trace the distribution of molecular gas with a resolution of $> 30''$. Since, the compressed layer of gas due to the feedback is expected to be thin, resolving it requires a higher angular resolution. The feedback region will also exhibit higher excitation of gas that needs to be verified with excitation studies. In addition, the ^{12}CO becomes optically thick for moderately dense clouds ($\sim 10^3$ cm^{-3} at 25 K for the (J = 1–0) transition) and consequently, provides unreliable measurements. This necessitates the need for observations with rarer isotopologues of CO. Finally, observations of the dispersed gas requires sensitivity to very low column densities. Therefore, we decided to use the Large APEX sub-Millimeter Array (LAsMA) seven pixel array on the Atacama Pathfinder EXperiment (APEX) 12 meter submillimeter telescope to observe the G305 complex in the J = 3-2 rotational transition of both ^{12}CO and its ^{13}CO isotopologue.

The paper is organized as follows. We describe the observation methods and data reduction techniques in Sect. 4.2. We then present the results and the following analyses of the data along with their discussions in Sects. 4.3 - 4.7. In Sect. 4.8 we summarize the findings of this paper.

4.2 Observation and data reduction

4.2.1 Observations

We mapped a $1° \times 1°$ area centered on $(l, b) = (305.0, 0.0)$. The observations were done between 2017 and 2019 using the APEX telescope (Güsten et al. 2006) under the project number M-099.F-9527A-2017. The APEX telescope is located at an altitude of 5100 m at Llano de Chajnantor, in Chile.[2]

The receiver employed for these observations was the LAsMA 7 pixel instrument operating in the frequency range of 270 − 370 GHz (Güsten et al. 2008). It is a hexagonal array of six pixels surrounding a central pixel. The outer array is separated from the central pixel by ∼ 2 FWHM. The pixels employ superconductor-insulator-superconductor (SIS) sideband separating mixers (2SB). The backend consisted of Fast Fourier Transform Spectrometers (FFTS4G) that cover an intermediate frequency (IF) bandwidth of 4–8 GHz instantaneously with 65536 spectral channels with a width of 61.03 kHz.

In order to observe both ^{13}CO ($\nu_{\rm rest}$ ∼ 330.588 GHz) and ^{12}CO (3-2) ($\nu_{\rm rest}$ ∼ 345.796 GHz) simultaneously the local oscillator frequency was set at 338.190 GHz. This frequency was chosen in order to avoid contamination of the ^{13}CO (3-2) lines due to bright ^{12}CO (3-2) emission from the image band. For this setup, the FWHM is ∼ 19″, and the velocity resolution is 0.053 km s^{-1}. The whole 1 square degree region was divided into four submaps – one for each quadrant centered around $l = 305.5°$, $b = 0°$. Each submap was further divided into nine smaller submaps of size $10' \times 10'$ each. Observations were performed in a position switching on-the-fly (OTF) mode. The reference-positions were carefully chosen and tested to ensure no emission was present in the velocity range of −150 to 50 km s^{-1} (see Sect. 4.1 for details about the reference positions). For each scan, the 7 pixel-array was rotated to an angle of 19.1° in equatorial coordinates to ensure minimal overlap between the pixels and maximize sky coverage. For each OTF scan, data were dumped every 7″ scanned. On reaching the edge of every mapped area, the array was shifted perpendicular to the scan direction by half the beam-width (9″) and the scan was then carried out in the reverse direction. This process was repeated until the whole submap was observed. The same submap was then observed in a 90° rotated frame to ensure Nyquist sampling was achieved along both directions and also to reduce systematic scanning effects. During each scan, a calibration measurement was made every 10-15 minutes. This setup of a sample spacing of ∼ 7″ along with a sampling time of 0.1 sec resulted in datacubes of size 10′ × 10′ in approximately 1 hour.

The calibration of the spectral lines was carried out using the `apexOfflineCalibrator` pipeline (Muders et al. 2006; Polehampton et al. 2019). It uses a three load chopper wheel method, which is an extension of the "standard" method used for millimeter observations (Ulich & Haas 1976) to calibrate the antenna temperature scale. To remove the spectral variations of the atmosphere across the bandpass, the ATM model (Pardo et al. 2001) was

[2]This publication is based on data acquired with the Atacama Pathfinder EXperiment (APEX). APEX is a collaboration between the Max-Planck-Institut für Radioastronomie, the European Southern Observatory and the Onsala Space Observatory.

Table 4.1: Position and Noise toward off-positions used in otf-mapping of G305.

RA [J2000]	Dec [J2000]	Freq.-Range [GHz]	Noise rms [K][a]
13:08:23.90	-60:48:13.0	330.50-330.65	1.001e-2
		345.70-345.85	1.068e-2
13:10:52.20	-64:47:37.0	330.50-330.65	1.984e-2
		345.70-345.85	1.884e-2
13:20:12.00	-64:42:01.0	330.50-330.65	2.116e-2
		345.70-345.85	2.077e-2
13:16:33.30	-60:43:19.0	330.50-330.65	2.357e-2
		345.70-345.85	2.176e-2

Notes. [(a)] The rms noise was obtained by averaging over all 7 pixels, albeit being at different offsets with respect to the position mentioned in the table.

used. The pipeline provides the flexibility to determine the opacity for the whole band pass as one number or to calculate a more accurate opacity channel by channel. We chose the latter for calibrating our data since the ^{13}CO line lies at the edge of an atmospheric water line at 325 GHz and hence an accurate accounting for this line in the bandpass is essential. After the calibration, the intensities are obtained on the T_A^* (corrected antenna temperature) scale. Apart from the atmospheric attenuation, this also corrects for rear spillover, blockage, scattering, and ohmic losses. All intensities stated in this paper are in the T_A^* scale unless specifically stated otherwise. Regular observations of Jupiter were done during the commissioning of the instrument and the observations of G305, resulting in a beam efficiency of $\eta_{mb} = 0.74$ with an uncertainty of about 10%. This efficiency value was used to convert intensities from T_A^* scale to the main beam brightness temperature (T_{mb}).

4.2.2 Data reduction

The data was reduced using the GILDAS package[3]. A velocity range of $-200\,\mathrm{km\,s^{-1}}$ to $200\,\mathrm{km\,s^{-1}}$ was extracted from every spectrum and resampled to an adequate velocity resolution of $0.5\,\mathrm{km\,s^{-1}}$ to reduce the noise. The velocity range $-150\,\mathrm{km\,s^{-1}}$ to $50\,\mathrm{km\,s^{-1}}$ was masked before fitting a 3rd order baseline to each spectrum. The reduced, calibrated data obtained from the different scans were then combined and gridded using a 6″ cell size. The gridding process includes a convolution with a Gaussian kernel with a FWHM size of one-third of the telescope FWHM beam width. The data cubes obtained have a final angular resolution of ∼ 20″. Spectra from all the pixels were then averaged to find the portions of the spectra containing line emission, which were then masked. The

[3] http://www.iram.fr/IRAMFR/GILDAS

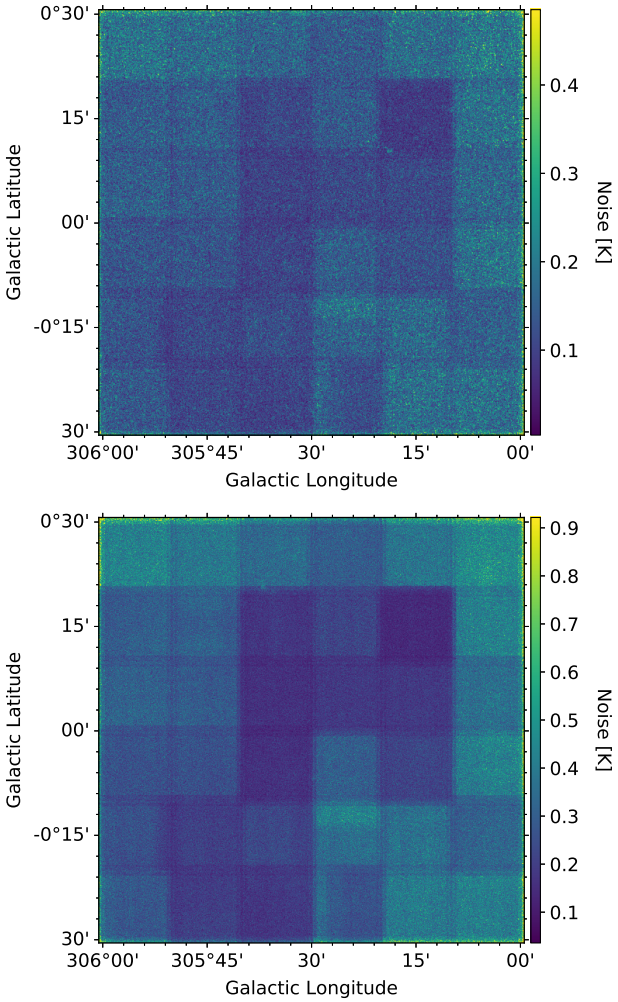

Figure 4.2: Pixel wise noise maps of ^{12}CO(3-2) (*top*) and ^{13}CO(3-2) (*bottom*) of the G305 GMC complex.

process of baseline removal was again repeated for the spectra of each pixel to obtain a more stable baseline and a cleaner map.

4.3 Integrated properties

4.3.1 Moment-0 maps

In order to create the integrated intensity ("moment-0") maps of the G305 region, a noise map of each grid-element (referred to as pixel from now onward) was first created for both the ^{12}CO and ^{13}CO J = 3-2 transitions. This was done by calculating the standard deviation for a part of the spectrum consisting of 100 emission free channels. Fig. 4.2 shows the pixel-wise noise of the whole region in both ^{12}CO and ^{13}CO J = 3-2 data

sets. The moment-0 map was produced by integrating the emission above 5σ between $-70\,\mathrm{km\,s^{-1}}$ and $10\,\mathrm{km\,s^{-1}}$. Fig. 4.3 shows our moment-0 maps of the G305 star forming complex. The ^{12}CO map traces the large scale, diffuse as well as hot gas very well.

The ^{13}CO map on the other hand is sensitive to higher column density gas and hence, traces the more compact, dense clumps in the complex[4]. We have divided the map into nine regions for ease of explanation. This demarcation of the regions was done visually to highlight relevant molecular gas features observed in the channel-maps. From the two integrated maps it can be seen that the central region of the giant molecular cloud has been cleared out of most of the high density gas. Although it is reasonable to believe that the central stars clusters are responsible for this, it still needs to be verified whether the amount of feedback from the stars in the complex can indeed carve out such a large hole. This will be explored in Sect. 4.5.

Looking at the gas content of the complex, we observe three bright dense molecular cloud complexes. One in the (Galactic) north (region V and VI in Fig. 4.3), one in the south (region VIII) and the third in the east (region III) of the central cavity. The northern and the southern complex are connected by a thin strip of high(er) column density tenuous gas (region VII) toward the west. Both of these complexes also show a carved-out hole in their center where one O and two B stars have been observed (Leistra et al. 2005; Borissova et al. 2019). The cloud to the east (III) is disconnected from the others but has a long very straight ($\sim 20 \times 2\,\mathrm{pc}$) filamentary structure (III and I) trailing away from the cavity itself. It has a central velocity of $\sim 40\,\mathrm{km\,s^{-1}}$ and a gradient of $\sim 0.25\,\mathrm{km\,s^{-1}pc^{-1}}$. Such filaments are found to be associated with many star-forming regions and are believed to play a crucial role in star-formation (André 2017). The northeast of the cavity appears as a wind-blown structure delineated by regions II, III, IV, and V. Towards the south of the cavity (between regions III and VIII), the gas also appears to have been dispersed by the feedback.

4.3.2 Velocity structure

Fig. 4.4 shows the average spectrum over the whole region. There is no confusion in the foreground except for some local emission at $\sim -4\,\mathrm{km\,s^{-1}}$ in ^{12}CO. The line profile is not Gaussian. All emission from the complex is found within the velocity range between -50 and $-26\,\mathrm{km\,s^{-1}}$ for ^{13}CO, and -55 and $-7\,\mathrm{km\,s^{-1}}$ for ^{12}CO.

Fig. 4.5 shows the channel maps of G305 for the range of velocities -50 to $-25\,\mathrm{km\,s^{-1}}$ with a spacing of $5\,\mathrm{km\,s^{-1}}$. Regions I and VIII are prominent in the range -25 to $-35\,\mathrm{km\,s^{-1}}$, while the other regions (II, III, IV, V, VI, and VII) emit in the range -35 to $-45\,\mathrm{km\,s^{-1}}$. The observed velocity structure is most likely a consequence of the interplay of the morphology of the cloud and the feedback from the central star clusters on the natal molecular cloud.

[4]Due to the high opacity of ^{12}CO and a resulting much lower effective critical density, the ^{13}CO transition probes significantly higher H_2 volume densities in the clouds

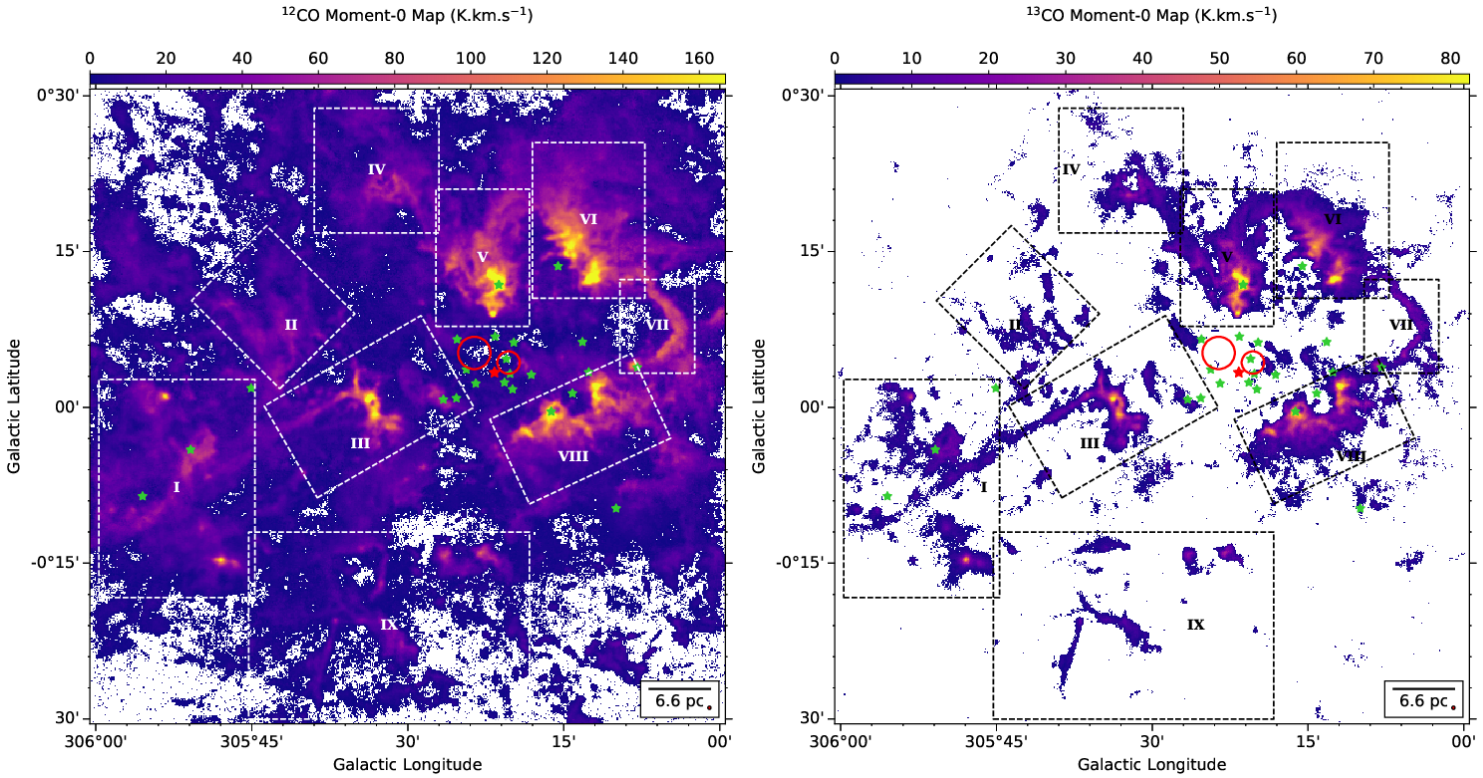

Figure 4.3: Moment-0 maps of ^{12}CO (3-2) [*left*] and ^{13}CO (3-2) [*right*] lines toward the G305 GMC complex. In both maps, the emission has been integrated over a velocity range from −70 to +10 km s^{-1}. Pixels with no emission > 5σ for at least three consecutive velocity channels have been excluded (seen in white). Overlaid on top as green stars are the position of stars as reported in Borissova et al. (2019). The red circles show the positions of the Danks 1 and 2 clusters, and the red star is WR48a. The numbered regions are discussed in the text.

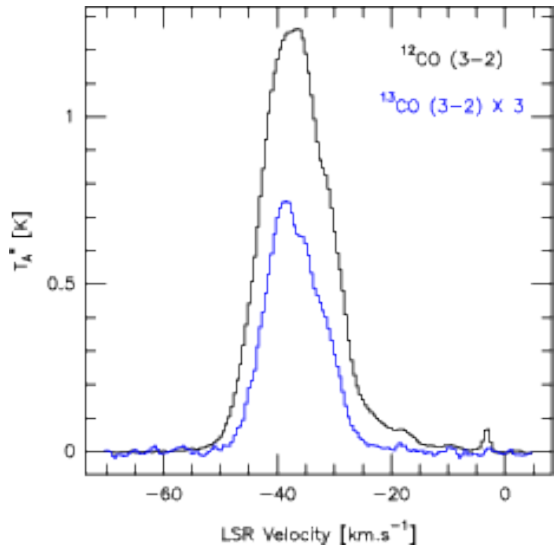

Figure 4.4: Averaged spectrum of ^{12}CO and ^{13}CO over the whole G305 giant molecular cloud complex. The ^{13}CO line has been scaled up by a factor of 3.

For a comprehensive analysis of the morphology of the cloud, we refer to Hindson et al. (2013) who studied the region reported here in more detail by comparing the molecular emission with the morphology of the surfaces of molecular clouds illuminated by the far-ultraviolet (FUV) photons of the stellar sources, commonly referred to as photon dominated regions (PDR) (Tielens & Hollenbach 1985). Our results are consistent with the picture presented by these authors.

4.4 LTE analysis

The CO data were combined to calculate the excitation temperature, optical depth, and column density. We assume that the molecular gas can be described as a system in Local Thermodynamic Equilibrium (LTE) and the brightness temperature (T_B) is equal to the measured T_{mb}. Then, solving the radiative transfer equation for an isothermal slab of CO radiating at a frequency ν we obtain:

$$\frac{T_B}{\mathrm{K}} = [J_\nu(T_{ex}) - J_\nu(T_{bg})] \cdot (1 - e^{-\tau_\nu}) \ , \tag{4.1}$$

where T_{ex} is the excitation temperature of the line; T_{bg} is the temperature of the cosmic microwave background; τ_ν is the optical depth; and, $J_\nu(T)$ is the equivalent temperature of a black body at temperature T which can be written as:

$$\frac{J_\nu(T)}{\mathrm{K}} = \frac{h\nu}{k_B} \left(\frac{1}{e^{h\nu/k_B T} - 1} \right) , \tag{4.2}$$

where h is the Planck's constant and k_B is the Boltzmann constant.

All the calculations were done on each l, b, v three-dimensional pixel (from here on referred to as voxel). The advantage of this methodology over that of deriving properties over the velocity integrated values is that all the subsequent properties derived are independent of any segmentation method used for source extraction.

To calculate the ^{12}CO excitation temperature, we adopt the textbook formalism (Wilson et al. 2013), which assumes that the ^{12}CO (3-2) line is optically thick. This was then used to determine the ^{13}CO optical depth and subsequently the ^{13}CO column density. Eq. 4.1 is used to calculate the excitation temperature. Using a value of 2.7 K for the (cosmic microwave radiation) background temperature, we obtain:

$$\frac{T_{ex}}{\mathrm{K}} = 16.6 \left[\ln\left(1 + \frac{16.6}{T_{12} + 0.04}\right)\right]^{-1} , \tag{4.3}$$

where we use T_{12} and T_{13} for the main-beam brightness temperature of ^{12}CO and ^{13}CO, respectively. All the voxels satisfied the condition $T_{12} > T_{13}$; so, we did not have any significant case of self-absorption in our data that would have rendered the excitation temperature derived from this method unreliable.

The optical depth is derived for each voxel from the excitation temperature obtained from ^{12}CO and the ^{13}CO intensity using the following equation derived from Eq. 4.1:

$$\tau_{13} = -\ln\left[1 - \frac{T_{13}}{15.9}\left(\frac{1}{e^{15.9/T_{ex}} - 1} - 0.0028\right)^{-1}\right] , \tag{4.4}$$

where τ_{13} denotes the optical depth of ^{13}CO (3-2) transition. Only those voxels that have an emission greater than 5σ are considered real.

The column density of ^{13}CO $J = 2$ level is calculated as:

$$\frac{N_{13}(J=2)}{\mathrm{cm}^{-2}} = \frac{8\pi}{c^3}\frac{g_2}{g_3}\frac{\nu^3}{A_{32}}\frac{1}{1 - e^{(-h\nu/k_B T_{ex})}}\tau_\nu \, dv , \tag{4.5}$$

where g_2 and g_3 are statistical weights of $J = 2$ and $J = 3$ rotational energy levels respectively; $A_{32} = 2.181 \times 10^{-6}\,\mathrm{s}^{-1}$ is the Einstein's A coefficient for the ^{13}CO (3-2) transition (taken from the Leiden Atomic and Molecular Database[5]; Schöier et al. 2005).

The rotational partition function, Z, can be approximated by

$$Z \approx \frac{k_B}{hB}\left(T_{ex} + \frac{hB}{3k_B}\right) , \tag{4.6}$$

where $B = h/(8\pi^2 \mathcal{I})$ is the rotation constant and is calculated using the moment of inertia $\mathcal{I} = \mu R_{CO}^2$, and μ is the reduced mass, and $R_{CO} = 0.112\,\mathrm{nm}$ is the mean atomic separation of the CO molecule.

Finally, using $N_{13}(J)$ and Z one can calculate the total column density of ^{13}CO using:

$$\frac{N_{13}}{\mathrm{cm}^{-2}} = N_{13}(J)\frac{Z}{2J+1}\exp\left[\frac{hBJ(J+1)}{k_B T_{ex}}\right] . \tag{4.7}$$

[5] https://home.strw.leidenuniv.nl/~moldata/CO.html

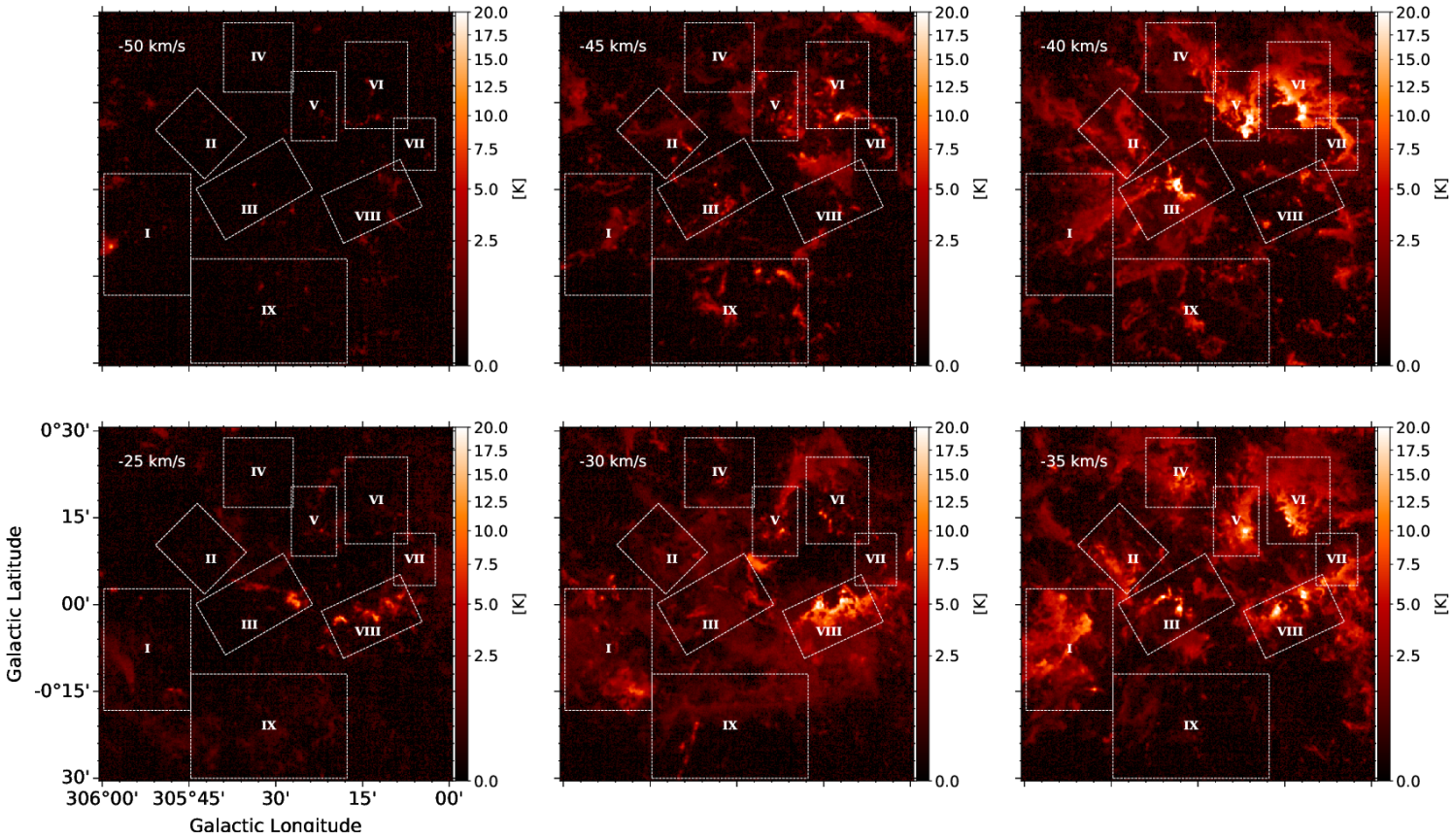

Figure 4.5: Channel maps of ^{12}CO(3-2) emission toward G305. The emission has been integrated over 5 km s^{-1} around the velocities indicated in each panel.

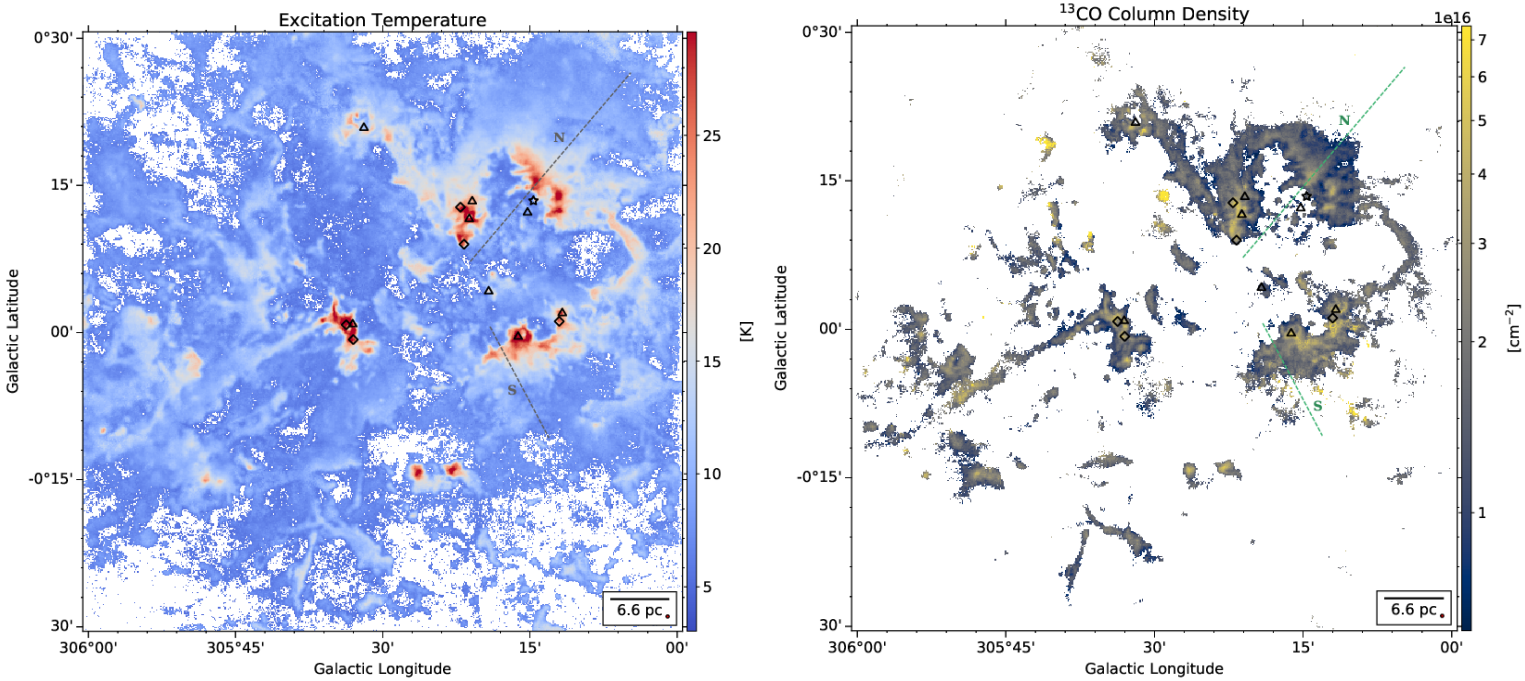

Figure 4.6: *Left*: Mean T_{ex} map of the G305 complex. For each pixel this was calculated by integrating over all the channels. Only those channels that had emission above 5σ noise level were considered. *Right* Integrated ^{13}CO Column Density map of G305. This was calculated by summing the ^{13}CO total column density per channel over all the channels. Overlaid on top, are the positions of the HII regions (triangles), UC HII regions (diamonds), and the BRC (star) as determined by Hindson et al. (2012, 2013).

Subthermal excitation

The analysis presented in this section is based on the assumption that LTE is applicable in all the voxels with detected emission. But for gas with densities below the critical density of CO (3-2) ($\approx 10^4\,\mathrm{cm}^{-3}$), the energy level populations will not follow the Boltzmann distribution and consequently the measured excitation temperature will be lower than the actual temperature of the gas. An underestimation of the excitation temperature will lead to an overestimation of the column density values according to Eq. 4.5. But, for optically thick emission the critical density can be effectively reduced (roughly by $1/\tau$) thereby making it possible for the gas to reach LTE at lower densities.

We tried to test whether the limit of large optical depth for ^{12}CO holds in regions where ^{13}CO is also detected. For this, we took the lowest detected ^{13}CO column density at a 5σ significance and estimated the ^{12}CO column density adopting a ^{12}CO/^{13}CO abundance ratio of 60. This value was calculated using the equation $12C/13C = 6.21D_{GC} + 18.71$ from Milam et al. (2005) where $D_{GC} \approx 6.6$ kpc is the galactocentric distance of G305. The estimated ^{12}CO column density corresponding to the lowest detected ^{13}CO column density is then $\sim 2.46\times10^{17}\,\mathrm{cm}^{-2}$. Eq. 4.5 was then used to calculate the velocity integrated optical depth for ^{12}CO(3-2) transition. We obtained $\int \tau_v dv \approx 149.193\,\mathrm{km\,s}^{-1}$ for an excitation temperature of 15 K. Assuming a Gaussian line profile with a standard deviation of $\sim 8.5\,\mathrm{km\,s}^{-1}$ (see Sect. 4.7.2 for the justification of the chosen value for standard deviation), the optical depth at the centroid velocity is given by $\tau_{12} = \left(\int \tau_v dv\right) / \left(\sigma_v \cdot \sqrt{2\pi}\right) \approx 7$. So, for pixels with detected ^{13}CO emission, the ^{12}CO optical depth is greater than 1. This along with the findings of Hindson et al. (2010) that the volume density of clumps in G305 ranges between 10^3–$10^4\,\mathrm{cm}^{-3}$ means that the emission from the pixels where both ^{12}CO and ^{13}CO are detected are most likely in LTE. In the other regions where only ^{12}CO emission is detected, the condition of LTE may not always apply and should be kept in mind while interpreting the results derived from them.

4.5 Effects of feedback on the molecular gas

4.5.1 Excitation temperature and column density maps

The integrated spectrum over the whole G305 region (see Fig. 4.4) does not show any obvious sign of confusion along the line of sight (the emission appears to come from one local standard of rest (LSR) velocity without foreground confusion at any other velocity channel). Hence, properties like excitation temperature and column densities integrated over the whole linewidth are very likely to be a good representation of the corresponding physical properties of the GMC.

Fig. 4.6 (left) shows the excitation temperature map of the complex where each pixel represents the mean ^{12}CO excitation temperature at the corresponding position. Fig. 4.6 (right) shows the ^{13}CO column density of the region summed over all velocity channels on a logarithmic scale. The hot regions toward the northern, southern, and western molecular clouds are coincident with the HII and UC HII regions existing in the region

(see Fig. 4.6; Hindson et al. 2012, 2013).

The UC HII regions are also located in regions of high column density surrounded by a region with relatively lower column density. One also notes some unconnected small regions where the column density seems to be much higher than in some of the densest regions inside the larger molecular clouds, notably at approximately $(l, b) \sim (305°42', +0°19'), (305°30', +0°13')$, and $(305°10', -0°8')$. Of these, only that at $\sim (305°30', +0°13')$ is associated with a diffuse H II region G305.4399+00.2103. For other sources, we have not found any counterparts in the literature.

In Fig. 4.6 we notice that the edge of the denser clouds show a marked jump in their excitation temperature at the side facing the central stellar clusters, which then tapers off as we move away from the center. This represents clear evidence that feedback from the stars acting on the edge of the dense gas is heating it. The exposed gas then acts as a shield for the rest of the cloud, resulting in a temperature profile that decreases as we move away from the center. Fig. 4.7 shows the profiles of ^{13}CO column density (top panel row) and excitation temperature (second row of panels from the top) along two different arbitrarily selected directions leading away from the center as marked on Fig. 4.6. These profiles have been obtained after smoothing the excitation temperature and column density maps to a resolution of 30″ in order to compare them with other ancillary data as will be evident in the following sections. The left panel shows the profile along the line marked N and the right panel shows that along S. As is evident from the excitation temperature profiles, the gas is heated on the leading edge of the molecular cloud facing the central cavity. The feedback from the stars results in a steep increase in the temperature by a factor of ~ 3 at the edge facing the center. The temperature then steadily drops as we move away from the center. As pointed out in Sect. 4.4 the excitation temperature before the leading edge of the profile may have been underestimated. So the increase in its value at the leading edge can be considered to be an upper limit. For the column density profiles, we notice that the northern profile also shows pronounced evidence for compression as the column density at the leading edge is enhanced significantly compared to the trailing edge. However, for the southern profile even if the leading edge of the cloud has a higher column density than the rest of the cloud, the decrease in column density as we move away from the center is not as pronounced. Due to the absence of significant ^{13}CO emission between the stars and the dense gas boundary, we were only able to determine a lower limit on the extent of the region that has an increased column density at the edge of the cloud (based on the minimum column density ($\approx 4.1 \times 10^{15}$ cm^{-2} corresponding to 5σ times the rms noise value probed by our observations). This lower limit factor of $\gtrsim 5$ for S and $\gtrsim 10$ for N still represents a large increase in column density at the edge of the cloud.

4.5.2 Rotational excitation

The energy from the feedback being deposited onto the molecular cloud from the stars may be used up to excite the CO molecules to their higher J rotational levels. In this section, we investigate whether feedback in G305 affects the rotational excitation in the molecular cloud. We complemented our data with ^{13}CO J = 2-1 data from the SEDIGISM

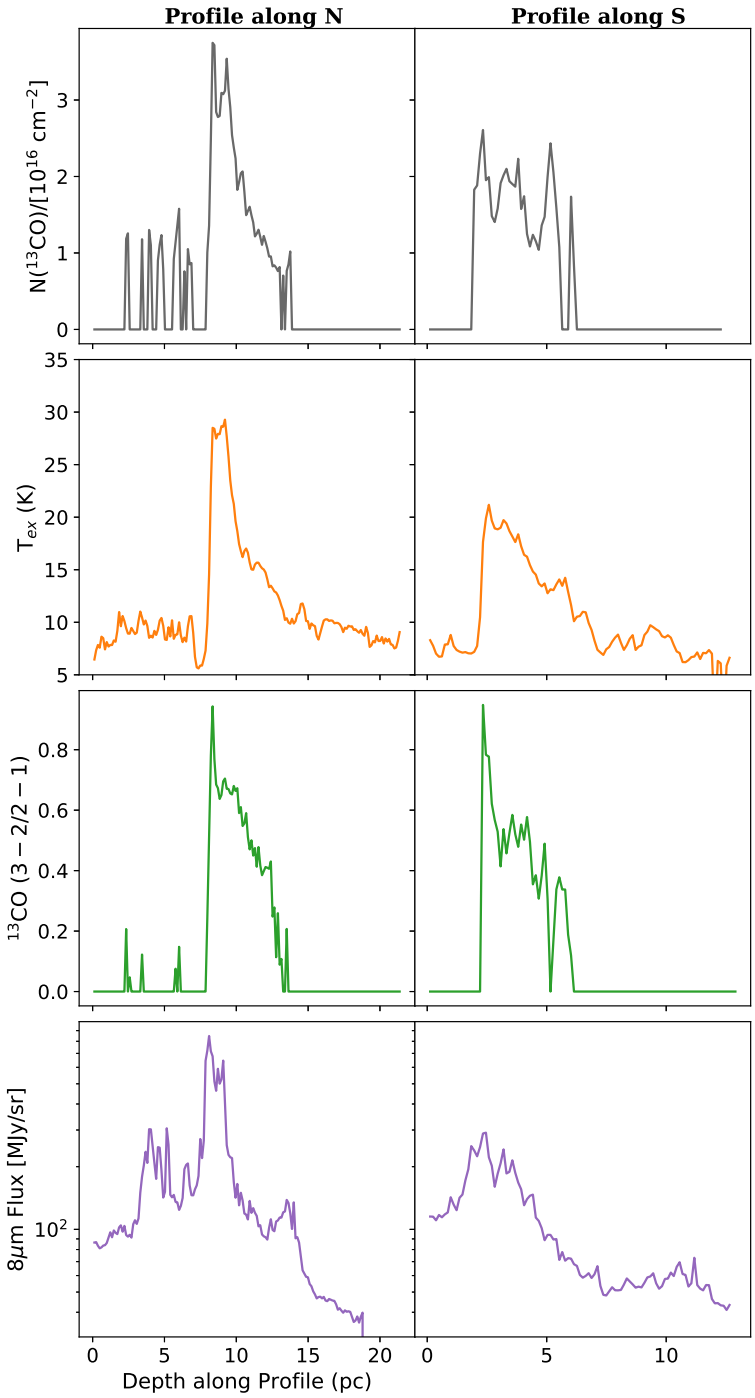

Figure 4.7: ^{13}CO Column Density (gray), Excitation Temperature (orange), ^{13}CO J = 3-2/J = 2-1 ratio (green), and 8μm Flux (purple) profiles for two separate directions in G305. The profiles were plotted outward from the center of the complex.

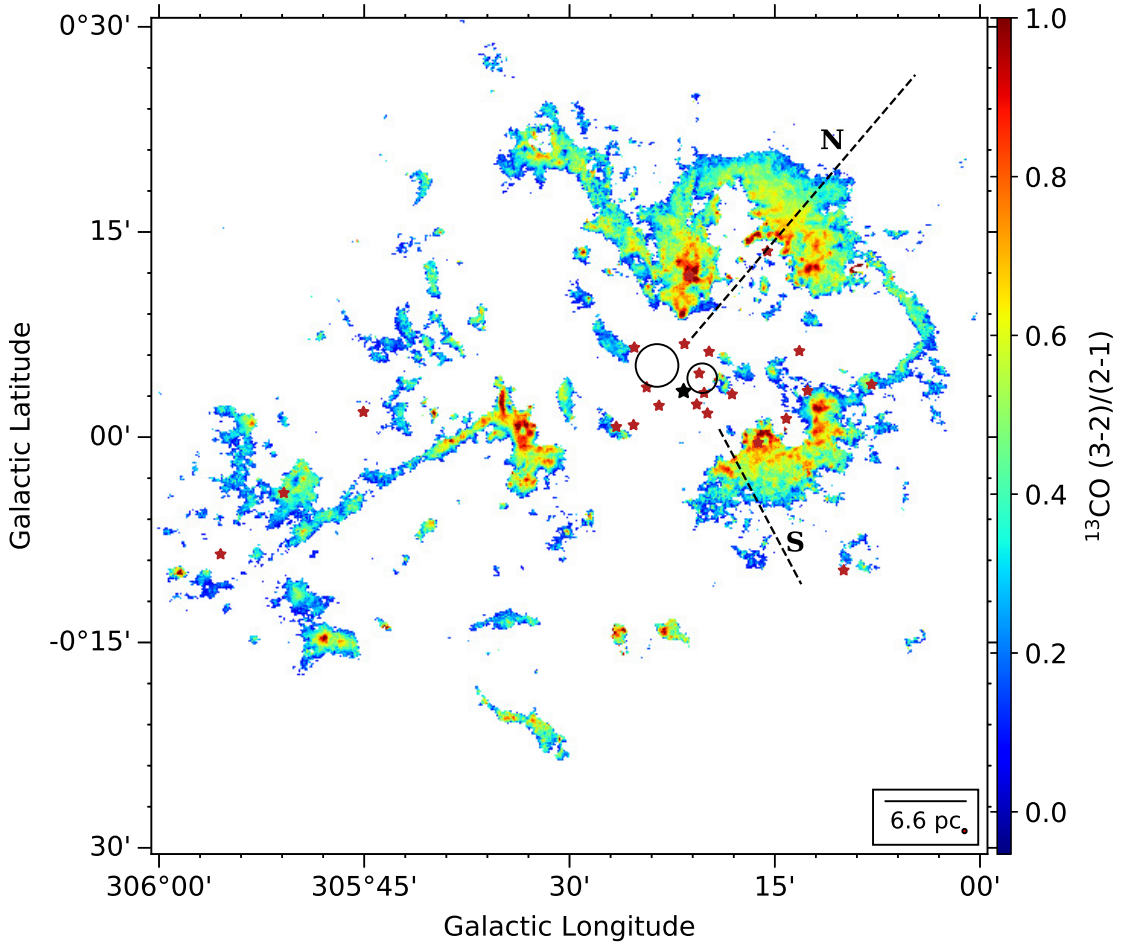

Figure 4.8: ^{13}CO J = 3-2/J = 2-1 ratio map of the G305 complex. The dashed lines show the direction along which the profiles of the excitation ratio was plotted in Fig. 4.7. The black circles show the locations of the Danks 1 and 2 clusters. The black star shows the position of WR48a, and the red stars show the positions of the stars from Borissova et al. (2019).

(Schuller et al. 2017) survey to create rotational excitation maps for the region.

For this, the LAsMA ^{13}CO J = 3-2 map was first smoothed to the 30″ angular resolution of the SEDIGISM map. In order to trace the excitation, the ^{13}CO J = 3-2/J = 2-1 intensity ratio was calculated over the whole map. Pixels with a signal-to-noise ratio (S/N from now on) of less than 5 were blanked. Warm and dense gas is excited to higher J levels resulting in a higher ^{13}CO (J = 3-2)/(J = 2-1) ratio.

Fig. 4.8 shows the map of the ratio of the two line intensities. It is evident that this ratio is higher on the side of the cloud facing the central cavity. We also show two directional profiles cut through the excitation map in Fig. 4.7 (third row of panels from the top). Both these profiles demonstrate the effect of feedback very well. In a very narrow region facing the center we see the excitation ratio almost equal to 1. For linear molecules, the rotational excitation can either increase by higher temperatures or larger volume densities

or a combination of both, indicating a higher pressure at the cloud surfaces. As we then move away from the center, the excitation ratio decreases fast, indicating that the front end of the cloud is acting as a shield for the rest of the gas trailing it.

4.5.3 Energetics of feedback

In this subsection, we try to explore whether the energy input from the central stars can account for the observed effects on the molecular gas morphology and excitation. Firstly, the OB stars inside the cavity of G305 can efficiently ionize the surrounding gas with the large amounts of ionizing photons they emit leading to photoevaporation of the cloud. Here, we estimate if this can lead to the observed size of the cavity given the age and type of stars in the complex. We follow the model used by Watkins et al. (2019) for a simple case of a spherical cloud of uniform density n_H being illuminated by a central stellar population emitting photons isotropically at rate $\mathcal{N}_i$. The radius of the central hole carved out by these photons in time t given an electron density n_e is given by the following equation:

$$R_{ion} = \left(\frac{3\mathcal{N}_i}{4\pi\alpha_B n_e^2} [1 - \exp(-n_e^2 \alpha_B t / n_H)] \right)^{\frac{1}{3}}, \tag{4.8}$$

where α_B is the recombination coefficient. Considering the stars from the Danks 1 and Danks 2 as well as those outside the two clusters as reported in Borissova et al. (2019) as the ionizing sources, we obtain $\mathcal{N}_i \approx 9.4 \times 10^{50}\,\mathrm{s}^{-1}$ using the stellar classification from Davies et al. (2012a); Borissova et al. (2019) and calculating the ionizing flux for different stellar types using Panagia (1973) and Crowther (2007). We adopt $n_H \approx 10^4\,\mathrm{cm}^{-3}$ and $\alpha_B = 2.7 \times 10^{-13}\,\mathrm{cm}^3\,\mathrm{s}^{-1}$ (Hindson et al. 2010, 2013), $n_e = [100 - 5000]\,\mathrm{cm}^{-3}$. Figure 4.9 shows the diameter of the ionized bubble as a function of time for a range of n_e values. Given the diameter of the central cavity is $\sim$ 10 pc wide along the north-south direction (between regions V and VIII) and $\sim$ 30 pc across the east-west direction (between regions III and VII), this would imply that the population of visible stars inside the complex can drive such a cavity via photoionization given an $n_e \sim 10^2\,\mathrm{cm}^{-3}$. But, this is a very simplistic view, as the starts in the cavity are not located at its center but are spread out over $\sim$ 20 pc. Also, electron density inside HII regions is not constant over time and varies from 10^2–$10^5\,\mathrm{cm}^{-3}$ depending on the diameter of the cavity as $n_e \propto D^{-1}$ (Kim & Koo 2001; Garay & Lizano 1999). A more realistic scenario would be one where the expansion of the cavity is initially driven by the Danks 2 system for the first 1.5 Myr which swepng out some of the ionized gas via strong winds (aided by the WR stars outside the Danks cluster) and thereby lowering the n_e for the next generation of stars in Danks 1 and the others. The subsequent generations of stars could then clear out the gas more effectively.

Next, we estimate whether the amount of energy input from the stars is large enough to cause the observed trend in the excitation line profiles, even if the nature of the profiles strongly suggests that feedback from the stars is heating the gas. For this, we first calculate the external pressure exerted by the stars on the cloud surface. Assuming that most of the energy input from stellar radiation comes from the ionizing photons, the pressure from stars can be estimated as $P_{\mathrm{star}} = \mathcal{N}_i \langle h\nu \rangle / 4\pi {R_s}^2\, c\, k$, where $\langle h\nu \rangle$ is the mean photon

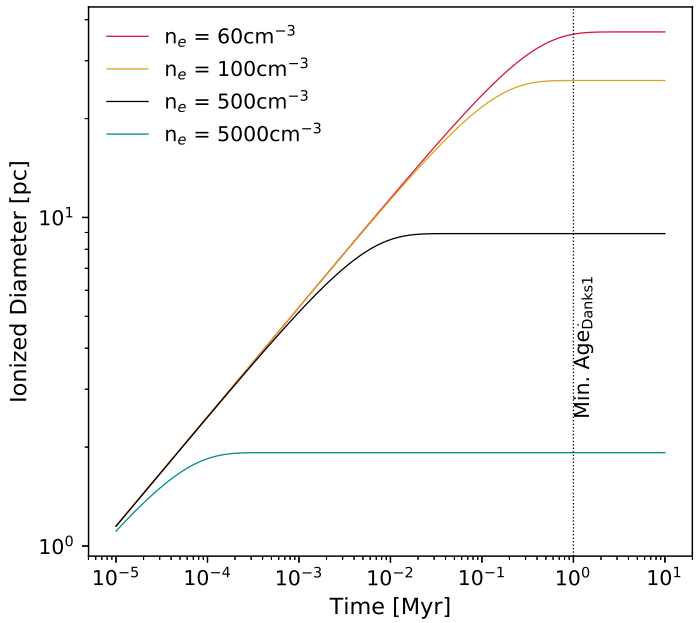

Figure 4.9: Time evolution of the ionization diameter of a spherical cloud of density $10^4\,\mathrm{cm}^{-3}$ being illuminated by Danks 1 and Danks 2 star clusters at its center for different electron density values. The vertical dotted line is the minimum age of the Danks 1 cluster take from Davies et al. (2012a).

energy of an O-star (assumed to be $\sim 15\,\mathrm{eV}$ (Pellegrini et al. 2007)), R_s is the distance of the cloud from the emitting star, c is the speed of light, and k is the Boltzmann's constant. We assume that the O5-O6V, B0-B1V, and B2-B3V stars found by Leistra et al. (2005) in the G305.3+0.2 cluster are the stars responsible for the observed excitation profile N, and Danks 1 is responsible for that in S. But the spectral classification of stars in Danks 1 by Davies et al. (2012a) spans a large range of ionizing flux values. In order to obtain a lower limit on the ionizing flux, we used the spectral type with the lowest ionizing flux, that is O6V for O4-6, O8V for O6-8/8If, B3V for O8-B3, B3I for O8-B3I, and WN9 for WNLh. We estimate a distance of 2.5 pc between the edge of the profile N and the stars, and $\sim 4\,\mathrm{pc}$ between Danks 1 and the edge of S. Using these values we obtain the external pressure from the stars for N and S to be $P_{\mathrm{star,N}} \sim 2.5\times10^5\,\mathrm{K\,cm^{-3}}$, and $P_{\mathrm{star,S}} \sim 2.6\times10^5\,\mathrm{K\,cm^{-3}}$ respectively. We then calculate the thermal pressure at the edge of the cloud facing the cavity and that at the far end away from the cavity. The pressure exerted by thermal motion inside a cloud can be estimated as $P_{th} = n(H_2)\,T\,\mathrm{K\,cm^{-3}}$. For the far end of the cloud in both cases N and S, we assume the density to be equal to the average value of clump densities from Table 5 in Hindson et al. (2013), that is $n(H_2) \sim 1.5\times10^3\,\mathrm{cm^{-3}}$. For the temperature we adopt a value of $T \sim 10\,\mathrm{K}$ for both N and S (see Fig. 4.7). So, for both N and S the thermal pressure in the far end of the cloud is $P_{th}^{far} = 1.5\times10^4\,\mathrm{K\,cm^{-3}}$. For the side of the profiles N and S facing the cavity, we need to deduce the value of n_{H_2}. For this, we assume that the pressure from the stars only compresses the cloud in a direction along

the plane of the sky. We can then equate the proportional increase in column density to that of the observed volume density. From Fig. 4.7 we calculate the proportional increase in column density at the edge facing the center compared to that away from the cavity to be ~ 4 for N and ~ 1.6 for S. Now calculating the thermal pressure at the edge of the profiles facing the central cavity we obtain $P^{near}_{th,N} = 28 \cdot 4 \cdot 1.5 \times 10^3 = 1.68 \times 10^5\,\mathrm{K\,cm^{-3}}$ and $P^{near}_{th,S} = 22 \cdot 1.6 \cdot 1.5 \times 10^3 = 5.28 \times 10^4\,\mathrm{K\,cm^{-3}}$. The difference in the thermal pressure between the leading and trailing edge for N and S is therefore $\Delta P_{th,N} \sim 1.53 \times 10^5\,\mathrm{K\,cm^{-3}}$ and $\Delta P_{th,S} \sim 3.78 \times 10^4\,\mathrm{K\,cm^{-3}}$ respectively. This difference in thermal pressure accounts for $\sim 61\%$ of $P_{\mathrm{star,N}}$ and less than $\sim 14.5\%$ of $P_{\mathrm{star,S}}$. Hence, for the profile N about 61% of the radiation pressure is going toward heating up the gas whereas for S this is less than 15%.

4.6 Characterizing feedback in G305

So far, the evidence of feedback on the molecular gas in G305 has been mostly based on morphology, with specific examples of profiles along selected directions. In this section, we attempt to quantitatively study the effect of feedback on the excitation of the gas at a global level over the whole cloud complex. In order to see this global nature of the gas excitation in feedback regions, we first need to identify as well as quantify where these feedback regions are.

4.6.1 Identifying feedback regions : GLIMPSE 8μm map

The 8 µm map obtained from the Galactic Legacy Infrared Mid-Plane Survey Extraordinaire (GLIMPSE: Benjamin et al. 2003; Churchwell et al. 2009) is a very useful tool to identify the regions of stellar feedback.

PDRs mark the boundary between the ionized and neutral gas in a molecular cloud (Rathborne et al. 2002). The FUV photons from stars excite polycyclic aromatic hydrocarbons (PAHs) on the surface of dense molecular clouds at the interface between the ionization front and the molecular gas (Tielens 2008). The PAHs absorb FUV radiation from hot stars and re-emit fluorescently in several broad bands at near and mid infrared (IR) wavelengths (Allamandola et al. 1989). The most luminous of these is within the 6.5 to 9 µm range covered by the 8 μm filter of the Infrared Array Camera (IRAC: Fazio et al. 2004) aboard the Spitzer Space Observatory that was employed for GLIMPSE. Hence, bright regions in 8 µm Spitzer/IRAC images correspond to regions subjected to large amounts of radiative feedback to FUV radiation from the stars.

Fig. 4.10 shows the Spitzer 8 μm image of the G305 region. The molecular gas in the region seems to be coextensive with the bright 8 μm emission. All of the CO emission in the region is associated with IR emission. In order to demonstrate the validity of the 8 μm flux as a tracer for feedback we plotted its profiles along the same direction as the excitation temperature, column density, and the ^{13}CO J = 3-2/J = 2-1 intensity ratio in Fig. 4.7. Before plotting the profile, the 8 µm map was first smoothed to the same resolution as the other excitation maps of 30″. At the edges of the higher column density clouds,

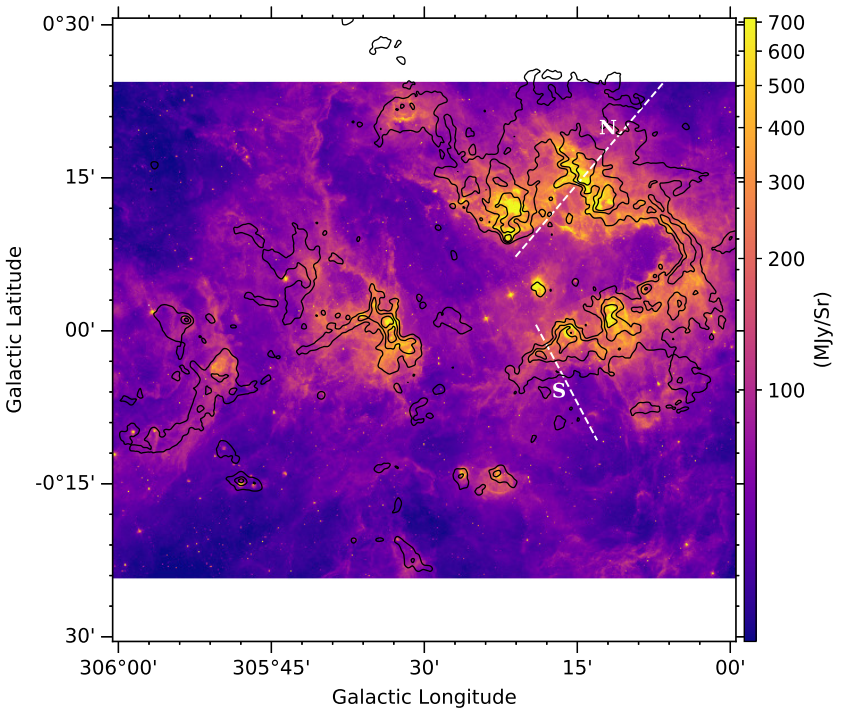

Figure 4.10: GLIMPSE 8 µm map of the G305 regions. The black contours correspond to the ^{12}CO J=3–2 integrated intensities of 30, 70, and 120 K km s^{-1} (50, 120, and 200σ, respectively). The dashed lines show the direction along which the profiles of the excitation ratio was plotted in Fig. 4.7.

we observe a sharp increase in the 8 μm flux (around a depth of 7 pc for N and 1.5 pc for S), marking the brightest parts of the PDRs of the clouds. This increase coincides with the increase in the gas excitation properties. Afterwards, all three properties decrease along with the 8 μm flux. The decreasing profile as we move away from the center also demonstrates that the PDR is effectively shielding the molecular cloud, absorbing the bulk of the FUV photons. Inside the denser cloud along N, the 8 μm profile also shows a second local peak (around a depth of 13 pc along the profile and at a depth of $\sim$ 6 pc from the edge of the high density cloud) before sharply falling off. This also coincides with the local peak in the column density as well as the rotational excitation (third panel in Fig. 4.7) profiles. But, the excitation temperature (first panel) does not show a distinct peak. An additional peak also exists at a depth of about 4 pc along N. This along with the peak coincident with the edge of the high density cloud appears to be part of a bubble shaped structure in Fig. 4.10. There is very little dense molecular material left around the former peak and the diffuse gas does not appear to be impacted from the feedback as can be seen from the excitation temperature profile corresponding to this peak. Some pockets of higher column density gas appear to be coincident with this peak. The feedback from the stars reported in Leistra et al. (2005) which are located inside the bubble are most likely responsible for this structure.

This 8 μm map was used as a template to identify regions of feedback based on their integrated flux. In order to quantify the feedback itself we assumed the 8 µm intensity to be a proxy for the feedback by radiation, that is higher intensity corresponds to stronger feedback. The properties of the molecular CO emission were then investigated in these feedback regions.

4.6.2 Molecular gas properties vs 8 μm flux

In this section we investigate how the excitation temperature derived from ^{12}CO emission, the ^{12}CO 3–2/2–1 intensity ratio, and the ^{13}CO column density vary with the degree of feedback traced by the integrated 8μm flux. For this, the regions within a given interval of 8 µm integrated flux were masked.

For every 8 μm flux interval, we investigated the aforementioned properties of the molecular emission of pixels within that mask. Since the GLIMPSE image does not cover the whole range of latitude of the LAsMA map, only the overlapping range of latitude was considered for the analysis. Moreover, the blanked pixels in the excitation map were ignored. A pixel scatter plot was then made for the 8 μm flux versus each of the three properties (see Fig. 4.11). Only those pixels with S/N>5 for all the properties being investigated were considered. This also ensured that the pixels with possible subthermal emission were avoided (these pixels are shown as translucent gray scatter plots in the figure). The color of the scatter points shows the density of points in its vicinity. The mean values of the properties are plotted as a function of 8 μm flux on top of the pixel scatter plot. A power-law function was then fitted to the mean values for all three properties and the results of the fits are also shown in the figure. As is evident from Fig. 4.11 excitation and rotational temperatures increase with increasing 8 μm flux. However, we only see a very modest increase in the median column density values for higher 8 μm flux. Additionally, we also see a set of scatter points that have a much steeper slope between 50 and 150 MJy.sr^{-1} for column density. This appears to be mostly from the regions which are far away from the central stars and receive very little feedback from them. Only one of these regions namely G305.4399+00.2103 is known to be a diffuse H II region in literature (Urquhart et al. 2014a). The other regions could also be prestellar sources collapsing under gravitation and therefore show high column densities. It is beyond the scope of this paper to explore the reason for the observed trend at lower 8 μm flux.

4.7 Dynamics of gas under feedback

In the preceding sections we have investigated the effects of feedback on the morphology of the gas and its excitation. In this section, we investigate the dynamical signature of this feedback. The shape of the spectrum in Fig. 4.4 is the sum of the spectra over all the pixels in the region. As has been seen already, the G305 region consists of various clouds moving at different velocities with respect to us. Additionally, the shape of the profile varies from pixel to pixel.

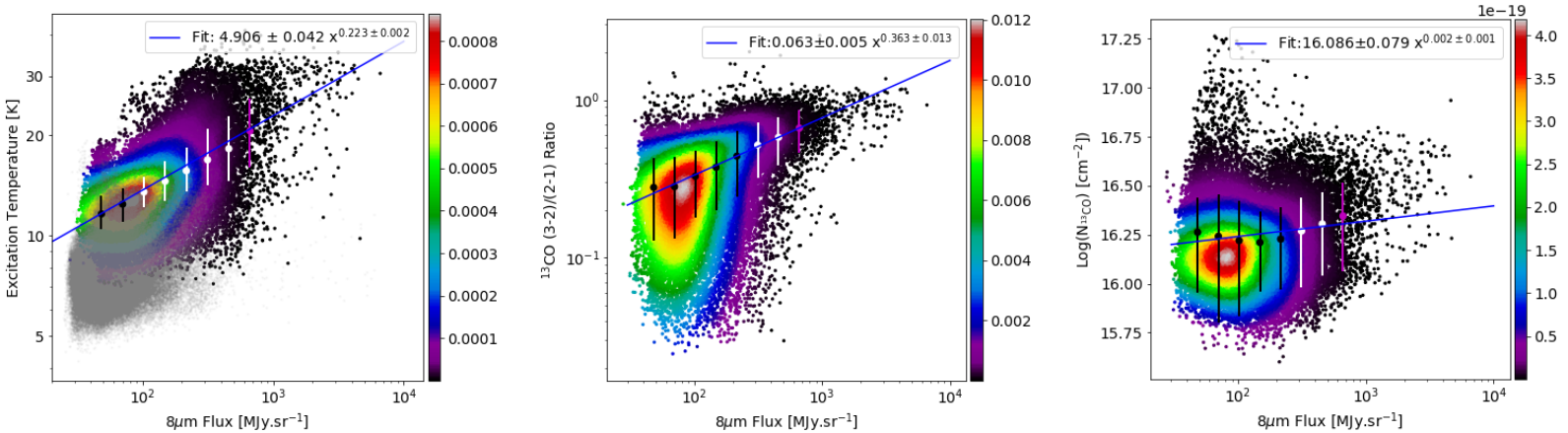

Figure 4.11: Pixel by pixel scatter plot of different gas properties versus 8 μm flux. The colors represent the probability density of the scatter points obtained by a kernel density estimate using Gaussian kernels. Overlaid on top are the mean values of the quantity probed along with their standard deviations plotted as a function of 8 μm flux. The blue line shows the power law fit to the mean values vs 8 μm flux. The results of the fit are shown at the top right corner of each panel. The gray translucent scatter points in the excitation temperature plot (*left*) correspond to the pixels which do not have a corresponding ^{13}CO detection and are not included in the power law fit.

It is impossible to disentangle the contribution of the line centroid velocities and the shape of the line profile from each pixel on the overall shape of the profile in Fig. 4.4. In the following sections, we study these line characteristics in a statistical way.

4.7.1 Velocity centroid probability distribution function

The probability distribution function (PDF) of velocities in observational or simulated datasets can be used to characterize a cloud's velocity structure. PDFs can show the degree of intermittency in the turbulent molecular cloud (Falgarone & Phillips 1990) through the shapes of their wings. Increasing intermittency causes a transition from Gaussian to exponential wings in velocity PDFs. In this section, we estimate the velocity PDF of G305 in order to reveal further effects of feedback on the molecular gas.

It is not possible to know the true velocity PDFs of the clouds from their observations, owing to the fact that the complete velocity information is not available for all three dimensions. Historically, two methods have been employed to deduce the true velocity PDF from observational data of spectral lines: Kleiner & Dickman (1985); Miesch & Bally (1994); Miesch et al. (1999); Ossenkopf & Mac Low (2002) used the distribution of the line centroid velocities to deduce the velocity PDFs. Alternatively, Falgarone & Phillips (1990) estimated the velocity PDFs from high S/N observations of single line profiles. Ossenkopf & Mac Low (2002) tested the realm of validity of both of these approaches and concluded that if the size of the observed map is larger or comparable to the depth of the cloud, the centroid velocity PDF reproduces the correct velocity distribution. In contrast, for small maps, the average line profiles comprise of a more comprehensive sampling of velocities, given their more comprehensive line-of-sight sampling and hence, provide a better approximation to the true velocity structure of the cloud.

The G305 complex is believed to have a flattened geometry (Hindson et al. 2013) in the plane of the sky. Hence, instead of the average line profile shown in Fig. 4.4, the centroid velocity PDF of the complex should be a good tracer of the actual velocity distribution. An added benefit of using the velocity centroid PDFs over using average line profiles is that local phenomena such as outflows that could bias the determination of the global velocity structure do not affect velocity centroid PDFs, since the broad wings of their line profiles leave the centroid velocity unaffected.

The centroid velocity is effectively the moment-1 value of each pixel. Its values were calculated from the ^{12}CO line using the formula,

$$\frac{v_c}{\mathrm{km\,s^{-1}}} = \frac{\sum_{i=1}^{N_{chan}} T_i \cdot v_i}{\sum_{i=1}^{N_{chan}} T_i}\,, \tag{4.9}$$

where N_{chan} is the total number of channels and T_i is the observed antenna temperature of the corresponding channel. Similarly to the moment-0 maps, only channels with signal greater than 5σ were included in the calculation. Once the centroid velocity for each pixel was obtained, the PDF was estimated using a normal histogram (i.e., the sum of the PDF P is normalized to unity). Pixels were partially weighted based on their S/N. Pixels

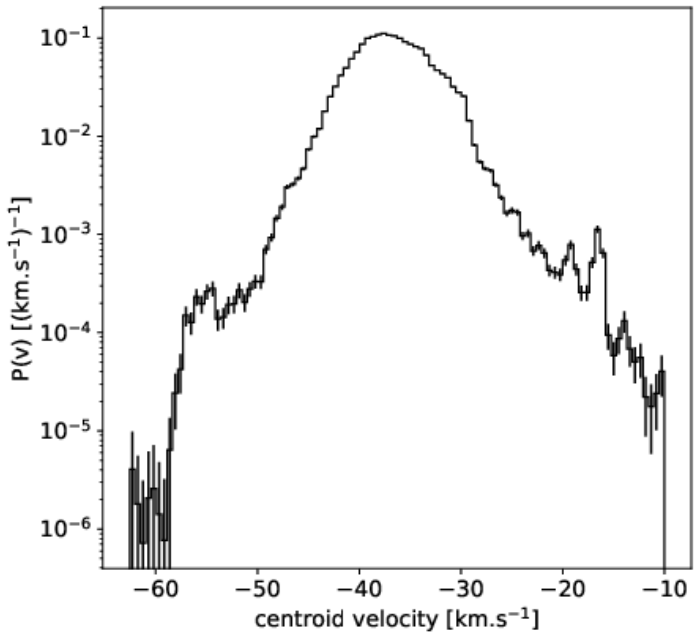

Figure 4.12: Probability density distribution of centroid velocities of ^{12}CO for the G305 molecular cloud complex. The error bars are statistical errors calculated as the square root of the histogram amplitudes.

with a S/N greater than 100 were assigned an S/N of 100 in order to prevent pixels with significant emission, with S/N >, say, 10 (but << 100) to be unreasonably downweighted.

Fig. 4.12 shows the centroid velocity PDF for the G305 complex. The shape of the wings in the velocity PDF suggests that the velocity distribution in the complex is not consistent with a Gaussian which would appear as a parabola on a log-lin plot. To quantify the shape of the distribution we calculate its statistical moments. The most frequently used moments are the mean ($\langle v_c \rangle$), variance (σ^2), and the Kurtosis (K) of the distribution defined as below:

$$\frac{\langle v_c \rangle}{\mathrm{km\,s^{-1}}} = \int_{-\infty}^{+\infty} dv_c P(v_c) v_c \,, \tag{4.10}$$

$$\frac{\sigma^2}{\mathrm{km^2\,s^{-2}}} = \int_{-\infty}^{+\infty} dv_c P(v_c) [v_c - \langle v_c \rangle]^2 \,, \text{ and} \tag{4.11}$$

$$K = \frac{1}{\sigma^4} \int_{-\infty}^{+\infty} dv_c P(v_c) [v_c - \langle v_c \rangle]^4. \tag{4.12}$$

The variance is a measure of the total turbulent mixing energy. The Kurtosis is a measure of the deviation from a Gaussian distribution. It assumes a value of three for a Gaussian distribution and six for a distribution with exponential wings. For our PDF we obtain the following values for the aforementioned moments :

$$\langle v_c \rangle = -37 \pm 7\,\mathrm{km\,s^{-1}}\,,$$
$$\sigma^2 = 4.0 \pm 0.9\,\mathrm{km^2\,s^{-2}}\,, \quad \text{and}$$
$$K = 5.1 \pm 1.0\,.$$

The Kurtosis of 5.1 ± 1.0 indicates that the velocity PDF of the complex has exponential wings. Using two-dimensional Burgers turbulence simulations, neglecting pressure forces, Chappell & Scalo (2001) showed that the velocity PDFs are Gaussian for models of decaying turbulence and have exponential wings for models driven by strong stellar winds.

4.7.2 Stacked spectra

The velocity centroid PDFs as seen in Sect. 4.7.1 contain information only about the central velocity of the gas. In this section, we investigate the effect of feedback on the line profiles of the G305 molecular cloud complex, especially whether the shape of the line profile in the regions where we expect feedback to be present is significantly different from those where we see little evidence of feedback. We also try to characterize the deviations, if any, as a function of the strength of the feedback.

We used the same method as in section 4.6.2 to quantify the strength of the feedback. Different 8 μm intensities were logarithmically distributed. These values were used as a threshold to create masks on the G305 region. Regions with 8 μm flux greater than the threshold were labeled as "inside feedback zone" and those outside were labeled "outside feedback zone". All the maps were reprojected onto the same two dimensional grid over the galactic longitude and latitude. All the spectra were then translated to a common central velocity based on their velocity centroids (see section 4.7.1 for how to calculate the velocity centroids). After aligning, a number of pixels equal to the square root of the total pixels in the respective zones were randomly selected. For these randomly chosen pixels, the spectra were averaged to obtain an average spectrum representing the "inside-" and "outside feedback zones". The spectra obtained by this method will be referred to as average stacked spectrum from now on. This process was then repeated 500 times to avoid any biases and obtain a more representative set of spectra for each region.

Fig. 4.13 shows the stacked spectra corresponding to the "inside-" and "outside feedback zones" for the G305 molecular cloud complex. We also derived a median stacked spectrum for each zone corresponding to all thresholds. This was obtained by calculating the median value for each channel over the 500 iterations performed. A few things become evident from Fig. 4.13. The spectra from the "inside feedback zones" are brighter than "outside feedback zones". With increasing feedback strength the peaks of the former also get brighter indicating that with stronger feedback more gas gets excited to the higher J transitions. There is not much overlap between the individual stacked spectra from the "outside-" and "inside feedback zones".

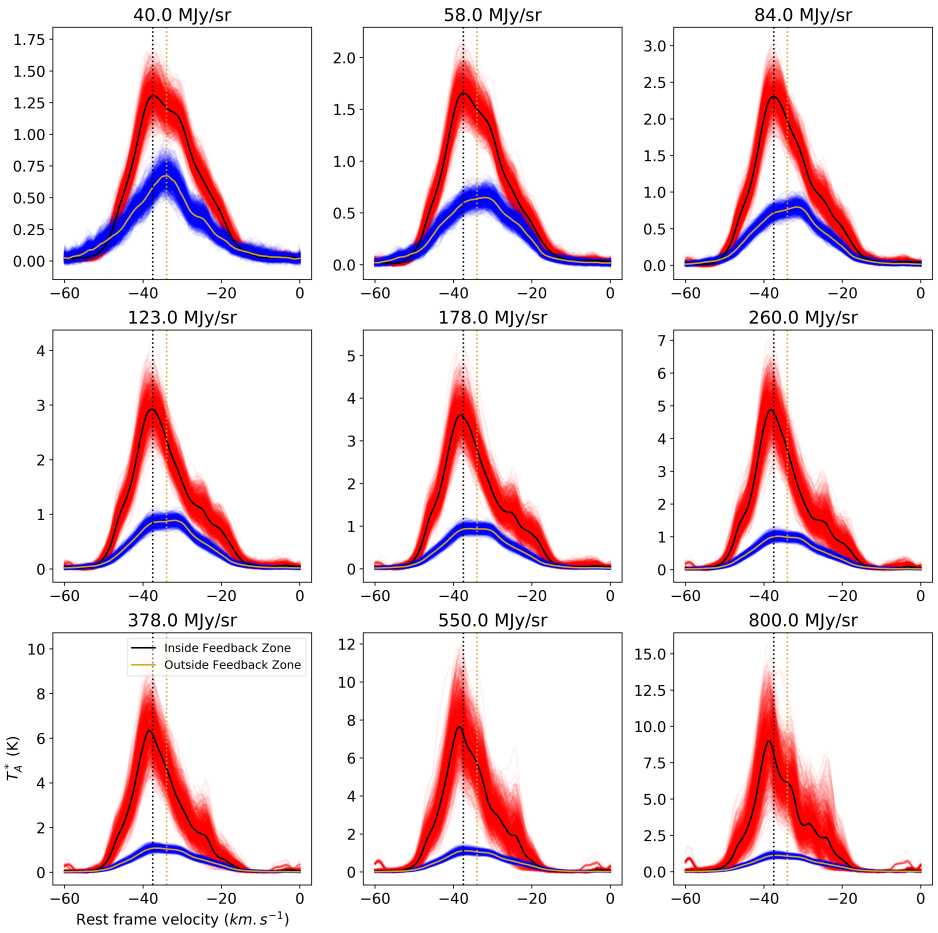

Figure 4.13: Stacked spectra of ^{12}CO(J=3–2) emission corresponding to the "inside-" (translucent red) and "outside feedback zones" (translucent blue) for different choices of GLIMPSE 8 μm flux thresholds (specified on top of each subplot). Each subplot consists of 500 stacked spectra each for both zones obtained by randomly selecting the square root of the total number of pixels from each zone. The black and golden spectra for each zone were obtained by calculating the median value for each channel over the 500 iterations performed. The black (golden) dotted line in all the subplots corresponds to the position of peak emission of the median stacked spectra inside (outside) the feedback zone corresponding to the threshold of 40 MJy sr^{-1}.

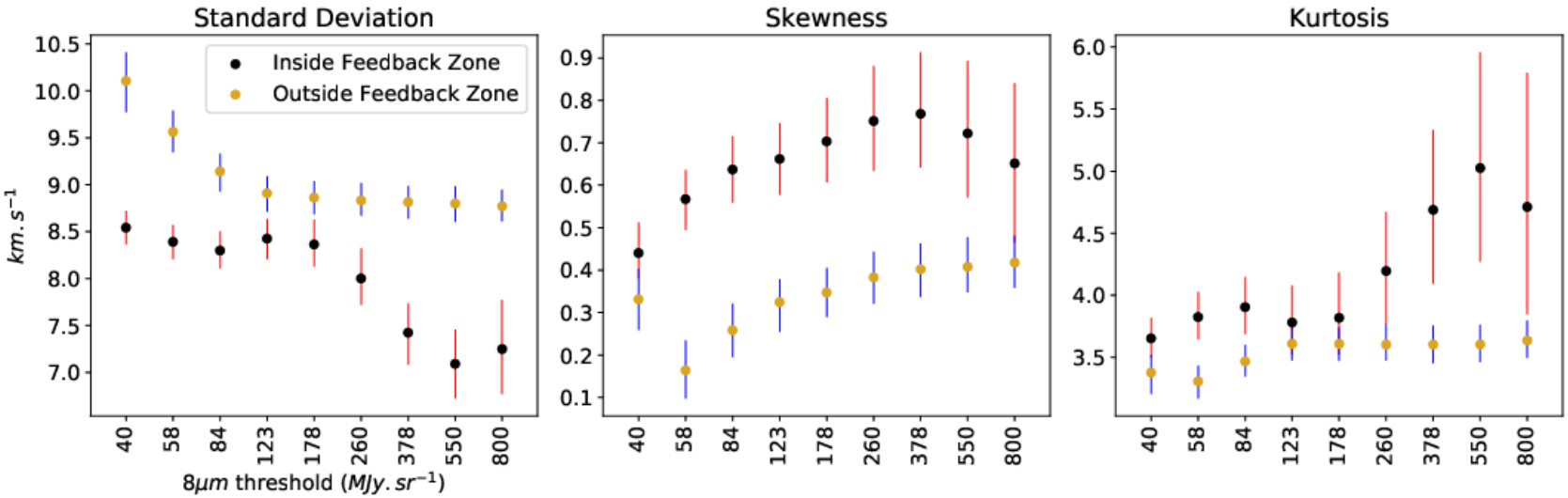

Figure 4.14: Variance (left panel), skewness (middle panel), and Kurtosis (right panel) of stacked spectra corresponding to "inside-" (black dots with red bars) and "outside feedback zones" (golden dots with blue bars) in Fig. 4.13 as a function of GLIMPSE 8 μm flux thresholds. The dots represent the median value and the bars span the 25 to 75 percentile spread of values from the 500 iterations for each threshold value.

Hence, the median profiles for the two regions for each threshold which look very different from each other are indeed representative of the actual differences between the two regions and are not in fact biased by any individual stacked spectra. This was also confirmed by running a Kolmogorov-Smirnov (KS) test (Kolmogorov 1933; Smirnov 1939) between the spectra inside and outside the thresholds. We placed $p < 0.05$ constraint to reject the null hypothesis that the spectra are drawn from the same population. The p-value measures the probability of random chance being responsible for the observed difference between the two spectra.

The test rejected the null hypothesis with overwhelming certainty ($p < 10^{-5}$). The median stacked spectrum from the "inside feedback zones" appear to be blue shifted compared to that from the "outside feedback zones". This is a consequence of the translation of the spectra to a common velocity using their moment-1 values. The spectra inside the feedback zones have a peak component that is at the same velocity as that outside the feedback zone. But in addition, the feedback from the stars seems to have pushed some gas away from us which shows up as the broad positively skewed part of the spectrum inside the feedback zone. This makes the moment-1 value of the overall spectrum to be redshifted from the true peak of the spectrum. Consequently, in the process of aligning all spectra along their moment-1 value, those inside the feedback zone appear to be blue shifted. Thus, the apparent blue shift of the stacked spectra from inside the feedback zone is evidence of the stellar feedback pushing gas away from us.

In order to characterize the stacked spectra in Fig. 4.13 we calculated their statistical moments. The moments used for these profiles are the variance (σ^2), skewness (S), and Kurtosis (K) :

$$\frac{\sigma^2}{\mathrm{km^2\,s^{-2}}} = \left(\int_{-\infty}^{+\infty} dv P(v)[v - \langle v\rangle]^2\right) / \left(\int_{-\infty}^{+\infty} dv P(v)\right), \tag{4.13}$$

$$S = \frac{1}{\sigma^3} \cdot \left(\int_{-\infty}^{+\infty} dv P(v)[v - \langle v\rangle]^3\right) / \left(\int_{-\infty}^{+\infty} dv P(v)\right), \text{ and} \tag{4.14}$$

$$K = \frac{1}{\sigma^4} \cdot \left(\int_{-\infty}^{+\infty} dv P(v)[v - \langle v\rangle]^4\right) / \left(\int_{-\infty}^{+\infty} dv P(v)\right). \tag{4.15}$$

Here, $P(v)$ is the antenna temperature of the spectrum at the velocity v, and $\langle v\rangle$ is the expectation value for the velocity of the spectrum given by $\langle v\rangle = \left(\int_{-\infty}^{+\infty} dv P(v) v\right) / \left(\int_{-\infty}^{+\infty} dv P(v)\right)$ km s^{-1}.

Fig. 4.14 demonstrates how these moments depend on the choice of the 8 μm flux threshold. A few things stand out from this result. We expect turbulence to result in broader line profiles. But contrary to expectations, the variance of the average stacked spectra from the "inside feedback zones" are mostly smaller than that from the "outside feedback zone". For the "outside feedback zones" the variance decreases until ~ 80 MJy sr^{-1} and then stays constant with increasing threshold. Looking at the variances of average stacked spectra for the "inside feedback zones", we observe that the variance stays constant irrespective of the choice of threshold until ~ 180 MJy sr^{-1} when it starts decreasing. We observe that the stacked spectra are consistently more skewed inside the

feedback regions than outside irrespective of the choice of threshold. A positive skewness implies that the profile's red wing is enhanced compared to the blue wing. As explained before, this hints at the gas being pushed away from us. For small threshold values, the stacked spectra in "outside feedback zones" have skewness close to zero. But, it increases with increasing threshold levels. Kurtosis of the stacked spectra in the "inside feedback zones" are mostly larger than those in the "outside feedback zone" indicating that the profiles have more pronounced wings for the gas impacted with feedback. For 8 μm flux thresholds above $\sim$ 180 MJy sr^{-1}, the Kurtosis of the spectra inside the feedback zone increases. For very high threshold values the Kurtosis shows a large spread. These regions correspond to those very close to the UC HII regions and hence show that the feedback in these regions is very effective at pushing gas away. This is also evident from the stacked spectra in Fig. 4.13 where secondary peaks are clearly visible showing gas clumps being pushed out. The Kurtosis of the spectra outside the feedback zone almost stays in the same range. We also observed that the trend followed by the Kurtosis is exactly opposite to the one followed by the variances for both inside and outside feedback zones. When the variances of stacked spectra decrease, the Kurtosis increases and vice versa.

4.7.3 Stacked spectra for 8 μm flux intervals

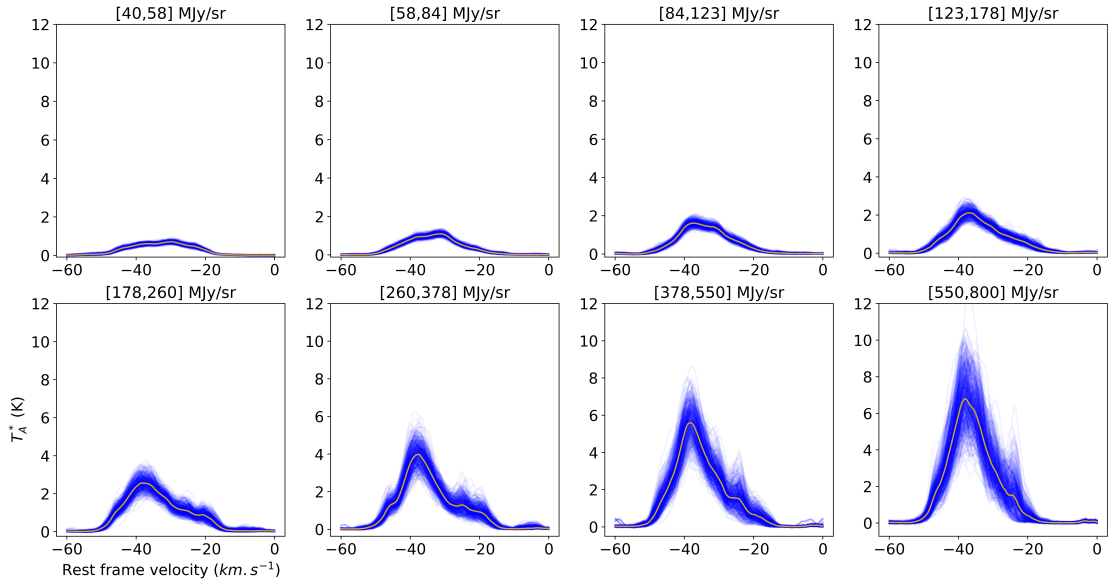

Figure 4.15: Stacked Spectra for regions corresponding to different choices of GLIMPSE 8 μm flux intervals. Each interval subplot consists of 500 stacked spectra (translucent blue), each corresponding to randomly selected pixels from the region. The golden spectra in each subplot corresponds to the median spectra for that interval obtained by taking the median channel intensity for each channel. The interval values are given on top of each subplot.

In the preceding section, the stacked spectra inside the feedback zone for a given threshold include the cumulative sum of the contributions from all pixels with 8 μm flux greater than the threshold value. It becomes difficult to identify the spectra representative of a given interval of 8 μm flux. For this, we decided to investigate the stacked spectra corresponding to intervals of 8 μm flux. Pixels corresponding to the flux intervals were masked and their stacked spectra were derived by randomly picking pixels corresponding to each mask, similar to that done in Sec.4.7.2. The process was repeated 500 times. A median spectrum was derived from the set of 500 stacked spectra corresponding to each mask by taking the median intensity of each channel. Fig. 4.15 shows the stacked spectra corresponding to the pixels in 8 μm flux intervals. The peaks of the profiles do increase with increasing flux as expected. In order to look at their properties, we calculated the statistical moments of each of the stacked spectra using Eq. 4.13 – 4.15. Their median along with the 5 to 95 percentile range of values spanned by the spread were then plotted as a function of the median value of the 8 μm flux interval. Fig. 4.16 shows the statistical moments as a function of 8 μm flux. The standard deviation initially decreases with increasing 8 μm flux but starts increasing with flux from $\sim$ 100 MJy sr^{-1} up until $\sim$ 215 MJy sr^{-1}. After this, the standard deviation of the stacked spectra decreases. The Kurtosis of the stacked spectra show the exact opposite trends to the standard deviation: where if the standard deviation decreases, the Kurtosis increases and vice versa. At the lowest range of probed 8 μm flux the stacked spectra seem to have a skewness approaching 0 and a Kurtosis close to 3, which hints at a Gaussian shape of its profile. The skewness of the stacked spectra then increases to 0.6 for an 8 μm flux of $\sim$ 100 MJy sr^{-1}, while it increases only a little (to 0.8) for higher values, around $\sim$ 600 MJy sr^{-1}.

To investigate possible causes for the trends we find in the statistical moments of the stacked spectra, we plotted the contours of 8 μm flux on top of ^{13}CO integrated intensity map. The relevant 8 μm flux values at which the statistical moments change directions are 84, 123, 178, 260, and 378 MJy sr^{-1}. Fig. 4.17 shows these contours overlaid on top of the ^{13}CO moment 0 map. Almost all of the dense gas traced by the ^{13}CO is contained inside the 123 MJy sr^{-1} contour. We expect the feedback from the central clusters to be deposited on the surface of the dense gas. As we examine the higher flux contours, they appear to surround the HII and UC HII regions in the complex (Hindson et al. 2012). It is possible that the high column density gas surface interacting with the feedback from the central clusters is responsible for the observed increase in skewness and Kurtosis, and the decrease in the standard deviation at $\sim$ 100 MJy sr^{-1}, as this is where we expect the feedback from the central stars to be deposited. As the 8 μm flux increases, the gas is impacted mostly by the stellar winds and ionizing radiation from embedded HII and UC HII regions which appears to be responsible for the increase in skewness as well as kurtosis and quite interestingly, the decrease in the standard deviation of the stacked line profiles. The ^{13}CO emission from our observation suffers from a lack of completeness as we do not sample a lot of low column density gas for a given 8 μm flux.

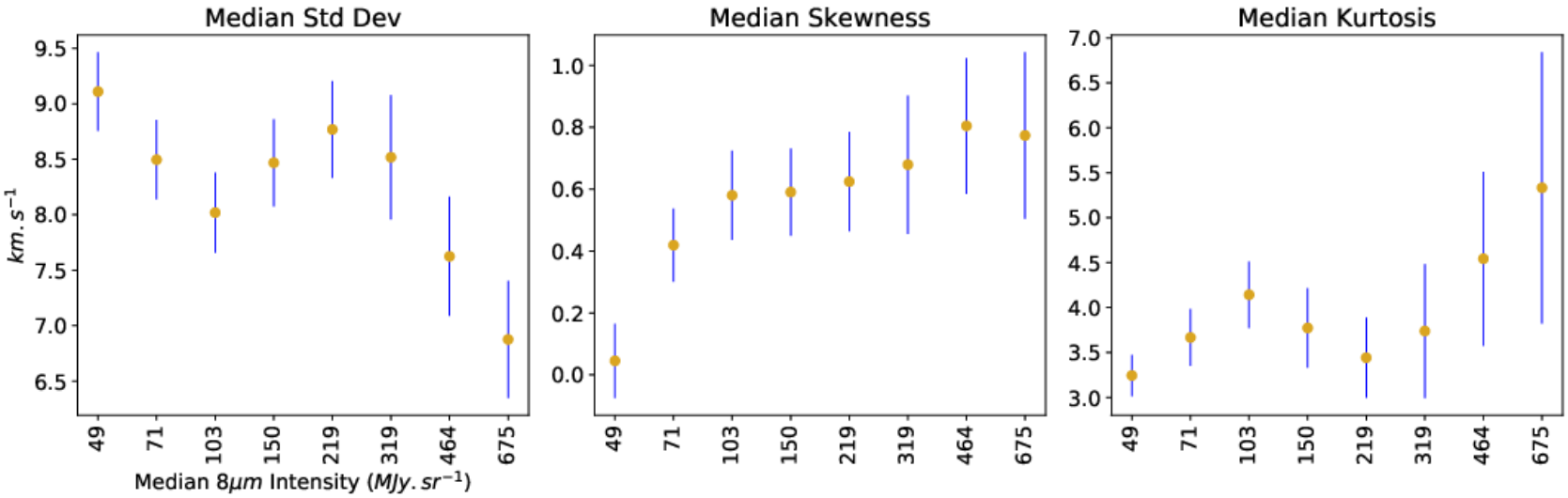

Figure 4.16: Variance (left panel), skewness (middle panel), and Kurtosis (right panel) of stacked spectra corresponding to GLIMPSE 8 μm flux intervals in Fig. 4.15 as a function of the median 8 μm flux for that interval. The golden circles represent the median of the distribution and the blue lines span the 5 to 95 percentile range of values for each set of 500 iterations per interval.

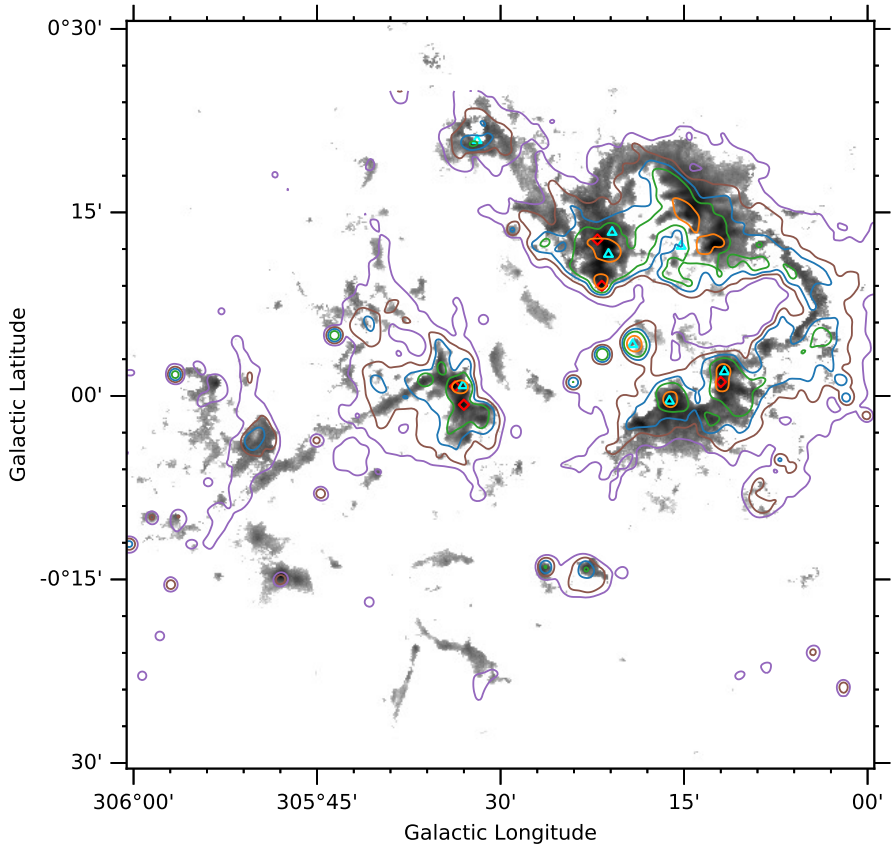

Figure 4.17: ^{13}CO J = 3-2 moment 0 map with GLIMPSE 8 μm contours corresponding to 84(purple), 123(brown), 178(blue), 260(green), and 550.(orange) MJy sr^{-1} overlaid on top. The HII and UC HII regions are marked by cyan triangles and red diamonds respectively.

Most of the spectra outside the masks are dominated by noise. In addition, the wings of the line profiles are also dominated by noise in many cases even when they are significantly detected in ^{12}CO. Since these wings correspond to the gas being expelled, it is difficult to trace them using ^{13}CO. Due to these reasons, it was not possible to repeat the stacked spectra analyses with ^{13}CO lines to gain any further insights into the causes of the observed trends. Examining the literature, we would like to emphasize that apparently this kind of analysis has not yet been performed, neither on any actual nor on simulated observations of molecular cloud complexes undergoing feedback. So far, this is a stand alone result and it needs to be seen if these observed trends in stacked spectra (if real) are unique to G305 or occur in other GMCs as well before making any meaningful speculations on the causes of these trends.

4.8 Summary

We observed the G305 star forming giant molecular cloud with the APEX telescope in the ^{12}CO and ^{13}CO J = 3-2 transitions in order to study the effects of feedback from the

hot, luminous stars at the center of the complex on the molecular gas. We summarize our findings below:

- The central region of the complex has been cleared out of most of the high column density gas as traced by the ^{13}CO emission. The calculations of energy input from the visible stars in the complex showed that they have enough energy input to drive the size of the cavity observed if the electron density (n_e) in the region is less than 500 cm^{-3}. A sequential formation of Danks 2 followed by Danks 1 and the other stars in the complex can explain the size of the observed cavity.

- ^{12}CO excitation temperature and ^{13}CO column density maps of the region were produced under the assumption of LTE. Ratio maps of the rotational excitation were also made using ^{13}CO J = 2-1 data from SEDIGISM and our ^{13}CO J = 3-2 data. The validity of LTE assumption was also tested and it was concluded that regions with simultaneous emission from both ^{12}CO and ^{13}CO are most likely in LTE.

- Excitation temperature maps, as well as ratio maps of the rotational excitation, show that the feedback is being deposited in a narrow region at the edge of the dense gas facing the central stellar complex heating it up. The gas then shows a decline in temperature as one moves away from the center. The column density also shows a marked increase at the edge of the denser gas, but unlike the excitation temperature, does not always decrease drastically as one moves away from the center.

- Line profiles along two directions were chosen at random to test if the energy input from the stars is responsible for this increased excitation of the gas. For the profile toward the north of the complex $\sim$ 61% of the radiation pressure from the nearby stars is being used up to heat and compress the gas at the surface of the cloud; whereas for that toward the south of the complex, $<$ 14.5% of the input radiation pressure from the star is going toward heating the gas.

- The *GLIMPSE* 8 μm flux, which is dominated by FUV-excited PAH emission, was used as a proxy to the feedback strength. The regions with higher 8 μm flux have higher median excitation temperatures, ^{13}CO column density as well as a higher median ^{13}CO J = 3-2/2-1 ratio.

- Investigating the impact of feedback on the dynamics of the gas showed that the centroid velocity probability distribution function of the pixels in the region showed exponential wings indicative of turbulence driven by strong stellar feedback.

- This was followed by stacking the spectra of the pixels and plotting the average stacked profiles. On assuming a certain 8 μm flux threshold, the stacked spectra with 8 μm flux above this threshold (assumed to indicate stronger feedback) showed systematically more skewed line profiles than the stacked spectra representing regions with 8 μm flux less than the threshold. The stacked spectra of regions with stronger feedback on average had narrower but much more winged profiles when

compared to those from regions with weaker feedback. This positive skew is most likely indicative of parts of the cloud complex being pushed away from us, which results in a positive wing of the overall stacked spectra. We also note that the standard deviation and the kurtosis of the stacked profiles show opposing trends when plotted as a function of 8 μm flux.

So, feedback from the OB stars at the center of G305 demonstrates measurable effects on the excitation as well as the dynamics of molecular gas around it.

Chapter 5

G305 giant molecular cloud : II. Effect of feedback on clump properties

This chapter was originally published as a paper titled "High resolution LAsMA ^{12}CO and ^{13}CO observation of the G305 giant molecular cloud complex: II. Effect of feedback on clump properties" in *Astronomy & Astrophysics* (Mazumdar et al. 2021b) [1]. Layout changes were made to adapt to the different print formats. This chapter is an abridged version of the accepted paper, as submitted to the publisher on 26 May, 2021. The appendix in the original publication has been added to the main body of this chapter. And the table made available online via this publication has been added as an appendix to this dissertation.

5.1 Introduction

G305 is one of the most massive and luminous star forming giant molecular clouds (GMC) in the Milky Way (Fig. 5.1). It is located $\sim$ 4 kpc (Clark & Porter 2004; Davies et al. 2012a; Borissova et al. 2019) away from us at $l \sim 305°$, $b \sim 0°$ in the Scutum-Crux spiral arm of the Galactic plane. Its center has been cleared of the interstellar molecular gas by the stellar winds and the ionizing front originating from massive stars belonging to two visible central clusters (Danks 1 and 2) consisting of 21 OB stars and the Wolf-Rayet star (WR48a) (Clark & Porter 2004; Davies et al. 2012a). A diffuse population of evolved massive stars has also been found to exist inside the cavity with ages similar to that of the two clusters (Leistra et al. 2005; Shara et al. 2009; Mauerhan et al. 2011; Davies et al. 2012a; Faimali et al. 2012; Borissova et al. 2019). The central cavity is also filled with ionized gas as shown by radio continuum observations by Hindson et al. (2012). Surrounding the central cavity is a thick layer of molecular gas (Hindson et al. 2010, 2013; Mazumdar et al. 2021a). Star formation tracers (water and methanol masers, HII and ultracompact (UC) HII regions and massive young stellar objects (MYSOs)) have also been reported by multiple studies (Clark & Porter 2004; Hindson et al. 2012; Lumsden et al. 2013; Urquhart et al. 2014a; Green et al. 2009, 2012). Figure 5.1 shows a three-color composite image of G305 highlighting three aspects of the complex. The 21.3 μm Midcourse Space Experiment (MSX) (Lumsden et al. 2013) image is shown in red and traces the hot dust being heated by the OB stars within the cavity and towards the edges where the ionization front is interacting with the surrounding molecular gas. The cold molecular gas traced by the integrated ^{13}CO (3–2) line emission (Mazumdar et al. 2021a, referred to as Paper I from here on) can be seen in

[1] P. Mazumdar et al. 2021, A&A, 656, A101, reproduced with permission from ©ESO

blue being shrouded by emission from the 8 μm filter of the Spitzer Infrared array camera (IRAC) (Churchwell et al. 2009) shown in green. The latter traces the polycyclic aromatic hydrocarbons (PAHs) whose emission is excited by the far-UV photons emanating from the stars in the central cavity.

The role played by feedback from high mass stars ($M > 8\,M_{\odot}$) on their surrounding interstellar medium (ISM) has been a subject of active research. As is the case in G305, these stars exist in massive clusters located inside GMCs (Motte et al. 2018). They inject energy and momentum into their natal clouds via very strong stellar winds, ionizing radiation and eventually, supernovae (Krumholz et al. 2014). Such feedback from OB stars can potentially enhance and/or disrupt the formation of subsequent generations of stars (Krumholz et al. 2014; Deharveng et al. 2010b), consequently playing a vital role in the evolution of GMCs (Zinnecker & Yorke 2007b). The G305 region, being a very extensively studied GMC, is a very good candidate to examine the effects of feedback on the GMC. Although circumstantial evidences of triggering in G305 exists (Clark & Porter 2004; Hindson et al. 2010), it has, as yet, not been definitively proven.

We observed G305 with the Atacama Pathfinder EXperiment (APEX) telescope to examine what effect this feedback from the central population of stars has on the molecular gas content of the GMC (Paper I). The molecular gas in the GMC was mapped in the ^{12}CO and ^{13}CO (3–2) lines. The temperature and column density of the gas facing the center of the cavity was found to be at least a factor of 2 higher than that of the part of the cloud facing away from it, demonstrating that the gas impacted by feedback gets heated and compressed and in turn shields the layers behind it. The rotational excitation of the gas traced by the 3–2/2–1 ^{13}CO line ratios showed similar enhancements at the edge of the cloud facing the center. Using 8 μm flux of the region as a proxy to the feedback strength, we demonstrated that regions experiencing feedback had higher median excitation temperatures, rotational excitation, and column density. Examination of the probability distribution function (PDF) of the centroid velocities revealed exponential wings and a stacked spectral analysis also revealed the emission profiles to be positively skewed (which we hypothesized was indicative of the gas being pushed away from us), all of which is consistent with the hypothesis that star formation has been triggered.

Having investigated the effects of feedback on the GMC as a whole, we are now interested in exploring the effects of feedback on the ability of the GMC to form subsequent generations of stars. GMCs show a hierarchical structure with clouds condensing into clumps that condense and fragment into cores, eventually forming stars (Blitz & Stark 1986; Lada 1992). Since clumps provide the environment and the raw material for star formation, the impact of feedback on the future generation of stars can be studied by their effect on the clump properties in a GMC. In this paper, we will decompose the molecular emission distribution in G305 into clumps and investigate their properties in an effort to study how feedback has affected clump properties and whether the observed star-formation has been triggered.

A broad classification of the effects of feedback on star-formation can lead to three different scenarios which we outline here:

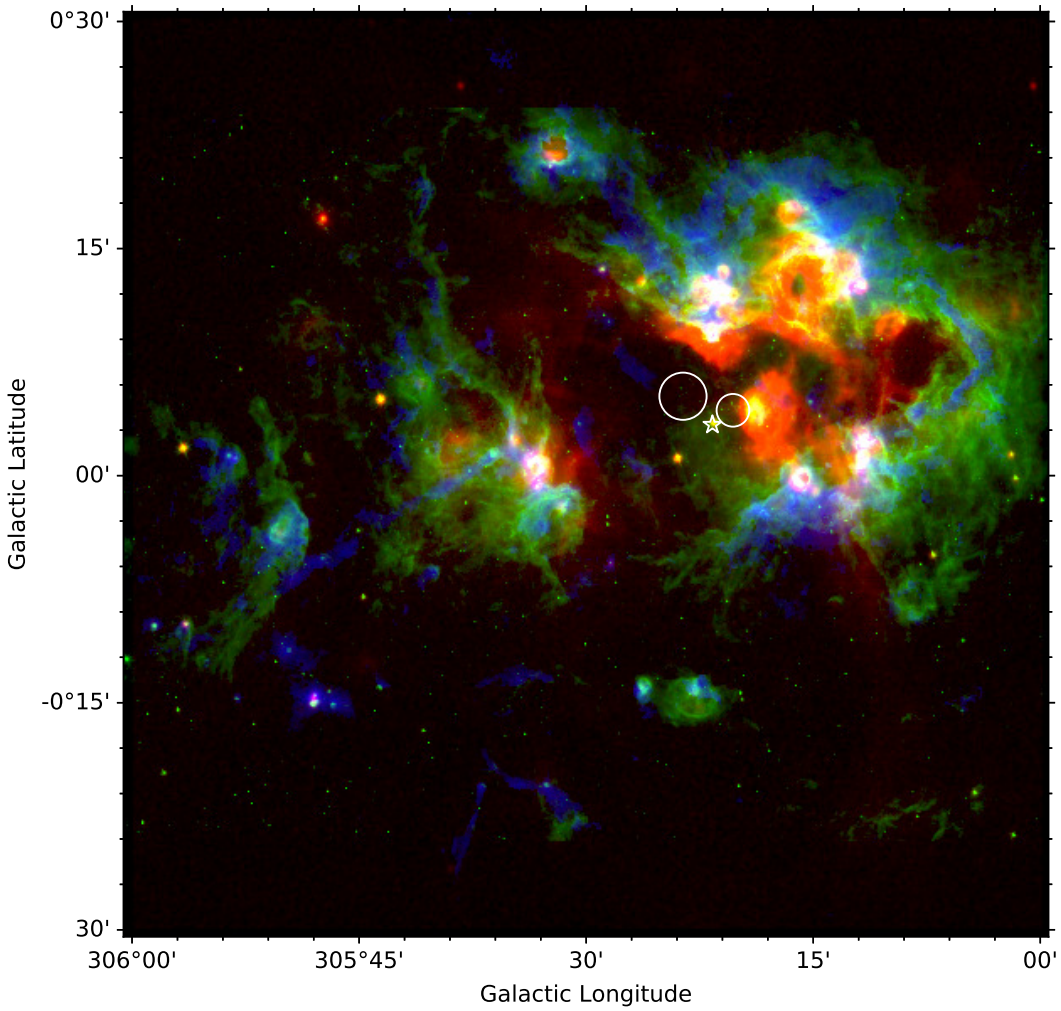

Figure 5.1: Three-color image (green = *Spitzer*-IRAC4 8 μm, red = Midcourse Space Experiment (MSX) 21.3 μm, blue = LAsMA (^{13}CO(3-2) moment-0)) of the G305 star-forming complex. The 21.3 μm emission is dominated by hot dust in the HII region. The colder gas is traced by the ^{13}CO(3-2) line emission. The interface between the ionized and molecular gas appears as a blend of green (strong 8 μm emission from PAHs), blue (colder molecular gas) and occasionally red (interfaces very close to HII regions). The positions of Danks 1 and 2 clusters have been marked with the smaller and the larger white circles respectively, and the wolf-rayet star WR48a has been marked as a white star.

1. Redistribution: The expansion of an HII region simply moves the star forming clumps to its edge. The molecular cloud is already seeded with dense clumps that would collapse to form stars. An apparent enhancement of star formation observed on the periphery of the HII region is not necessarily caused by the HII region. However, overall star formation has not been enhanced. We call this the "redistribution" scenario.

2. Dispersion: In high mass star forming regions feedback is very strong and can simply disperse most of the molecular material via various mechanisms (Krumholz et al. 2014, and references therein), thereby suppressing the ability of the GMC to form stars. We call this "dispersion" scenario.

3. Triggering: In this case, the feedback from the stars actually enhances or induces star-formation in the natal cloud. Many mechanisms are known or hypothesized to be responsible for triggering, e.g. supernovae (de Geus 1992; Nagakura et al. 2009, and references therein), cloud-cloud collisions (for a comprehensive review, see Fukui et al. 2021), collect and collapse (Elmegreen & Lada 1977; Dale et al. 2007), radiation driven implosion (Bertoldi 1989; Bertoldi & McKee 1990; Kessel-Deynet & Burkert 2003; Lee & Chen 2007). In G305, there has been an indication of the "collect and collapse" (C&C) mechanism playing a role in triggering star formation (Hindson et al. 2010). The C&C model was first proposed by Elmegreen & Lada (1977). In this scenario, the expanding warm ionized gas sweeps up a shell of shocked cool neutral gas. This compressed and shocked layer may become gravitationally unstable along its surface on a "long" timescale. This process allows massive dense fragments to form, which quickly fragment in turn leading to the formation of a cluster of stars of roughly the same age. We will therefore concentrate our efforts on testing this specific triggering mechanism in G305.

In this paper we aim to find out which of the three scenarios mentioned above is dominant. Based on observations of NH_3 inversion lines, Hindson et al. (2010) found the concentration of star formation tracers in G305 to be enhanced inside a clump that faces the ionizing sources. The analysis presented in (Hindson et al. 2010) is consistent with a triggering scenario but, the evidence is circumstantial. In order to robustly determine which of the three scenarios presented above dominates, we need to study the statistical properties of clumps, especially those related to star forming properties of the clumps, e.g. their masses, luminosity to mass ratios, surface mass densities. If the feedback is simply moving the clumps around, there should not be any significant difference in the mass distribution function of the clumps in G305 when compared to the Galactic average. For the "disruptive" case we would expect to see fewer clumps and fewer massive clumps. And finally, if triggering is dominant, we expect to see more massive clumps when compared to the Galactic average and, in case of an increased star forming efficiency, a higher luminosity to mass ratio.

We discuss the observations and methods of data reduction in Sec. 5.2. In Sec. 5.3, we introduce the ancillary survey data used to aid our analysis. Sec. 5.4 and 5.5 explains the

details of the clump extraction method and how their properties were estimated. Sec. 5.6 explores the effect feedback has on certain clump properties and how this may support or reject different scenarios presented in this section. In Sec. 5.7 we compare the properties of G305 clumps with the average Galactic sample to provide support for one of the three scenarios. Finally, Sec. 5.8 presents the summary of our findings.

5.2 Observations and Data Reduction

The Atacama Pathfinder Experiment (APEX) (Güsten et al. 2006) telescope[2] was used to observe the 1 squared degree region spanning a longitude range $305° < l < 306°$ and latitude $-0.5° < b < 0.5°$. The Large APEX sub-Millimeter Array (LAsMA) receiver (Güsten et al. 2008) was used to observe the $J = 3-2$ transitions of ^{12}CO ($\nu_{\rm rest} \sim 345.796$ GHz) and ^{13}CO ($\nu_{\rm rest} \sim 330.588$ GHz) simultaneously.

The details of the observations, calibrations as well as data reduction have been described in Paper I. Here we briefly summarize the whole process. The local oscillator frequency was set at 338.190 GHz in order to avoid contamination of the ^{13}CO (3-2) lines due to bright ^{12}CO (3-2) emission from the image band. The whole region was observed using a position switching on the fly (OTF) technique in perpendicular directions in order to avoid systematic scanning effects. The data was calibrated using a three load chopper wheel method, which is an extension of the "standard" method used for millimeter observations (Ulich & Haas 1976) to calibrate the antenna temperature T_A^* scale. The data was reduced using the GILDAS package[3]. Baseline subtraction was done on each spectrum after masking the velocity range -150 km s^{-1} to 50 km s^{-1} in order to avoid fitting emission features. The average of all the spectra was then used to mask the channels containing line emissions and baseline fitting was repeated to obtain a cleaner and flatter baseline. The resulting reduced spectra were then gridded with a 6″ cell (referred to as a pixel from now onward) and convolved with a Gaussian kernel with a full width at half maximum (FWHM) size of one-third of the telescope FWHM beam width. The final datacube has a spatial resolution of $\sim 20''$, and a velocity resolution of 0.5 km s^{-1}. In order to obtain the rms noise, the standard deviation was calculated over a range of 100 emission-free spectral channels for each pixel. Fig. 5.2 shows the distribution of the noise in the G305 region for both ^{12}CO and ^{13}CO lines. The noise distribution peaks at 0.13 K for ^{12}CO and 0.29 K for ^{13}CO . These values were therefore adopted to be the rms noise (referred to from now as σ_{noise}) for each map.

5.3 Ancillary Data

In order to compare and analyze G305 clump properties with the Galactic clumps, we have used the clump catalogs from the ATLASGAL (Schuller et al. 2009; Contreras et al. 2013; Urquhart et al. 2014b) and CHIMPS (Rigby et al. 2016) surveys. The Galactic

[2]This publication is based on data acquired with the Atacama Pathfinder EXperiment (APEX). APEX is a collaboration between the Max-Planck-Institut für Radioastronomie, the European Southern Observatory and the Onsala Space Observatory.

[3]http://www.iram.fr/IRAMFR/GILDAS

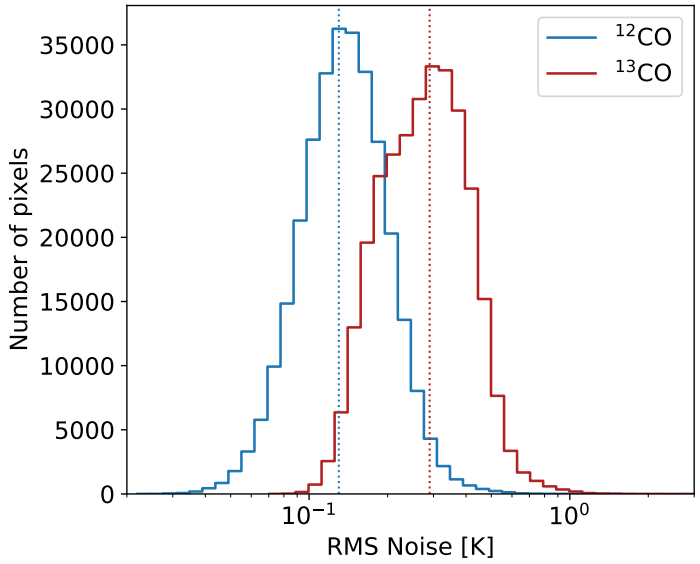

Figure 5.2: Histogram distribution of rms noise values for the LAsMA map of the G305 region. The ^{12}CO map's distribution peaks at 0.13 K and that of ^{13}CO peaks at 0.29 K as indicated by the blue and red dotted lines respectively.

clumps derived from the ATLASGAL survey (Urquhart et al. 2018) have the advantage of having a similar resolution as the LAsMA data (19″). Additionally, there is a good agreement in the sensitivity between the ATLASGAL data and the ^{13}CO intensity map as can be seen in Fig. 5.3. The sensitivity to column density of both the data sets are also very similar with LAsMA tracing column densities down to $\log(N(H_2)[cm^{-2}] \sim 21.46$ (see Paper I) and ATLASGAL being sensitive to clumps with column densities down to $\log(N(H_2)[cm^{-2}] \sim 21.5$ (Schuller et al. 2009; Urquhart et al. 2018). On the other hand, CHIMPS survey uses the same spectral line (^{13}CO(3-2)) used in our survey, which makes the comparison of properties more straightforward. But the clumps extraction from CHIMPS survey has been done on a smoothed dataset of resolution $\sim$ 27″ (Rigby et al. 2019). Hence, in order to compare the properties of the G305 clumps with the CHIMPS Galactic clumps, we created an additional smoothed datacube and repeated all the analysis that follows in parallel. While creating this new dendrogram, a structure was now considered independent only if it were at least the size of the new beam. All comparisons of properties with the CHIMPS clumps shown in this paper are based on the smoothed datacube.

In order to compare the properties of G305 clumps with any Galactic sample, similar spatial scales are more important than similar angular resolution. Therefore, a distance limited sample ($3.5 < d < 4.5$ kpc) of Galactic clumps has been used for comparison with clumps in G305. All references to the Galactic sample of clumps in this paper implicitly imply this distance limited sample. For the CHIMPS survey, it is possible to choose a different range of distances to avoid smoothing our dataset in order to compare similar clump sizes. But that leads to fewer clumps in the CHIMPS sample (factor 1.5 fewer

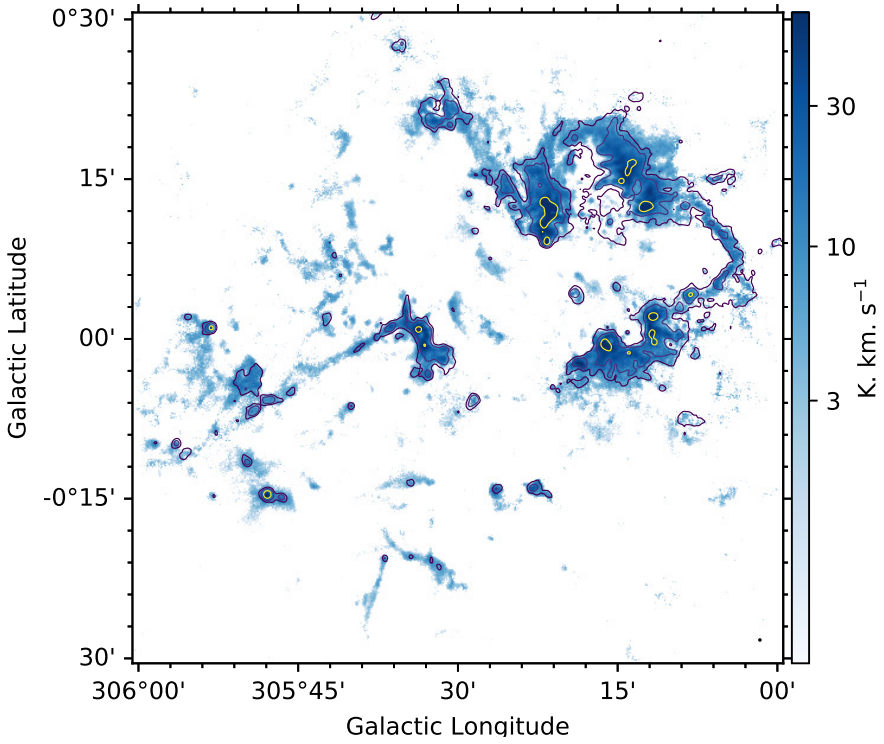

Figure 5.3: ^{13}CO(3-2) moment-0 map of the G305 region. Overlaid on top are the contours of ATLASGAL corresponding to intensities 0.6, 1 and 3 Jy/beam.

clumps). Therefore, the former method was adopted for comparison with the CHIMPS sample.

5.4 Extracting clumps: Dendrogram

The clump catalog was created using the dendrogram analysis developed by Rosolowsky et al. (2008). It decomposes the intensity data cube into a nested hierarchy of structures called leaves, branches and trunks. The leaves are the highest lying structures (with the brightest intensity) in this hierarchy and they generally represent the resolution element achievable by the survey designs. They consist of a collection of isocontours that contain only one local maximum within them. Branches are the structures that contain other leaves and branches inside them and trunks are the largest contiguous structures at the bottom of this hierarchy. Trunks by definition could also be leaves that are single isolated structures without any parent structure. Hence each structure is identified by `astrodendro` as either a leaf or a branch depending on whether it has a lower hierarchy of structures under it.

The dendrogram algorithm `astrodendro`[4] was run on the data cube in position-

[4]astrodendro is a Python package to compute dendrograms of Astronomical data (`http://www.dendrograms.org/`).

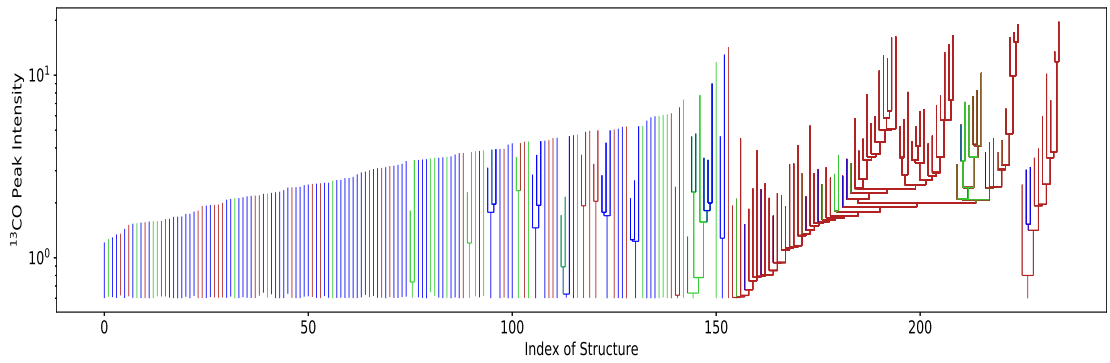

Figure 5.4: Dendrogram of G305 on ^{13}CO spectral cube. The structures that show greater than ~ 67% overlap with the 8 μm mask (regions with 8 μm flux greater than 100 MJy/sr representing molecular gas influenced by feedback from the central star clusters in G305.) are colored red; those with partial overlap (between 10 - 67%) are colored green; and the structures with less than 10% overlap with the 8 μm mask are colored blue.

position-velocity (ppv) space. A lower limit (min_value) of $5\sigma_{noise}$ was set to avoid getting structures with peak intensity below the noise threshold. Additionally, a structure was considered independent only if its peak intensity differed by at least $5\sigma_{noise}$ from the nearest local maximum (min_delta). Each structure was required to have an area equal to the area of the beam to be considered real. In the velocity space a minimum width of 4 channels (= 2 km s^{-1}) was implemented to prune (get rid of unwanted structures due to noise in the data) the dendrogram. Figure 5.4 shows the resulting dendrogram of the ^{13}CO data cube. The branching shows the fragmentation of a cloud into smaller and denser clumps.

5.5 Catalog of clump properties

Once the dendrogram was created, the `astrodendro` package was used to create a catalog of some basic properties of all the structures. These include their positions, mean and RMS velocities, total fluxes and the projections of their major and minor axes (called $\sigma_{\rm maj}$ and $\sigma_{\rm min}$) on the position-position plane (Rosolowsky & Leroy 2006). The radius of the clumps is defined by $R_{\rm eq} = \eta * \sqrt{\sigma_{\rm maj} * \sigma_{\rm min}}$, where η is a factor that relates the radius of a spherical cloud to its one dimensional RMS size $\sqrt{\sigma_{\rm maj} * \sigma_{\rm min}}$. For consistency with Solomon et al. (1987); Rosolowsky & Leroy (2006); Colombo et al. (2019); Rigby et al. (2019) we adopt the value $\eta = 1.91$. The velocity dispersion (σ_v) is calculated as the intensity weighted second moment of the velocity axis. The flux of the region is the sum (zeroth moment) of all the emission in the region. The physical radius of the clumps and their luminosities were calculated using $R_{\rm pc} = Rd$ and $L = Fd^2$ respectively, where $d = 3.8$ kpc is the distance to G305 (Clark & Porter 2004; Borissova et al. 2019).

Masses of the clumps were calculated using the column density maps. Sect. 4 of Paper I describes in detail how the column density map was obtained for the region. We

present a brief summary of the method here. Assuming that ^{12}CO is optically thick, the excitation temperature T_{ex} of each pixel in the position-position-velocity space (referred to from now onward as voxel) was calculated under the assumption of local thermodynamic equilibrium (LTE). Then, the ^{13}CO optical depth was derived for each voxel from the excitation temperature obtained from ^{12}CO and the ^{13}CO intensity. Subsequently, the ^{13}CO column density for each voxel was calculated using the derived excitation temperature and optical depth. Since the column density derived is only available for those pixels with a significant emission in ^{13}CO , all the properties calculated (and consequently all discussions about the clump properties) from here on are only applicable to the clumps extracted from the dendrogram of the ^{13}CO map of the region. As mentioned in Sec. 5.3 this has the added advantage of having a similar sensitivity to ATLASGAL data as well as using the same transition as the CHIMPS survey.

The column density over all the voxels corresponding to each clump in the dendrogram were added and the mass of the structure was then calculated using the equation:

$$M = \mu\, m_p\, R_{13}^{-1} \sum_{lmv} N_{13}(\mathrm{total})_{\mathrm{lbv}}\, \Delta\mathrm{x}\Delta\mathrm{y} \tag{5.1}$$

where μ is the mean mass per H_2 molecule, taken to be 2.72, accounting for a helium fraction of 0.25 (Allen 1973), m_p is the mass of a proton, R_{13}^{-1} is the abundance ratio of H_2 compared with ^{13}CO, and Δx and Δy are the resolution element in parsec calculated using the distance of the source and the resolution element. The conversion R_{13}^{-1} is calculated in two steps, and we adopt a ratio of R_{12}/R_{13} that varies as a function of Galactocentric distance as prescribed by Milam et al. (2005), and a value of $R_{12} = 8.5 \times 10^{-5}$ (Frerking et al. 1982) is adopted for all sources. R_{12}/R_{13} has a value of approximately 59.7 for G305's Galactocentric distance of 6.6 kpc.

The masses of the clumps and their radii were also used to calculate their density($n(H_2)$) and surface mass densities using:

$$n(H_2) = 15.1 \times M/(4/3\,\pi R_{\mathrm{eq}}^3) \tag{5.2}$$

$$\Sigma = M/\pi\, R_{\mathrm{eq}}^2 \tag{5.3}$$

Here M is in $\mathrm{M}_\odot$, R_{eq} is in pc, $n(H_2)$ is in cm^{-3}, and Σ is in $\mathrm{M}_\odot/\mathrm{pc}^2$. The factor of 15.1 is to convert the density to appropriate units.

The dynamical state of the clumps, i.e. whether they are gravitationally stable, collapsing or dissipating is examined using the virial theorem. With only gravitational forces the virial theorem reads $2K + \Omega = 0$ where K is the kinetic energy and Ω is the gravitational energy. The virial parameter is defined as the ratio of the virial mass of a spherically symmetric cloud to its total mass as given below:

$$\alpha_{\mathrm{vir}} = \frac{3\sigma_{\mathrm{v}}^2 R_{\mathrm{eq}}}{GM}. \tag{5.4}$$

Here, σ_{v} is the velocity dispersion of the clump and G is the gravitational constant.

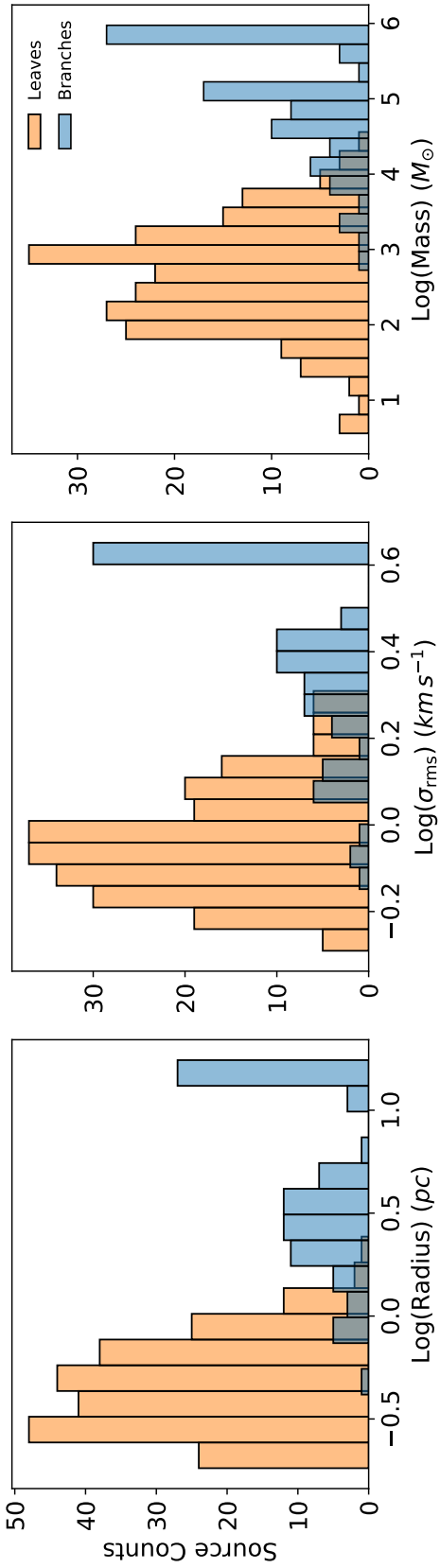

Figure 5.5: Comparison of radii (left), velocity dispersions (center), and masses (right) of leaves and branches in G305.

This is the definition used by MacLaren et al. (1988). We also assume a spherical density distribution $\rho(r) = 1/r^2$. In the absence of pressure supporting the cloud, $\alpha_{\rm vir} < 1$ means that the cloud is gravitationally unstable and collapsing whereas for $\alpha_{\rm vir} > 2$ means that the kinetic energy is higher than the gravitational energy and hence the cloud is dissipating. A value of $\alpha_{\rm vir}$ between 1 and 2 is interpreted to be an approximate equilibrium between the gravitational and kinetic energies. A cloud undergoing gravitational collapse can also show $\alpha_{\rm vir} \sim 2$ as the rapid infall can manifest as a large velocity dispersion (Kauffmann et al. 2013).

The dendrogram resulted in a total of 337 structures of which 235 (69.73%) are leaves, 102 (30.27%) are branches. Fig. 5.5 shows properties of leaves and branches to demonstrate their differences. Table 5.1 shows 20 randomly selected clumps in the G305 giant molecular cloud. The whole table for all the structures has been provided in the Appendix A.

5.6 Effect of feedback on G305 clumps

The radiation and ionization front from the OB stars in the central cavity can affect the masses as well as the velocity dispersion of the clumps in G305. It can inject turbulence which should manifest as broad linewidths of the clumps. It can also compress and destabilize the clumps resulting in an increase in their surface mass densities.

5.6.1 Insufficient velocity resolution

Before we investigate the effects of feedback on the linewidths of clumps we first calculate whether we possess enough resolution in velocity to discern any differences that might occur in their linewidths due to feedback.

Assuming that the observed width of a clump is solely attributed to its turbulence, we can write the turbulent pressure in a clump as,

$$P_{\rm NT} = n({\rm H_2}) m_{\rm H_2} \sigma^2 / k \,, \tag{5.5}$$

where k is the Boltzmann's constant and σ is its velocity dispersion in one-dimension. If all the turbulent pressure is being delivered to the clumps by the stars in the center of G305 then $P_{\rm star} = P_{\rm NT}$, where $P_{\rm star}$ is given by,

$$P_{\rm star} = Q(H^0)\langle h\nu \rangle / 4\pi d^2 c k \,, \tag{5.6}$$

where $Q(H^0)$ is the number of H ionizing photons per second emitted by the stars, $\langle h\nu \rangle$ is the mean photon energy of an O-star ($\sim$ 15eV Pellegrini et al. (2007)), d is the distance of the star (cluster) from the cloud surface, and c is the speed of light. It is tricky to calculate $P_{\rm star}$ given that the distance to each cloud is different and the stars are also not localized.

Table 5.1: Properties of the 20 randomly selected structures (leaves and branches) derived from the ^{13}CO dendrogram of G305.

Catalog Index	Structure Type	x_c	y_c	Radius	v_{rms}	log(Lum)	log(Mass)	α_{vir}	$\log(n(H_2))$	$\log(\bar{F}_{8\,\mu m})$
		(°)	(°)	(pc)	(km s^{-1})	(K km s^{-1} pc^2)	($M_\odot$)		(cm^{-3})	(MJy/sr)
18	branch	305.284	0.161	13.8	4.0	3.54	5.77	0.26	2.9	2.36
24	branch	305.804	-0.235	2.5	1.9	2.18	4.37	0.25	3.76	1.74
28	branch	305.222	0.119	10.7	4.5	3.3	5.54	0.43	3.0	2.39
53	branch	305.284	0.161	13.8	4.0	3.54	5.77	0.26	2.91	2.36
60	branch	305.246	-0.014	2.5	1.9	2.48	4.72	0.12	4.09	2.52
67	leaf	305.231	-0.025	0.7	0.7	1.52	3.77	0.05	4.7	2.35
84	branch	305.865	-0.045	4.2	1.4	2.43	4.54	0.17	3.21	2.02
86	leaf	305.612	0.143	0.8	1.8	0.99	3.69	0.35	4.58	1.8
116	leaf	305.175	0.254	0.5	0.9	0.01	1.66	5.67	3.21	2.15
119	leaf	305.223	0.324	0.6	1.0	0.54	2.68	0.82	3.95	2.06
123	leaf	305.928	-0.1	0.3	1.2	0.05	2.02	2.35	4.33	1.7
129	leaf	305.208	0.141	0.6	0.7	0.72	2.88	0.31	4.09	2.1
137	branch	305.576	-0.006	4.4	2.1	2.72	4.91	0.17	3.53	2.4
159	branch	305.361	0.2	1.0	2.3	1.99	4.23	0.21	4.81	2.99
187	branch	305.564	0.002	2.3	1.8	2.42	4.61	0.12	4.09	2.53
249	leaf	305.67	0.025	0.6	1.5	0.71	2.74	1.62	3.95	2.29
267	leaf	305.552	-0.055	0.7	1.2	1.16	3.47	0.23	4.49	2.29
272	leaf	305.681	0.307	0.9	0.9	1.14	3.65	0.13	4.3	1.91
292	leaf	305.493	0.01	0.3	0.8	-0.28	1.84	1.71	4.11	1.82
321	leaf	305.28	-0.153	0.6	1.0	0.32	1.86	5.77	3.1	1.76

Notes. The full table has been made available electronically.

But in order to obtain an upper limit on the value of $P_{\rm star}$ we assume the total ionizing radiation of Danks 1 and 2 combined. In Danks 1 we have 2 O8-B3 and 1 O8-B3I stars for which we adopt the value corresponding to 3 O8V stars from Table 2 of Panagia (1973). Similarly, we use O4V values for the 3 O4-6 stars, O6V values for the O6-8 and 2 O6-8If stars. For the 3 WNLh stars we adopt the value corresponding to WN-3w from table 2 of Crowther (2007). Therefore for Danks 1 we have a maximum ionizing flux equal to $3.67 \times 10^{50}\,{\rm s}^{-1}$. For Danks 2, there are 3 O6 (O6-8), 4 O8 (O8-9 / O8-B3I), and 1 WC7 (WC7-8) stars (we have ignored the F8-G1 star). Assuming all these belong to class V, we get $8.03 \times 10^{49}\,{\rm s}^{-1}$. Hence, Danks 1 and 2 have a combined maximum Lyc photon output of $4.473 \times 10^{50}\,{\rm s}^{-1}$. The value of d is assumed to be 4 pc which is approximately the closest distance of clumps in the northern and southern complex to the Danks cluster. Plugging these into Eq. 5.6, we obtain a value of $P_{\rm star} \sim 1.36 \times 10^6\,{\rm K\,cm}^{-3}$. This corresponds to a velocity dispersion of $\sigma = 1.06\,{\rm km\,s}^{-1}$ given an H_2 density of $10^4\,{\rm cm}^{-3}$. Since our dataset has a velocity resolution of $0.5\,{\rm km\,s}^{-1}$, it is difficult to discern the effects of feedback on the velocity dispersion of the clumps, which will realistically be much smaller than $\sim 1\,{\rm km\,s}^{-1}$.

The linewidths of the clumps were plotted as a function of the 8 μm flux and no dependence was observed between the linewidths of the clumps at the highest hierarchical level (leaves) and the strength of the feedback on the clumps supporting our claim (see Fig. 5.6. The branches, however, do show a positive correlation with the 8 μm flux. This could be the result of the size versus linewidth relationship of the clumps. On dividing the linewidths by the size of the structures (Heyer et al. 2009) the leaves still do not show any strong dependence of this property on the incident 8 μm flux. But the branches do have a weak positive dependence on the incident 8 μm flux. This indicates that at larger scales, feedback from the stars does inject turbulence into the GMC. Similar results were also seen in Paper I where the stacked spectra showed a positive dependence of their skewness and kurtosis on the incident 8um flux.

5.6.2 Surface mass densities of clumps vs 8 μm

In Paper I we discussed the role of the Galactic Legacy Infrared Mid-Plane Survey Extraordinaire (GLIMPSE: Benjamin et al. 2003; Churchwell et al. 2009) 8 μm continuum map as an indicator for feedback strength. As a proxy to the strength of feedback on each clump, we calculated the average 8 μm flux over each clump. For this, a mask was extracted for each structure by projecting it onto the position-position plane and the 8 μm flux was averaged over the mask. Table 5.1 also shows the mean 8 μm flux associated with each structure.

A significant issue with this analysis is that the 8 μm map is a 2 dimensional projection on the plane of G305 and hence it is possible for clumps to appear to be affected by feedback just because of their projection. In order to test whether the associated 8 μm fluxes actually correspond to the clumps we first compared the morphology of the 8 μm emission with the ^{13}CO integrated intensity map. Fig. 5.7 shows the GLIMPSE map with the ^{13}CO integrated intensity contours overlaid on top. There exists a very good

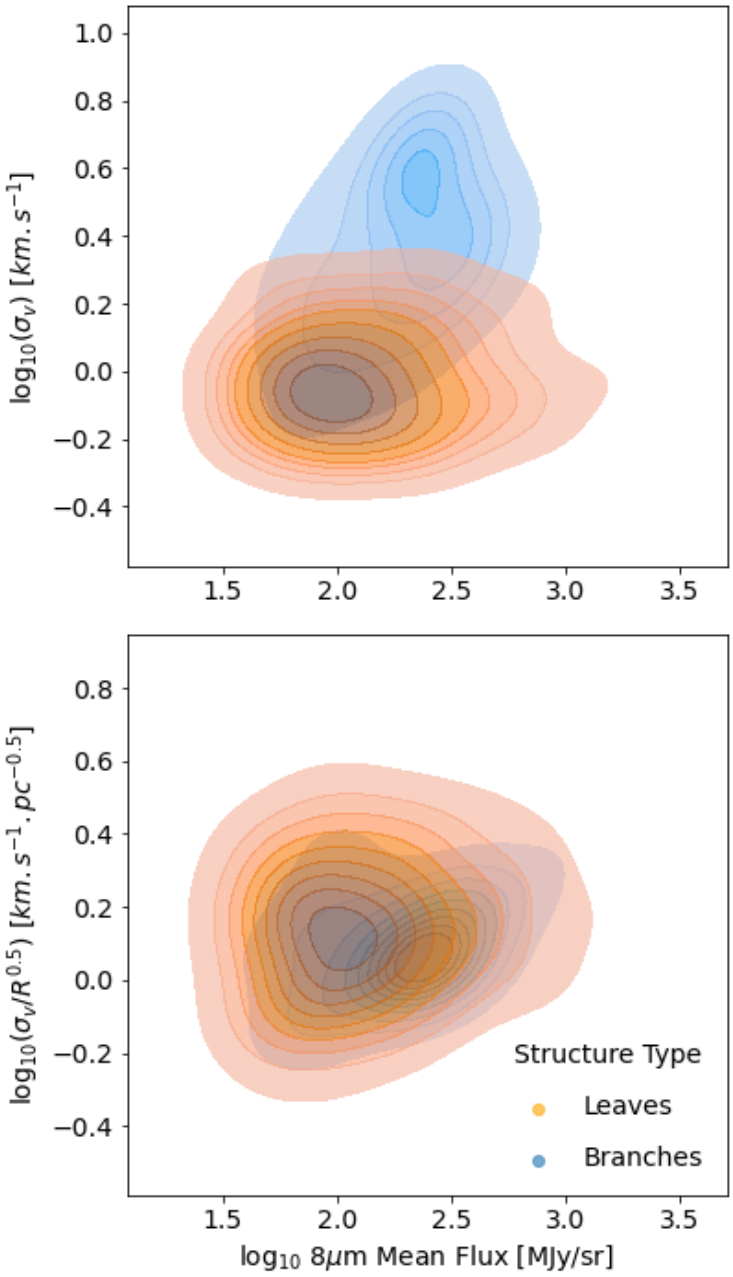

Figure 5.6: Linewidths for G305 clumps as a function of the incident 8 μm flux.

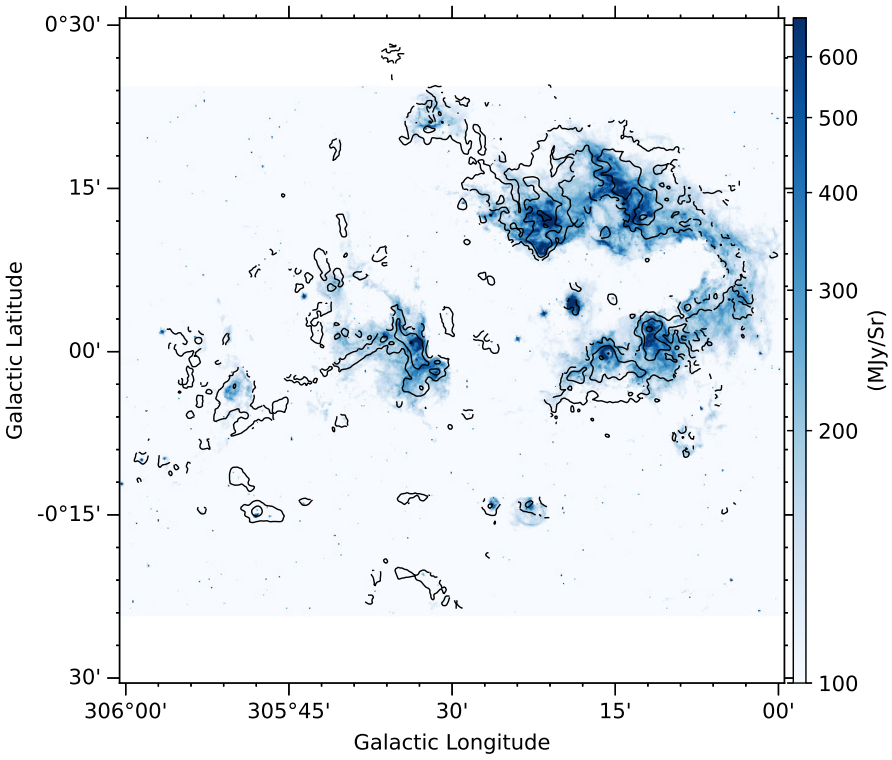

Figure 5.7: GLIMPSE 8 µm map of the G305 regions. The black contours correspond to the ^{13}CO J=3–2 integrated intensities of 5(5σ), 20(20σ) and 80 (80σ) K km s^{-1}.

correlation between the two. So, we safely assume here that all the 8 μm emission is originating in G305. We then investigated whether any leaves in the dendrogram had the same position but different velocities along the line of sight. We found only about 1% of the leaves ($\sim$ 7% if branches are included) had positions within one beam size distance of another leaf (or branch). Additionally, Hindson et al. (2013) looked at the morphology of the molecular gas emission and argued that the G305 complex has a flattened geometry instead of a spherical structure. Taking these factors into consideration, one can safely ignore the effects of projection on the associated 8 μm fluxes for the clumps.

Fig. 5.8 shows the two-dimensional kernel density estimate (KDE) distribution of the clump surface mass density as a function of 8 μm flux. The leaves and branches of the dendrogram have been plotted separately. We observe that the surface mass density of the clumps increases with increasing 8 μm flux indicating that in regions of stronger feedback the clumps are more massive. A positive correlation between the surface mass density of the clumps and the incident 8 μm flux is indicative of triggering in G305. In the "redistribution" scenario we would have expected no correlation between the two quantities and in the case of the "disruptive" scenario one should observe a negative correlation.

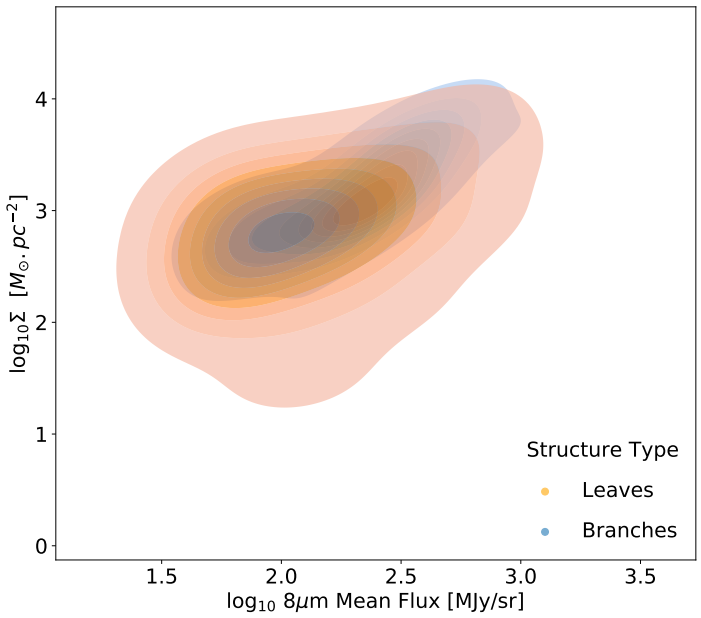

Figure 5.8: Surface mass density of clumps in G305 as a function of 8μm flux.

5.6.3 Inside and outside the feedback zone

The analysis described in the previous subsection motivated us to follow an approach similar to that presented in Paper I. Based on an 8 μm threshold a "feedback zone" was defined as the pixels with 8 μm flux larger than the threshold. The value of this threshold was chosen to be 100 MJy/sr corresponding to the first inflection point in Fig. 15 of Paper I. We believe this contour corresponds to the isosurface where the stellar feedback gets deposited first. Then each clump was assigned a tag depending on the extent of its overlap with the "feedback zone". Clumps with more than 67% overlap with the "feedback zone" were tagged "Mostly Inside"; those with an overlap between 10 and 67% were tagged "Partly Inside", and those with less than 10% overlap with the "feedback zone" were tagged "Outside". This classification is not based on any physics but in order to aid the explanation that is to follow. Using this classification results in 95 leaves (40.4%) that were "mostly inside", 40 leaves (17.0%) were "partly inside", and 100 leaves (42.6%) were "outside" the feedback zone. The same was done with branches which led to 75 branches (73.6%) "mostly inside", 14 (13.7%) "partly inside", and 13 (12.7%) "outside" the feedback zone.

Fig. 5.9 shows the probability density distribution of the surface mass densities of the structures based on their tags. There is a clear trend of increasing surface mass density in association with the overlap with the feedback zone. A Kolmogorov-Smirnov (KS) test (Kolmogorov 1933; Smirnov 1939) was performed on the pairs of these distributions to test the hypothesis that these samples of surface mass densities have been taken from the same population. In the case of leaves only the "mostly inside" and the "outside"

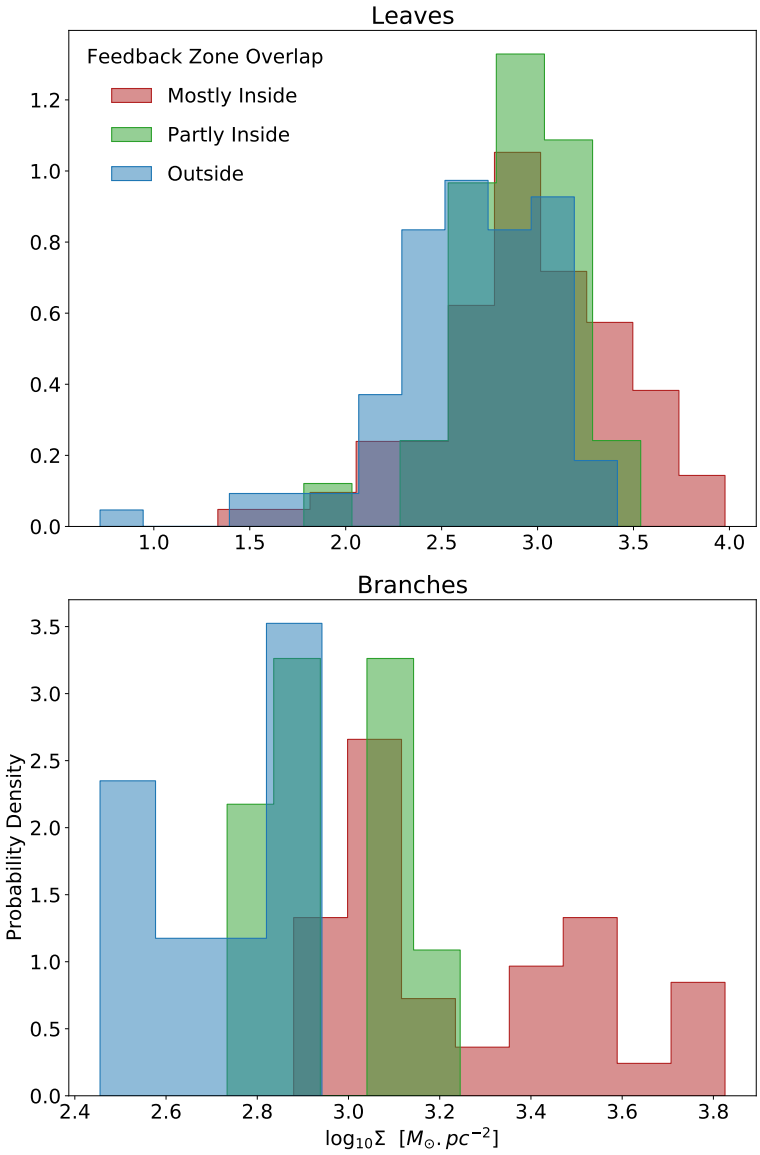

Figure 5.9: Histogram of the probability density of surface mass densities of leaves (top) and branches (bottom) based on their overlap with the "feedback zone" defined using an 8 μm threshold of 100 MJy/sr.

samples rejected the null hypothesis (p-value = 0.0011%). The other pair of samples did not reject the null hypothesis (p-value = 0.12 for "mostly inside" vs "partly inside" and 0.18 for "partly inside" vs "outside"). But the branches in the "mostly inside" category were significantly different from "mostly outside" one (p-value<< 0.0013) but not from the "partly inside" ones (p-value=0.002). These findings support the collect and collapse model that predicts the clumps to be more massive under feedback.

Another prediction of the C&C model is that there will be a higher level of fragmenta-

tion in the cloud being affected by feedback. To test this, we color coded the structures of the dendrogram in Fig. 5.4 based on their tags. We observe the largest hierarchical structure almost completely lies "mostly inside" the feedback zone with some structures being "partly inside". The structures outside the feedback zone show very little fragmentation. This is further support for the C&C model in the case of G305.

5.7 G305 vs Galactic clumps

We have seen so far that feedback from the central cluster of stars has a significant impact on the clumps in G305. This suggests that the properties of the clumps in G305 should be significantly different from the average sample of Galactic clumps. In order to test this, we compared the properties of G305 clumps with those of the Galactic sample of clumps derived from ATLASGAL and CHIMPS.

Fig. 5.10 shows the distribution of different properties of clumps in G305 along with the Galactic sample derived for both ATLASGAL clumps (Urquhart et al. 2018; Contreras et al. 2013) and CHIMPS clumps (Rigby et al. 2019). In order to compare the clumps properties only the CHIMPS clumps with the highest reliability flag (= 3) were considered (Rigby et al. 2019).

The radii of the clumps in G305 are smaller than the CHIMPS clumps. This could be because of the differences in the clump extraction method used by (Rigby et al. 2019). Compared to the dendrogram clumps, the `FELL-WALKER` method (Berry 2015) would have slightly larger areas. In comparison to ATLASGAL, the G305 clumps appear to have a different distribution. But this difference is not significant as confirmed by performing a KS-test on the radius of the two populations (p-value=0.0022).

The linewidths of the G305 clumps appear to have a different distribution from the ATLASGAL and CHIMPS samples. A KS-test resulted in a p-value$<<$ 0.0013 for both the populations confirming this. The ATLASGAL survey used the NH_3 spectral line to estimate linewidths whereas the CHIMPS survey used the same line used in our observations and hence this comparison is more straightforward. We observe the linewidths to be higher in the case of G305 clumps when compared to the CHIMPS population of Galactic clumps.

The G305 clumps show a much broader distribution of masses compared to ATLASGAL. The higher sensitivity of our observations would explain why we see more clumps of smaller masses as compared to ATLASGAL as these would not be detected in the ancillary survey. In comparison to the CHIMPS population of clumps, the masses of G305 clumps are much higher. G305 also has a higher fraction of heavier clumps compared to the ATLASGAL sample. This is indicative of some form of triggering. A KS test on the masses of the two populations resulted in a p-value « 0.0013 for masses of G305 clumps as compared to the Galactic sample (for both ATLASGAL and CHIMPS populations) indicating that the G305 clumps are significantly different from the Galactic average.

The last panel in Fig. 5.10 shows the distribution of virial parameters of the G305 clumps. We see a broader distribution when compared to ATLASGAL clumps. A large

proportion of clumps in G305 appear to have $\alpha_{\rm vir} << 2$. According to Kauffmann et al. (2013) this is indicative of high-mass star formation in G305. We also see a much higher fraction of clumps in G305 with $\alpha_{\rm vir} >> 2$ which may be indicative of turbulence disrupting and dissipating clumps. Interestingly, the smoothed dendrogram does not have clumps with very high $\alpha_{\rm vir}$ values. This could be attributed to the bias towards larger structures in the smoothed dataset leading to more clumps with heavier masses. A KS-test on the virial parameters of the G305 and Galactic clumps indicated these properties being drawn from significantly different populations (p-value$<<$ 0.0013).

Triggering in G305

Proving that triggering is responsible for enhanced star formation is a difficult task. Often it is done by looking at the morphological signposts like star-formation at the rim of an expanding shell of HII regions (Deharveng et al. 2005; Zavagno et al. 2005; Urquhart et al. 2007; Thompson et al. 2012). In G305, Hindson et al. (2013) looked at star-formation in different phases and compared their distribution in the complex to suggest that the most likely cause of triggering is the collect and collapse process. However, they did not find any conclusive evidence that the star-formation happening in G305 has been triggered. They calculated the time needed for the gas to fragment into stars and suggested that while in some cases the age of the triggering stars was old enough to be responsible for the stars in their vicinity to be triggered. In many other cases, the stars responsible for triggering may not be old enough to drive the formation of the HII and UC HII regions. But the fragmentation time-scale estimates were based on assumptions about the initial ambient atomic density and the Lyman continuum photon rate both of which are difficult to measure, making their suggestions inconclusive. So far in this paper, we have explored whether the feedback from the stars is indeed triggering star formation in G305 by looking at their impact on the clumps which are the reservoirs of the new generation of stars.

The luminosity to mass ratio (L/M) of clumps is a good indicator of the evolutionary stage in star formation (see Urquhart et al. 2018; Molinari et al. 2008). A higher star forming efficiency would mean that more clumps are in more evolved stages of forming stars leading to a flatter cumulative distribution function of their L/M. In G305, if the clumps are simply being moved around without any effect on their star forming efficiency, then the L/M distribution of the clumps in G305 should not vary significantly from the Galactic average. Fig. 5.11 shows the cumulative distribution function (CDF) of the L/M for the ATLASGAL clumps in G305 compared to that of the overall ATLASGAL Galactic sample. All the L/M values were taken from ATLASGAL as the calculation of the luminosity is quite different between our dataset and ATLASGAL. This would eliminate any uncertainties and systematic differences due to the difference in methods used to calculate masses and luminosities. The clumps in G305 show significantly higher L/M than the Galactic average as is shown by the CDF. A KS test on the two clump samples returned a p-value$<<$ 0.0013. Therefore, the null hypothesis is quite overwhelmingly rejected indicating that the clumps in G305 show higher star forming efficiency compared to the Galactic average. This rules out the "redistribution" and "disruption" scenarios.

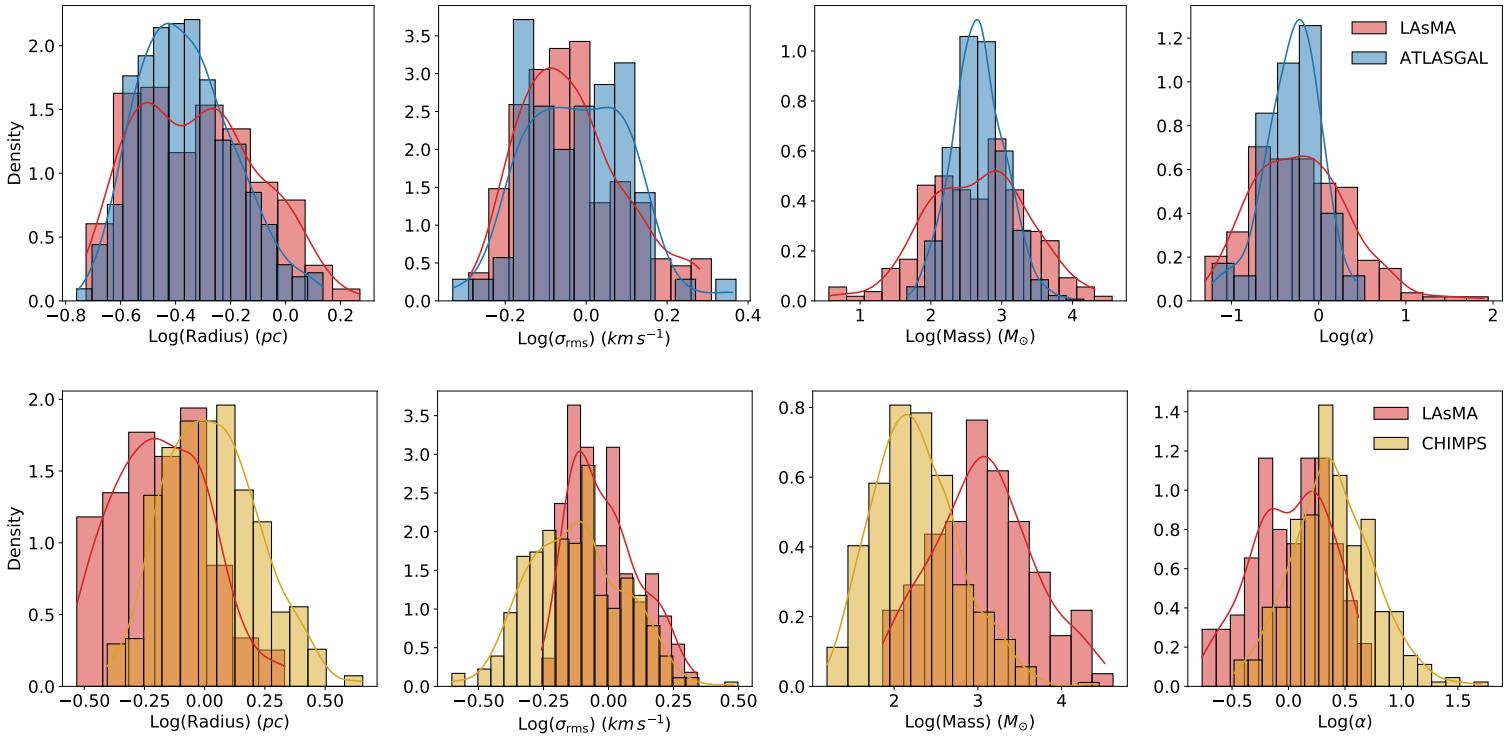

Figure 5.10: Comparison of properties of LAsMA clumps in G305 with a Galactic sample derived from ATLASGAL (top panel) and CHIMPS (bottom panel) surveys.

These clumps may not have a one to one correspondence with the ^{13}CO clumps derived in the previous sections, but that does not negate the validity of the finding here.

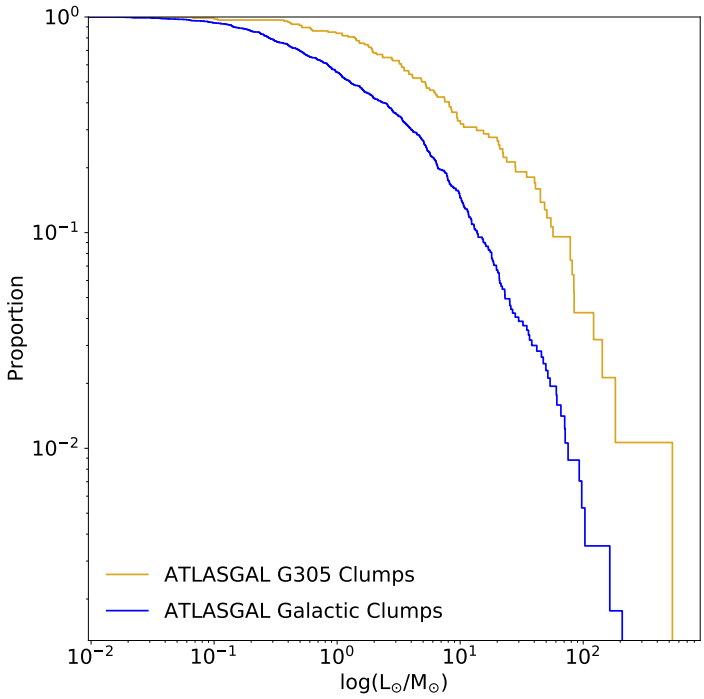

Figure 5.11: CDF of L_{clumps}/M_{clumps} in G305 compared to that of the ATLASGAL Galactic clumps.

Finally, in case of triggering, if C&C is the dominant mechanism in play then we would observe more massive clumps as C&C causes the clump to accumulate mass. Fig. 5.12 shows the CDF of the clump masses in G305 compared to the Galactic average. In addition to the ATLASGAL, we also included the CHIMPS clumps. The method used to measure clump properties in our paper is identical to that used by Rigby et al. (2019). Fig. 5.12 shows the CDF of clump masses in G305 compared to the Galactic sample taken from ATLASGAL as well as CHIMPS. For both cases, the clumps in G305 show a much flatter CDF than the Galactic average. A KS test between G305 clumps and ATLASGAL (CHIMPS) clumps yielded a p-value$<<$ 0.0013 again rejecting the null hypothesis that the G305 LAsMA clumps and the Galactic ATLASGAL (CHIMPS) clumps belong to the same distribution. The flatter slope of the clump mass CDF of G305 proves that C&C is the dominant mechanism inside the GMC.

5.8 Summary

We observed the G305 region with the LAsMA receiver on the APEX telescope using the ^{12}CO (3–2) and ^{13}CO (3–2) lines in order to test the effect of feedback from the central

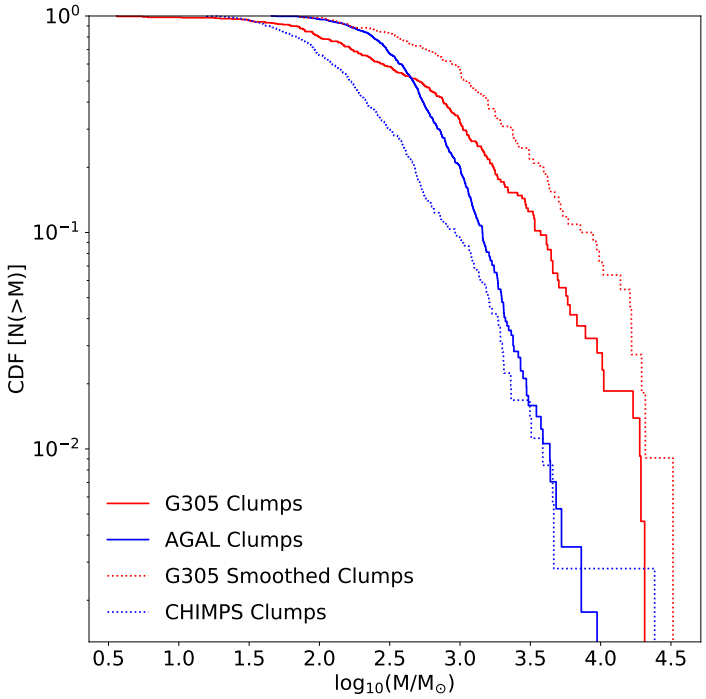

Figure 5.12: CDF of LAsMA clump masses in G305 compared to that of the Galactic clump sample from ATLASGAL and CHIMPS.

cluster of stars on the clump properties.

We decomposed the molecular cloud into clumps using the Dendrogram analysis on the ^{13}CO datacube. We followed up by creating a catalog of clump properties. We tested the effect of feedback on two main clump properties namely linewidths and surface mass densities. Using the 8 μm emission map of the region as a proxy to feedback strength, we examined the correlation of the surface mass densities of the clumps with the incident average 8 μm flux. We then masked the "feedback zone" based on an 8 μm flux threshold of 100 MJy/sr. The extent of overlap of each clump with the "feedback zone" was used to determine whether it was mostly inside, partly inside or outside the feedback zone. The properties of these three populations of clumps were separately studied. We followed this up with a comparison of the properties of clumps in G305 as a whole to a distance limited sample of Galactic clumps taken from ATLASGAL and CHIMPS surveys assuming that the Galactic sample of clumps is similar to a population of clumps that are quiescent. The cumulative distribution function (CDF) of the masses as well as the L/M ratios of the clumps (the latter having been derived entirely from ATLASGAL data) in G305 was obtained and compared to that of the Galactic average. We summarize our main findings below :

- Our data does not possess enough velocity resolution to discern the effect of feedback on the linewidths of the clumps.

- The surface mass densities of the clumps in the region are positively correlated to the incident average 8 μm flux.
- The surface mass densities of the clumps mostly inside the feedback zone are the largest, followed by that of the clumps partly inside and outside the feedback zone respectively indicating that feedback is triggering their the star forming ability.
- Clumps inside the feedback zone show a much higher level of fragmentation than those partly inside or outside it.
- The probability density function (PDF) of the properties of G305 clumps are significantly different than those of the clumps derived from a distance limited Galactic sample of clumps indicating clear evidences of triggering.
- The CDF of both the masses and L/M ratios of the clumps in G305 are significantly flatter than that of the Galactic average. This is a strong evidence for triggering (more specifically the collect and collapse mechanism), not redistribution or dispersion, being the dominant mechanism in G305.

Therefore, we obtain multiple evidences demonstrating that the feedback from the central cluster of stars in G305 is triggering the collapse of the molecular cloud complex.

Part V

Current Status and Conclusions

Chapter 6

Current status of LAsMAGal

6.1 LAsMAGal: Current status

Alongside G305, observations of LAsMAGal were continued from the test region of Chapter 3 in a continuous manner towards increasing Galactic longitude. The Galaxy was divided into regions (tiles) of size 0.5×0.5 square degrees centered in the galactic longitude on $b = 0°$ and $|b| < 0.25°$. The Galactic longitude was also divided into two tiles of width 0.5 degrees centered on 0.25° and 0.75° of the longitude and stepping in galactic longitude by 0.5°. The tiles were named by the position of their center (e.g., the Galactic longitude 347 to 348° was covered by two tiles named G347.25 and G347.75. The observed data was transported back to Bonn, where it was reduced offline using a reduction pipeline. The design of this pipeline is described below.

6.1.1 Reduction pipeline

A reduction pipeline was created in order to reduce all LAsMAGal data with minimal human input. This was done using the GILDAS package[1]. Figure 6.1 shows a flowchart representation of the reduction pipeline. The major steps of this flowchart are enumerated below.

1. The user provides the name of the tile, the name of its reference position, and the line of interest (either ^{12}CO (3−2) or ^{13}CO (3−2)).

2. The pipeline then searches all the data files [2] for observations corresponding to the given off position name and line setting. These observations are averaged and stored separately for each pixel.

3. The pipeline then goes through all the data files looking for observations corresponding to the given tile name and line setting. While conducting the search, it ignores all the bad scans whose numbers are stored in a separate file (which gets updated regularly after new data is observed). A bad scan is classified as a scan that was started during an observation but did not finish for one of many reasons e.g., calibrator crashing due to large data rate, incorrect reference position provided during observations, scan being canceled by the operator, etc. The observer updates the observing log with the bad scan numbers, which are then added to the final file containing the list of bad scans.

[1] http://www.iram.fr/IRAMFR/GILDAS

[2] at APEX, data calibrated in a T_A^* scale is stored in class format

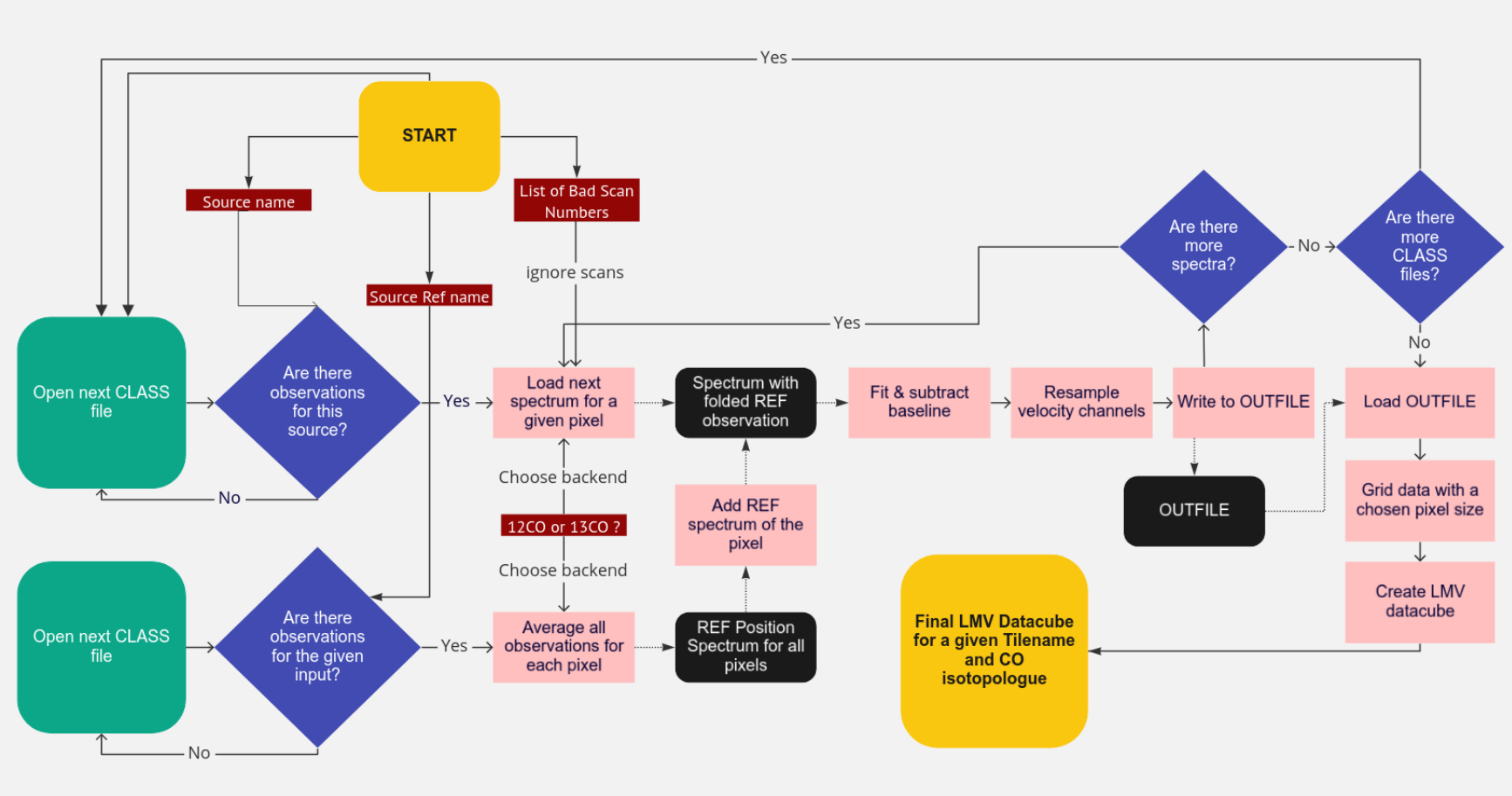

Figure 6.1: A flowchart summarizing the reduction pipeline used to reduce all the data from the LAsMAGal survey.

4. The reference spectrum of the corresponding pixel is first added to each observation to remove any weak emission lines that manifest as absorption in the source spectra. An ideal reference position has two properties: it is not far away (a few arc minutes) from the source on the sky and also has no significant emission above the noise background. However, for a survey of the Milky Way, it is extremely difficult, and at times, impossible, to find an ideal reference position near the source position, as CO emission is ubiquitous between the galactic longitudes abs $b < 1$ beyond which it still persists as faint emission. A solution to this problem is finding a reference position with a very weak emission and then adding it back to the source spectrum to cancel out the absorption feature resulting from the former during calibration. Therefore, a reference position for our survey was deemed to be acceptable if it had emission lines weaker than 200 mK.

5. A 3rd order baseline is then fitted to the velocity range of -200 to 200 km s^{-1} and subtracted from each spectrum. Before fitting the baseline, the velocity window of -150 to 20 km s^{-1} is masked to avoid fitting emission lines.

6. Following this, the spectrum is resampled in velocity space to obtain a final spectral resolution of 0.5 km.s^{-1}.

7. The reduced spectrum is finally stored in a separate file.

8. Once all the spectra corresponding to the tile name have been processed, they are tabulated and gridded onto a grid with a pixel size of 6″ in order to ensure Nyquist sampling. The final product is a 3-dimensional spectral cube.

6.1.2 Integrated intensity map : Far edge of the Galactic Bar

After being reduced by the pipeline, the final datacubes were first used to create a distribution function of all the voxel intensities. Figure 6.2 shows the resulting distribution. These voxels can be modeled as being normally distributed about a mean excitation temperature of 0.006 K with a standard deviation of 0.13 K. At an excitation temperature of 20 K typically existent in molecular clouds, (see Sect. 5.1.2 of Heyer & Dame 2015) and optically thin gas, this translates to a ^{12}CO column density sensitivity of $\sim 10^{15}$ cm^{-2} or an H_2 column density of a few times 10^{19} cm^{-2} on assuming an abundance of [CO]/[H_2]=1 $\times$ 10^{-4}.

This suggests that the survey data is indeed very sensitive to diffuse molecular gas. We created the integrated intensity maps using the LAsMAGal data to verify this. For this, an RMS noise map was created for each tile using the same method as explained in Chapter 3. Then, all voxels with a signal-to-noise ratio (SNR) < 5 were flagged. Following this, all the velocity channels between -200 and +10 km s^{-1} for each pixel were integrated to obtain the final moment-0 map of the region. Figure 6.3 shows the integrated intensity map of the region observed thus far. As expected from the noise analysis, the data appears to trace diffuse gas exceptionally well. This is very promising since it can be used to investigate the filamentary structure of molecular clouds, trace diffuse outflows to identify star-forming clouds, and fine-tune theoretical models of the Milky Way.

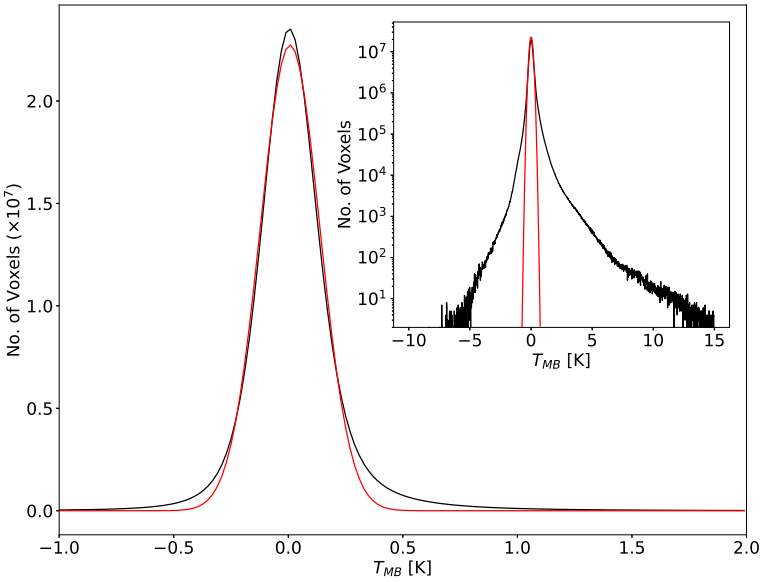

Figure 6.2: Histogram of all voxels in LAsMAGal for ^{12}CO (3−2) . The black line represents the observed data and the red line represents the best fit Gaussian to the distribution, which is of the form $0.96 \times e^{(-(x-0.006)^2/(2\times 0.13^2))}$. The embedded plot shows the Gaussian fit on a logarithmic scale.

Some empty regions inside the map have not been observed yet; namely, the two rectangular regions at the Galactic coordinates $(l, b) = (346.7, 0.0°)$ and $(347.3, 0.15°)$. These regions are planned to be covered in the coming observing runs.

In addition to the integrated intensity map of the full Galactic velocity range, we also show the moment-0 maps for the velocity ranges [-130,-110], [-110,-60], and [-60,10] km s^{-1} in Figure 6.4. These windows were chosen to cover most of the emission from the 3kpc arm, Norma arm, and Scutum-Centaurus arm of the Galaxy. This can also be verified by inspecting the total spectrum of the whole region. Figure 6.5 shows the average spectrum of the whole region from Fig.6.3.

6.2 Summary

This chapter presents a small summary of the current status of LAsMAGal. A detailed description of the pipeline has been provided. Using this pipeline, a continuous region spanning Galactic longitudes between 345° and 349.5°, barring a couple of holes that are planned to be observed during the upcoming runs, has been observed and reduced. A brief analysis of the sensitivity of the survey data obtained so far was also presented, indicating the survey's excellent sensitivity towards very diffuse clouds. This was also demonstrated with the integrated intensity maps of the region observed so far.

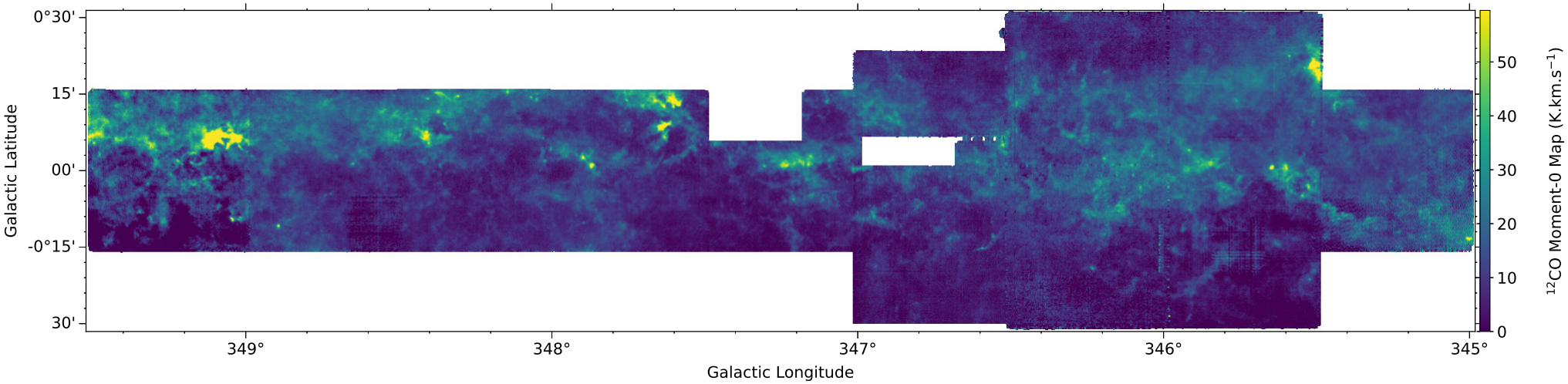

Figure 6.3: ^{12}CO (3–2) integrated emission (T_{MB}) map of the region covered in LAsMAGal towards the far end of the Galactic bar.

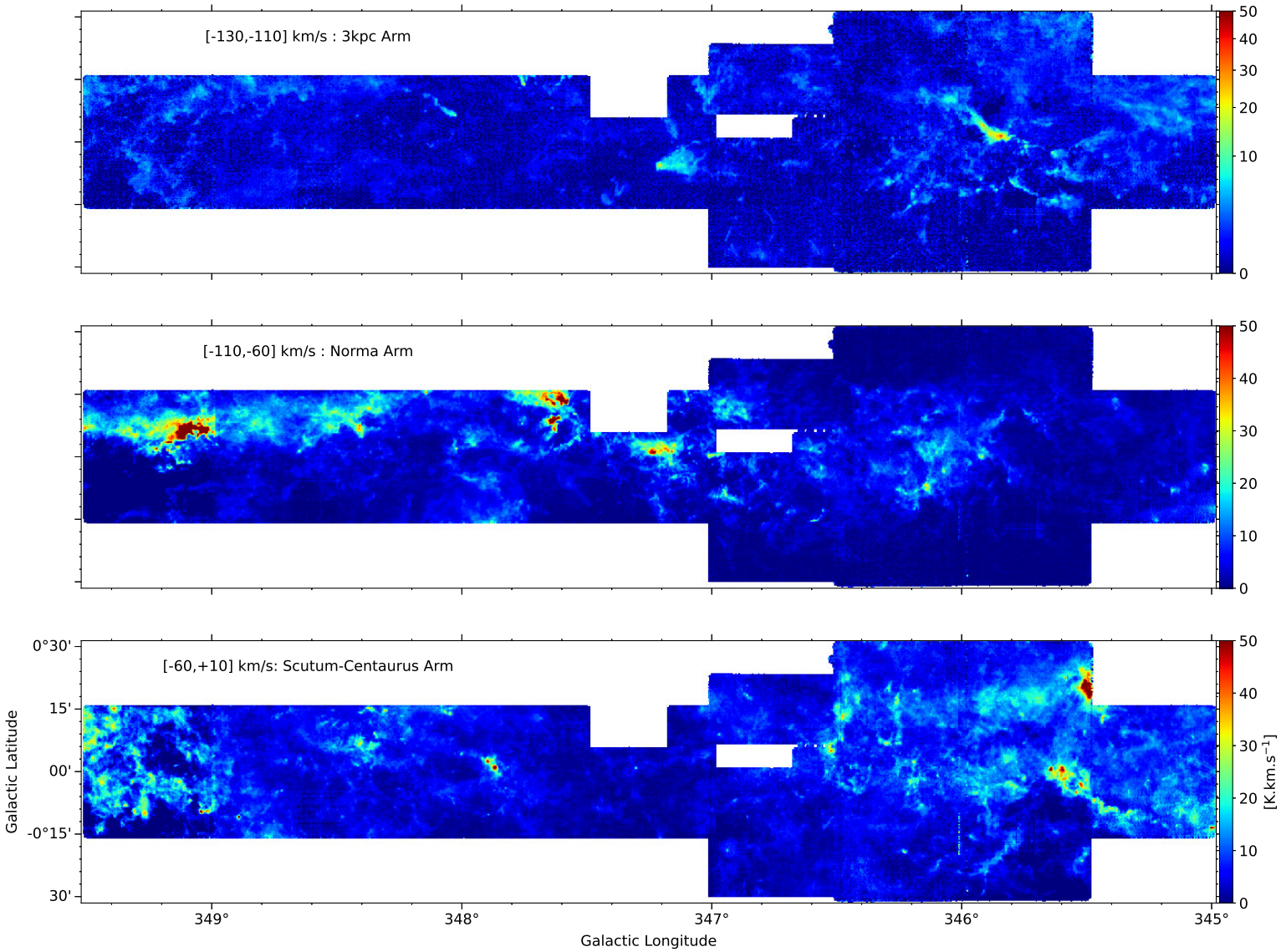

Figure 6.4: ^{12}CO (3−2) T_{MB} moment-0 maps for different velocity ranges covered so far towards the far edge of the Galactic Bar. The color bar is in the units of K.km.s^{-1}. The color map for the top panel has been distributed according to a square-root function to make diffuse gas more prominent.

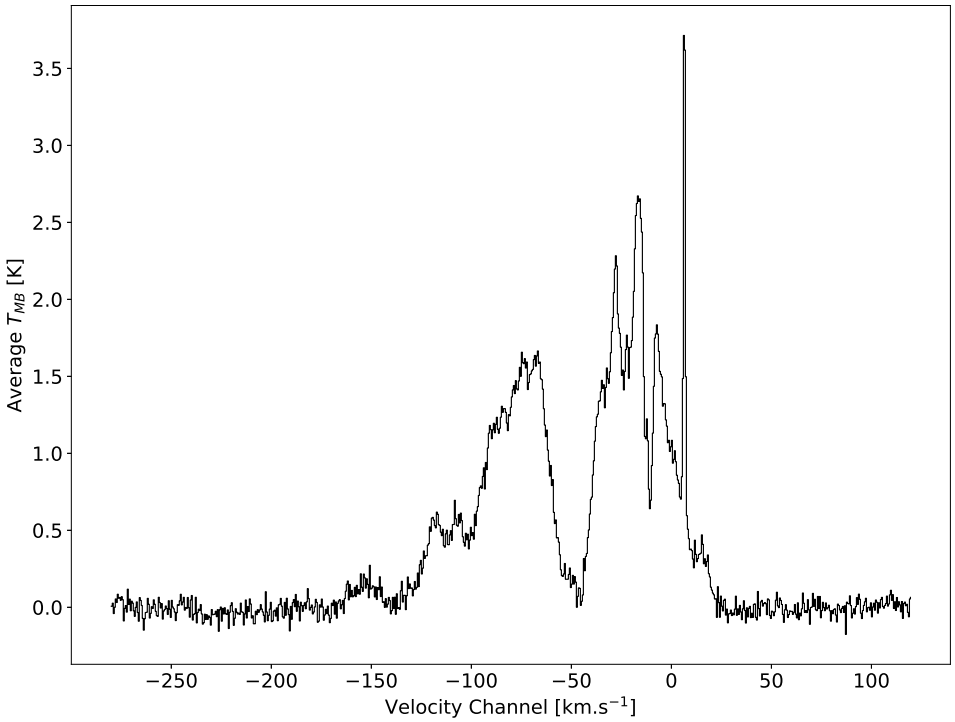

Figure 6.5: Average spectrum of the whole observed region of LAsMAGal towards the far edge of the Galactic Bar.

Chapter 7

Conclusions

Radio and (sub)millimeter astronomy has made the study of the molecular clouds (MCs), the birth-place of all visible stars, possible. Their formation, morphology, physical conditions, and many other aspects are active research areas. Since the beginning of the 21st century, molecular cloud surveys have helped us further our understanding of these structures, the theory of star-formation, and the structure of the Milky Way. This dissertation takes another step toward understanding MCs by conducting the first-of-its-kind large-scale high-resolution survey of giant molecular clouds (GMCs) in the Milky Way (LAsMAGal), covering ^{12}CO and ^{13}CO (3−2) lines simultaneously. The newly installed 7-pixel receiver on the APEX telescope called LAsMA, operating in the 345 GHz atmospheric window, was chosen to be used for this survey. This dissertation has been divided into five separate parts.

The first part of this dissertation provides a broad overview of the different phases in which the interstellar medium exists, followed by a description of molecular clouds and the theory of star-formation. After this, a brief overview of the mechanisms by which molecular clouds emit radiation, and the subsequent journey the emitted photons take to reach us on Earth is given. This then provides the motivation for the work carried out during the span of the Ph.D. thesis.

In the second part, the commissioning of the newly installed instrument, LAsMA, was presented. This involved three major tests. First, the relative positioning of all the pixels was determined using beam maps on planets. Then, the response of individual pixels in the array was tested as a function of their rotation angle. We found that each pixel showed a sinusoidal dependence on the angle of derotation. However, the response of the average of all pixels, which is the relevant quantity of interest for the mapping purposes of this thesis, did not show a significant dependence on the angle of derotation. The average response of the array was thus used to determine its effective beam efficiency, which was found to be about 90% of the central pixel's efficiency (which is what is usually measured during calibrations before observation runs). Lastly, the sideband rejection of the receiver was tested for all pixels at different local oscillator (LO) frequencies as well as intermediate frequency (IF) values. This was then used to determine the LO frequency most suitable for carrying out a survey of the inner Galaxy in the ^{12}CO (3−2) and ^{13}CO (3−2) lines using the LAsMA receiver.

In the third part of the thesis, the feasibility of the survey was tested. The far edge of the Galactic Bar was chosen as a test region. Different observing set-ups and strategies were tested in this region. The final chosen set up had step sizes of 7″ and 9″ in the $x - y$ directions respectively. A dump time of 0.1s was used for the observations. This set-up

resulted in a high sensitivity to faint diffuse molecular gas: the survey showed a factor of 4 improvement in the noise level compared to the SEDIGISM survey, which is the most relevant survey of the dense molecular gas towards the planned region of coverage for LAsMAGal. This sensitivity will enable more detailed studies of the filamentary nature of the molecular gas in the Galaxy and the detection of new star-forming regions by discovering outflows. It will also help to build a better model of the Galaxy by providing more information about the diffuse gas in the inter-arm regions. Additionally, this survey can also be used along with SEDIGISM to obtain excitation properties of the gas, enabling us to determine various physical properties of the gas, e.g., temperature, column density, and optical depth. In combination with source distances, this will also enable us to determine cloud masses and densities.

In the fourth part, the capabilities of the survey were demonstrated in a science case study of the G305 giant molecular cloud complex. This GMC is a very prominent high mass star-forming region in the southern sky. It consists of tens of hot, luminous stars at its center that are injecting a large amount of energy in the form of bright UV radiation and strong winds as feedback into the gas around it. This region provides an ideal laboratory to investigate the effects of feedback from high-mass stars on their parent clouds.

In the first chapter of this part, we first investigated how this feedback from the central star cluster affects the gas around it. We found that the central region of the complex has been cleared out of most of the high column density gas. Calculations of the energy input from the visible stars in the complex showed that they could be responsible for clearing out such a large cavity at the center of G305. Sequential formation of the star cluster Danks 2 followed by Danks 1 and the other stars in the complex can explain the size of the observed cavity. Assuming local thermodynamic equilibrium (LTE), whose validity was successfully tested subsequently, we produced ^{12}CO excitation temperature and ^{13}CO column density maps of the region. Combining SEDIGISM data of the region with LAsMAGal data, we also obtained 3–2 to 2–1 line ratio maps. These maps were used to test the effects of feedback on the excitation properties of the gas. We found that feedback was heating and compressing the gas in a narrow region of the cloud facing the stars at the center. The fraction of the incident energy from the stars being expended towards this varied widely; towards the north of the complex, about 60% of the energy went towards heating and compressing the gas, whereas, towards the south, it was only about 15%. Using 8 μm radiation as a proxy for the feedback strength, we created pixel-wise scatter plots of the excitation temperatures, 3–2 to 2–1 line ratios, and column densities along with the 8 μm emission. As expected, regions with stronger feedback generally showed a higher excitation of the gas. The effects of feedback on the gas dynamics were also tested by plotting the centroid velocity probability distribution function (PDF) for the region. The centroid velocity PDF demonstrated exponential wings, which indicated that turbulence in the gas was being driven by strong stellar feedback in the form of winds. We then tested the dynamical properties of the gas as a function of feedback strength by stacking the spectra of the pixels and plotting the average stacked profiles. We discovered that the gas experiencing stronger feedback showed systematically more positively skewed line profiles. On average, these line profiles were narrower (lower

standard deviation) but had more pronounced wings (higher kurtosis). We postulated that the positive skew meant that parts of the cloud complex were being pushed away from us, resulting in a positive wing of the overall stacked spectra. The standard deviation and the kurtosis of the stacked profiles, however, showed opposing trends when plotted as a function of 8 μm flux. Further analysis of stacked spectra towards other GMCs is needed in order to shed light on the significance of this result and warrant an explanation for the causes of this trend.

In the next chapter, we then decomposed the ^{13}CO (3−2) data cube into clumps using a dendrogram analysis in order to explore the effects feedback has on the star-forming properties of the clumps in G305. Various properties of the clumps, e.g., their sizes, masses, densities, virial parameters, etc. were calculated and cataloged. Examining the correlation of the surface mass densities of the clumps with the incident average 8 μm flux revealed a positive correlation between the two, indicating that clumps with stronger feedback are more massive than those experiencing less strong feedback. The clumps were also categorized into “mostly inside" (overlap >67%), “partly inside" (10%> overlap <67%), and “outside" (overlap <10%) subsamples based on their overlap with a 8 μm flux mask. The star formation efficiencies of all the three subsamples were significantly different from each other. The clumps also showed a much higher degree of fragmentation in regions with stronger feedback, indicating that their formation has been triggered by feedback. Finally, comparing the statistical properties of the clumps in G305 with the Galactic average (assumed to represent a population of clumps not affected by feedback) derived using the ATLASGAL 870 μm dust continuum and CHIMPS ^{13}CO (3–2) surveys revealed that the clump properties in G305 were significantly different from the Galactic average. G305 clumps were much heavier and had higher luminosity to mass ratios. The cumulative distribution function (CDF) of both these properties showed that they were top-heavy (or flatter) when compared to the Galactic average. The difference in the CDF was statistically significant, which provides strong evidence for triggered star formation (more specifically via the collect and collapse mechanism) in G305.

In the fifth and final part of this dissertation, we presented the current status of LAsMAGal, which has covered about 5° of Galactic longitude towards the far end of the Galactic Bar. We discussed the pipeline that has been developed for reducing the LAsMAGal data and then presented the moment-0 map of the region that has been covered so far towards the region. In addition, the success of the science case study on G305 has motivated the observation of other prominent star-forming giant molecular cloud complexes like the NGC 6334 and G333. An analysis similar to that done in G305 is now being done on the NGC 6334 region, which, we hope, will shed further light on how feedback from OB stars impacts their surroundings and influences the formation of stars in their natal cloud.

The work presented throughout this dissertation altogether not only emphasizes the advantage of a new high-resolution survey like LAsMAGal but also makes it an imperative next step in unraveling the mysteries hidden inside molecular clouds.

Bibliography

Allamandola, L. J., Tielens, A. G. G. M., & Barker, J. R. 1989, ApJS, 71, 733 (Cited on page 101.)

Allen, C. W. 1973, Astrophysical quantities (Cited on page 125.)

Allen, R. J., Hogg, D. E., & Engelke, P. D. 2015, AJ, 149, 123 (Cited on page 11.)

André, P. 2017, Comptes Rendus Geoscience, 349, 187 (Cited on page 89.)

André, P., Men'shchikov, A., Bontemps, S., et al. 2010, A&A, 518, L102 (Cited on page 19.)

Andre, P., Ward-Thompson, D., & Barsony, M. 1993, ApJ, 406, 122 (Cited on pages 22 and 23.)

Ballesteros-Paredes, J., André, P., Hennebelle, P., et al. 2020, Space Sci. Rev., 216, 76 (Cited on pages 10, 18 and 39.)

Ballesteros-Paredes, J., Hartmann, L., & Vázquez-Semadeni, E. 1999, ApJ, 527, 285 (Cited on page 39.)

Barnes, P. J., Muller, E., Indermuehle, B., et al. 2015, ApJ, 812, 6 (Cited on page 67.)

Baug, T., Wang, K., Liu, T., et al. 2021, MNRAS, 507, 4316 (Cited on page 27.)

Beltrán, M. T., Cesaroni, R., Zhang, Q., et al. 2011, A&A, 532, A91 (Cited on page 26.)

Benjamin, R. A., Churchwell, E., Babler, B. L., et al. 2003, PASP, 115, 953 (Cited on pages 101 and 129.)

Berry, D. S. 2015, Astronomy and Computing, 10, 22 (Cited on page 134.)

Bertoldi, F. 1989, ApJ, 346, 735 (Cited on pages 28, 29, 85 and 120.)

Bertoldi, F. & McKee, C. F. 1990, ApJ, 354, 529 (Cited on pages 29 and 120.)

Beuther, H. 2007, in Triggered Star Formation in a Turbulent ISM, ed. B. G. Elmegreen & J. Palous, Vol. 237, 148–154 (Cited on page 26.)

Beuther, H., Meidt, S., Schinnerer, E., Paladino, R., & Leroy, A. 2017, A&A, 597, A85 (Cited on page 69.)

Blitz, L. & Shu, F. H. 1980, ApJ, 238, 148 (Cited on page 19.)

Blitz, L. & Stark, A. A. 1986, ApJ, 300, L89 (Cited on page 118.)

Blitz, L. & Williams, J. P. 1999, arXiv e-prints, astro (Cited on page 19.)

Bok, B. J. & Reilly, E. F. 1947, ApJ, 105, 255 (Cited on page 18.)

Bonnell, I. A., Bate, M. R., Clarke, C. J., & Pringle, J. E. 2001a, MNRAS, 323, 785 (Cited on page 24.)

Bonnell, I. A., Bate, M. R., & Zinnecker, H. 1998, MNRAS, 298, 93 (Cited on page 24.)

Bonnell, I. A., Clarke, C. J., Bate, M. R., & Pringle, J. E. 2001b, MNRAS, 324, 573 (Cited on page 24.)

Borissova, J., Roman-Lopes, A., Covey, K., et al. 2019, AJ, 158, 46 (Cited on pages 79, 83, 85, 89, 90, 98, 99, 117 and 124.)

Brunthaler, A., Menten, K. M., Dzib, S. A., et al. 2021, A&A, 651, A85 (Cited on page 26.)

Burton, M., Walsh, A., & Balasubramanyam, R. 2002, in Astronomical Society of the Pacific Conference Series, Vol. 267, Hot Star Workshop III: The Earliest Phases of Massive Star Birth, ed. P. Crowther, 355 (Cited on page 26.)

Carlhoff, P., Nguyen Luong, Q., Schilke, P., et al. 2013, A&A, 560, A24 (Cited on page 69.)

Carpenter, J. M. 2000, AJ, 120, 3139 (Cited on page 22.)

Cerviño, M. & Luridiana, V. 2004, A&A, 413, 145 (Cited on page 27.)

Chabrier, G. 2003, PASP, 115, 763 (Cited on page 24.)

Chappell, D. & Scalo, J. 2001, MNRAS, 325, 1 (Cited on page 107.)

Chevance, M., Kruijssen, J. M. D., Hygate, A. P. S., et al. 2020, MNRAS, 493, 2872 (Cited on page 19.)

Churchwell, E., Babler, B. L., Meade, M. R., et al. 2009, PASP, 121, 213 (Cited on pages 101, 118 and 129.)

Clark, J. S. & Porter, J. M. 2004, A&A, 427, 839 (Cited on pages 83, 84, 85, 117, 118 and 124.)

Clarke, C. J., Bonnell, I. A., & Hillenbrand, L. A. 2000, in Protostars and Planets IV, ed. V. Mannings, A. P. Boss, & S. S. Russell, 151 (Cited on page 24.)

Clemens, D. P., Yun, J. L., & Heyer, M. H. 1991, ApJS, 75, 877 (Cited on page 18.)

Colombo, D., Duarte-Cabral, A., Pettitt, A. R., et al. 2021, arXiv e-prints, arXiv:2110.06071 (Cited on page 39.)

Colombo, D., Rosolowsky, E., Duarte-Cabral, A., et al. 2019, MNRAS, 483, 4291 (Cited on page 124.)

Comoretto, G., Palagi, F., Cesaroni, R., et al. 1990, A&A, 84, 179 (Cited on page 26.)

Contreras, Y., Schuller, F., Urquhart, J. S., et al. 2013, A&A, 549, A45 (Cited on pages 121 and 134.)

Cox, D. P. & Smith, B. W. 1974, ApJ, 189, L105 (Cited on page 7.)

Cragg, D. M., Sobolev, A. M., Ellingsen, S. P., et al. 2001, MNRAS, 323, 939 (Cited on page 26.)

Cragg, D. M., Sobolev, A. M., & Godfrey, P. D. 2002, MNRAS, 331, 521 (Cited on page 26.)

Crowther, P. A. 2007, ARA&A, 45, 177 (Cited on pages 99 and 129.)

Cyganowski, C., Brogan, C., Hunter, T., & Churchwell, E. 2010, in American Astronomical Society Meeting Abstracts, Vol. 215, American Astronomical Society Meeting Abstracts #215, 345.04 (Cited on page 26.)

Dale, J. E., Bonnell, I. A., Clarke, C. J., & Bate, M. R. 2005, MNRAS, 358, 291 (Cited on page 28.)

Dale, J. E., Bonnell, I. A., & Whitworth, A. P. 2007, MNRAS, 375, 1291 (Cited on page 120.)

Dame, T. M., Hartmann, D., & Thaddeus, P. 2001, ApJ, 547, 792 (Cited on pages 58 and 67.)

Davies, B., Clark, J. S., Trombley, C., et al. 2012a, MNRAS, 419, 1871 (Cited on pages 83, 84, 85, 99, 100 and 117.)

Davies, B., de La Fuente, D., Najarro, F., et al. 2012b, MNRAS, 419, 1860 (Cited on page 70.)

de Geus, E. J. 1992, A&A, 262, 258 (Cited on page 120.)

Deharveng, L., Schuller, F., Anderson, L. D., et al. 2010a, A&A, 523, A6 (Cited on page 83.)

Deharveng, L., Schuller, F., Anderson, L. D., et al. 2010b, A&A, 523, A6 (Cited on page 118.)

Deharveng, L., Zavagno, A., & Caplan, J. 2005, A&A, 433, 565 (Cited on page 135.)

Dempsey, J. T., Thomas, H. S., & Currie, M. J. 2013, ApJS, 209, 8 (Cited on page 67.)

Dobbs, C. L., Krumholz, M. R., Ballesteros-Paredes, J., et al. 2014, in Protostars and Planets VI, ed. H. Beuther, R. S. Klessen, C. P. Dullemond, & T. Henning, 3 (Cited on page 39.)

Draine, B. T. 2003, ARA&A, 41, 241 (Cited on page 12.)

Draine, B. T. 2011, Physics of the Interstellar and Intergalactic Medium (Cited on page 36.)

Duarte-Cabral, A., Acreman, D. M., Dobbs, C. L., et al. 2015, MNRAS, 447, 2144 (Cited on pages 39 and 69.)

Duarte-Cabral, A., Colombo, D., Urquhart, J. S., et al. 2021, MNRAS, 500, 3027 (Cited on page 39.)

Dubner, G. & Giacani, E. 2015, A&A Rev., 23, 3 (Cited on page 28.)

Duerr, R., Imhoff, C. L., & Lada, C. J. 1982, ApJ, 261, 135 (Cited on page 25.)

Eden, D. J., Moore, T. J. T., Plume, R., & Morgan, L. K. 2012, MNRAS, 422, 3178 (Cited on page 69.)

Elmegreen, B. G. 1985, in Protostars and Planets II, ed. D. C. Black & M. S. Matthews, 33–58 (Cited on page 17.)

Elmegreen, B. G. 1993, in Protostars and Planets III, ed. E. H. Levy & J. I. Lunine, 97 (Cited on page 17.)

Elmegreen, B. G., Efremov, Y., Pudritz, R. E., & Zinnecker, H. 2000, in Protostars and Planets IV, ed. V. Mannings, A. P. Boss, & S. S. Russell, 179 (Cited on page 24.)

Elmegreen, B. G. & Lada, C. J. 1977, ApJ, 214, 725 (Cited on pages 28 and 120.)

Elmegreen, D. M. 1980, ApJ, 242, 528 (Cited on page 69.)

Evans, Neal J., I. 1999, ARA&A, 37, 311 (Cited on page 10.)

Faimali, A., Thompson, M. A., Hindson, L., et al. 2012, MNRAS, 426, 402 (Cited on pages 80, 85 and 117.)

Falgarone, E. & Phillips, T. G. 1990, ApJ, 359, 344 (Cited on page 105.)

Fall, S. M., Krumholz, M. R., & Matzner, C. D. 2010, ApJ, 710, L142 (Cited on page 28.)

Fazio, G. G., Hora, J. L., Allen, L. E., et al. 2004, ApJS, 154, 10 (Cited on page 101.)

Federrath, C. & Klessen, R. S. 2013, ApJ, 763, 51 (Cited on page 40.)

Ferrière, K. M. 2001, Reviews of Modern Physics, 73, 1031 (Cited on pages 7, 9 and 10.)

Field, G. B. 1965, ApJ, 142, 531 (Cited on page 39.)

Field, G. B., Goldsmith, D. W., & Habing, H. J. 1969, ApJ, 155, L149 (Cited on page 5.)

Frail, D. A., Goss, W. M., Reynoso, E. M., et al. 1996, AJ, 111, 1651 (Cited on page 26.)

Fraknoi, A., Morrison, D., & Wolff, S. C. 2016, Astronomy (OpenStax) (Cited on page 12.)

Frerking, M. A., Langer, W. D., & Wilson, R. W. 1982, ApJ, 262, 590 (Cited on page 125.)

Fukui, Y., Habe, A., Inoue, T., Enokiya, R., & Tachihara, K. 2021, PASJ, 73, S1 (Cited on page 120.)

Garay, G. & Lizano, S. 1999, PASP, 111, 1049 (Cited on page 99.)

Gatto, A., Walch, S., Naab, T., et al. 2017, MNRAS, 466, 1903 (Cited on page 28.)

Gray, M. D., Doel, R. C., & Field, D. 1991, MNRAS, 252, 30 (Cited on page 26.)

Green, J. A., Caswell, J. L., Fuller, G. A., et al. 2009, MNRAS, 392, 783 (Cited on pages 85 and 117.)

Green, J. A., Caswell, J. L., Fuller, G. A., et al. 2012, MNRAS, 420, 3108 (Cited on pages 85 and 117.)

Gritschneder, M., Naab, T., Walch, S., Burkert, A., & Heitsch, F. 2009, ApJ, 694, L26 (Cited on page 28.)

Güsten, R., Baryshev, A., Bell, A., et al. 2008, in Society of Photo-Optical Instrumentation Engineers (SPIE) Conference Series, Vol. 7020, Proc. SPIE, 702010 (Cited on pages 47, 86 and 121.)

Güsten, R., Nyman, L. Å., Schilke, P., et al. 2006, A&A, 454, L13 (Cited on pages 45, 86 and 121.)

Habets, G. M. H. J. & Heintze, J. R. W. 1981, , 46, 193 (Cited on page 17.)

Haffner, L. M., Reynolds, R. J., Tufte, S. L., et al. 2003, ApJS, 149, 405 (Cited on page 7.)

Hartmann, L., Ballesteros-Paredes, J., & Bergin, E. A. 2001, ApJ, 562, 852 (Cited on page 39.)

Harwit, M. 1988, Astrophysical Concepts (Cited on page 17.)

Herbst, E. 1995, Annual Review of Physical Chemistry, 46, 27 (Cited on page 5.)

Heyer, M. & Dame, T. M. 2015, ARA&A, 53, 583 (Cited on pages 19, 77 and 145.)

Heyer, M., Krawczyk, C., Duval, J., & Jackson, J. M. 2009, ApJ, 699, 1092 (Cited on page 129.)

Hindson, L., Thompson, M. A., Urquhart, J. S., Clark, J. S., & Davies, B. 2010, MNRAS, 408, 1438 (Cited on pages 40, 84, 85, 95, 99, 117, 118 and 120.)

Hindson, L., Thompson, M. A., Urquhart, J. S., et al. 2012, MNRAS, 421, 3418 (Cited on pages 84, 94, 96, 112 and 117.)

Hindson, L., Thompson, M. A., Urquhart, J. S., et al. 2013, MNRAS, 435, 2003 (Cited on pages 79, 84, 85, 91, 94, 96, 99, 100, 105, 117, 131 and 135.)

Hoare, M. G., Purcell, C. R., Churchwell, E. B., et al. 2012, PASP, 124, 939 (Cited on page 26.)

Hodapp, K.-W. 1994, ApJS, 94, 615 (Cited on page 22.)

Hou, L. G. & Han, J. L. 2014, A&A, 569, A125 (Cited on page 69.)

Hoyle, F. & Ellis, G. R. A. 1963, Australian Journal of Physics, 16, 1 (Cited on page 7.)

Jackson, J. M., Simon, R., Shah, R., et al. 2004, in Astronomical Society of the Pacific Conference Series, Vol. 317, Milky Way Surveys: The Structure and Evolution of our Galaxy, ed. D. Clemens, R. Shah, & T. Brainerd, 49 (Cited on page 67.)

Jenkins, E. B. 1978, ApJ, 219, 845 (Cited on page 7.)

Kauffmann, J., Pillai, T., & Goldsmith, P. F. 2013, ApJ, 779, 185 (Cited on pages 127 and 135.)

Kessel-Deynet, O. & Burkert, A. 2003, MNRAS, 338, 545 (Cited on page 120.)

Kim, K.-T. & Koo, B.-C. 2001, ApJ, 549, 979 (Cited on page 99.)

Klein, B., Hochgürtel, S., Krämer, I., et al. 2012, A&A, 542, L3 (Cited on page 49.)

Kleiner, S. C. & Dickman, R. L. 1985, ApJ, 295, 466 (Cited on page 105.)

Klessen, R. S. 2001, ApJ, 556, 837 (Cited on page 24.)

Klessen, R. S. & Burkert, A. 2000, ApJS, 128, 287 (Cited on page 24.)

Klessen, R. S. & Burkert, A. 2001, ApJ, 549, 386 (Cited on page 24.)

Kolmogorov, A. 1933, Inst. Ital. Attuari, Giorn., 4, 83 (Cited on pages 110 and 132.)

Kroupa, P. 2001, MNRAS, 322, 231 (Cited on page 24.)

Krumholz, M. R., Bate, M. R., Arce, H. G., et al. 2014, in Protostars and Planets VI, ed. H. Beuther, R. S. Klessen, C. P. Dullemond, & T. Henning, 243 (Cited on pages 26, 27, 28, 40, 83, 118 and 120.)

Krumholz, M. R., Dekel, A., & McKee, C. F. 2012, ApJ, 745, 69 (Cited on page 40.)

Krumholz, M. R., Klein, R. I., McKee, C. F., Offner, S. S. R., & Cunningham, A. J. 2009, Science, 323, 754 (Cited on page 27.)

Krumholz, M. R. & Matzner, C. D. 2009, ApJ, 703, 1352 (Cited on page 28.)

Kudritzki, R. P., Puls, J., Lennon, D. J., et al. 1999, A&A, 350, 970 (Cited on page 27.)

Kurtz, S., Cesaroni, R., Churchwell, E., Hofner, P., & Walmsley, C. M. 2000, in Protostars and Planets IV, ed. V. Mannings, A. P. Boss, & S. S. Russell, 299–326 (Cited on page 26.)

Kylafis, N. D. & Norman, C. A. 1991, ApJ, 373, 525 (Cited on page 26.)

Lada, C. J. 1987, in Star Forming Regions, ed. M. Peimbert & J. Jugaku, Vol. 115, 1 (Cited on pages 22 and 23.)

Lada, C. J. & Lada, E. A. 2003, ARA&A, 41, 57 (Cited on pages 19, 22, 24 and 25.)

Lada, C. J., Lombardi, M., & Alves, J. F. 2010, ApJ, 724, 687 (Cited on page 78.)

Lada, E. A. 1992, ApJ, 393, L25 (Cited on page 118.)

Lada, E. A., Depoy, D. L., Evans, Neal J., I., & Gatley, I. 1991, ApJ, 371, 171 (Cited on page 22.)

Larson, R. B. 1969, MNRAS, 145, 271 (Cited on pages 20 and 22.)

Ledrew, G. 2001, JRASC, 95, 32 (Cited on page 17.)

Lee, H.-T. & Chen, W. P. 2007, ApJ, 657, 884 (Cited on page 120.)

Leistra, A., Cotera, A. S., Liebert, J., & Burton, M. 2005, AJ, 130, 1719 (Cited on pages 85, 89, 100, 102 and 117.)

Li, Z.-Y. & Nakamura, F. 2006, ApJ, 640, L187 (Cited on page 27.)

Lumsden, S. L., Hoare, M. G., Urquhart, J. S., et al. 2013, ApJS, 208, 11 (Cited on pages 85 and 117.)

MacLaren, I., Richardson, K. M., & Wolfendale, A. W. 1988, ApJ, 333, 821 (Cited on page 127.)

Masunaga, H. & Inutsuka, S.-i. 1999, ApJ, 510, 822 (Cited on page 21.)

Masunaga, H. & Inutsuka, S.-i. 2000, ApJ, 531, 350 (Cited on page 22.)

Matzner, C. D. 2002, ApJ, 566, 302 (Cited on page 28.)

Matzner, C. D. 2007, ApJ, 659, 1394 (Cited on page 27.)

Matzner, C. D. & McKee, C. F. 2000, in American Astronomical Society Meeting Abstracts, Vol. 195, American Astronomical Society Meeting Abstracts #195, 135.07 (Cited on page 25.)

Mauerhan, J. C., Van Dyk, S. D., & Morris, P. W. 2011, AJ, 142, 40 (Cited on pages 85 and 117.)

Mazumdar, P., Wyrowski, F., Colombo, D., et al. 2021a, A&A, 650, A164 (Cited on pages 83, 117, 118, 121, 122, 124, 129 and 132.)

Mazumdar, P., Wyrowski, F., Urquhart, J. S., et al. 2021b, A&A, 656, A101 (Cited on page 117.)

McKee, C. F. & Holliman, John H., I. 1999, ApJ, 522, 313 (Cited on page 19.)

McKee, C. F. & Ostriker, E. C. 2007, ARA&A, 45, 565 (Cited on page 39.)

McKee, C. F. & Ostriker, J. P. 1977, ApJ, 218, 148 (Cited on pages 5 and 7.)

McKee, C. F. & Tan, J. C. 2002, Nature, 416, 59 (Cited on page 24.)

McKee, C. F. & Williams, J. P. 1997, ApJ, 476, 144 (Cited on page 19.)

Mebold, U., Winnberg, A., Kalberla, P. M. W., & Goss, W. M. 1982, A&A, 115, 223 (Cited on page 10.)

Mellema, G., Arthur, S. J., Henney, W. J., Iliev, I. T., & Shapiro, P. R. 2006, ApJ, 647, 397 (Cited on page 28.)

Menten, K. M. 1991, in Astronomical Society of the Pacific Conference Series, Vol. 16, Atoms, Ions and Molecules: New Results in Spectral Line Astrophysics, ed. A. D. Haschick & P. T. P. Ho, 119–136 (Cited on page 26.)

Miesch, M. S. & Bally, J. 1994, ApJ, 429, 645 (Cited on page 105.)

Miesch, M. S., Scalo, J., & Bally, J. 1999, ApJ, 524, 895 (Cited on page 105.)

Milam, S. N., Savage, C., Brewster, M. A., Ziurys, L. M., & Wyckoff, S. 2005, ApJ, 634, 1126 (Cited on pages 95 and 125.)

Millar, T. J. 1997, IAU Symposium, 178, 75 (Cited on page 26.)

Miville-Deschênes, M.-A., Murray, N., & Lee, E. J. 2017, ApJ, 834, 57 (Cited on pages 17 and 18.)

Molinari, S., Bally, J., Noriega-Crespo, A., et al. 2011, ApJ, 735, L33 (Cited on page 18.)

Molinari, S., Pezzuto, S., Cesaroni, R., et al. 2008, A&A, 481, 345 (Cited on page 135.)

Motte, F., Bontemps, S., & Louvet, F. 2018, ARA&A, 56, 41 (Cited on pages 83 and 118.)

Motte, F., Schilke, P., & Lis, D. C. 2003, ApJ, 582, 277 (Cited on page 69.)

Muders, D., Hafok, H., Wyrowski, F., et al. 2006, A&A, 454, L25 (Cited on page 86.)

Myers, P. C. 1998, ApJ, 496, L109 (Cited on page 24.)

Nagakura, T., Hosokawa, T., & Omukai, K. 2009, MNRAS, 399, 2183 (Cited on page 120.)

Nguyen Luong, Q., Motte, F., Schuller, F., et al. 2011, A&A, 529, A41 (Cited on page 69.)

Oliveira, I., Olofsson, J., Pontoppidan, K. M., et al. 2011, ApJ, 734, 51 (Cited on page 12.)

Ossenkopf, V. & Mac Low, M. M. 2002, A&A, 390, 307 (Cited on page 105.)

Panagia, N. 1973, AJ, 78, 929 (Cited on pages 99 and 129.)

Pardo, J. R., Cernicharo, J., & Serabyn, E. 2001, IEEE Transactions on Antennas and Propagation, 49, 1683 (Cited on page 86.)

Pellegrini, E. W., Baldwin, J. A., Brogan, C. L., et al. 2007, ApJ, 658, 1119 (Cited on pages 100 and 127.)

Pestalozzi, M. R., Minier, V., & Booth, R. S. 2005, A&A, 432, 737 (Cited on page 26.)

Pettitt, A. R., Dobbs, C. L., Acreman, D. M., & Bate, M. R. 2015, MNRAS, 449, 3911 (Cited on page 69.)

Pokhrel, R., Myers, P. C., Dunham, M. M., et al. 2018, ApJ, 853, 5 (Cited on pages 19 and 21.)

Polehampton, E., Hafok, H., & Muders, D. 2019, APEX Calibration and Data Reduction Manual, Atacama Pathfinder EXperiment (APEX), aPEX Report APEX-MPI-MAN-0012, Revision 1.3 (Cited on page 86.)

Pratap, P., Dickens, J. E., Snell, R. L., et al. 1997, ApJ, 486, 862 (Cited on page 19.)

Ragan, S. E., Henning, T., Tackenberg, J., et al. 2014, A&A, 568, A73 (Cited on pages 39 and 69.)

Ramírez Alegría, S., Borissova, J., Chené, A. N., et al. 2014, A&A, 564, L9 (Cited on page 70.)

Rathborne, J. M., Burton, M. G., Brooks, K. J., et al. 2002, MNRAS, 331, 85 (Cited on page 101.)

Rathborne, J. M., Johnson, A. M., Jackson, J. M., Shah, R. Y., & Simon, R. 2009, ApJS, 182, 131 (Cited on page 69.)

Reid, M. J., Menten, K. M., Brunthaler, A., et al. 2019, ApJ, 885, 131 (Cited on page 69.)

Reynolds, R. J. 1991, in The Interstellar Disk-Halo Connection in Galaxies, ed. H. Bloemen, Vol. 144, 67 (Cited on page 7.)

Rigby, A. J., Moore, T. J. T., Eden, D. J., et al. 2019, A&A, 632, A58 (Cited on pages 19, 39, 68, 122, 124, 134 and 137.)

Rigby, A. J., Moore, T. J. T., Plume, R., et al. 2016, MNRAS, 456, 2885 (Cited on pages 39, 67 and 121.)

Rogerson, J. B., York, D. G., Drake, J. F., et al. 1973, ApJ, 181, L110 (Cited on page 7.)

Rosen, A. L., Offner, S. S. R., Sadavoy, S. I., et al. 2020, Space Sci. Rev., 216, 62 (Cited on page 25.)

Rosolowsky, E. & Leroy, A. 2006, PASP, 118, 590 (Cited on pages 19 and 124.)

Rosolowsky, E. W., Pineda, J. E., Kauffmann, J., & Goodman, A. A. 2008, ApJ, 679, 1338 (Cited on pages 67 and 123.)

Russeil, D., Zavagno, A., Adami, C., et al. 2012, A&A, 538, A142 (Cited on page 79.)

Russell, H. N. 1914, Popular Astronomy, 22, 275 (Cited on page 17.)

Sadaghiani, M., Sánchez-Monge, Á., Schilke, P., et al. 2020, A&A, 635, A2 (Cited on page 79.)

Salpeter, E. E. 1955, ApJ, 121, 161 (Cited on page 24.)

Scalo, J. M. 1986, Fund. Cosmic Phys., 11, 1 (Cited on page 24.)

Schöier, F. L., van der Tak, F. F. S., van Dishoeck, E. F., & Black, J. H. 2005, A&A, 432, 369 (Cited on page 92.)

Schuller, F., Csengeri, T., Urquhart, J. S., et al. 2017, A&A, 601, A124 (Cited on pages 45, 67, 74, 77 and 98.)

Schuller, F., Menten, K. M., Contreras, Y., et al. 2009, A&A, 504, 415 (Cited on pages 45, 68, 121 and 122.)

Schuller, F., Urquhart, J. S., Csengeri, T., et al. 2021, MNRAS, 500, 3064 (Cited on page 39.)

Shara, M. M., Moffat, A. F. J., Gerke, J., et al. 2009, AJ, 138, 402 (Cited on pages 85 and 117.)

Shu, F. H., Allen, A., Shang, H., Ostriker, E. C., & Li, Z.-Y. 1999, in NATO Advanced Study Institute (ASI) Series C, Vol. 540, The Origin of Stars and Planetary Systems, ed. C. J. Lada & N. D. Kylafis, 193 (Cited on page 27.)

Smirnov, N. V. 1939, Bull. Math. Univ. Moscou, 2, 3 (Cited on pages 110 and 132.)

Smith, R. J., Glover, S. C. O., Clark, P. C., Klessen, R. S., & Springel, V. 2014, Monthly Notices of the Royal Astronomical Society, 441, 1628 (Cited on page 11.)

Sobolev, A. M., Cragg, D. M., & Godfrey, P. D. 1997, A&A, 324, 211 (Cited on page 26.)

Solomon, P. M., Rivolo, A. R., Barrett, J., & Yahil, A. 1987, ApJ, 319, 730 (Cited on page 124.)

Spitzer, Lyman, J. 1956, ApJ, 124, 20 (Cited on page 7.)

Steiman-Cameron, T. Y., Wolfire, M., & Hollenbach, D. 2010, ApJ, 722, 1460 (Cited on page 69.)

Stutzki, J., Bensch, F., Heithausen, A., Ossenkopf, V., & Zielinsky, M. 1998, A&A, 336, 697 (Cited on page 67.)

Sugitani, K. & Ogura, K. 1994, ApJS, 92, 163 (Cited on page 84.)

Testi, L., Birnstiel, T., Ricci, L., et al. 2014, in Protostars and Planets VI, ed. H. Beuther, R. S. Klessen, C. P. Dullemond, & T. Henning, 339 (Cited on page 12.)

Thompson, M. A., Urquhart, J. S., Moore, T. J. T., & Morgan, L. K. 2012, MNRAS, 421, 408 (Cited on pages 29, 40 and 135.)

Thompson, M. A., Urquhart, J. S., & White, G. J. 2004, A&A, 415, 627 (Cited on page 85.)

Tielens, A. G. G. M. 2008, ARA&A, 46, 289 (Cited on page 101.)

Tielens, A. G. G. M. & Hollenbach, D. 1985, ApJ, 291, 722 (Cited on page 91.)

Tsuboi, M. & Miyazaki, A. 2012, PASJ, 64, 111 (Cited on page 19.)

Ulich, B. L. & Haas, R. W. 1976, ApJS, 30, 247 (Cited on pages 86 and 121.)

Urquhart, J. S., Figura, C. C., Moore, T. J. T., et al. 2014a, MNRAS, 437, 1791 (Cited on pages 69, 85, 103 and 117.)

Urquhart, J. S., König, C., Giannetti, A., et al. 2018, MNRAS, 473, 1059 (Cited on pages 122, 134 and 135.)

Urquhart, J. S., Moore, T. J. T., Csengeri, T., et al. 2014b, MNRAS, 443, 1555 (Cited on page 121.)

Urquhart, J. S., Thompson, M. A., Morgan, L. K., et al. 2007, A&A, 467, 1125 (Cited on page 135.)

van der Tak, F. F. S., Black, J. H., Schöier, F. L., Jansen, D. J., & van Dishoeck, E. F. 2007, A&A, 468, 627 (Cited on page 77.)

van Dishoeck, E. F. 2014, Faraday Discussions, 168, 9 (Cited on pages 5 and 12.)

van Dishoeck, E. F. & van der Tak, F. F. S. 2000, in From Molecular Clouds to Planetary, ed. Y. C. Minh & E. F. van Dishoeck, Vol. 197, 97 (Cited on page 26.)

Vázquez-Semadeni, E., Gazol, A., & Scalo, J. 2000, ApJ, 540, 271 (Cited on page 20.)

Vázquez-Semadeni, E., González-Samaniego, A., & Colín, P. 2017, MNRAS, 467, 1313 (Cited on page 24.)

Vink, J. S., de Koter, A., & Lamers, H. J. G. L. M. 2000, A&A, 362, 295 (Cited on page 27.)

Walch, S. K., Whitworth, A. P., Bisbas, T., Wünsch, R., & Hubber, D. 2012, MNRAS, 427, 625 (Cited on page 28.)

Watkins, E. J., Peretto, N., Marsh, K., & Fuller, G. A. 2019, A&A, 628, A21 (Cited on page 99.)

Whitworth, A. 1979, MNRAS, 186, 59 (Cited on page 25.)

Wilson, T. L., Rohlfs, K., & Hüttemeister, S. 2013, Tools of Radio Astronomy (Cited on page 92.)

Wolfire, M. G., Hollenbach, D., & McKee, C. F. 2010, ApJ, 716, 1191 (Cited on page 11.)

Wolfire, M. G., McKee, C. F., Hollenbach, D., & Tielens, A. G. G. M. 2003, ApJ, 587, 278 (Cited on pages 6 and 9.)

Wood, D. O. S. & Churchwell, E. 1989, ApJS, 69, 831 (Cited on page 25.)

Wu, S.-W., Bik, A., Bestenlehner, J. M., et al. 2016, A&A, 589, A16 (Cited on page 17.)

Zavagno, A., Deharveng, L., Brand, J., et al. 2005, in Massive Star Birth: A Crossroads of Astrophysics, ed. R. Cesaroni, M. Felli, E. Churchwell, & M. Walmsley, Vol. 227, 346–351 (Cited on page 135.)

Zinnecker, H. & Yorke, H. W. 2007a, ARA&A, 45, 481 (Cited on page 83.)

Zinnecker, H. & Yorke, H. W. 2007b, ARA&A, 45, 481 (Cited on page 118.)

Appendix A

Catalog of G305 clumps' properties

Table A.1: Catalog of properties of leaves and branches derived from the ^{13}CO dendrogram of G305.

Index	Type	x_c [°]	y_c [°]	Radius [pc]	v_{rms} [km s^{-1}]	log(Lum) [pc^2 K km s^{-1}]	log(Mass) [M$_\odot$]	α_{vir}	log(n_{H_2}) [cm^{-3}]	log($\bar{F}_{8\,\mu m}$)
0	b	305.145	0.206	0.9	1.0	1.288	3.1	0.47	3.8	2.3
1	l	305.505	-0.117	0.3	0.9	0.210	2.2	1.44	4.1	1.8
2	l	305.145	0.206	0.9	1.0	1.270	3.1	0.43	3.8	2.3
3	l	305.150	0.238	0.3	0.6	-0.538	nan	nan	nan	2.2
4	l	305.146	0.190	0.3	0.5	-0.215	nan	nan	nan	2.4
5	b	305.354	-0.081	0.4	1.2	0.301	2.0	4.60	3.6	2.1
6	l	305.350	-0.085	0.3	1.0	-0.292	nan	nan	nan	2.1
7	l	305.356	-0.079	0.3	0.9	0.100	2.0	1.77	4.1	2.1
8	l	305.443	-0.256	0.2	1.1	-0.658	nan	nan	nan	1.8
9	b	305.285	0.164	14.1	4.2	3.647	5.8	0.26	2.9	2.3
10	b	305.285	0.164	14.1	4.2	3.642	5.8	0.26	2.9	2.3
11	b	305.285	0.164	14.1	4.2	3.646	5.8	0.26	2.9	2.3
12	b	305.284	0.163	14.1	4.1	3.632	5.8	0.25	2.9	2.3
13	b	305.284	0.163	14.1	4.1	3.617	5.8	0.25	2.9	2.3
14	b	305.284	0.162	14.0	4.1	3.595	5.8	0.25	2.9	2.3
15	b	305.284	0.163	14.1	4.1	3.635	5.8	0.25	2.9	2.3
16	b	305.284	0.163	14.1	4.1	3.625	5.8	0.25	2.9	2.3

Index	Type	x_c [°]	y_c [°]	Radius [pc]	v_{rms} [km s^{-1}]	log(Lum) [pc^2 K km s^{-1}]	log(Mass) [$M_\odot$]	α_{vir}	log(n_{H_2}) [cm^{-3}]	log($\bar{F}_{8\,\mu m}$)
17	b	305.284	0.161	13.9	4.0	3.559	5.8	0.26	2.9	2.4
18	b	305.284	0.161	13.8	4.0	3.537	5.8	0.26	2.9	2.4
19	b	305.284	0.162	14.0	4.1	3.602	5.8	0.25	2.9	2.3
20	b	305.285	0.163	14.1	4.1	3.629	5.8	0.25	2.9	2.3
21	b	305.284	0.163	14.1	4.1	3.631	5.8	0.25	2.9	2.3
22	b	305.285	0.164	14.1	4.2	3.647	5.8	0.26	2.9	2.3
23	b	305.285	0.164	14.1	4.2	3.648	5.8	0.26	2.9	2.3
24	b	305.804	-0.235	2.5	1.9	2.180	4.4	0.25	3.8	1.7
25	b	305.285	0.163	14.1	4.1	3.629	5.8	0.25	2.9	2.3
26	b	305.284	0.162	14.0	4.0	3.576	5.8	0.25	2.9	2.4
27	b	305.284	0.162	13.9	4.0	3.569	5.8	0.25	2.9	2.4
28	b	305.222	0.119	10.7	4.5	3.300	5.5	0.43	3.0	2.4
29	b	305.284	0.161	13.9	4.0	3.545	5.8	0.26	2.9	2.4
30	b	305.239	-0.014	3.8	2.8	2.931	5.2	0.13	4.0	2.4
31	b	305.240	-0.014	3.7	2.8	2.899	5.2	0.14	4.0	2.4
32	b	305.283	0.160	13.7	4.0	3.511	5.7	0.28	2.9	2.4
33	b	305.284	0.162	14.0	4.0	3.579	5.8	0.25	2.9	2.4
34	b	305.284	0.162	14.0	4.1	3.599	5.8	0.25	2.9	2.3
35	b	305.222	0.117	10.6	4.5	3.277	5.5	0.45	3.0	2.4
36	b	305.283	0.161	13.8	4.0	3.526	5.8	0.27	2.9	2.4
37	b	305.241	-0.011	3.3	2.7	2.762	5.0	0.17	4.0	2.5
38	l	305.177	0.002	0.6	1.0	0.820	3.0	0.40	4.3	2.5
39	b	305.284	0.162	14.0	4.1	3.598	5.8	0.25	2.9	2.3
40	b	305.448	0.008	1.0	2.0	1.293	3.2	1.57	3.8	1.9
41	l	305.919	-0.209	0.3	0.9	0.155	2.5	0.69	4.5	1.9
42	b	305.222	0.119	10.8	4.5	3.313	5.5	0.42	3.0	2.4
43	b	305.241	-0.012	3.5	2.7	2.807	5.1	0.16	4.0	2.5

Index	Type	x_c [°]	y_c [°]	Radius [pc]	v_{rms} [km s^{-1}]	log(Lum) [pc^2 K km s^{-1}]	log(Mass) [M$_\odot$]	α_{vir}	log(n_{H_2}) [cm^{-3}]	log($\bar{F}_{8\,\mu m}$)
44	b	305.242	-0.010	3.2	2.7	2.693	4.9	0.19	4.0	2.5
45	b	305.241	-0.012	3.4	2.7	2.783	5.0	0.16	4.0	2.5
46	l	305.445	0.005	0.9	0.6	0.913	3.0	0.22	3.7	1.9
47	b	305.284	0.163	14.1	4.1	3.617	5.8	0.25	2.9	2.3
48	l	305.944	-0.166	0.3	1.3	-0.036	2.2	2.61	4.2	2.2
49	b	305.284	0.161	13.9	4.0	3.551	5.8	0.26	2.9	2.4
50	l	305.312	-0.039	0.7	1.8	1.426	3.6	0.36	4.7	2.3
51	l	305.930	-0.184	0.6	1.4	0.494	2.2	4.77	3.5	1.9
52	b	305.284	0.161	13.9	4.0	3.554	5.8	0.26	2.9	2.4
53	b	305.284	0.161	13.9	4.0	3.541	5.8	0.26	2.9	2.4
54	b	305.121	0.013	0.9	1.6	1.308	3.1	1.23	3.8	2.2
55	l	305.143	-0.159	0.5	1.0	0.728	2.8	0.54	4.3	2.1
56	b	305.238	-0.013	3.8	2.9	2.939	5.2	0.14	4.0	2.4
57	b	305.133	-0.026	0.4	1.7	0.155	nan	nan	nan	2.0
58	l	305.113	0.190	0.3	1.3	-0.328	nan	nan	nan	2.3
59	l	305.795	-0.249	1.4	1.7	1.970	4.2	0.16	4.3	1.8
60	b	305.246	-0.014	2.5	1.9	2.483	4.7	0.12	4.1	2.5
61	b	305.237	-0.007	2.9	2.4	2.578	4.8	0.19	4.0	2.6
62	l	305.866	-0.078	1.1	0.5	0.907	2.5	0.68	2.9	2.0
63	l	305.107	0.010	0.3	0.7	0.041	2.1	0.83	4.3	2.2
64	l	305.281	-0.148	1.0	0.7	0.886	2.8	0.49	3.4	1.8
65	l	305.166	-0.147	0.6	0.7	0.681	2.9	0.23	4.1	2.0
66	b	305.260	-0.018	1.7	1.9	2.281	4.5	0.14	4.4	2.5
67	l	305.231	-0.025	0.7	0.7	1.519	3.8	0.05	4.7	2.3
68	l	305.434	0.002	0.3	0.6	0.149	2.3	0.49	4.2	1.9
69	l	305.124	0.013	0.8	0.8	0.939	3.0	0.35	3.9	2.2
70	l	305.453	0.015	0.5	0.6	0.286	2.5	0.47	3.9	1.9

Index	Type	x_c [°]	y_c [°]	Radius [pc]	v_{rms} [km s^{-1}]	log(Lum) [pc^2 K km s^{-1}]	log(Mass) [$M_\odot$]	α_{vir}	log(n_{H_2}) [cm^{-3}]	log($\bar{F}_{8\,\mu m}$)
71	l	305.225	-0.104	0.5	1.0	0.364	2.9	0.46	4.4	1.7
72	l	305.181	-0.076	0.6	1.0	0.636	3.0	0.39	4.3	2.0
73	b	305.851	-0.058	4.6	3.2	2.565	4.7	0.62	3.3	2.0
74	l	305.265	-0.132	0.3	0.8	0.033	2.3	0.79	4.3	1.7
75	l	305.144	-0.125	0.4	1.4	-0.051	nan	nan	nan	2.1
76	b	305.445	0.010	0.8	0.7	0.543	2.7	0.51	3.6	1.9
77	b	305.851	-0.058	4.6	3.2	2.571	4.7	0.64	3.3	2.0
78	l	305.338	0.333	0.6	0.7	-0.114	0.8	34.91	2.0	2.0
79	l	305.157	-0.132	0.4	0.8	-0.004	1.4	5.99	3.3	2.1
80	l	305.286	-0.107	0.4	1.2	0.342	2.7	0.61	4.6	1.8
81	l	305.218	-0.075	0.2	0.7	-0.252	2.1	0.72	4.5	2.0
82	l	305.133	-0.030	0.2	1.1	-0.377	nan	nan	nan	2.0
83	b	305.131	-0.027	0.4	3.3	0.888	2.7	7.33	4.3	2.0
84	b	305.865	-0.045	4.3	1.4	2.432	4.5	0.17	3.2	2.0
85	l	305.060	0.060	0.9	1.9	1.325	3.2	1.46	3.9	2.3
86	l	305.612	0.143	0.8	1.8	0.992	3.7	0.35	4.6	1.8
87	b	305.340	-0.077	0.9	1.0	0.750	3.1	0.44	3.8	2.1
88	l	305.134	-0.022	0.2	1.1	-0.432	nan	nan	nan	2.0
89	l	305.196	0.003	1.0	1.2	1.736	4.0	0.09	4.6	2.6
90	l	305.269	-0.015	1.1	1.4	2.103	4.3	0.07	4.7	2.6
91	l	305.058	0.027	0.5	1.5	0.605	2.3	3.22	3.9	2.2
92	l	305.451	0.114	1.2	0.6	1.335	3.3	0.14	3.7	1.7
93	b	305.365	0.209	2.9	2.7	2.896	5.1	0.11	4.3	2.5
94	l	305.618	-0.350	0.5	0.9	0.812	3.0	0.27	4.4	1.8
95	l	305.346	-0.082	0.7	0.9	0.544	3.0	0.42	4.1	2.1
96	l	305.229	-0.053	0.6	0.6	0.725	3.2	0.11	4.4	2.2
97	l	305.178	-0.020	0.5	1.0	0.639	2.9	0.46	4.3	2.5

Index	Type	x_c [°]	y_c [°]	Radius [pc]	v_{rms} [km s^{-1}]	log(Lum) [pc^2 K km s^{-1}]	log(Mass) [$M_\odot$]	α_{vir}	log(n_{H_2}) [cm^{-3}]	log($\bar{F}_{8\,\mu m}$)
98	b	305.364	0.205	2.6	2.6	2.843	5.1	0.10	4.4	2.6
99	b	305.217	0.245	4.4	2.3	2.928	5.1	0.12	3.8	2.4
100	b	305.209	0.233	5.5	2.4	2.984	5.2	0.14	3.5	2.4
101	l	305.886	-0.247	0.3	1.0	0.444	2.8	0.42	4.7	1.8
102	l	305.717	0.107	0.5	0.6	-0.187	nan	nan	nan	1.9
103	b	305.363	0.201	2.4	2.5	2.778	5.0	0.10	4.5	2.6
104	b	305.230	0.252	3.4	2.3	2.859	5.1	0.11	4.0	2.5
105	b	305.230	0.252	3.2	2.3	2.816	5.0	0.11	4.1	2.5
106	l	305.637	-0.405	1.1	0.8	1.117	3.2	0.36	3.6	1.7
107	l	305.949	-0.095	0.4	1.0	0.436	2.5	1.05	4.2	1.7
108	l	305.329	-0.067	0.4	0.9	0.243	2.5	0.66	4.2	2.1
109	b	305.577	-0.006	4.5	2.2	2.734	4.9	0.18	3.5	2.4
110	l	305.850	0.019	0.4	0.8	0.577	2.5	0.68	4.1	2.0
111	b	305.902	-0.011	2.6	1.2	1.926	4.1	0.18	3.4	1.9
112	l	305.199	0.028	0.8	1.6	1.826	4.0	0.13	4.9	2.8
113	b	305.399	0.236	5.9	2.5	3.040	5.3	0.14	3.5	2.4
114	l	305.233	0.210	0.2	0.6	-0.125	2.4	0.25	4.8	2.7
115	b	305.363	0.200	2.3	2.5	2.756	5.0	0.10	4.5	2.6
116	l	305.175	0.254	0.5	0.9	0.013	1.7	5.67	3.2	2.1
117	b	305.230	0.252	3.3	2.3	2.836	5.0	0.11	4.0	2.5
118	l	305.247	0.334	0.6	1.0	0.659	2.7	0.94	3.9	2.0
119	l	305.223	0.324	0.6	1.0	0.542	2.7	0.82	3.9	2.1
120	l	305.727	-0.231	0.4	0.7	0.668	2.7	0.27	4.4	1.9
121	l	305.826	-0.196	1.2	1.0	1.470	3.8	0.16	4.0	1.7
122	l	305.344	-0.103	0.3	0.9	0.049	2.3	0.91	4.4	1.9
123	l	305.928	-0.100	0.3	1.2	0.053	2.0	2.35	4.3	1.7
124	l	305.317	-0.092	0.5	0.6	0.384	2.9	0.18	4.3	1.9

Index	Type	x_c [°]	y_c [°]	Radius [pc]	v_{rms} [km s^{-1}]	log(Lum) [pc^2 K km s^{-1}]	log(Mass) [$M_\odot$]	α_{vir}	log(n_{H_2}) [cm^{-3}]	log($\bar{F}_{8\,\mu m}$)
125	l	305.341	-0.062	0.3	0.6	-0.018	2.0	0.78	4.1	2.1
126	l	305.958	-0.041	0.3	0.8	-0.032	1.9	1.71	4.1	1.7
127	b	305.902	0.003	2.2	1.2	1.782	4.0	0.19	3.5	1.9
128	l	305.900	0.014	1.5	1.1	1.649	3.9	0.17	3.9	1.9
129	l	305.208	0.141	0.6	0.7	0.717	2.9	0.31	4.1	2.1
130	b	305.364	0.206	2.7	2.6	2.852	5.1	0.10	4.4	2.5
131	b	305.362	0.193	1.8	2.4	2.595	4.8	0.11	4.6	2.7
132	l	305.420	0.248	0.3	0.7	-0.081	1.9	1.47	4.1	2.2
133	b	305.229	0.249	2.8	2.2	2.714	4.9	0.11	4.1	2.5
134	l	305.859	-0.203	0.4	0.8	0.215	2.0	1.86	3.7	1.7
135	l	305.478	-0.100	0.5	1.9	0.926	3.1	1.09	4.5	1.7
136	l	305.862	-0.022	0.2	0.8	0.029	2.0	1.14	4.4	1.9
137	b	305.576	-0.006	4.4	2.1	2.717	4.9	0.17	3.5	2.4
138	l	305.053	0.083	0.6	1.8	1.064	3.0	1.58	4.2	2.4
139	l	305.688	0.097	0.4	1.0	0.655	2.6	0.77	4.2	2.3
140	b	305.524	0.345	2.7	2.1	2.183	4.4	0.30	3.7	2.1
141	b	305.492	0.308	4.4	2.0	2.451	4.7	0.26	3.3	2.1
142	l	305.940	-0.179	1.2	0.9	1.289	3.2	0.42	3.6	1.9
143	l	305.882	-0.144	0.5	1.1	0.785	2.8	0.71	4.3	1.9
144	l	305.835	-0.067	1.9	1.1	2.103	4.3	0.08	4.0	2.1
145	l	305.312	-0.071	0.5	0.7	0.480	2.8	0.23	4.3	1.9
146	l	305.316	-0.036	0.4	0.7	0.851	3.0	0.12	4.7	2.4
147	b	305.711	0.122	1.8	2.1	1.719	3.6	1.25	3.5	1.9
148	b	305.364	0.206	2.8	2.6	2.858	5.1	0.11	4.3	2.5
149	l	305.417	0.202	0.5	0.6	0.757	3.0	0.13	4.4	2.2
150	b	305.528	0.348	2.1	1.9	1.861	4.1	0.39	3.7	2.2
151	l	305.539	0.340	0.7	1.6	1.226	3.5	0.34	4.6	2.4

Index	Type	x_c [°]	y_c [°]	Radius [pc]	v_{rms} [km s^{-1}]	log(Lum) [pc^2 K km s^{-1}]	log(Mass) [$M_\odot$]	α_{vir}	log(n_{H_2}) [cm^{-3}]	log($\bar{F}_{8\,\mu m}$)
152	l	305.879	-0.096	0.3	0.9	0.114	1.9	1.97	4.1	1.9
153	l	305.905	-0.044	0.9	0.9	0.866	3.2	0.32	3.8	1.8
154	l	305.869	-0.011	0.3	0.7	0.137	2.0	1.32	4.0	1.8
155	b	305.708	0.038	1.6	1.5	1.621	3.6	0.65	3.5	1.9
156	l	305.675	0.113	0.6	1.3	0.970	3.2	0.47	4.4	2.1
157	l	305.455	0.121	0.5	0.6	0.394	2.4	0.59	3.7	1.7
158	l	305.407	0.179	0.5	1.9	0.870	3.2	0.87	4.6	2.4
159	b	305.361	0.200	1.0	2.3	1.985	4.2	0.21	4.8	3.0
160	b	305.492	0.308	4.4	2.0	2.456	4.7	0.26	3.3	2.1
161	b	305.521	0.345	1.8	1.7	1.612	3.9	0.48	3.7	2.3
162	l	305.963	-0.196	0.3	1.2	0.004	1.8	4.95	4.0	1.9
163	l	305.990	-0.116	0.4	1.0	0.318	2.2	1.59	4.1	1.6
164	l	305.893	-0.080	1.0	0.7	0.897	3.2	0.22	3.8	1.8
165	l	305.238	0.007	0.2	1.0	0.185	2.4	0.64	4.8	2.3
166	b	305.567	-0.004	3.4	2.0	2.648	4.9	0.13	3.8	2.4
167	l	305.507	0.045	1.0	1.6	1.355	3.7	0.38	4.2	1.8
168	l	305.135	0.066	1.0	1.1	1.440	3.6	0.17	4.2	2.3
169	b	305.111	0.080	1.8	1.3	1.792	4.0	0.22	3.8	2.3
170	b	305.087	0.095	0.9	1.3	1.348	3.6	0.31	4.3	2.2
171	l	305.749	0.117	0.4	1.2	0.320	2.2	2.73	3.9	1.8
172	l	305.367	0.209	0.2	1.0	0.627	2.9	0.19	5.5	2.9
173	l	305.158	0.308	0.3	0.9	-0.444	0.8	23.57	3.1	1.9
174	l	305.553	0.363	0.7	0.8	1.027	3.2	0.17	4.3	2.1
175	l	305.597	0.454	0.7	1.9	0.986	3.0	1.65	4.1	nan
176	l	305.141	-0.162	0.3	0.8	-0.638	nan	nan	nan	2.0
177	l	305.131	-0.027	0.4	1.3	0.789	2.7	1.10	4.3	2.0
178	b	305.562	-0.003	2.7	2.0	2.581	4.8	0.12	4.1	2.5

Index	Type	x_c [°]	y_c [°]	Radius [pc]	v_{rms} [km s^{-1}]	log(Lum) [pc^2 K km s^{-1}]	log(Mass) [$M_\odot$]	α_{vir}	log(n_{H_2}) [cm^{-3}]	log($\bar{F}_{8\,\mu m}$)
179	l	305.307	0.006	0.3	1.1	0.079	1.9	3.55	3.9	2.2
180	b	305.565	-0.003	3.2	2.0	2.597	4.8	0.13	3.9	2.5
181	b	305.561	-0.001	2.5	1.8	2.526	4.7	0.11	4.1	2.5
182	l	305.679	0.041	0.3	0.8	0.176	2.3	0.68	4.5	2.1
183	l	305.099	0.084	0.3	1.0	0.618	2.8	0.32	4.9	2.2
184	l	305.457	0.200	0.3	0.5	-0.301	1.0	4.99	3.2	2.4
185	l	305.357	0.301	0.5	1.1	0.637	2.9	0.53	4.4	2.0
186	l	305.349	0.413	0.3	0.8	0.041	1.9	1.72	3.9	nan
187	b	305.564	0.002	2.3	1.8	2.423	4.6	0.12	4.1	2.5
188	b	305.565	0.006	1.9	1.6	2.371	4.5	0.10	4.2	2.6
189	l	305.139	0.009	0.2	1.3	-0.310	0.6	78.02	3.0	2.2
190	l	305.225	0.069	0.3	0.8	-0.149	1.7	2.96	3.7	1.9
191	l	305.082	0.102	0.5	0.9	0.765	3.0	0.30	4.4	2.1
192	l	305.772	0.141	0.3	1.0	0.193	2.1	1.79	4.1	1.9
193	l	305.511	-0.123	0.9	1.0	0.841	2.9	0.77	3.6	1.8
194	l	305.093	-0.075	0.3	1.5	0.305	1.9	6.14	4.1	2.0
195	l	305.154	0.042	0.8	0.7	0.931	3.1	0.18	4.0	2.2
196	b	305.709	0.025	1.0	0.8	1.175	3.4	0.19	4.0	1.9
197	l	305.708	0.024	0.9	0.8	1.115	3.3	0.17	4.1	1.9
198	l	305.181	0.043	0.2	0.7	0.068	2.5	0.23	5.0	2.4
199	l	305.226	0.051	0.3	0.8	0.025	2.2	0.96	4.4	2.3
200	l	305.703	0.060	0.8	1.4	0.999	3.1	0.84	3.9	1.9
201	b	305.712	0.117	1.6	1.2	1.320	3.4	0.55	3.4	1.9
202	l	305.240	0.259	1.2	1.3	2.083	4.3	0.08	4.6	2.6
203	l	305.104	0.246	0.6	1.4	1.027	2.9	0.96	4.2	2.0
204	b	305.150	-0.127	0.6	1.8	0.822	2.6	3.01	3.9	2.1
205	l	305.556	-0.011	0.3	0.8	0.715	2.9	0.15	5.3	2.7

Index	Type	x_c [°]	y_c [°]	Radius [pc]	v_{rms} [km s^{-1}]	log(Lum) [pc^2 K km s^{-1}]	log(Mass) [M$_\odot$]	α_{vir}	log(n_{H_2}) [cm^{-3}]	log($\bar{F}_{8\,\mu m}$)
206	l	305.657	-0.015	0.7	1.9	1.064	3.5	0.55	4.6	2.1
207	l	305.149	0.017	0.2	0.7	-0.009	1.9	0.83	4.4	2.6
208	l	305.369	0.346	0.3	0.8	-0.056	1.6	2.74	3.9	1.9
209	l	305.486	0.384	0.7	1.4	0.980	2.9	1.29	3.8	2.0
210	l	305.723	0.038	0.3	0.7	0.009	2.4	0.44	4.4	1.8
211	b	305.316	0.065	0.7	1.4	0.973	3.1	0.75	4.2	2.9
212	l	305.245	0.072	0.6	0.7	-0.046	1.5	5.73	2.7	2.0
213	l	305.700	0.132	0.7	0.9	0.833	3.0	0.36	4.0	2.0
214	b	305.437	0.241	2.0	1.2	1.951	4.2	0.12	3.9	2.1
215	l	305.526	-0.033	0.5	0.9	1.157	3.3	0.11	4.9	2.5
216	l	305.125	0.004	0.3	0.6	-0.569	nan	nan	nan	2.1
217	l	305.157	0.003	0.4	0.8	0.338	2.6	0.40	4.4	2.4
218	l	305.643	0.023	0.3	1.0	0.137	2.2	1.11	4.5	2.3
219	l	305.805	0.121	0.4	1.2	0.535	2.7	0.73	4.6	1.7
220	b	305.206	0.215	1.2	2.0	2.106	4.3	0.17	4.6	2.6
221	l	305.389	0.259	0.4	1.4	0.484	2.8	0.88	4.6	2.1
222	l	305.348	0.321	0.5	0.6	0.452	2.9	0.22	4.2	2.0
223	l	305.508	0.349	1.2	0.7	1.340	3.6	0.12	3.9	2.2
224	b	305.546	-0.355	2.0	1.8	1.771	4.0	0.49	3.6	1.8
225	l	305.086	-0.252	0.6	1.0	0.700	2.5	1.25	3.8	1.8
226	l	305.510	-0.150	0.2	1.0	-0.367	1.5	4.59	4.0	1.7
227	b	305.804	-0.099	2.2	1.3	1.913	4.2	0.15	3.8	1.9
228	l	305.546	-0.093	0.2	1.3	-0.097	1.9	2.97	4.4	2.1
229	l	305.320	0.069	0.3	1.0	0.303	2.5	0.68	4.5	3.2
230	l	305.715	0.112	0.8	0.8	0.872	3.0	0.37	3.9	2.0
231	l	305.424	0.230	1.3	1.2	1.572	3.8	0.19	4.1	2.2
232	l	305.385	0.225	0.6	0.8	0.819	3.0	0.24	4.3	2.5

Index	Type	x_c [°]	y_c [°]	Radius [pc]	v_{rms} [km s^{-1}]	log(Lum) [pc^2 K km s^{-1}]	log(Mass) [$M_\odot$]	α_{vir}	log(n_{H_2}) [cm^{-3}]	log($\bar{F}_{8\,\mu m}$)
233	b	305.223	0.236	2.2	2.1	2.396	4.6	0.17	4.1	2.6
234	l	305.416	0.248	0.2	0.7	-0.076	2.1	0.63	4.5	2.2
235	l	305.450	0.374	0.3	1.2	0.330	2.2	1.93	4.2	1.9
236	l	305.072	-0.241	0.4	1.0	0.167	1.8	4.18	3.7	1.7
237	l	305.155	-0.131	0.3	0.7	0.049	2.1	0.89	4.1	2.1
238	l	305.168	0.079	0.2	0.7	-0.056	2.0	0.77	4.5	2.1
239	l	305.657	0.094	0.5	1.0	0.435	2.6	0.91	4.0	2.0
240	l	305.676	0.133	0.2	1.2	-0.149	1.5	6.94	3.9	1.9
241	b	305.095	0.166	1.6	1.3	1.881	4.1	0.16	4.0	2.3
242	l	305.367	0.157	0.6	0.8	1.304	3.5	0.07	4.9	2.8
243	l	305.360	0.196	0.4	0.9	0.984	3.2	0.14	4.9	3.1
244	l	305.461	0.256	1.0	0.8	1.208	3.4	0.16	4.0	1.9
245	l	305.269	0.298	0.6	0.7	1.035	3.2	0.11	4.5	2.5
246	l	305.379	-0.237	0.9	1.2	1.666	3.7	0.19	4.3	2.3
247	l	305.562	0.012	0.6	0.8	1.440	3.5	0.08	4.7	2.8
248	l	305.627	0.020	0.4	1.0	0.253	2.4	1.07	4.2	2.3
249	l	305.670	0.025	0.6	1.5	0.711	2.7	1.62	3.9	2.3
250	l	305.455	0.199	0.3	1.4	0.322	2.4	1.68	4.6	2.3
251	l	305.203	0.232	0.6	0.8	1.462	3.7	0.07	4.8	2.5
252	l	305.160	0.245	0.6	0.6	0.558	2.8	0.24	4.0	2.1
253	l	305.424	0.294	0.3	1.7	0.512	2.5	2.13	4.5	2.0
254	l	305.426	0.358	0.3	0.8	-0.036	1.7	2.26	4.0	1.8
255	l	305.591	-0.164	0.3	0.8	-0.180	2.0	1.49	4.0	1.7
256	l	305.767	-0.063	0.2	1.1	-0.066	2.2	1.23	4.7	1.7
257	b	305.720	-0.045	1.4	0.8	1.221	3.4	0.27	3.5	1.8
258	l	305.593	0.002	0.4	0.9	0.590	2.8	0.42	4.4	2.3
259	l	305.631	0.000	0.3	1.0	0.354	2.9	0.27	5.0	2.3

Index	Type	x_c [°]	y_c [°]	Radius [pc]	v_{rms} [km s^{-1}]	log(Lum) [pc^2 K km s^{-1}]	log(Mass) [$M_\odot$]	α_{vir}	log(n_{H_2}) [cm^{-3}]	log($\bar{F}_{8\,\mu m}$)
260	l	305.313	0.060	0.3	0.7	0.320	2.6	0.27	4.6	2.7
261	b	305.094	0.165	1.2	1.1	1.584	3.8	0.17	4.1	2.3
262	b	305.093	0.163	1.3	1.1	1.643	3.8	0.16	4.1	2.3
263	l	305.209	0.204	0.6	1.7	1.767	4.0	0.13	5.3	2.8
264	l	305.160	0.309	0.3	0.7	0.127	2.2	0.69	4.2	2.0
265	l	305.813	-0.144	0.3	0.6	-0.108	1.5	2.63	3.6	1.7
266	l	305.675	-0.112	0.7	1.0	1.090	3.3	0.26	4.3	1.9
267	l	305.552	-0.055	0.7	1.2	1.159	3.5	0.23	4.5	2.3
268	l	305.730	-0.049	1.0	0.8	1.043	3.3	0.24	3.8	1.8
269	l	305.091	0.161	0.9	1.0	1.267	3.5	0.20	4.1	2.3
270	l	305.152	0.187	0.5	0.6	0.491	2.6	0.30	4.1	2.4
271	l	305.706	0.228	0.4	0.9	0.367	2.2	1.47	3.8	1.7
272	l	305.681	0.307	0.9	0.9	1.143	3.6	0.13	4.3	1.9
273	l	305.505	-0.387	0.7	1.0	0.517	2.7	1.01	3.7	1.9
274	b	305.552	-0.350	1.7	1.5	1.550	3.9	0.35	3.8	1.8
275	l	305.536	-0.356	1.0	1.2	1.227	3.6	0.24	4.2	1.8
276	l	305.442	-0.244	0.9	0.9	1.522	3.5	0.16	4.2	2.1
277	l	305.576	-0.225	1.2	0.9	1.386	3.5	0.22	3.8	1.8
278	l	305.701	-0.150	0.3	0.9	0.207	2.2	1.12	4.2	1.7
279	l	305.306	-0.105	0.4	0.5	0.196	2.0	0.84	3.7	1.9
280	l	305.767	-0.085	0.7	0.7	0.878	3.3	0.12	4.2	1.7
281	l	305.212	-0.043	0.8	1.3	1.064	3.0	0.88	3.8	2.4
282	l	305.686	0.095	0.5	1.3	0.476	2.0	6.78	3.4	2.3
283	l	305.070	0.127	0.4	0.8	0.371	2.6	0.53	4.2	2.2
284	l	305.707	0.144	0.5	0.7	0.617	2.9	0.21	4.3	1.9
285	l	305.273	0.164	0.2	0.8	-0.180	2.0	1.32	4.3	2.7
286	l	305.127	0.207	0.3	0.8	0.585	2.8	0.26	4.8	2.2

Index	Type	x_c [°]	y_c [°]	Radius [pc]	v_{rms} [km s^{-1}]	log(Lum) [pc^2 K km s^{-1}]	log(Mass) [M$_\odot$]	α_{vir}	log(n_{H_2}) [cm^{-3}]	log($\bar{F}_{8\,\mu m}$)
287	l	305.433	0.318	0.4	1.1	0.299	2.3	1.85	4.0	1.9
288	l	305.516	0.333	0.4	0.6	0.786	3.2	0.07	4.8	2.0
289	l	305.147	-0.122	0.3	0.6	0.121	2.3	0.36	4.5	2.1
290	l	305.811	-0.106	1.0	0.8	1.183	3.8	0.07	4.3	1.8
291	l	305.693	-0.033	0.5	0.8	0.605	2.8	0.37	4.1	1.9
292	l	305.493	0.010	0.3	0.8	-0.284	1.8	1.71	4.1	1.8
293	l	305.249	0.190	0.2	0.7	-0.420	1.9	0.75	4.6	2.4
294	l	305.148	0.199	0.2	1.1	-0.319	nan	nan	nan	2.5
295	l	305.424	0.212	0.2	0.7	-0.456	1.3	3.37	4.0	2.3
296	l	305.272	0.244	0.3	0.8	0.496	2.7	0.23	5.0	2.7
297	l	305.252	0.078	0.9	0.9	1.089	3.4	0.20	4.1	1.9
298	b	305.651	0.122	1.0	1.1	1.074	3.3	0.42	3.9	2.1
299	l	305.486	0.168	0.8	0.8	0.873	3.3	0.20	4.1	1.8
300	l	305.114	0.190	0.4	0.7	0.340	2.5	0.33	4.4	2.3
301	l	305.151	0.207	0.2	0.9	-0.056	1.4	4.76	3.9	2.5
302	l	305.669	0.192	0.8	0.9	1.147	3.5	0.16	4.2	1.9
303	l	305.378	0.259	0.3	0.6	-0.022	2.2	0.43	4.6	2.1
304	l	305.582	-0.085	0.3	0.7	0.225	2.4	0.43	4.5	2.1
305	l	305.643	0.112	0.7	1.0	0.747	2.9	0.58	4.0	2.1
306	l	305.256	0.151	0.6	0.8	0.493	2.4	0.91	3.6	2.4
307	l	305.694	0.236	0.3	0.8	-0.076	1.7	2.23	3.8	1.9
308	l	305.328	0.275	0.7	0.7	1.068	3.3	0.14	4.3	2.2
309	l	305.879	-0.149	0.3	1.0	-0.143	1.3	13.14	3.2	1.9
310	l	305.236	0.193	0.2	0.9	-0.102	2.2	1.03	4.5	2.7
311	l	305.294	0.214	0.3	0.8	0.199	2.4	0.48	4.7	2.5
312	l	305.665	0.142	0.5	0.7	0.346	3.0	0.16	4.5	2.0
313	l	305.487	0.221	0.6	0.9	0.952	3.6	0.08	4.8	2.1

Index	Type	x_c [°]	y_c [°]	Radius [pc]	v_{rms} [km s^{-1}]	log(Lum) [pc^2 K km s^{-1}]	log(Mass) [M$_\odot$]	α_{vir}	log(n_{H_2}) [cm^{-3}]	log($\bar{F}_{8\,\mu m}$)
314	l	305.588	-0.264	0.3	0.7	-0.092	1.9	1.20	4.2	1.7
315	l	305.224	0.069	0.3	0.8	-0.051	1.9	1.89	3.8	1.9
316	l	305.400	0.198	0.2	0.7	-0.215	1.6	1.99	4.0	2.4
317	l	305.272	0.270	0.2	1.3	-0.187	2.1	1.97	4.7	2.7
318	l	305.513	0.354	0.6	1.2	-0.076	nan	nan	nan	2.2
319	l	305.263	-0.128	0.3	1.3	0.215	2.3	1.95	4.2	1.7
320	l	305.265	0.182	0.5	1.3	0.860	3.1	0.51	4.5	2.5
321	l	305.280	-0.153	0.6	1.0	0.322	1.9	5.77	3.1	1.8
322	l	305.316	0.070	0.5	0.6	0.114	1.9	1.82	3.4	3.0
323	l	305.300	0.085	1.0	0.7	1.033	3.1	0.33	3.6	2.1
324	l	305.894	0.015	0.4	0.9	-0.097	nan	nan	nan	2.0
325	l	305.231	0.223	0.3	0.8	-0.092	2.2	0.84	4.5	2.7
326	l	305.576	-0.341	0.6	0.7	0.819	3.2	0.13	4.5	1.7
327	l	305.848	-0.065	0.4	0.7	-0.357	nan	nan	nan	2.3
328	l	305.371	0.219	0.3	1.3	-0.097	1.5	10.66	3.8	2.5
329	l	305.529	-0.057	0.4	0.7	-0.119	1.8	1.77	3.7	2.2
330	l	305.305	0.191	0.5	1.1	0.464	2.7	0.70	4.3	2.5
331	l	305.152	0.239	0.4	1.2	-0.337	nan	nan	nan	2.2
332	l	305.979	-0.167	0.6	0.8	0.993	3.1	0.22	4.3	2.0
333	l	305.130	-0.029	0.2	1.2	-0.585	nan	nan	nan	1.9
334	l	305.299	0.168	0.4	0.9	0.241	2.4	0.90	4.2	2.1
335	l	305.133	-0.028	0.3	1.8	-0.569	nan	nan	nan	1.9
336	l	305.129	0.209	0.2	0.7	-0.854	nan	nan	nan	2.2

Ph.D. Dissertation